

NASA Contractor Report 3986

NASA-CR-3986 19860018591

Measurements of a Turbulent Horseshoe Vortex Formed Around a Cylinder

W. A. Eckerle and L. S. Langston

GRANT NSG-3238
JUNE 1986

LIBRARY COPY

JUN 1986
LANGLEY RESEARCH CENTER
LIBRARY, NASA
HAMPTON VIRGINIA

NASA



NF02268

NASA Contractor Report 3986

Measurements of a Turbulent Horseshoe Vortex Formed Around a Cylinder

W. A. Eckerle

*United Technologies Research Center
East Hartford, Connecticut*

L. S. Langston

*University of Connecticut
Storrs, Connecticut*

Prepared for
Lewis Research Center
under Grant NSG-3238

NASA

National Aeronautics
and Space Administration

**Scientific and Technical
Information Branch**

1986



TABLE OF CONTENTS

	Page
SYMBOLS	iv
SUMMARY	vii
INTRODUCTION	1
EXPERIMENTAL CONFIGURATION	3
Wind Tunnel	3
Flow Uniformity	3
Test Section	4
Test Model	6
Design	6
Afterbody	8
Probe Configuration	9
Five-Hole Probe	9
Probe Traverser	10
Data Acquisition System	10
Hardware	10
Software	11
RESULTS	13
Boundary Conditions	13
Surface Static Pressure Measurements	16
Endwall	16
Cylinder	17
Five-Hole Probe Measurements	18
Endwall Region	19
Test-Section Midspan	23
Boundary Layer Development in the Plane of Symmetry.	24
Pressure Loss	26
Surface Flow Visualizations	28
Technique	28
Endwall Visualization	29
Cylinder Visualization	31
Discussion of Vortex Formation	32
CONCLUSIONS	34
REFERENCES	35
FIGURES	38
APPENDIXES	
A - EXPERIMENTAL UNCERTAINTIES	104
B - TABULATED DATA	110

SYMBOLS

C_f	skin-friction coefficient, $\tau/(1/2 \rho U_\infty^2)$
C_P	pitot pressure coefficient, $(P_p - P_{S_0})/q_0$
C_{P_S}	static pressure coefficient $(P_S - P_{S_0})/q_0$
C_{P_T}	loss coefficient, $(P_{T_0} - P_T)/q_0$
\bar{C}_{P_T}	mass-averaged loss coefficient, equation (10)
D	cylinder diameter, 29.85 cm
h	test-section entrance height, 30.48 cm
H	boundary-layer shape factor, δ/θ_x
n	exponent in power law profile representation, $2/(H-1)$
P_1-P_5	five-hole probe pressures, figure 17
P_p	local pitot pressure
P_S	local static pressure
P_{S_0}	reference static pressure near test-section entrance
P_T	local total pressure
P_{T_0}	reference total pressure near test-section entrance
q	local dynamic pressure
q_0	reference dynamic pressure near test-section entrance
R	radial distance from instrumented-disk center, figure 25
Re_D	Reynolds number based on the cylinder diameter
Re_θ	Reynolds number based on boundary-layer momentum thickness
u	velocity in x-direction

u_τ	friction velocity, $\sqrt{\tau/\rho}$
u^+	universal velocity, u/u_τ
U	local velocity magnitude
U_0	reference velocity magnitude near test section entrance
U_∞	velocity at boundary-layer edge
v	velocity in y-direction
w	velocity in z-direction
x, y, z	orthogonal coordinate system as defined in figure 25
y^+	universal coordinate perpendicular to endwall, yu_τ/ν
y_{ms}	distance of midspan from endwall, 0.511 D
z_0	lower limit of mass-averaged loss integral, either 0 or D/2
z_w	distance from test-section plane of symmetry to sidewall, 0.91 m

Greek

β	position angle relative to plane of symmetry, figure 25
δ	boundary-layer thickness
δ^*	boundary-layer displacement thickness
η	profile factor, equation (9)
ρ	density
μ	viscosity
ν	kinematic viscosity, μ/ρ
ϕ	pitch angle, figure 17

θ corrected yaw angle, same sign convention as θ_{cal} , figure 17

θ_{cal} yaw angle correction for five-hole probe calibration, figure 17

θ_{meas} uncorrected yaw angle

θ_x boundary-layer momentum thickness

SUMMARY

As a uniform viscous fluid flow approaches wall-mounted structures such as a cascade of turbine airfoils, the boundary layers formed on the bounding walls (endwalls) separate in front of each airfoil. They then roll up into a horseshoe vortex system that is swept downstream around each airfoil. This vortex system and its formation can greatly influence both aerodynamic losses and heat transfer on endwall and airfoil regions.

This experimental investigation involved the aerodynamic measurement of the formation of a symmetrical horseshoe vortex system in front of and around a single large diameter right cylinder centered between the side walls of a wind tunnel. Test conditions included a Reynolds number of 5.5×10^5 and endwall turbulent boundary layer thicknesses of 13 percent, both based on cylinder diameter. Detailed surface flow visualization and static pressure measurements, and extensive mean velocity and pressure measurements in and around the vortex system flow field were made.

The results lend new insight into the formation and development of the vortex system. The actual vortex formation did not occur in the lateral plane of symmetry of the cylinder, but originated at a significant angular distance away from it. Also, contrary to the multiple vortex systems reported by others, only a single primary vortex and saddle point were found. The scale of the separation process occurring at the saddle point was found to be much smaller than the scale of the approaching boundary layer thickness.

Although the data presented are for the symmetrical endwall flow around a cascade of cylinders, the results can be used to shed light on such phenomena as the nonsymmetrical endwall flow in axial turbomachinery. The data can also be used as a test case for three dimensional computational fluid mechanics computer codes.



INTRODUCTION

As a result of the rapid development of computational hardware in the last decade, gas turbine engine designers have the opportunity to develop analysis techniques that can be used to significantly improve engine performance and durability. Numerical solutions of equations governing engine viscous internal flows are gaining acceptance as an alternative to costly experimentation in the development of new designs. To this end, the gas turbine community has been developing three-dimensional fluid dynamic codes that take advantage of extensive available computing power. Verification of these codes has been difficult because data characterizing these complex flows has been meager or nonexistent. Detailed measurements quantifying these flow fields are necessary to fully utilize the analysis techniques.

In particular, a turbulent boundary layer approaching a local obstruction, such as when annulus wall boundary layers encounter airfoils and support struts, has not been well documented. Studies to date show that fluid outside the boundary layer has enough momentum to overcome the streamwise pressure gradient generated by the obstacle. Low momentum flow in the boundary layer, however, cannot negotiate the local adverse pressure gradient and separates from the wall. The separation process creates a reverse flow region in front of the obstacle, bringing higher momentum flow from outside the boundary layer close to the wall. As the reverse flow convects around the obstacle, the streamwise and reverse flow interaction leads to the formation of a vortex system. A leg of the vortex passes around each side of the obstacle creating the characteristic horseshoe-like shape when viewed from above.

The reverse flow and vortex structure significantly alter local flow and heat transfer characteristics. The flow visualization of figure 1, obtained by Gaugler and Rusell (ref. 1) using the technique developed by Langston and Boyle (ref. 2), dramatically demonstrates the effect of this separation process on the endwall of a turbine vane cascade. The figure is a black and white print of the actual data. Blue ink dots (dark shade in fig. 1) were placed upstream of the separation zone and red dots (light shade) placed downstream of the separation. These two regions are distinct in the flow visualization. Almost the entire endwall in the passages is covered with light shade, indicating that the separation strongly impacts heat transfer and aerodynamic losses throughout the cascade's endwall region. This implies that details of the separation process must be accurately modeled to calculate flow parameters and temperature distribution through the cascade.

The symmetrical separation of boundary layer flow normal to a single cylinder (or a cascade of cylinders) is perhaps the simplest of geometries that demonstrate the horseshoe vortex phenomenon (e.g., ref. 3), while the

vortex system formed on the endwall of a cascade of turbine airfoils (e.g., refs. 1 and 4), might be considered to be one of the most complex of the family of such flows.

This paper deals with the experimental study of the simple cylinder vortex system. Aerodynamic measurements were made to define the horseshoe vortex system formed around a single cylinder mounted between endwalls in a wind tunnel. Because of the existence of the sidewalls of the tunnel, the cylinder model approximates one element of a cascade of cylinders. The tests were carried out at a relatively high Reynolds number with turbulent boundary layers on the endwalls. The objectives of the study were as follows:

1. There have been a number of studies carried out to measure and explain cylinder endwall flow and these have been reviewed by Eckerle (ref. 1). The conclusion of this review is that few or no measurements have been taken in the vortex region itself, especially in the region of vortex formation. Also, in most studies, the scale of the experiment was too small for accurate and detailed measurements. In the study presented here, measurements were made in the vortex region, and the cylinder model scale was about 100 times larger than the pressure probe scale.

2. Often it is possible to study and understand a simple member of a fluid flow family to explain and predict the behavior of a more complex member of that family. The study here represents the flow into a cascade of cylinders with zero angle of attack (no lift), at a Reynolds number based on cylinder diameter representative of many turbomachinery applications and with a large scale that would be difficult to achieve in an airfoil cascade. One objective then is to shed more light on the important problem of endwall flows in turbine cascades.

3. The measurements were taken in such a way (i.e., inlet and exit conditions to a control volume with interior flow measurements) that they can be used as a test case for three-dimensional computational fluid mechanics computer codes.

EXPERIMENTAL CONFIGURATION

The horseshoe vortex flow structure was investigated with a single cylinder immersed in a turbulent boundary layer. This simple and symmetric geometry created a strong secondary flow without the added complexity of an asymmetric flow field. Because of the symmetry, detailed flow measurements were required in only one quadrant of the test section. This represented a significant reduction in experimental data gathering since a large scale experiment was designed to minimize probe effects.

Wind Tunnel

Testing was conducted in the University of Connecticut Low Speed Wind Tunnel. This tunnel was an open circuit, suction type incorporating an inlet with a 9:1 contraction ratio, a 1.2 m long constant - area transition section for developing separate turbulent boundary layers on the top and bottom endwalls, and a 1.8 m long constant-area test section. Flow from the test section dumped into a large plenum and subsequently exhausted into the laboratory via a centrifugal fan and 75 HP motor. The maximum velocity that could be delivered to the test section, which had a 0.3 x 1.8 m cross section, was 30.5 m/sec.

A settling chamber built for these tests at the tunnel entrance effectively isolated the tunnel from the laboratory. A bellmouth on the front of the chamber served to catch flow. The entrance height was 2.8 m, while the chamber width matched that of the 1.8 m wide tunnel. Prior to entering the chamber, the flow passed through a porous plate (23 percent porosity), 15 cm of 0.3 cm cell honeycomb, and a fine mesh screen. The porous plate created a pressure drop to smooth out local nonuniformities in the entering flow. The flow then fully developed as it passed through the honeycomb's high length/diameter passages. This process removed streamwise vorticity from the entering flow. The fine mesh screen broke up any wakes created by the plate and honeycomb. After this conditioning process, the flow was contracted before passing through the transition section. Figure 2 is a photograph of the wind tunnel in its location inside the laboratory.

Flow Uniformity. - Even though the tunnel was in close proximity to the laboratory walls, the settling chamber arrangement created a reasonably uniform flow field at the test-section entrance. A pitot pressure profile measured near the test section entrance at the tunnel centerline is contained in figure 3. Corresponding boundary-layer parameters are listed in Table I.

TABLE I. - BOUNDARY-LAYER PARAMETERS FOR CENTERLINE TRAVERSE

Tunnel Endwall	δ/h	δ^*/h	θ_x/h	δ^*/θ_x
Floor	0.083	0.0122	0.0091	1.34
Ceiling	0.092	0.0148	0.0109	1.36

The data are expressed as pressure coefficients using the total and dynamic pressures measured at the same streamwise location near the tunnel sidewalls for reference conditions. The profile is substantially symmetric, although the ceiling boundary layer was approximately 15 percent thicker than the floor boundary layer. Core-flow pressure coefficients in the profile are close to 1.0 indicating transverse uniformity of the entrance flow. Additional traverses acquired at 30.5 cm intervals across the test-section entrance plane contained a maximum core-flow total pressure deviation of less than one percent of the reference value.

Test section. - With the attainment of good flow symmetry, only one end-wall flow region needed to be documented. Since probes used in the test program were cantilevered from a positioner, which was an integral part of the test-section ceiling, probe interference effects were smaller for measurements near the test-section floor. The floor was modified to mate with the test model and to incorporate endwall instrumentation.

Floor Modification: The existing plexiglass floor was replaced with two aluminum plates. A support plate, figure 4, was bolted to the test-section angle iron frame. The remainder of the floor was a rotatable instrumented disk, figure 5, that fit concentrically inside the support plate. The floor disk, which contained static pressure taps, holes to concentrically mount the test cylinder, and an access hole for passing cylinder instrumentation lines out of the test section, was clamped to the underside of the support plate. Clamping was accomplished with four toggle clamps and four cam follower assemblies equally spaced around the disk.

The cam followers were mounted into slides, as shown in figure 6. This arrangement allowed the floor disk to be retracted from the support plate and rotated in the following manner. The toggle clamps were released, enabling the floor disk to rest on the cam followers. The cam followers were lowered, via the adjustment bolts shown in figure 6, until the O-ring seal was clear of the support plate. The floor disk, and therefore the static pressure taps, could then be rotated to position the taps as desired. With this design,

detailed endwall static pressure distributions were obtained with a minimum number of pressure taps. Since the cylinder mounted concentrically on the instrumented floor disk, detailed cylinder surface pressure distributions could also be obtained with a minimum of pressure taps.

The instrumented disk was accurately and repeatably located with index holes machined near the disk's outer edge. Since the disk had a large diameter, holes could easily be placed at one degree increments. A spring-loaded pin assembly, attached to the support plate, served as the reference for the disk angular location. Figure 7 is a photograph of a portion of the inverted test section floor showing the pin indicator, index holes, a toggle clamp, and a cam-follower assembly.

The pressure tap locations on the instrumented disk are listed in Table II. The radial and angular positions correspond to the polar coordinate system shown in figure 5.

TABLE II. - INSTRUMENTED FLOOR DISK STATIC PRESSURE TAP LOCATIONS

β -deg R-cm	-20	-10	0	10	20	± 40	± 60	± 80	90
	24.8	15.9	15.0	16.5	17.1	22.9	22.9	22.9	15.0
	32.4	18.4	17.8	19.1	19.7	30.5	30.5	30.5	
	39.4	21.0	20.3	21.6	22.2	38.1	38.1	38.1	
		23.5	22.9	24.1	24.8				
		26.0	25.4	26.7	27.3				
		28.6	27.9	29.2	29.8				
		31.1	30.5	31.8	32.4				
		33.7	33.0	34.3	34.9				
		36.8	35.6	38.1	39.4				
		41.9	40.6	43.2	44.5				
		47.0	45.7	48.3	49.5				
		53.3	50.8	55.9	58.4				
		63.5	61.0	66.0	68.6				
			71.1						

Taps were staggered along the disk radius at angular locations $\beta = -10, 0, 10,$ and 20 degrees. These taps provided pressures along any radial line every 0.64 cm for $15 < R < 35.6$ cm, every 1.27 cm for $35.6 < R < 50.8$ cm, and every 2.54 cm for $50.8 < R < 71.1$ cm by successively rotating each of the four lines

of taps to a desired angular location. Additional taps permitted acquisition of pressures to check flow symmetry. Static taps were also machined in the support plate to define boundary conditions. Locations for these taps are indicated in figure 4.

A photograph of the assembled test-section floor, taken with the floor inverted prior to installation in the tunnel, is shown in figure 8. The plug in the center of the instrumented floor disk was installed in the disk's access hole to permit tunnel checkout testing prior to the cylinder's installation. The small lines are stainless steel tubes that were epoxied to each of the pressure taps.

The angle iron support members sagged under the weight of the new floor. Adjustable trusses, incorporated into the test section frame, leveled the tunnel floor to within 0.125 cm.

Ceiling and Probe Positioner: An integral part of the test-section ceiling and this test program was the probe positioner assembly. This assembly consisted of two positioning disks and a series of support plates. A sketch of the disks is contained in figure 9. The probe extended through the hole in the small disk to the test section. Movement of the small disk positioned the probe to the radial position of the large disk corresponding to the desired probe position. The large disk then rotated the probe to the desired traverse location. For a given position of the disks, the probe could be moved to any point inside a 40 cm diameter circle. The support plates, shown disassembled with the disks in figure 10, could be interchanged so that the positioning disks could be moved to different ceiling locations covered by the support plates.

The positioning disks were mechanized as shown in figure 11. Gears were installed on top of each disk. The smaller gear was raised above the larger gear with a spacer plate. This arrangement permitted a D.C. motor and potentiometer to be connected to each gear. The motors and potentiometers accurately provided remote angular positioning of the disks.

Test Model

Design. - The experimental model was a cylinder that spanned the test section. The cylinder diameter was a compromise of two design constraints. A large-diameter cylinder, orders of magnitude larger than the probe, was desirable to minimize probe interference effects. At the same time the cylinder diameter was limited by the tunnel size. If the cylinder was too large, interference with the test-section sidewalls could alter the desired flow field.

Cylinder surface static pressures were calculated for inviscid flow through a cascade of cylinders to determine a desirable cylinder diameter. The plane of symmetry between the cylinders corresponded with the tunnel sidewalls. Calculations were performed for a range of cylinder diameters using a code developed at the University of Iowa. This code was based on the technique of Hess and Smith (ref. 5). The deviation of static pressure at ninety degrees from that for potential flow around a single cylinder was used to indicate the sidewall interference effects, since this pressure was most sensitive to the presence of the walls. A nominal cylinder diameter of 30.5 cm was chosen. This size decreased the calculated 90-deg static pressure by only five percent yet provided a model scale 100 times that of a five-hole probe.

The off-body static pressure distribution for this geometry was calculated using the inviscid analysis of Barber (ref. 6). Data from several angular planes are shown in figure 12 along with the distributions for potential flow around a single cylinder. Only a small effect of the sidewalls on pressures upstream of the cylinder can be discerned. The largest deviations occur in the 90-deg plane. Pressure coefficients in this plane are approximately five percent smaller (more negative) than those for a single isolated cylinder. The confining effect of the sidewalls, then, only insignificantly altered the pressure distribution leading to flow separation.

A sketch of the test model is shown in figures 13 and 14. The cylinder was fabricated from commercially available tubing with a nominal O.D. and wall thickness of 30.5 cm and 2.54 cm, respectively. The tubing was accurately turned down to an O.D. of 29.85 cm and polished to obtain a smooth surface finish. The cylinder concentrically bolted to the instrumented floor disk via the attachment holes shown in figure 5. An O ring provided the seal between the cylinder base and the instrumented floor disk. The top of the cylinder remained unattached allowing the cylinder to rotate with the floor disk. The cylinder also mated with the probe positioner that formed a portion of the test-section ceiling. Ensuring a seal between the cylinder and probe positioner disks was difficult. Since the positioner consisted of disks that rotated over the cylinder, only a small force could be exerted to gain a seal. A soft foam-type material that easily compressed was affixed to the top of the cylinder. A ridge was machined into the cylinder top surface to support the gasket against shear forces created by the relative rotation between the probe positioner disks and the cylinder. A disk using an O-ring seal was installed near the top of the cylinder, as shown in figure 14, to prohibit leakage of ambient air through the inside of the cylinder to the test section. The foam-type gasket only needed to seal against the much smaller circumferential pressure variation. Figure 15 is a photograph of the cylinder mounted in the tunnel.

Designing the cylinder to rotate with the instrumented floor disk enabled detailed cylinder surface pressure distributions to be obtained with a minimum of pressure taps. The tap locations on the cylinder are given in Table III. Pressure taps were staggered along the cylinder axis at four angular positions corresponding with the staggered rows of taps on the instrumented floor disk. Additional taps were included to check flow symmetry. Static pressures could be obtained every 0.64 cm on the lower half of the cylinder. Lines connected to the pressure taps were routed out of the cylinder through the access hole in the center of the instrumented floor disk.

TABLE III. - TEST CYLINDER STATIC PRESSURE TAP LOCATIONS

β -deg	-20	-10	0	10	20	± 40	± 60	± 80	90
y-cm	3.8	0.3	2.5	1.9	1.3	5.1	5.1	5.1	15.2
	8.9	3.2	5.1	4.4	3.8	10.2	10.2	10.2	
	14.0	5.7	7.6	7.0	6.4	15.2	15.2	15.2	
		8.3	10.2	9.5	8.9	22.9		22.9	
		10.8	12.7	12.1	11.4				
		13.3	15.2	14.6	14.0				
		22.9	17.8	22.9	22.9				
			20.3						
			22.9						
			25.4						
			27.9						

Afterbody. - An afterbody was fabricated to mate with the downstream side of the cylinder. The afterbody was designed to eliminate unsteadiness introduced into the upstream separation region by vortex shedding in the cylinder wake. Figure 16 is a sketch of the afterbody design. The afterbody, fabricated from aluminum, consisted of two side plates connected by three braces for rigidity. The upstream edge of the side plates had a machined radius that tangentially mated with the cylinder at the 90-deg plane. Gasket material was placed on all the afterbody's edges to prevent leakage. The afterbody length displaced the base region to the exit of the test section.

During the initial phase of the program, tests with the afterbody installed indicated a nonsymmetric flow field around the cylinder. In addition, the endwall saddle-point location determined from flow visualization tests varied from test to test. The afterbody effectively divided the test section into two constant area passages downstream of the cylinder. Evidently an unacceptable bistable flow structure set up as the flow divided itself between the two passages. As a result, this test program was conducted without the afterbody.

Probe Configuration

Five-Hole Probe. - Interior fluid measurements were obtained with a five-hole probe. The tip geometry for the probe, United Sensor Model DC-.093-24-F, is shown in figure 17. The probe tip diameter was 0.24 cm instead of the stock configuration of 0.32 cm. In addition, the tip was ogival rather than a standard truncated cone. The corners of the truncated cone, even though they contain large obtuse angles, cause inconsistencies in the calibration. (See Camarata et al. ref. 7.) The ogival tip makes the probe calibration less sensitive to changes in Reynolds number. The probe tip was aligned with the shaft axis (which is the reason for the "shephard's crook") so that the tip rotated but did not translate as the probe was rotated about the shaft axis. The nomenclature for the pressure taps is in figure 17. Tap 1 was the impact pressure while taps 2 and 3 were for nulling the probe in yaw. Taps 4 and 5 provided dynamic pressure and pitch angle from the calibration.

The probe was calibrated in an air jet from a 3.8 cm diameter nozzle. The sign convention used for the calibration, which was accomplished at a dynamic head of approximately 6.6 cm of water, is in figure 18. Yaw angle, θ_{cal} , was defined as the angle between the plane formed by the tip and the shaft of the probe and the projection of the velocity vector on the plane perpendicular to the shaft. Pitch angle ϕ , defined as the angle between the velocity vector and the plane perpendicular to the probe shaft, was varied from -29 to +30 degrees. For each calibration pitch angle, the probe was nulled in yaw by rotating the probe about the shaft axis until P_2 equaled P_3 . The resultant yaw angle, measured relative to a flag mounted on the shaft, was θ_{cal} . Pressures from the remaining taps were recorded to generate calibration curves shown in figure 19.

Measurements were likewise acquired in the wind tunnel. At a given spatial location in the flow field, the probe was rotated until the pressures from taps 2 and 3 were equal. The probe rotation, θ_{meas} , was measured relative to the core flow direction upstream of the cylinder. The sign convention for θ_{meas} was that shown in figure 17. The pressures P_1 , P_4 , and P_5 were recorded for each point. The data were reduced as follows. From the pressure ratio $(P_4 - P_5) / (P_1 - (P_4 + P_5) / 2)$, the pitch angle ϕ was determined from

figure 19A. Knowing ϕ , the parameter $(P_1 - (P_4 + P_5)/2)/q$ was determined from figure 19B and local dynamic pressure was calculated. Also using ϕ , figure 19C provided the parameter $(P_T - P_1)$ to calculate local total pressure. Similarly, figure 19D provided the calibration yaw angle θ_{cal} . Flow yaw angle, θ , was the sum of θ_{cal} and θ_{meas} . The Bernoulli equation was used to calculate local static pressure from the local total and dynamic pressures.

Probe Traverser. - An L.C. Smith Model BBR 16360 traverser positioned the probe. The traverser was mounted to the small gear with a bulkhead fitting as shown in figure 11. An access hole for installing and removing the probe was created through mating holes in the gear, spacer plate, and small positioner plate. Since the hole diameter had to be slightly larger than the 1.27 cm shephard's crook to allow passage of the probe, the bulkhead fitting which held the traverser was bored out and could not be used for sealing around the probe. Instead, ambient air was prevented from passing around the probe into the test section by a seal in the small positioning disk. With the probe in place and held by the traverser, a removable plug, shown in figure 20, was slipped over the probe tip inside the test section. (A recess, machined into the plug, allowed the plug to pass around the shephard's crook.) The plug fit into the positioner disk, as shown in figure 21, and bolted to the spacer plate. Sealing was accomplished by compressing a rubber washer between two steel washers in the plug, as shown in figure 22. The bulkhead fitting cap provided the sealing force through a long compression sleeve. This assembly also provided an effective technique for quick and safe removal of the delicate probes.

Data Acquisition System

Hardware. - Experimental data were acquired with an ADAC Corporation data acquisition system (DAS) shown in figure 2. The main components of the system were a Digital Equipment Corporation (DEC) LSI 1102 microcomputer with 32K words RAM, the DEC RT-11 operating system, a DEC VT100 terminal, ADAC dual 8-inch floppy disk drives, ADAC analog to digital and digital to analog convertors with software support packages, and an Axion IMP miniprinter. This system also contained an ADAC 1664 TTL input/output board that enabled the data system to send and receive signals across 64 ports. A control circuit interfaced between the 1664 TTL board and a model 555-48 CBM 48-port scanivalve.

A layout of the various components used with the DAS is shown in figure 23. The overall instrumentation setup involved connecting the various static taps and probes to the laboratory scanivalve box. The box, controlled by the DAS, sequentially connected each pressure to a single differential pressure transducer. Output from the transducer was integrated and sent to a Hewlett Packard (HP) model 3455A digital voltmeter, rather than to the DAS analog to

digital (A/D) converter because the converter resolution of 0.0012 volts was not low enough to accurately convert the transducer's millivolt signal. The DAS accessed the voltmeter through an IEEE buss. Other experimental outputs, such as flow temperature and probe position, were converted using the DAS A/D converter. All data were recorded on 8 inch floppy disks and subsequently reduced. The reduced data could be printed on the miniprinter, allowing immediate analysis.

The transducer was a Barocel (Gould type 590) with a range of 134.6 cm of water and a full scale output of ten volts. It was calibrated using a Von Essen-Delft type 250 Betz micromanometer accurate to 0.0010 cm of water. The transducer calibration was nearly linear (a least squares curve fit had a standard deviation of 0.00055 cm of water). Because the transducer was sensitive to the temperature rise caused by recirculating the room air through the tunnel, the transducer was mounted in an insulated box to slow the temperature transients. Temperature changes only shifted the calibration, without altering the slope. With the linear transducer calibration, temperature effects could be corrected by referencing all outputs to the output at zero pressure difference. The transducer reference pressure was connected to one scanivalve port to provide the zero pressure output for each test run. Teeing one pressure and the transducer reference pressure to the Betz micromanometer established a reference pressure that was hand recorded and compared with the transducer reading. This comparison indicated the accuracy of the calibration and provided a continual verification that the calibration had remained constant.

Software. - A flow chart of the program used for acquiring data with the DAS is in figure 24. Initially the program read input constants from a scratch file. The constants included run number, number of channels and number of samples to be collected from the DAS A/D converter, number of ports on the scanivalve to be sampled, number of samples to be gathered from each port, scanivalve stepping rate, and barometric pressure at the beginning of the run. Since the values of these constants could be changed external to the program, it could be used for a variety of instrumentation setups. The program opened a data file and assigned the current run number to that file. Acquisition constants along with the current time and date were entered into the file for reference purposes. Data from the DAS A/D converter were then collected, with the converted voltages stored in the data file. The collection rate was manually set on the DAS A/D board, which could sample up to 12 kHz. The program then used the following method to record signals from the scanivalve transducer: the program first sent the scanivalve to its home port and read the output signal from the scanivalve to ensure the scanivalve had stepped properly. The program then waited a specified period (15-20 seconds) for the transducer signal to be integrated before recording voltages from the HP A/D converter using the IEEE buss instrumentation. The transducer signal was slowly recorded (2 Hz) over 10-25 seconds (20-50 samples) to resolve low

frequency oscillations in the integrated signal. Next, the program sequentially stepped the scanivalve, repeating the above process for the number of ports defined by the acquisition constants. Finally, the program collected data from the DAS A/D converter a second time at the end of the run and closed the data file. Thus, the outputs connected to the DAS A/D board could be averaged over the duration of the run.

A program was also developed to reduce static pressure tap data. This program read the data stored on floppy disks, averaged the samples, computed average and standard deviations, and converted the pressure data to coefficients using the formula:

$$C_{P_s} = \frac{P_s - P_{s0}}{(P_T - P_s)_0}$$

where $P_s - P_{s0}$ was the pressure calculated from the transducer signal using the transducer calibration, and $(P_T - P_s)_0$ was the difference between the core flow total and static pressures measured with a pitot-static probe near the sidewall of the documented quadrant at the test-section entrance. In addition, the program calculated the average test-section entrance velocity and velocity head for the run based on the reference pressures.

A second program reduced the five-hole probe acquired data. This program contained tables of the calibration parameters shown in figure 19. Local static, total, and dynamic pressures, along with the local pitch and yaw angles, were calculated by linearly interpolating between the calibration points. The program used these results to calculate various velocity components and pressure coefficients required for analysis purposes. Both reduction programs could be run immediately following data acquisition to provide real-time analysis.

RESULTS

The test results are described in four sections. Initially the test-section entrance boundary condition is documented along with the floor static pressure distribution near the sidewalls. Subsequently the static pressure distributions on the endwall and cylinder surfaces are presented followed by a characterization of the five-hole probe measurements. Comparisons of the data with potential-flow calculations and experimental results described in the literature are also discussed. The flow field implied by limiting streamlines indicated by endwall and cylinder surface flow visualizations is then integrated with the vortex characteristics deduced from the other measurements to characterize the vortex formation process.

A schematic of the test section along with the coordinate system used in this effort are shown in figure 25. The origin of the coordinate systems coincides with the cylinder and disk center on the lower endwall. Angular and radial positions are denoted by β and R , respectively. Cartesian coordinates representing streamwise, vertical, and transverse locations, are x , y , and z , respectively. The experiment was designed to create vertical and horizontal planes of symmetry at the test-section centerline and midheight, respectively. As shown in figure 25, the lower quadrant on the right side of the test-section, when viewed facing downstream, was chosen for documentation.

All of the presented results were measured with a nominal test-section entrance dynamic pressure of five centimeters of water. These conditions correspond to $Re_D = 5.5 \times 10^5$. An uncertainty analysis for the data acquisition is included in Appendix A. A tabulation of the data is contained in Appendix B.

Boundary Conditions

The mean flow conditions near the test-section boundary were documented with the support plate static pressure taps and pitot-static probe traverses. The core flow turbulence intensity was measured with a hot-wire probe. Data were recorded with the cylinder installed in the test section.

The floor static pressure distribution measured near the test-section entrance is shown in figure 26. Blockage created by the cylinder caused a slight transverse static pressure gradient. The peak pressure at the tunnel centerline was approximately seven percent of the reference dynamic pressure above the reference static pressure. Away from the centerline, static pressure symmetrically decreased and approached the reference value near the tunnel sidewalls.

Static pressure variation in the streamwise direction measured near the tunnel sidewalls is shown in figure 27. The two distributions are similar, with the pressure decreasing in the streamwise direction. At the $x = 0$ plane, the pressure was approximately 22 percent of the dynamic head below the reference condition. The data in figures 26 and 27 document the flow symmetry about the tunnel centerline.

The flow field entering the test section was characterized with pitot-static probe traverses. Since the experiment contained two planes of symmetry, only the quadrant shown in figure 25 was documented in detail. Results from traverses acquired at the tunnel centerline, $z/D = 1.021$, and $z/D = 2.043$, are shown in figure 28. (Though a failure in the blower impeller precluded taking additional traverses with the cylinder installed, more closely spaced traverses acquired during shakedown tests indicated uniform test-section entrance conditions.) The velocity distributions are normalized by the freestream velocity at the edge of the boundary layer. Although the freestream velocity varied across the entrance plane due to the cylinder blockage, as shown in figure 29, the normalized profiles are nearly identical. From the perspective of a velocity power law, the profiles are well represented by the $1/5.7$ power-law shape shown in figure 28. The basis for this exponent value is defined later in the discussion concerning the plane of symmetry boundary-layer development.

The boundary-layer parameters calculated for the above three traverses are shown in Table IV.

TABLE IV. - TEST-SECTION ENTRANCE BOUNDARY-LAYER PARAMETERS WITH CYLINDER INSTALLED

$x/D = -2.72$

z/D	δ/D	δ^*/D	θ_x/D	δ^*/θ_x	C_f	Re_θ
0	0.099	0.0154	0.0114	1.35	0.0028	6149
1.021	0.099	0.0160	0.0118	1.36	0.0029	6156
2.043	0.097	0.0152	0.0113	1.35	0.0029	6037

The skin-friction coefficient was calculated using a technique developed by Clauser. The skin-friction velocity, u_τ , is given by $\sqrt{\tau/\rho}$. Using u_τ to normalize the mean velocity distribution, the inner twenty percent of the boundary layer, excluding the viscous sublayer, can be universally represented by the following expression, where y^+ has been substituted for yu_τ/ν :

$$u^+ = \frac{u}{u_\tau} = 5.6 \log y^+ + 4.9 \quad \text{for } y^+ \geq 10 \quad (1)$$

Defining the local skin-friction coefficient, C_f , as $\tau/(1/2\rho U_\infty^2)$, equation (1) can be rewritten as a universal family in terms of the velocity ratio u/U_∞ and Re_y with C_f as a parameter:

$$\frac{u}{U_\infty} = \sqrt{\frac{C_f}{2}} \left[5.6 \log \left(Re_y \sqrt{\frac{C_f}{2}} \right) + 4.9 \right] \quad (2)$$

A sample Clauser plot is in figure 30. With the experimental data acquired near the endwall plotted in this form, C_f was determined from the best fit to the data. The coefficients, shown in Table IV, are nearly identical across the entrance plane.

The pitot-static probe was too large to acquire data in the viscous sublayer. A correlation developed by Burton (ref. 8) for the mean velocity in the sublayer was used in the calculation of displacement and momentum thicknesses. This correlation is given by

$$y = \frac{v}{U_\infty} \sqrt{\frac{2}{C_f}} \left(u^+ + \left(\frac{u^+}{8.74} \right)^7 \right) \quad (3)$$

The mean velocity distribution in the sublayer, calculated with this correlation and the above determined skin-friction coefficients, was matched with that from the pitot-static probe. The combined distributions were integrated to determine the two integral boundary-layer thicknesses. The data in Table IV show little variation in these parameters. The shape factor, δ^*/θ_x , is also quite uniform and at a level typical of a constant-pressure turbulent boundary layer on a flat plate, as indicated by Schlichting (ref. 9).

Turbulence in the core flow was measured using a hot-wire probe with a single wire oriented perpendicular to the main flow. The turbulence intensity was less than one percent.

Surface Static Pressure Measurements

Static pressure measurements were obtained on the endwall and cylinder surfaces using pressure taps located at the positions shown in Tables II and III. Detailed distributions were acquired in the quadrant shown in figure 25. Additional measurements were made in the other quadrants to check the flow symmetry. The pressures are presented in coefficient form using the polar coordinate system defined in figure 25. These measurements are important because they are the only nonintrusive measurements in these tests. They serve as a basis for comparison with the flow visualization patterns and five-hole probe results.

Endwall. - Plane of Symmetry: The endwall static pressure distribution in the plane of symmetry, $\beta = 0$, is presented in figure 31. Radial locations are normalized by the cylinder diameter, and the ordinate corresponds to the cylinder leading edge. Upstream of the separation region, the distribution displays a characteristic rise in pressure due to the blockage of the cylinder. Unlike the potential-flow distribution shown by the solid line, the experimental distribution begins to decrease a short distance downstream of the saddle point determined from the endwall flow visualizations. The distribution displays a local minimum approximately two tenths of a cylinder diameter from the cylinder leading edge, then increases rapidly from that point to a value of one at the endwall-cylinder junction. The coefficient value of one indicates that loss-free core flow stagnated at the junction. Location of the saddle point in an adverse pressure gradient, not at the local peak pressure, is consistent with the work of Langston and Wagner (ref. 10). They applied Oswatitch's model to saddle-point behavior and predict that the saddle point occurs in an adverse pressure gradient.

The data in figure 31 also provide an indication of the flow unsteadiness in this region. Data at several radial locations were acquired during four different runs. The data repeatability is quite good upstream of the saddle point and near the cylinder, indicative of relatively steady flow in these regions. In the separated zone between the cylinder and saddle point, a significant range in the measured pressures is apparent and is attributed to flow unsteadiness in the vicinity of the rather substantial pressure gradients. McMahon, et. al. (ref. 12) also found high turbulence levels in the corresponding region of their experiment.

The experimental pressure distribution parallels the potential-flow distribution upstream of the saddle point. The experimental values, however, are slightly lower in magnitude. This difference is a result of the mean flow accelerating through the test section due to boundary-layer buildup on the uncountoured endwall surfaces. Experimental pressures in figure 31 are corrected for the thickening boundary layer. The correction represents the decrease in pressure associated with a one-dimensional flow passing through a duct with contracting sides simulative of the measured boundary-layer

thickening. The corrected pressures are close to the potential-flow values, though the values upstream of the saddle point are higher. This difference is consistent with the five-hole probe results which show that the static pressure was not constant through the boundary layer. Static pressures measured near the endwall are larger than core-flow values, which will be shown to be well represented by the potential flow solution.

The experimental distribution in figure 31 is plotted with the limited results of Ram (ref. 13) and East and Hoxey (ref. 14) in figure 32. These experiments were conducted in large wind tunnels so that corrections for thickening boundary layers are insignificant. Static pressures measured upstream of the saddle point are close to the corrected values from this experiment, although Ram's data are slightly higher than the other two sets. Ram's results in the separation zone exhibit the same trend as data from this experiment.

Documented Quadrant: Potential-flow and measured endwall static pressure contours throughout the documented quadrant are shown in figure 33. The potential-flow results are for a cascade of cylinders spaced to simulate the test-section sidewalls. These potential-flow calculations were discussed previously with respect to the cylinder design. Comparing these results, the pressure distributions are quite similar outside of the separation region. The experimental pressure coefficients (representing 1007 pressure tap readings) are slightly lower due to the small acceleration of the mean flow caused by the endwall boundary layers. Inside the separation region, the experimental contours display a large dip near $R/D = 0.72$. This dip, which was observed in the plane of symmetry data, persists around the cylinder up to approximately $\beta = 60$ deg. Beyond this angular plane, the dip is no longer present, and the experimental contours are shaped more like that of the potential flow contours. This similarity indicates that the strong pressure field associated with the mean flow acceleration around the cylinder, which is represented by the potential-flow solution, negated the local pressure minimum created in the separation region. The experimental pressures near the cylinder and 90-deg plane are higher than the potential-flow values. Evidently, the separation in the cylinder wake retarded the approaching flow next to the cylinder, creating the higher static pressures.

Cylinder. - The cylinder surface lateral pressure distribution at five angular positions is shown in figure 34. The distribution along the stagnation line ($\beta = 0$) is constant except for the slight dip near the endwall region. The cylinder saddle-point location determined from the cylinder flow visualizations is in the range $0.031 < y/D < 0.068$. For this range, the pressure distribution indicates that the cylinder saddle point was situated in an adverse pressure gradient, as with the endwall saddle point.

Proceeding around the cylinder from the stagnation line, the profiles up to the 45-deg plane are relatively flat, but they display a slight pressure increase near the endwall. The profiles at higher angular locations become increasingly distorted, taking on a bowed shape. This distortion can be attributed to the separation in the cylinder wake. Humphreys (ref. 15) and Farrell and Blessman (ref. 16) show, for an approaching two-dimensional flow, spanwise variations in cylinder surface pressure distribution that were caused by instabilities in the downstream separation. Although the Re_D of 5.5×10^5 in this experiment is slightly larger than that for which these variations were observed, the variations were highly dependent on the end conditions. Wake instabilities for the low aspect ratio cylinder used in this experiment can be expected to be enhanced by the endwall separations.

The cylinder angular pressure distribution is in figure 35. Profiles obtained near the endwall ($y/D = 0.011$), the quarter-span ($y/D = 0.255$), and the midspan ($y/D = 0.511$) are displayed. The distribution for potential flow through a cascade of cylinders is also shown. The experimental values agree with potential-flow values up to approximately 45 deg. At larger angles, the experimental pressures are higher than the potential-flow distribution. Data presented by Hoerner (ref. 17) for two-dimensional flow around a single cylinder is also in figure 35. Since the experimental profiles are in reasonable agreement with Hoerner's data, even up to the 90-deg plane, the cylinder surface mean pressure distribution is predominantly like that expected for two-dimensional viscous flow. The spanwise pressure variations created by the endwall separation are small due to the manner in which the endwall separation occurred. Core flow entered the endwall region near the plane of symmetry, immersing the entire cylinder span in loss-free flow. This flow was nearly uniformly accelerated around the cylinder, leading to a surface pressure distribution much like that for two-dimensional flow.

Five-Hole Probe Measurements

Data were acquired with a five-hole probe in the angular planes defined by $\beta = -5, 0, 5, 25, 45,$ and 90 deg. The probe was traversed at 81 radial locations to define the flow field adjacent to and inside of the separation region. Data were recorded from $y/D \cong 0.0085$ to the test-section midspan. This smaller value, approximately one probe tip diameter from the endwall, represents the lowest point for which data could be acquired without endwall interference. This determination was primarily based on endwall static data acquired in this test program with and without the probe in proximity of a static pressure tap. Camarata et. al. (ref. 7) also used this guideline in their tests. The data acquired in the $\beta = -5$ -deg plane are not presented in detail since they were acquired only to document the flow symmetry. A listing of all the reduced data, including static and total pressure coefficients, yaw angle, pitch angle, and velocity ratio, are included in Appendix B.

Endwall Region. - Data obtained up to 0.2 cylinder diameters from the endwall are discussed. The data in the region between $y/D = 0.2$ and the test-section midspan ($y/D = 0.511$) do not substantially vary from the midspan values. The endwall-region data are presented in the form of in-plane velocity vectors, static pressure contours, and total pressure contours.

In-Plane Velocity Vectors: The in-plane velocity components for the angular planes given by $\beta = 0, 5, 25, 45,$ and 90 deg are presented. The data are displayed as vectors centered at the measurement point. The in-plane pitch angles are based on the in-plane components, not on the total velocity measured with the five-hole probe. The vectors are normalized by the reference velocity measured at the test-section entrance. The ordinate and abscissa in the figures represent the cylinder O.D. and endwall, respectively.

The plane of symmetry velocity vectors are shown in figure 36. Upstream of the endwall saddle point the vectors take on the appearance of a two-dimensional boundary layer, though vortex stretching is present. The outer edge of the approaching boundary layer at $R/D \cong 0.94$ is at $y/D \cong 0.13$. Downstream of the saddle point, reverse flow was not measured until $R/D = 0.766$. The separation streamline between forward and reverse flow is very shallow. A straight line drawn from the saddle point to the streamline location at $R/D = 0.766$ represents a separation angle of approximately four degrees. The shallowness of this line is markedly different from the multiple vortex models developed in the literature, e.g. that of Baker (ref. 18).

Following the flow field from the saddle point toward the cylinder, the velocity vectors indicate that flow in the boundary layer and outside of the boundary layer pitched downward, rotated 180 degrees, and proceeded toward the saddle point. Blank areas are present in the traverses nearest the cylinder because the flow pitch angle was out of the probe calibration range ($-29 \leq \phi \leq 30$ deg). Data were acquired in these regions, however, to qualitatively determine the flow direction. The yaw angles determined for the traverse at $R/D = 0.638$ are shown in figure 37. The shaded symbols, which represent data acquired outside the probe calibration range, are uncorrected for pitch angle effects. Based on the authors' experience with probe calibrations at large pitch angles, the corrections would be on the order of two to ten degrees. The data in figure 37 show that flow in the region $0.04 < y/D < 0.08$ was in the direction of the cylinder. The change between forward and reverse flow was quite abrupt. The yaw angle changed approximately 140 deg between $y/D = 0.037$ and 0.045 . This pattern typifies that of the other traverses where reverse flow was measured.

The plane of symmetry flow pattern deduced from the five-hole probe data, surface static pressure data, and surface flow visualizations is sketched in figure 38. Loss-free fluid from outside the boundary layer stagnated at the endwall-cylinder junction. Five-hole probe measurements at $R/D = 0.596$ contain substantial negative pitch angles up to $y/D \cong 0.3$, indicating that flow from approximately two approaching boundary thicknesses away from the endwall entered the juncture region. The reverse flow accelerated as it moved away from the endwall-cylinder juncture to accommodate the incoming flow, which separated at a shallow angle. The favorable endwall static pressure gradient is consistent with this pattern. At approximately $R/D = 0.72$, reverse flow started stagnating with incoming flow. The abrupt reverse flow deceleration caused by the blockage is indicated by the strong endwall adverse pressure gradient in this region. The reverse flow did not roll up to form a vortex, however. The vectors clearly show that a closed vortex was not present in the plane of symmetry, though positive pitch angles in a portion of the reverse flow at $R/D = 0.72$ and $y/D = 0.02$ may indicate the start of the vortex formation. Rather than rolling up, flow passed out of the plane and proceeded tangentially around the cylinder. Note that the reverse flow was confined to the lower 15 percent of the boundary layer as it passed out of the plane.

The velocity vectors and corresponding flow pattern in the 5-deg plane are shown in figures 39 and 40, respectively. The data display similar trends to those observed in the plane of symmetry. Flow from both inside and outside the boundary layer pitched downward and formed a recirculation zone. Reverse flow closer to the cylinder accelerated toward the separation line. As in the plane of symmetry, the reverse flow a small distance away from the endwall eventually was blocked by the incoming flow and tended to pass tangentially out of the plane rather than to roll up into a vortex. The velocity magnitudes near the endwall for $0.74 < R/D < 0.86$ are small. These low in-plane velocities correspond to flow from the plane of symmetry region passing tangentially through the plane. The rudiments of a vortex are again present in the traverse at $R/D = 0.72$, where the reverse flow had a small positive pitch.

Velocity vectors for the 25-deg plane are displayed in figure 41. The vectors show a well-formed vortex. The vortex, then, became fully formed somewhere between the 5-deg and 25-deg planes. The vortex center in the 25-deg plane was at $R/D \cong 0.71$ and $y/D \cong 0.035$. This was approximately one third of the incoming boundary-layer thickness from the endwall. The vortex itself was confined to a region less than one boundary-layer thickness from the endwall. The radial location of the vortex center is close to that of the local static pressure minimum on the endwall in this plane.

The velocity vectors in the 45-deg plane, figure 42, also define a fully formed vortex. Between the 25-deg and 45-deg planes, the vortex center moved radially outward to $R/D = 0.735$. As in the 25-deg plane, the in-plane velocities next to the endwall between the vortex and separation line were small because this region contained tangential flow from the plane of symmetry region.

The vortex structure in the 90-deg plane was much weaker than that in the 45-deg plane. The velocity vectors in figure 43 faintly show a vortex center at $R/D = 0.80$ and $y/D = 0.07$. The vortex was not symmetric, with the secondary flow near the endwall stronger than that on the core-flow side of the vortex. The reduced vortex strength, which was also indicated by the endwall static pressure distribution, can be attributed to the streamwise acceleration of the mean flow around the cylinder.

Static Pressure Contours: Local static pressure was calculated from the five-hole probe results using Bernoulli's equation. Static pressure coefficient contours corresponding to the velocity vector plots are shown in figures 44 to 48.

Upstream of the endwall saddle point, the static pressure contours in the plane of symmetry are nearly vertical except near the endwall surface. The pressures adjacent to the endwall were larger than those measured in the core flow. This trend was seen before in the comparison between potential-flow and corrected endwall static pressures in the plane of symmetry (fig. 31). The assumption of constant static pressure through the two-dimensional boundary layer at a given streamwise location upstream of the saddle point is inaccurate. The cylinder created a stronger adverse pressure gradient in the viscous sublayer.

The pressure distribution closer to the cylinder was significantly skewed by the recirculating flow. A local pressure minimum at $y/D \cong 0.04$ and $R/D \cong 0.73$ is marked by the closed contours. The velocity vectors show that this small minimum is not associated with a vortex. The minimum pressure in the plane was adjacent to the endwall at the same radial location. This minimum is associated with the reverse flow first accelerating away from the cylinder and then decelerating when blocked by the streamwise flow. The coefficients near the cylinder are close to one. They indicate that low-loss fluid from outside the boundary layer passed next to the cylinder at a low velocity prior to stagnating at the endwall cylinder junction.

The pressure contours for the 5-deg plane, figure 45, are similar to those in the plane of symmetry. Closed contours are centered around a slightly lower local minimum at $y/D \cong 0.04$. The minimum pressure in the plane was next to the endwall at $R/D \cong 0.73$. Due to the acceleration of the flow around

the cylinder, the coefficients next to the cylinder are lower than those in the plane of symmetry.

The contours in the 25-deg plane, figure 46, clearly correspond to the well-formed vortex structure shown in the corresponding velocity vector plot. The center of the closed pressure contours corresponds with the vortex center indicated by the velocity vectors. The static pressure coefficient at the vortex center is 40 percent of the test-section entrance dynamic head below the test-section midspan coefficient measured at the same radial position. The pressure contours indicate that the pressure distribution upstream of the separation line was also substantially altered by the vortex structure.

The closed contours in the 45-deg plane, shown in figure 47, again are centered about the vortex center that is indicated by the corresponding velocity vector plot. The pressure coefficient corresponding to the vortex center is 45 percent of the test-section entrance dynamic head below the midspan value at the same radial location. This pressure was not the smallest recorded pressure in the plane, however. The pressures adjacent to the cylinder were lower due to the two-dimensional acceleration of the flow around the cylinder. The contour lines representing the flow close to the cylinder are nearly vertical, as would be expected for a two-dimensional type flow. The region with vertical contours is larger than that shown for the 25-deg plane.

In the 90-deg plane, where the vortex strength was significantly reduced, pressure profiles in figure 48 show that pressure at the vortex core was only slightly less than surrounding pressure. The contours tend to be vertical and increase in value radially outward. The pressure field associated with the two-dimensional acceleration of the flow around the cylinder was clearly dominant. The vortex had only a small local effect on the pressure distribution.

Total Pressure Contours: Total pressure data from the five-hole probe measurements have been expressed as loss coefficients:

$$C_{P_T} = \frac{P_{T_0} - P_T}{q_0} \quad (4)$$

where the test-section entrance conditions are again used for references. The loss contours for the plane of symmetry are shown in figure 49. Upstream of the saddle point, the contours are nearly horizontal, like an attached two-dimensional boundary layer. The edge of the boundary layer approaching the saddle point was at $y/D \cong 0.13$. Downstream of the saddle point, the low-loss contour bends around and touches the abscissa at $R/D \approx 0.54$. This pattern shows the radial extent of the low-loss fluid in front of the cylinder. The contours show the high total pressure loss associated with the low-loss fluid accelerating away from the endwall-cylinder junction. The region of highest loss, $C_{p_T} = 0.6$, occurred at $R/D \sim 0.74$, where reverse flow next to the endwall interacted with streamwise flow.

The loss distribution in the 5-deg plane is nearly identical to that of figure 49. For the 25-deg plane, however, the contours in figure 50 show high losses at the location corresponding to the vortex. The losses at the vortex center were 80 percent of the entrance dynamic pressure. Though these losses associated with the rollup were high, they were localized. The region of low losses adjacent to the cylinder location is larger than the same region in the plane of symmetry.

The contours for the 45-deg plane, figure 51, are similar to those for the 25-deg plane. Again, a high-loss region is associated with the vortex core and a low-loss region is adjacent to the cylinder.

For the 90-deg plane, the contours in figure 52 indicate that the high-loss region is displaced to the same location as the vortex center. The high-loss fluid created during the rollup process, then, simply accumulated at the vortex center and passed around the cylinder with the vortex. The magnitude of the losses in the vortex did not increase during the passage from the 25-deg to the 90-deg plane. The size of low-loss fluid region adjacent to the cylinder increased only a small amount from that same region in the 25-deg plane.

Test-Section Midspan. - Midspan values for a large aspect ratio cylinder should agree with the inviscid solution through the 45-deg plane. Beyond the 45-deg plane, the separation in the cylinder wake influences flow near the cylinder. With a cylinder aspect ratio in this test of only one, however, the endwall separations could have altered the midspan values. This comparison with the potential-flow solution indicates that the horizontal plane of symmetry for the low aspect ratio cylinder of this test can be considered as an inviscid boundary.

The midspan static pressure distribution measured in the plane of symmetry appears in figure 53 along with the potential-flow values. As with the endwall pressures, the coefficients are less than the potential-flow

values. By applying the appropriate boundary layer correction to the pressures measured upstream of the saddle point, the potential-flow solution agrees with experimental results. Although local corrections for pressures measured above the separated boundary layer cannot be calculated, the uniform difference between the measured and potential-flow values near the saddle point suggests that corrections applied to regions upstream of the saddle point are valid for regions slightly downstream of the saddle point as well. Since the flow decelerated and eventually stagnated at the cylinder leading edge, the boundary-layer correction for the pressures measured closer to the cylinder is small. The data in figure 53 show this trend. The difference between the distributions decreases to zero at the cylinder leading edge.

The midspan pressure distributions for the 25-, 45-, and 90-deg planes are shown in figure 54 and are accompanied by potential-flow profiles for both a single cylinder and a cylinder cascade. Pressures measured at locations farther from the cylinder are less than the potential-flow values. Differences are again like the corrections applied to the plane of symmetry measurements. The pressures measured close to the cylinder in the 25- and 45-deg planes agree with the potential-flow solution. The small pressure gradient imposed by the increasing endwall boundary-layer thickness was almost completely negated by the two-dimensional pressure field setup around the cylinder. Data measured in the 90-deg plane next to the cylinder are significantly less than the potential-flow values. This difference, which was also seen in the cylinder surface static pressure data (fig. 35), is attributed to the separation in the cylinder wake.

The measured midspan yaw angle distributions for the 25-, 45-, and 90-deg planes are shown with potential-flow values in figure 55. The potential-flow angles correspond to flow through a cylinder cascade. The angles calculated for flow around a single cylinder are nearly identical to those for the cylinder cascade. The measured data in figure 55 are in agreement with the potential-flow distributions throughout the flow region. The largest deviations are in the 90-deg plane. A small crossflow moving radially outward from the cylinder was present at the midspan. The resultant yaw angle was approximately 3 deg throughout the plane.

The agreement shown in the above comparisons indicates that the midspan flow can be represented as potential flow. The boundary condition at the midspan plane of symmetry, then, can be specified with a potential-flow calculation. In defining the boundaries for the calculation, the endwall contours should incorporate the previously discussed boundary-layer corrections.

Boundary Layer Development in the Plane of Symmetry. - The boundary layer approaching the endwall saddle point was characterized using the five-hole probe measurements. Since the plane of symmetry flow upstream of the saddle

point is two dimensional, the boundary-layer displacement thickness, momentum thickness, shape factor, and wall shear stress were calculated with the same two-dimensional correlations used to characterize the boundary layer at the test-section entrance.

The variation in the skin-friction coefficient along the plane of symmetry is shown in figure 56. The coefficients decrease in value from 0.0028 at the test-section entrance to an assigned value of zero at the saddle point. The coefficients far upstream of the saddle point agree with the two-dimensional correlation of Ludweig and Tillmann (ref. 19):

$$C_f = 0.246e^{-1.561H} Re_0^{-0.268} \quad (5)$$

The correlation breaks down and overpredicts the coefficients near the saddle point.

The coefficients measured by East and Hoxey are also in figure 56. Because of the thicker boundary layer in their experiment, their values are lower than those of this experiment. The Ludweig-Tillmann correlation approaches their experimental value at the farthest upstream point but again overpredicts the experimental coefficients near the saddle point. The saddle points for the two experiments are at the same normalized radial location.

Calculated shape factors along the plane of symmetry are plotted in figure 57. The shape factor progressively increases from the test-section entrance value of 1.35. The shape factor at the saddle point could not be calculated since Burton's (ref. 8) laminar sublayer correlation is not defined for $C_f = 0$. Extrapolation of the distribution in figure 57 indicates the boundary layer separated where $H \cong 2$. The shape factors calculated by East and Hoxey show the same trend. An extrapolation of their data shows that the boundary-layer shape factor in their experiment was approximately the same at separation.

For a given normalized radial location, the shape factor calculated for East and Hoxey's thicker boundary layer is less than the corresponding value from this experiment. The boundary-layer parameters for the two experiments can be correlated using the technique discussed by Schlichting (ref. 9). Mean velocity profiles are assumed to be represented by a power law profile:

$$\frac{u}{U_\infty} = \left(\frac{y}{\delta}\right)^{1/n} \quad (6)$$

Using this velocity distribution and performing the required integrations, the following expressions relating the boundary-layer parameters are:

$$\delta^*/\delta = \frac{1}{n+1} ; \theta_x/\delta = \frac{n}{(n+1)(n+2)} ; H = \frac{n+2}{n} \quad (7)$$

A profile factor η is given by:

$$\eta = 1 - \left(\frac{u(\theta_x)}{U_\infty} \right)^2 \quad (8)$$

where $u(\theta_x)$ denotes the velocity in the boundary layer at $y = \theta_x$. The significance of the profile factor is that velocity profiles for a favorable pressure gradient correspond to $\eta < 0.46$, for a constant pressure correspond to $\eta = 0.46$, and for an adverse pressure gradient correspond to $\eta > 0.46$. Using the power law formulation for the mean velocity, the profile factor can be related to the shape factor:

$$\eta = 1 - (\theta_x/\delta)^{2/n} = 1 - \left(\frac{H-1}{H(H+1)} \right)^{H-1} \quad (9)$$

Thus a unique relationship exists between the shape and profile factors independent of the boundary-layer physical size.

Several experimental profiles are plotted in figure 58 using the power law formulation. The profiles, acquired at points with significantly different shape factors, are correlated in this formulation. The relationship between the shape and profile factors (equation (9)) is shown in figure 59 along with data from this and East and Hoxey's experiment. The predicted curve fits the data from this experiment and deviates only slightly from the East and Hoxey results. The experimental values for η are all greater than 0.46, consistent with the adverse pressure gradient.

Detailed data were not acquired in this study upstream of the separation line except in the plane of symmetry. The agreement shown in the plane of symmetry implies that the detailed East and Hoxey results can be used to characterize the flow upstream of the region where five-hole probe measurements were acquired in the present study.

Pressure Loss. - The mass-averaged pressure loss at any streamwise plane in the test section is given by:

$$\overline{C_{P_T}} = \frac{\int_{z_0}^{z_w} \int_0^{y_{ms}} C_{P_T} u \, dy \, dz}{\int_{z_0}^{z_w} \int_0^{y_{ms}} u \, dy \, dz} \quad (10)$$

where, because of the low Mach numbers, density is assumed to be uniform in the plane. The limits in equation (10) reflect the two planes of symmetry. The sidewall boundary layers were not measured and are not included in the loss calculation. This definition was used to calculate the average loss at the test-section entrance ($x/D = -2.72$) and 90-deg ($x/D = 0.0$) planes.

As explained previously, Burton's (ref. 8) correlation was used to calculate velocities in the viscous sublayer of the entrance plane. Because this correlation could not be used in the separated region of the 90-deg plane, a parabolic segment was fit between the lowest five-hole probe data point and the endwall. The experimental values in equation (10) were integrated assuming straight line segments between the data points.

Loss distributions for the entrance and 90-deg planes are in figures 60 and 61, respectively. Each point represents the mass-averaged loss of a particular traverse. The losses calculated across the entrance plane are reasonably uniform at four percent of the reference dynamic pressure. The 90-deg plane losses are nonuniform. Adjacent to the cylinder, the losses are quite low since low-loss fluid from the core flow occupied this region. Relatively high losses at $z/D \cong 0.8$ are associated with high-loss fluid that accumulated in the vortex core during the rollup process. Farther away from the cylinder, $z/D > 1.15$, losses level out at around five percent of the reference dynamic pressure.

Control volume has only a small effect on these loss calculations. Average loss in the entrance plane does not depend on control volume because of the uniform loss distribution. Though the loss distribution in the 90-deg plane is nonuniform, average loss in the plane is approximately equal to the average of the traverses acquired outside of $z/D = 1.5$. The average value for the 90-deg plane, then, is not strongly weighted by losses outside the separation region.

A check on the integration procedure for calculating the above losses was accomplished by comparing the calculated mass flow through each of the planes (the denominator in equation (10)). Mass flow through the 90-deg plane was 3.4 percent above that in the entrance plane. This agreement indicates that the above integration procedure provided accurate values for $\overline{C_{P_T}}$.

A comparison for the above loss calculations is the loss for an equivalent turbulent boundary layer developing on a flat plate without a cylinder. Substituting the power law formulation for the velocity distribution (equation (6)) into equation (10) yields:

$$\overline{C_{PT}} = \frac{\frac{n}{n+1} - \frac{n}{n+3}}{\frac{n}{n+1} \left(\frac{MS}{\delta} \right)^{\frac{n+1}{n}}} \quad (11)$$

where $n = \frac{2}{H-1}$ from equation (7). The calculated loss coefficient at the test-section entrance centerline, using measured boundary-layer parameters, is $\overline{C_{PT}} = 0.038$. This value is very close to the 0.039 value calculated by integrating experimental data. In the absence of a pressure gradient, Schlichting (ref. 9) gives the following expression for the boundary-layer thickness as a function of streamwise distance:

$$\delta(x) = 0.37 x \left(\frac{U_{\infty} x}{\nu} \right)^{-1/5} \quad (12)$$

Equation (12) was used to estimate the flat-plate boundary-layer development of a flow starting with the test-section entrance conditions. The boundary-layer thickness was calculated for a length equal to $x/D = 2.72$ (the distance to the 90-deg plane). The calculated value of δ was substituted into equation (11), resulting in a loss coefficient of 0.054. This value is identical to the measured loss in the 90-deg plane. It is concluded, then, that the overall loss associated with the horseshoe vortex formation is small. Langston, et. al. (ref. 4) found the same trend in their cascade experiment. The measured losses in the initial portion of the cascade were only slightly larger than those measured upstream of the saddle point. Significant losses, measured farther downstream in the passage, were associated with the interaction of the passage vortex with the airfoil suction surface in the region of uncovered turning.

Surface Flow Visualizations

Technique. - A qualitative picture of the flow field adjacent to the endwall and cylinder surfaces is indicated by the direction of the limiting streamlines in these regions. A technique developed by Langston and Boyle (ref. 2) was used to visualize these surface streamlines. This technique

involved attaching drafting film dotted with permanent ink on the endwall and cylinder surfaces. Best results were achieved with ink dots that had dried for several days before testing. Just prior to turning on the wind tunnel, a thin continuous coating of oil of wintergreen (synthetic methyl salicylate) was sprayed on the film. The ink dots dissolved and diffused into the oil coating. When the tunnel was turned on and quickly brought up to operating conditions, the dissolved ink flowed in response to the wall shear forces. Each ink dot acted as a stationary source of ink to produce a well-defined ink trace. Within a few minutes, the oil of wintergreen evaporated, and the ink traces left a permanent picture of the surface streaklines. These streaklines were used to locate separation and attachment points and lines. The nature of the flow processes near the cylinder and endwall surfaces was inferred from the patterns.

This technique proved to be superior to other ink-type flow visualization techniques primarily because of the evaporation characteristics of the oil of wintergreen. The viscosity of the visualization medium is a critical factor with some of the other techniques. In regions with relatively high velocities, a high viscosity medium is required to resist the strong shear forces. In many cases, the medium is carried downstream, leaving a void in the flow-visualization pattern. Alternatively, a low viscosity medium is needed in relatively low velocity regions to avoid medium accumulation. The result of this compromise on visualizing the surface flow around an obstacle has been that the flow visualization pattern is void of the medium near the separation line and suffers from an agglomeration of medium near the saddle point. The endwall flow visualizations of Baker (ref. 18) and Moore and Forlini (ref. 20) indicate this problem. Consequently, the interpretation of the patterns regarding the nature of the internal flow field has been inconclusive. The oil of wintergreen viscosity is relatively low. Distinct ink traces were obtained even near the saddle point. The oil evaporates quickly in the high velocity regions, however, so that the ink is not carried out of these regions.

One problem associated with this technique was recognized. If an excessive amount of oil was sprayed on the surface in the separated region, a small dam of oil was created around the cylinder by flow moving back toward the separation line. The dam altered the path of the reverse flow and caused a skewing of the streakline pattern in the separation region. This problem was mitigated by applying only a very thin oil coating in the separation region in front of the cylinder. Streaklines were obtained by repeated applications over several runs.

Endwall Visualization. - A portion of the surface streaklines on the endwall in front of the cylinder is shown in figure 62. A saddle point can be identified where the forward and reverse streaklines combine in the plane of

symmetry. The separation line corresponding with the saddle point has been drawn on the visualization. The precise location of the line is somewhat difficult to determine from the ink traces. It is hard to discern where the ink traces are actually combining to form the separation line as opposed to merely converging.

The saddle point radial location, measured from the cylinder center, is approximately 0.89 cylinder diameters. This normalized saddle point location, repeated during many flow visualization tests, agrees with the results of Boyle (ref. 21) and East and Hoxey (ref. 14) which were acquired for cylinders with diameters one half and twice the cylinder diameter of this experiment. Unlike the case of two-dimensional flow separation, where separation position can vary from test-to-test, the saddle-point position remained constant from run-to-run. Near the cylinder, an attachment point can be discerned in the plane of symmetry. The corresponding attachment line is not easily identifiable. No other singular points can be seen in the flow visualization. All of the streaklines between these two points indicate flow moving toward the separation line.

A larger view of the streakline pattern around the cylinder is shown in figure 63. The saddle point (denoted by the + sign) and attachment point previously identified in the plane of symmetry are also evident in figure 63. A sketch of the flow pattern is shown in figure 64. The flow visualization pattern indicates another region of converging streaklines between the separation line and cylinder. (This convergence is also apparent in figure 51, though not as dramatically.) A line of accumulated ink is formed by the streaklines beginning approximately 15 deg off the plane of symmetry. The streak pattern between the plane of symmetry and $\beta = 15$ deg indicates that reverse flow moved toward the separation line and then proceeded tangentially around the cylinder. Beyond the 15-deg plane, reverse flow streaklines abruptly stop leading to the line of accumulated ink. This pattern indicates that reverse flow adjacent to the endwall was entrained into the fluid interior in the vicinity of the 15-deg plane. Since the five-hole probe data show that the horseshoe vortex was formed between the 5-deg and 25-deg planes, this pattern suggests that flow adjacent to the endwall rolled into the vortex at approximately the 15-deg plane. Determination of whether the surface line corresponding to the accumulated ink is a limiting streamline is difficult. In the work of Lighthill (ref. 22), a separation line must originate from a singular point of a particular type, a saddle point, as the separation line identified in this experiment does. The flow visualization clearly shows that the line of accumulated ink does not extend from a saddle point in the plane of symmetry. In his terminology, then, a separation line is not associated with the flow adjacent to the endwall being entrained into the vortex. Tobak and Peak (ref. 23) have developed a concept that a separation line does not necessarily originate from a saddle point. They categorize separation lines originating at a saddle point as global lines of separation and separation

lines not originating from saddle points as local lines of separation. In this context, the line of accumulated ink could be interpreted as a local separation line. However, there is little evidence to indicate that the end-wall flow outside the line of accumulated ink separated. The streaklines indicate that this flow simply moved tangentially around the cylinder adjacent to the line of accumulated ink. The streaklines suggest a convergence of streamlines in the vicinity of the accumulated ink but do not conclusively indicate a combining of streamlines as required for a separation line.

Other endwall flow visualization results also indicate a single separation line and saddle point. The flow visualization pattern obtained by East and Hoxey (ref. 14), using oil, is similar to those of this experiment. A photograph of the endwall pattern, contained in figure 65, also shows a line formed by an accumulation of ink between the streamlined cylinder and the separation line. But a second saddle point clearly was not present in the plane of symmetry. The region adjacent to the separation line again appears to have been filled by ink emanating from the plane of symmetry region. The medium deposited between the accumulated oil and separation line does not show a second attachment line. The presence of a single saddle point in front of a cylinder was also observed by Langston and Boyle (ref. 2) in their endwall visualizations which were obtained with the technique used in this experiment.

Cylinder Visualization. - Flow visualizations obtained on the cylinder surface elucidate the flow pattern at the endwall-cylinder junction. Streaklines that formed on the upper portion of the cylinder are shown in figure 66. The vertical plane of symmetry is at the center of the pattern. Near the cylinder midspan, the ink in the plane of symmetry flowed downward. The shear forces near the stagnation line were too small to negate gravitational effects in this region. The ink in the plane of symmetry started flowing upward at approximately two approaching boundary-layer heights from the endwall. This pattern implies that flow from outside the approaching boundary layer entered the separation region. This pattern was previously identified with five-hole probe results. A saddle point and associated separation line can be discerned where the flow separated near the top of the cylinder. The attachment point on the endwall flow visualization indicates that the flow reattached to the endwall close to the cylinder. The downward flow pattern on the cylinder surface adjacent to the endwall indicates that a vortex may have been formed at the endwall-cylinder juncture. The close proximity of the separation and attachment lines means that the vortex would have been small.

Surface streaklines on the bottom portion of the cylinder, shown in figure 67, are similar to those on the top portion. The saddle point, however, is closer to the endwall and not as easily discerned. The difference can be attributed to gravitational effects. On the top of the cylinder, the gravitational forces enhanced the downward ink flow, creating an indicated

saddle point 0.068 cylinder diameters from the endwall. In the recirculation zone near the bottom of the cylinder, gravity retarded the corresponding ink flow, producing an indicated saddle point 0.031 cylinder diameters from the endwall. The actual saddle-point is probably in between these two biased values. The endwall attachment point is 0.013 cylinder diameters from the cylinder (figs. 62 and 63). If a vortex was present at the endwall-cylinder juncture, the vortex had an oblong cross section.

Work by Sparrow, et. al. (ref. 24), Goldstein and Karni (ref. 25), and Goldstein, et. al. (ref. 26) using naphthalene sublimation, shows the presence of a vortex structure in the endwall-cylinder juncture region. Goldstein and Karni concluded that two vortices were present at the endwall-cylinder juncture in their experiment. The size of the hypothesized vortices was incredibly small. A trench that the vortices formed at the cylinder base was on the order of $0.4 \delta^*$ wide. In their experiment, this distance was only 0.9 mm. Unfortunately, the results of Goldstein and Karni and Sparrow are contradictory. For example, Goldstein and Karni measured higher Sherwood numbers near the endwall than measured in the freestream. Sparrow, on the other hand, shows reduced mass transfer near the endwall relative to that in the two-dimensional flow region. In any case, the recirculation region near the endwall-cylinder juncture in this experiment probably contained a vortex. The close proximity of the cylinder saddle point and endwall attachment point precluded making five-hole probe measurements to document the recirculation zone. The recirculation region was so small, however, that the fluid dynamics in this region had little or no effect on the main vortex characteristics. No attempt was made to document the flow in this region.

Discussion of Vortex Formation

The vortex pattern deduced from the experimental data is shown in figure 68. Near the plane of symmetry, low-loss fluid from outside the approaching boundary layer passed next to the cylinder, stagnated at the endwall-cylinder junction, where flow visualizations indicate a small vortex formed, and proceeded back toward the saddle point. Streamwise flow inside the boundary layer followed the same pattern, turning inside of the low-loss fluid. As a consequence of the reverse flow and incoming flow interaction, the reverse flow accelerated away from the cylinder. Reverse flow very close to the endwall passed beneath the incoming separated flow and proceeded to the saddle point region before turning to pass tangentially around the cylinder next to the separation line. Since the streamwise flow separated at a shallow angle, reverse flow passing a small distance away from the endwall was blocked by the incoming flow, forcing the reverse flow to decelerate. Rather than rolling up into a vortex, the reverse and incoming flow tended to turn and pass tangentially around the cylinder. Significant losses in total pressure are typically associated with two flows interacting in this manner. The high

losses measured in the center of the vortex subsequent to its formation, then, may indicate that this flow collected at the vortex center. Reverse flow away from the plane of symmetry followed the same pattern, but flow close to the endwall that passed beneath the separated incoming flow turned before reaching the separation line because flow from the plane of symmetry region already occupied the space next to the separation line. Moving away from the plane of symmetry, the endwall region next to the separation line and beneath incoming separated flow progressively filled, forcing the endwall flow to turn closer to the cylinder. Eventually the accelerating reverse flow could not adjust to the sharp turning required to pass tangentially around the cylinder in the same manner. Rather, the reverse flow tended to be entrained into the fluid interior leading to the formation of the vortex. The reverse and incoming flow apparently wrapped around the high loss fluid created in the plane of symmetry region. The endwall visualization pattern indicates that flow adjacent to the endwall became involved in the vortex beginning at $\beta = 15$ deg. The five-hole probe measurements show that the vortex was present in the 25-deg plane but not the 5-deg plane.

This flow pattern does not support the multiple vortex pattern given by Baker (ref. 18) and Moore and Forlini (ref. 20). That pattern was developed from endwall flow visualization; no interior measurements were acquired to verify this model. These experimentors interpreted the line of accumulated ink identified in this experiment as a separation line emanating from a second saddle point in the plane of symmetry. Based on the flow topology, a nodal point of attachment and corresponding attachment line must be present between the saddle points, though the nodal point and attachment line could not be discerned in the endwall flow visualizations. The flow visualization medium placed between the upstream separation line and the line of accumulated ink was carried away. For this combination of two endwall separation lines and two attachment lines, the experimentors inferred the four-vortex model sketched in figure 69. The system includes a main vortex, a pair of counter-rotating vortices beneath the main vortex, and a small vortex tucked in the endwall-cylinder junction, all of which form in the plane of symmetry.

This complex system was not present in this experiment. The endwall flow visualization clearly shows a single saddle point while the interior flow field measurements indicate a single horseshoe vortex that formed away from the plane of symmetry.

CONCLUSIONS

This project documented the flow field in the endwall region around a cylinder. This documentation leads to the following conclusions:

1. A single endwall saddle point and a single endwall attachment point were observed in the endwall flow visualization pattern. The multiple singular points required for the four-vortex model were not present.
2. The five-hole probe measurements indicate that a single main vortex was formed. Though the rudiments of a vortex were observed in the plane of symmetry and the 5-deg plane, the vortex was fully formed between the 5-deg and 25-deg planes. The flow visualization pattern indicates that the flow adjacent to the endwall initially rolled up near the 15-deg plane.
3. The main vortex was confined to a region less than one boundary-layer thickness from the endwall. The vortex core moved radially outward and slightly away from the endwall as the vortex passed around the cylinder.
4. The vortex strength was significantly reduced between the 45-deg and 90-deg planes.
5. The losses associated with the vortex rollup were localized and offset by the transport of core flow into the endwall region next to the cylinder.
6. Measured flow conditions at the test-section midspan are close to those for potential flow through a cascade of cylinders.
7. Because the cylinder was covered by low-loss fluid, the lateral pressure distribution was reasonably uniform. The angular distribution was like that for two-dimensional viscous flow around a cylinder.
8. The plane of symmetry results in this experiment and that of East and Hoxey are in agreement. This agreement implies that the detailed data acquired by East and Hoxey can be used to characterize the flow upstream of the five-hole probe measurements acquired in this study.
9. A key implication of these experimental results for gas turbine engines is that flow in the saddle-point region does not exhibit swirl.

REFERENCES

1. Gaugler, R. E. and Russell, L. M., "Flow Visualization Study of a Horseshoe Vortex in a Turbine Stator Cascade," NASA Technical Paper, 1884, 1982.
2. Langston, L. S. and Boyle, M. T., "A New Surface-Streamline Flow-Visualization Technique," *Journal of Fluid Mechanics*, Vol. 125, pp. 53-57, 1982.
3. Eckerle, W. A., "Horseshoe Vortex Formation Around a Cylinder," Ph.D. Thesis, University of Connecticut, Storrs, Connecticut, May 1985.
4. Langston, L. S., Nice, M. L. and Hooper, R. M., "Three-Dimensional Flow Within a Turbine Cascade Passage," *Trans. ASME, Journal of Engineering for Power*, Vol. 99, January 1977, pp. 21-28.
5. Hess, J. L., and Smith, A. M. O., "Calculation of Potential Flow Around Arbitrary Bodies," *Progress in Aeronautical Sciences*, Vol. 8, D. Kuchelmann, ed., Pergamon Press, 1967, pp. 1-138.
6. Barber, T. J., and Weingold, H. D., "Vibratory Forcing Functions Produced by Nonuniform Cascades," *Trans. ASME, Journal of Engineering for Power*, Vol. 100, No. 1, January 1978, pp. 82-88.
7. Camarata, F. J., Hooper, R. M., and Nice, M. C., "Experimental Investigation of Passage Flow in Baseline Build of Large-Scale Turbine Cascades," United Aircraft Research Labs Report R75-212632, June, 1975.
8. Burton, R. A., "A Simple Universal Velocity Profile Equation," *Tech. Note, AIAA Journal*, Vol. 3, No. 4, 1965, pp. 784-785.
9. Schlichting, H., Boundary-Layer Theory, McGraw-Hill, 1968, pp. 596-651.
10. Langston, L. S. and Wagner, C. A., "A Streamline Model for a Saddle Point of Separation," Submitted to the *Journal of Fluid Mechanics*, October 1983.
11. Oswatitsch, K., "Die Ablosungsbedingung von Grenzschichten," *Symposium on Boundary Layer Research, International Union of Theoretical and Applied Mechanics*, Edited by Gortler, Springer Verlag, Berlin, 1958.
12. McMahon, H., Hubbartt, J., and Kubendran, L., "Mean Velocities and Reynolds Stresses Upstream of a Simulated Wing-Fuselage Juncture," NASA CR 3695, June 1983.

REFERENCES

13. Ram, V. V., "Untersuchungen uber die Eckengrenzschicht an einem Kreiszyylinder mit Seitenwand," Report 63/46, Institute of Fluid Mechanics, Technische Hochschule, Braunschweig, 1963.
14. East, L. F. and Hoxey, R. P., "Low Speed Three-Dimensional Turbulent Boundary Layer Data," Royal Aircraft Establishment, Tech. Rep. No. 69041, Parts I and II, 1969.
15. Humphreys, J. S., "On a Circular Cylinder in a Steady Wind at Transition Reynolds Numbers," Journal of Fluid Mechanics, Vol. 9, Part 4, pp. 603-611.
16. Farrell, C., and Blessmann, J., "On Critical Flow Around Smooth Circular Cylinders," Journal of Fluid Mechanics, Vol. 136, pp. 375-391.
17. Hoerner, S. F., Fluid-Dynamic Drag, Published by the author, 1965.
18. Baker, C. J., "Vortex Flow Around the Bases of Obstacles," Ph.D. Thesis, Univesity of Cambridge, Cambridge, England, September 1978.
19. Ludweig, H. and Tillman, W., "Investigation of the Wall Shearing Stress in Turbulent Boundary Layers," NACA TM 1285, May 1952.
20. Moore, J., and Forlini, T. J., "A Horseshoe Vortex in a Duct," Trans. of the ASME, Journal of Engineering for Gas Turbines and Power, Vol. 106, July 1984, pp. 668-676.
21. Boyle, M. T., "Three Dimensional Separation and Vortex Formation," Ph.D. Thesis, University of Connecticut, Storrs, Connecticut, 1984.
22. Lighthill, M. J., Laminar Boundary Layers, Edited by L. Rosenhead, Oxford University Press, pp. 60-82.
23. Tobak, M. and Peake, D. J., "Topology of Three Dimensional Separated Flows," Ann. Rev. Fluid Mechanics, Vol. 14, pp. 61-85, 1982.
24. Sparrow, E. M., Stahl, T. J. and Traub, P., "Heat Transfer Adjacent to the Attached End of a Cylinder in Crossflow," Internation Journal of Heat and Mass Transfer, Vol. 27, No. 2, 1984, pp. 233-242.

REFERENCES

25. Goldstein, R. J., and Karni, J., "The Effect of a Wall Boundary Layer on Local Mass Transfer from a Cylinder in Cross Flow," Trans. ASME, Journal of Heat Transfer, Vol. 106, May 1984, pp. 260-267.
26. Goldstein, R. J., Chyu, M. K. and Hain, R. C., "Measurement of Local Mass Transfer on a Surface in the Region of the Base of a Protruding Cylinder with a Computer-Controlled Data Acquisition System," Journal of Heat Transfer, Gallies, 1983.

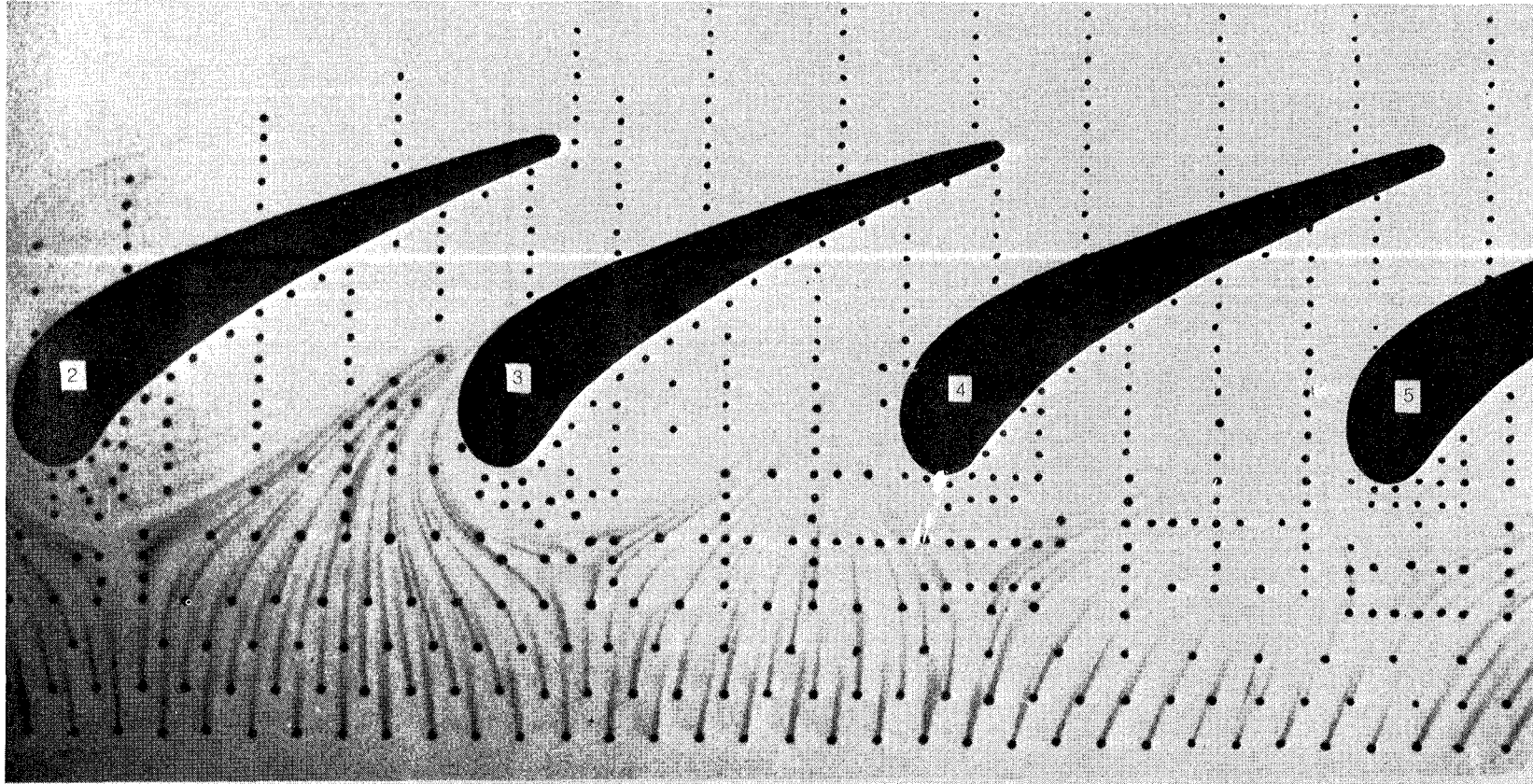


Figure 1 Turbine Cascade Endwall Flow Visualization

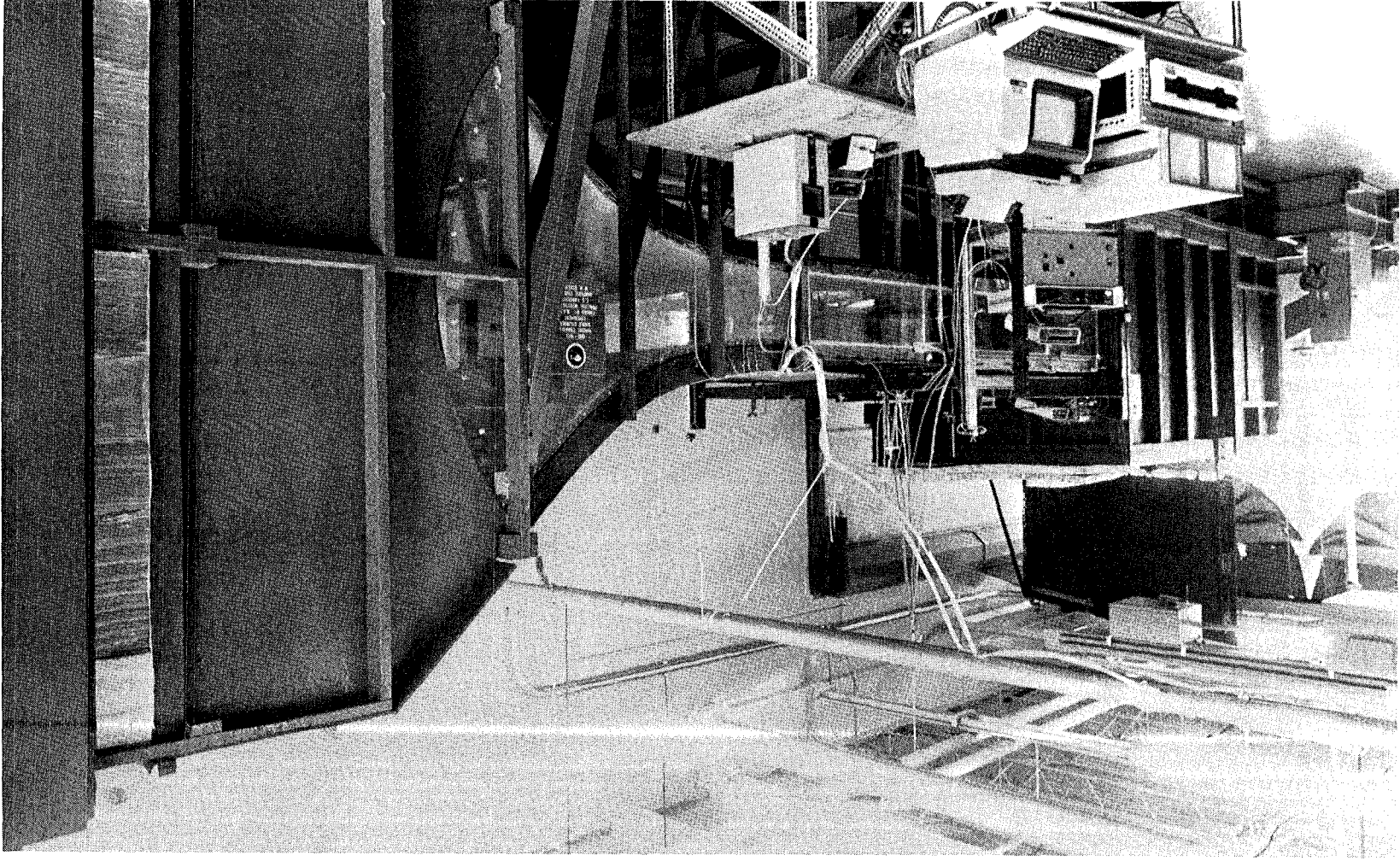


Figure 2 Wind Tunnel with Settling Chamber

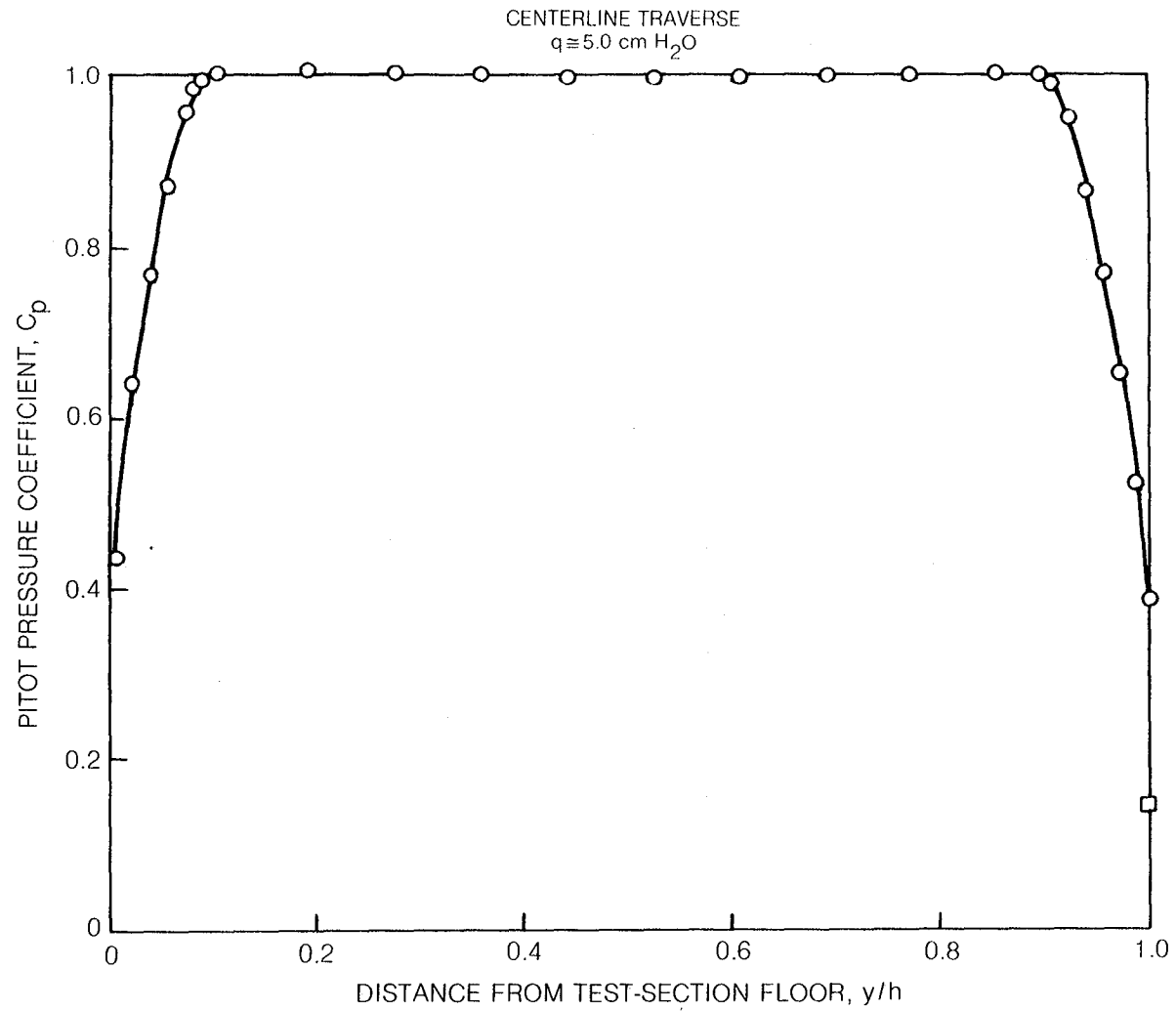
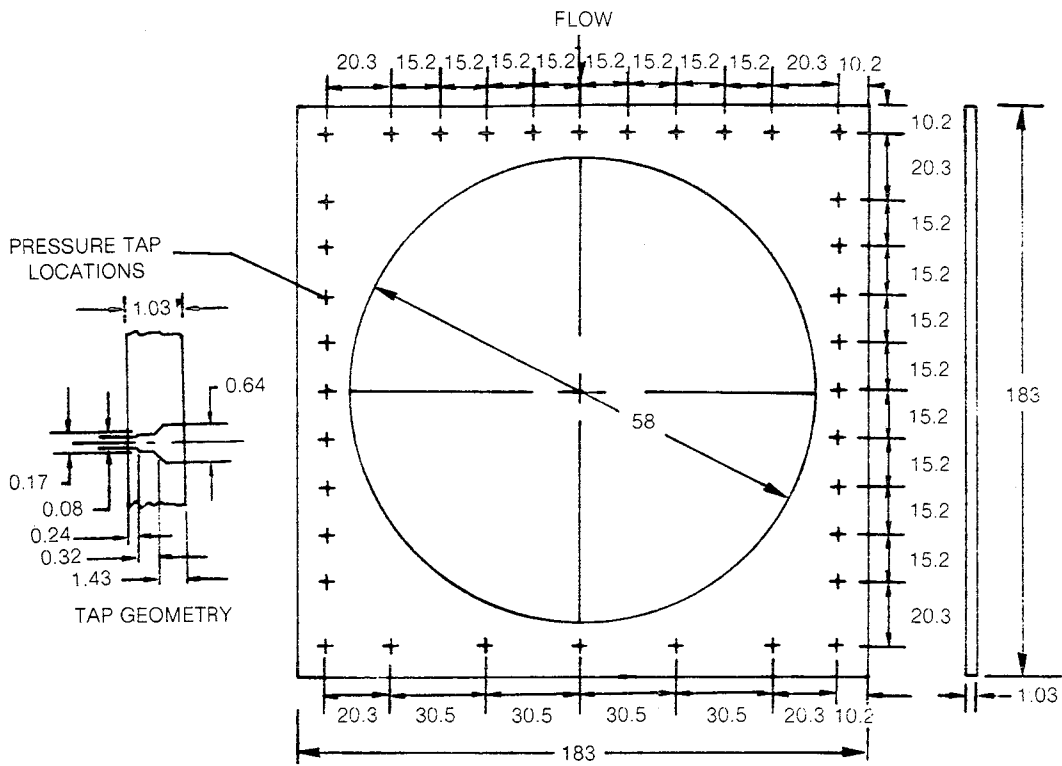
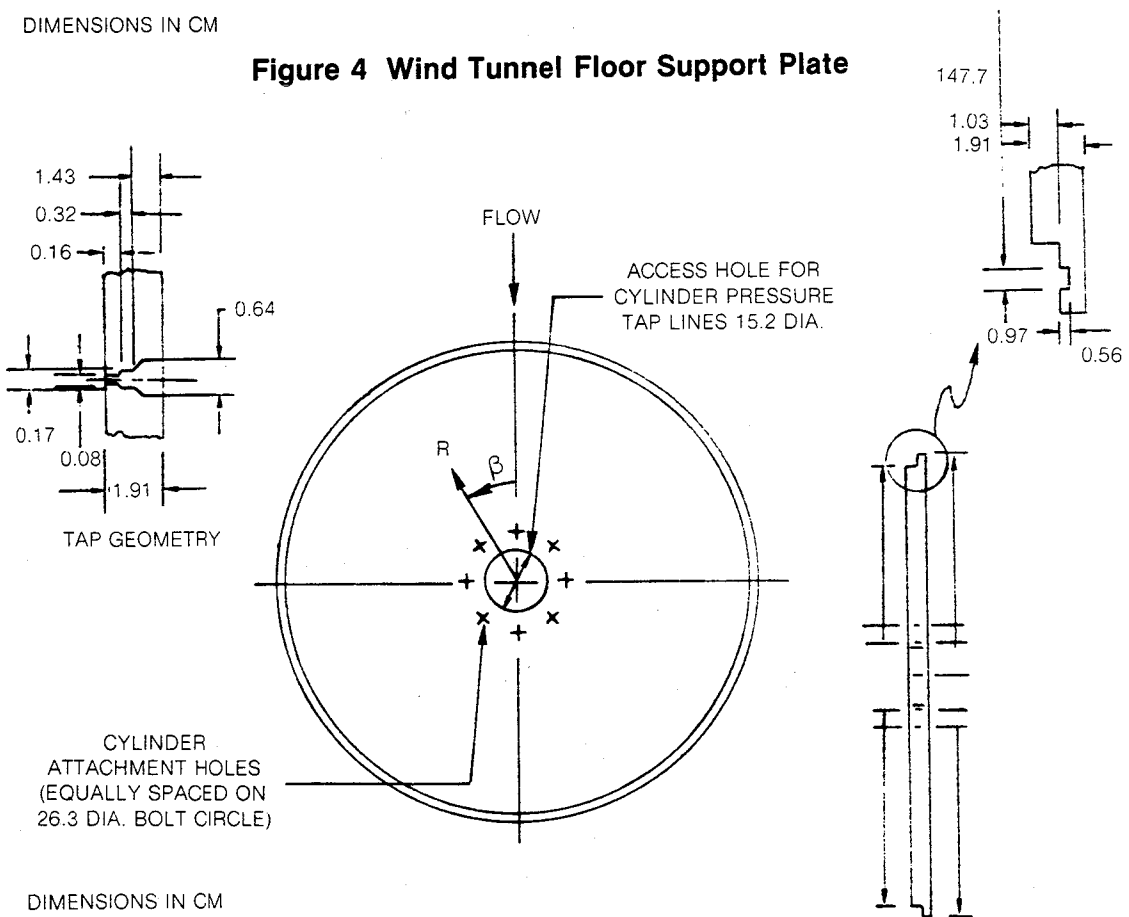


Figure 3 Pitot Pressure Profile Near Test-Section Entrance



DIMENSIONS IN CM

Figure 4 Wind Tunnel Floor Support Plate



DIMENSIONS IN CM

**Figure 5 Wind Tunnel Floor Instrumented Disk
(See Table II for Tap Locations)**

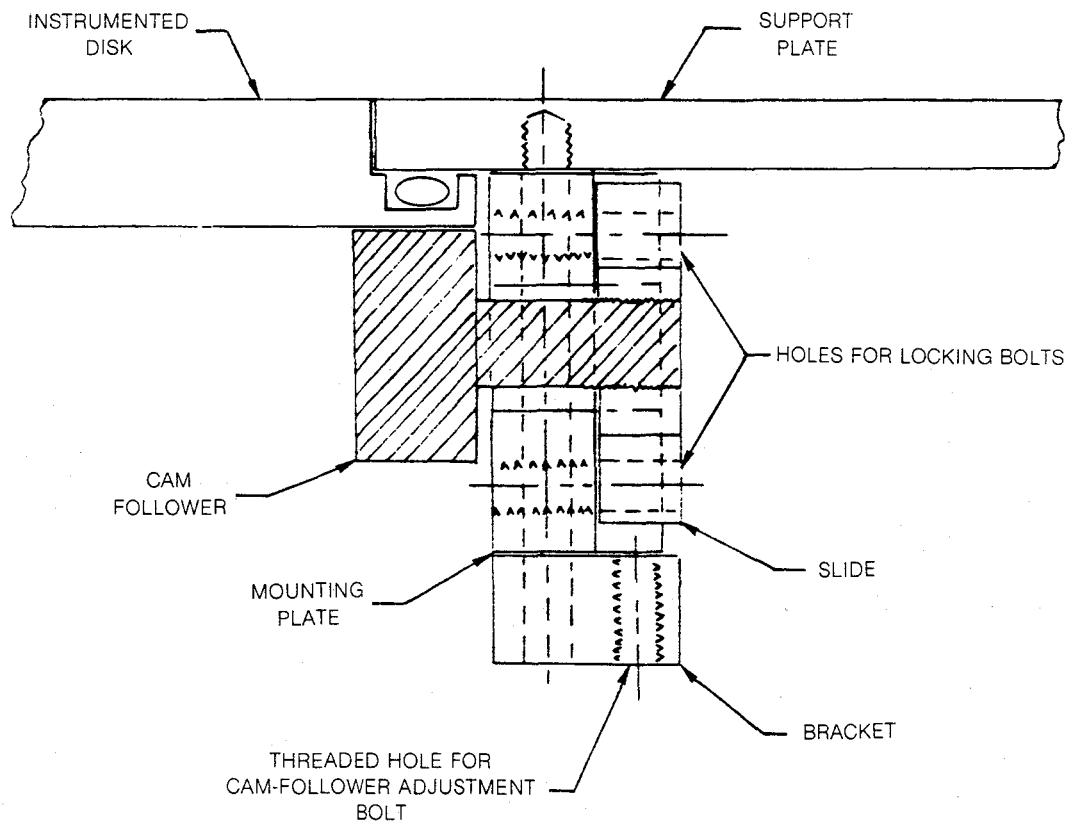


Figure 6 Cross-Sectional View of Cam-Follower Slide Assembly

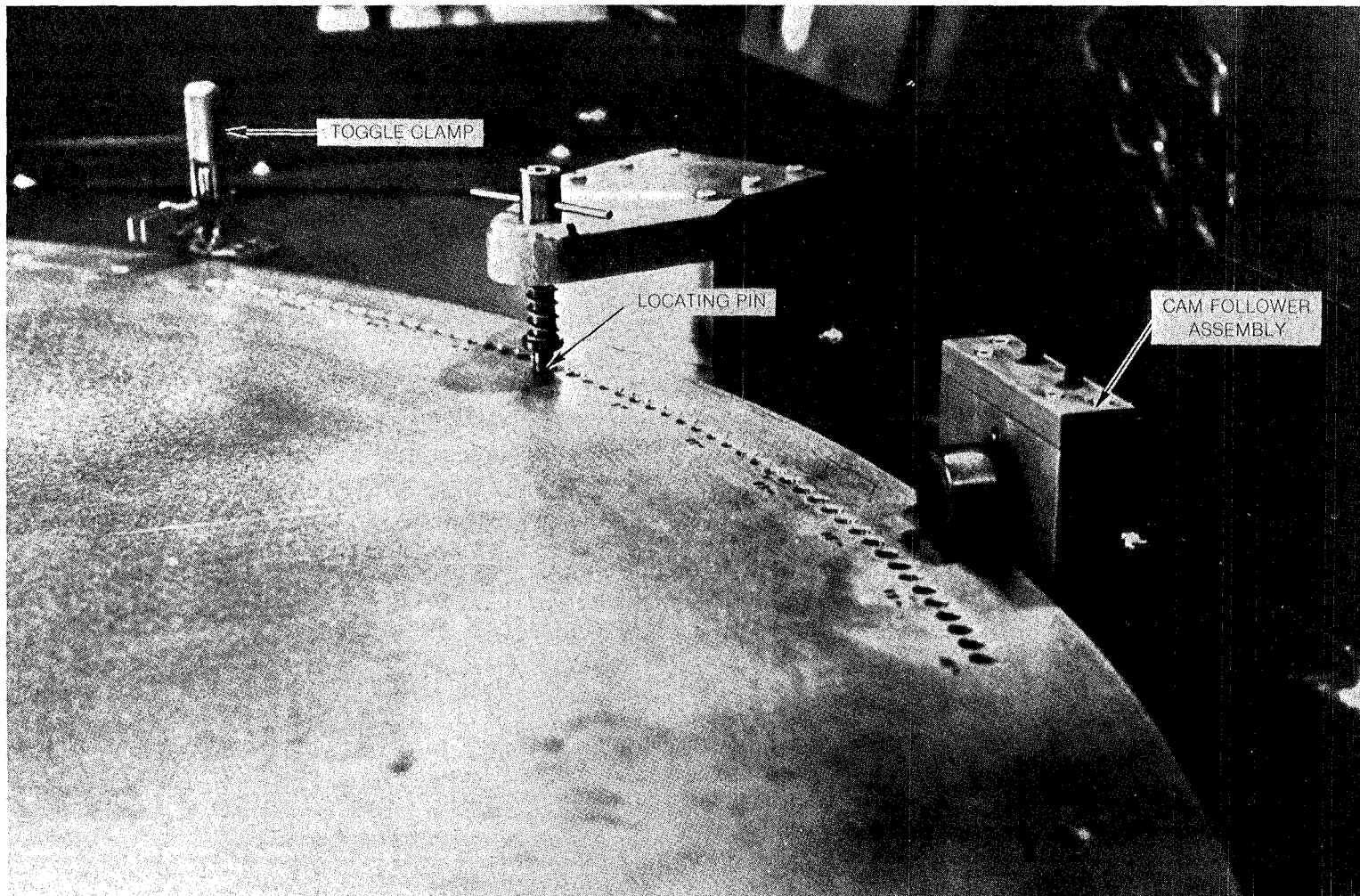


Figure 7 Photograph of Inverted Test-Section Floor Showing Indicator and Index Holes for Angular Positioning of Instrumented Disk

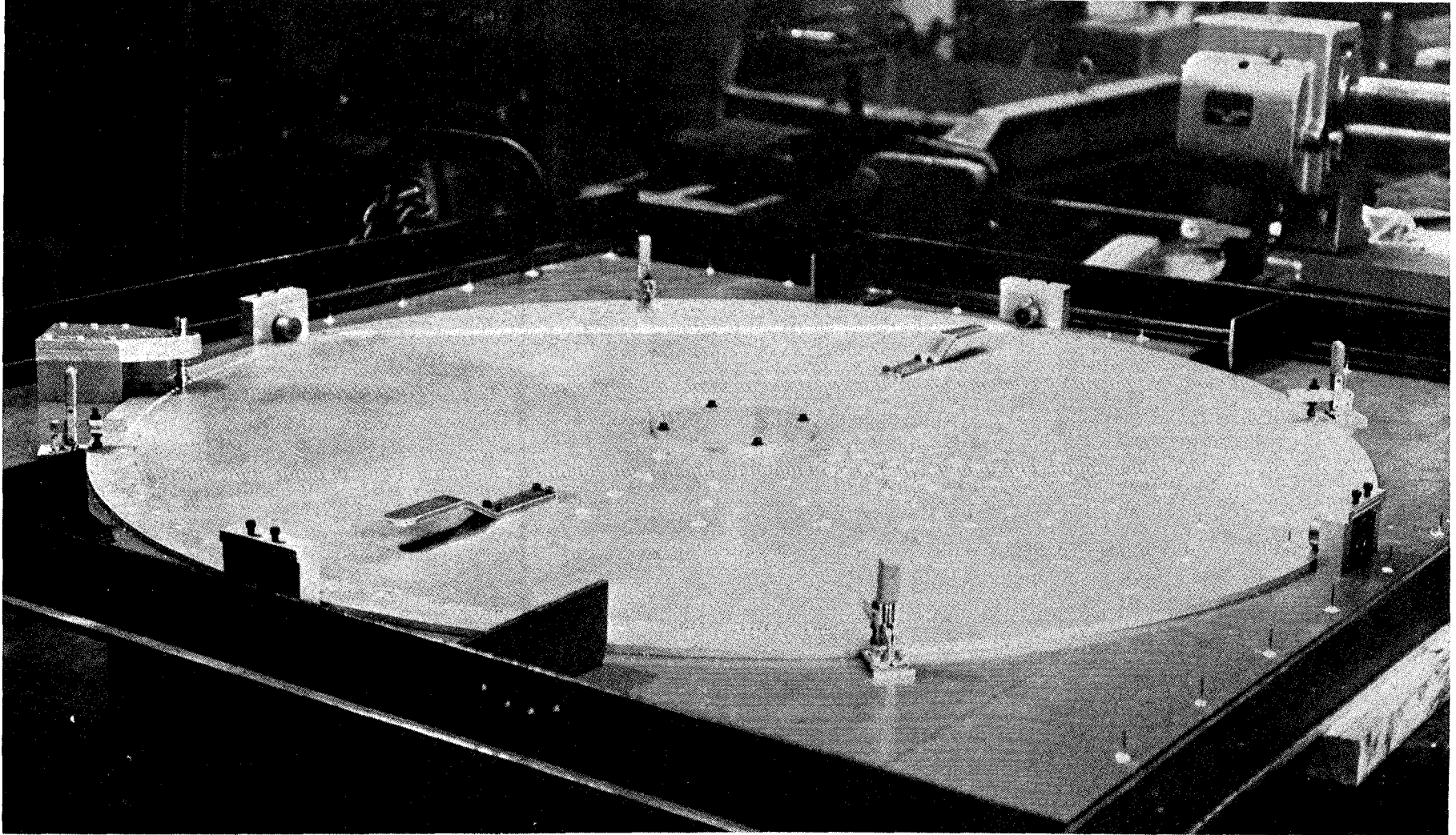
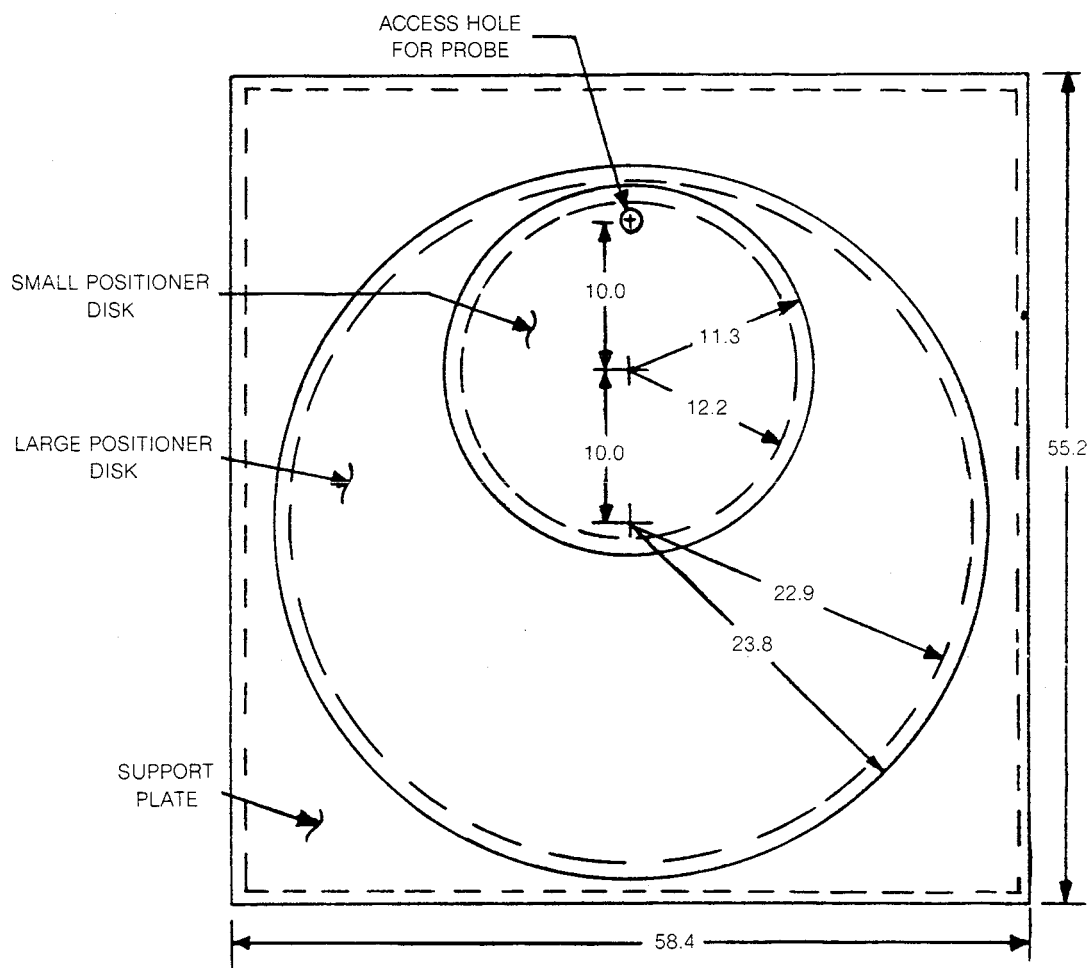


Figure 8 Photograph of Inverted Test-Section Floor



DIMENSIONS IN CM

Figure 9 Probe Positioner Disks

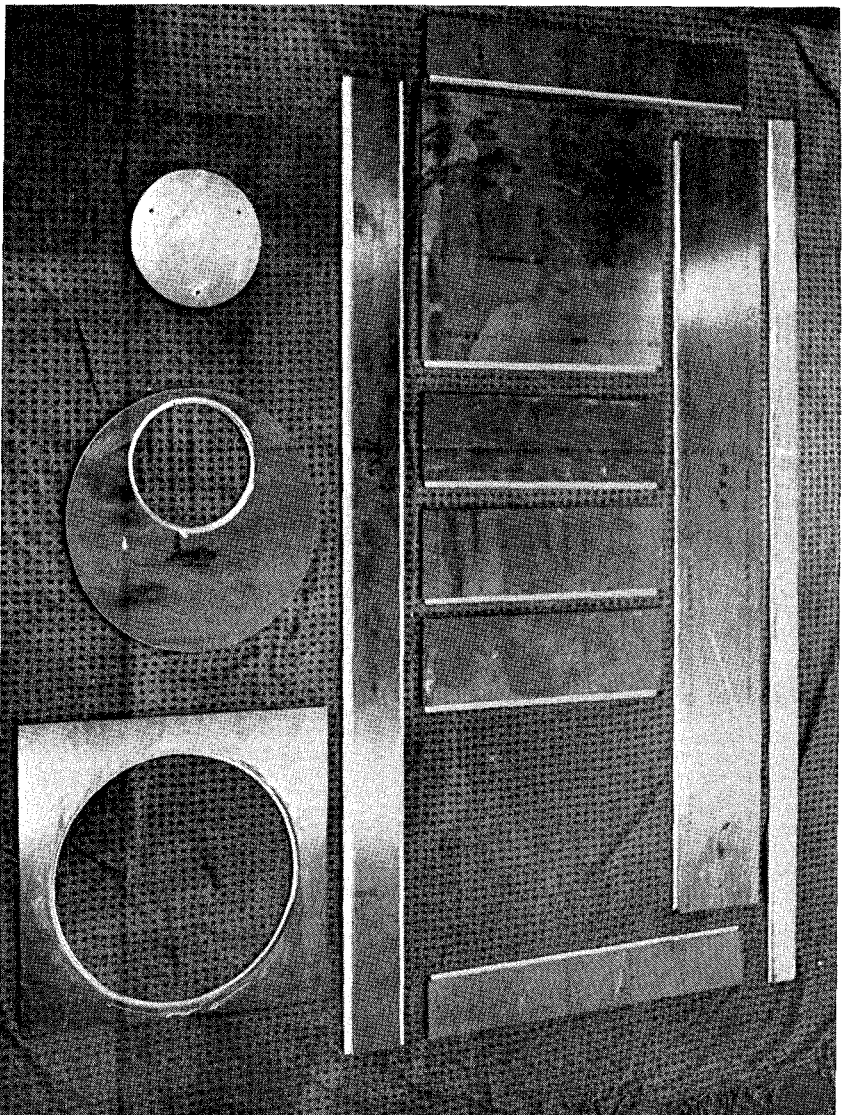


Figure 10 Probe Positioner Assembly

47

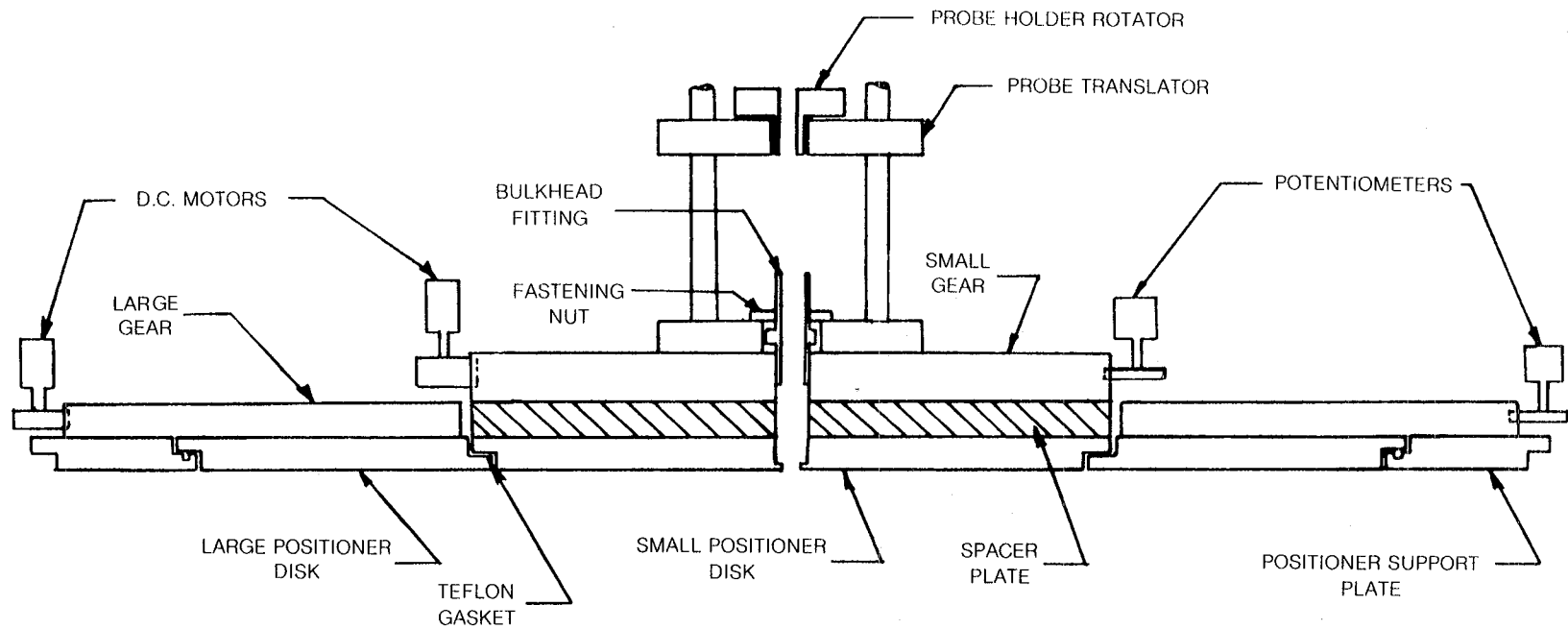


Figure 11 Cross-Sectional View of Motorized Probe Positioner with Mounted Probe Traverser

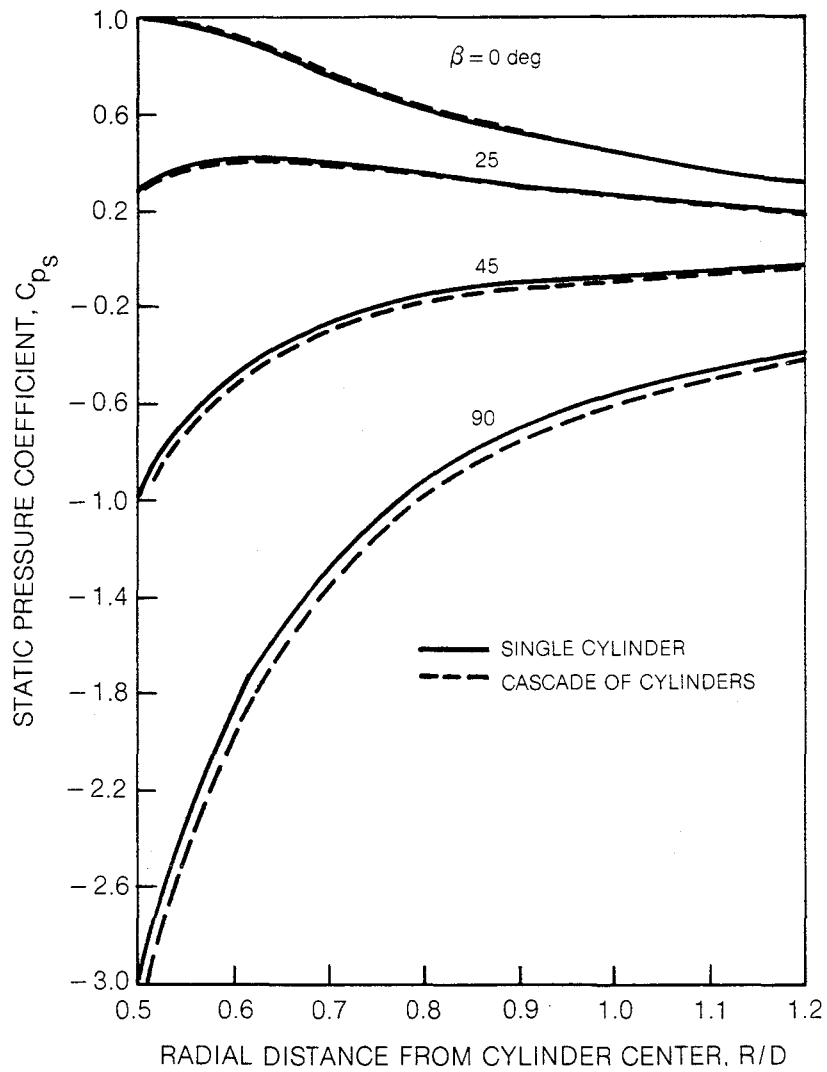


Figure 12 Potential-Flow Static Pressure Distribution Around a Single Cylinder and Cascade of Cylinders

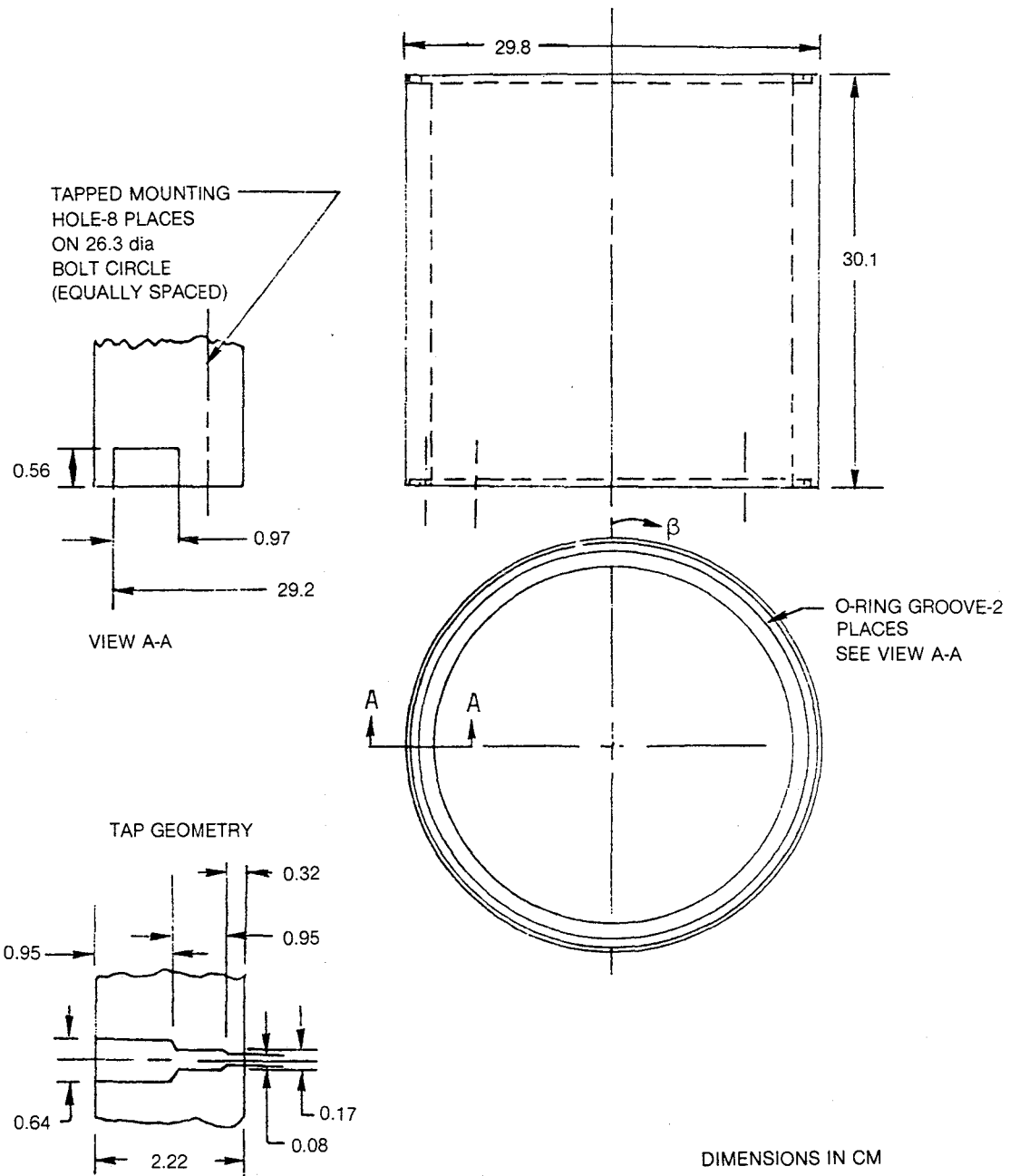
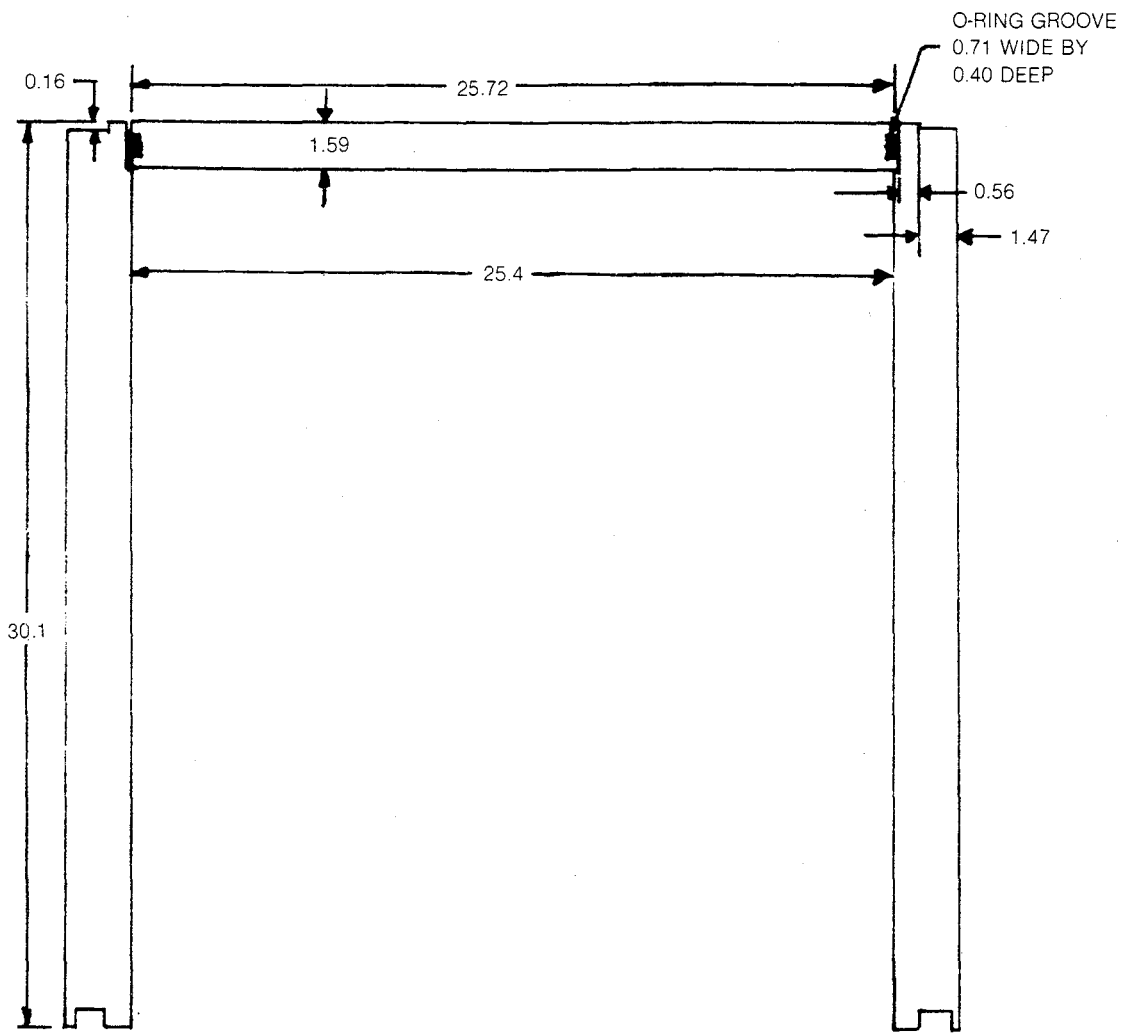


Figure 13 Cylinder Test Model



DIMENSIONS IN CM

Figure 14 Cross-Sectional View of Cylinder Showing Sealing Technique

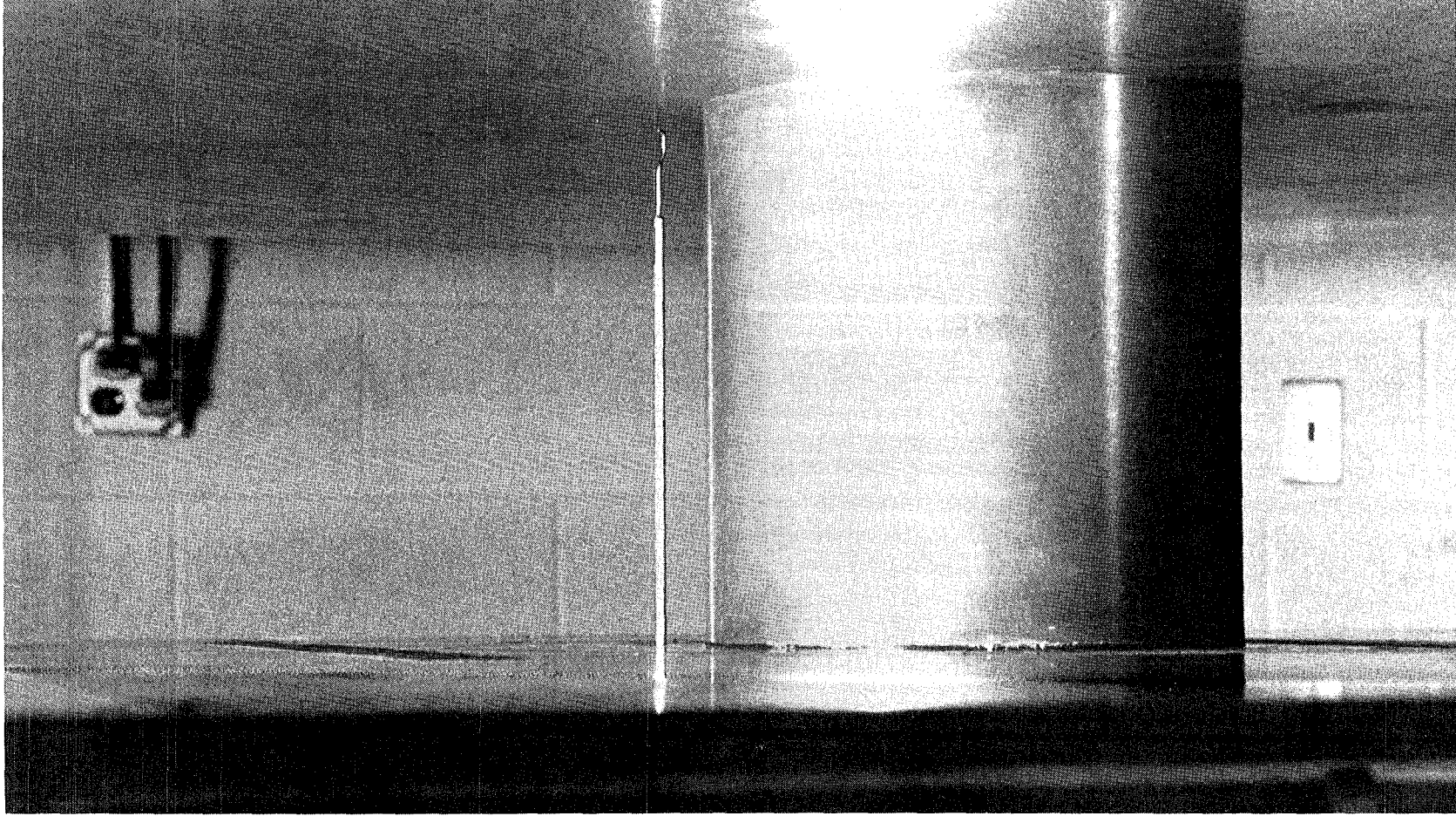


Figure 15 Test Cylinder Mounted in Wind Tunnel Test Section

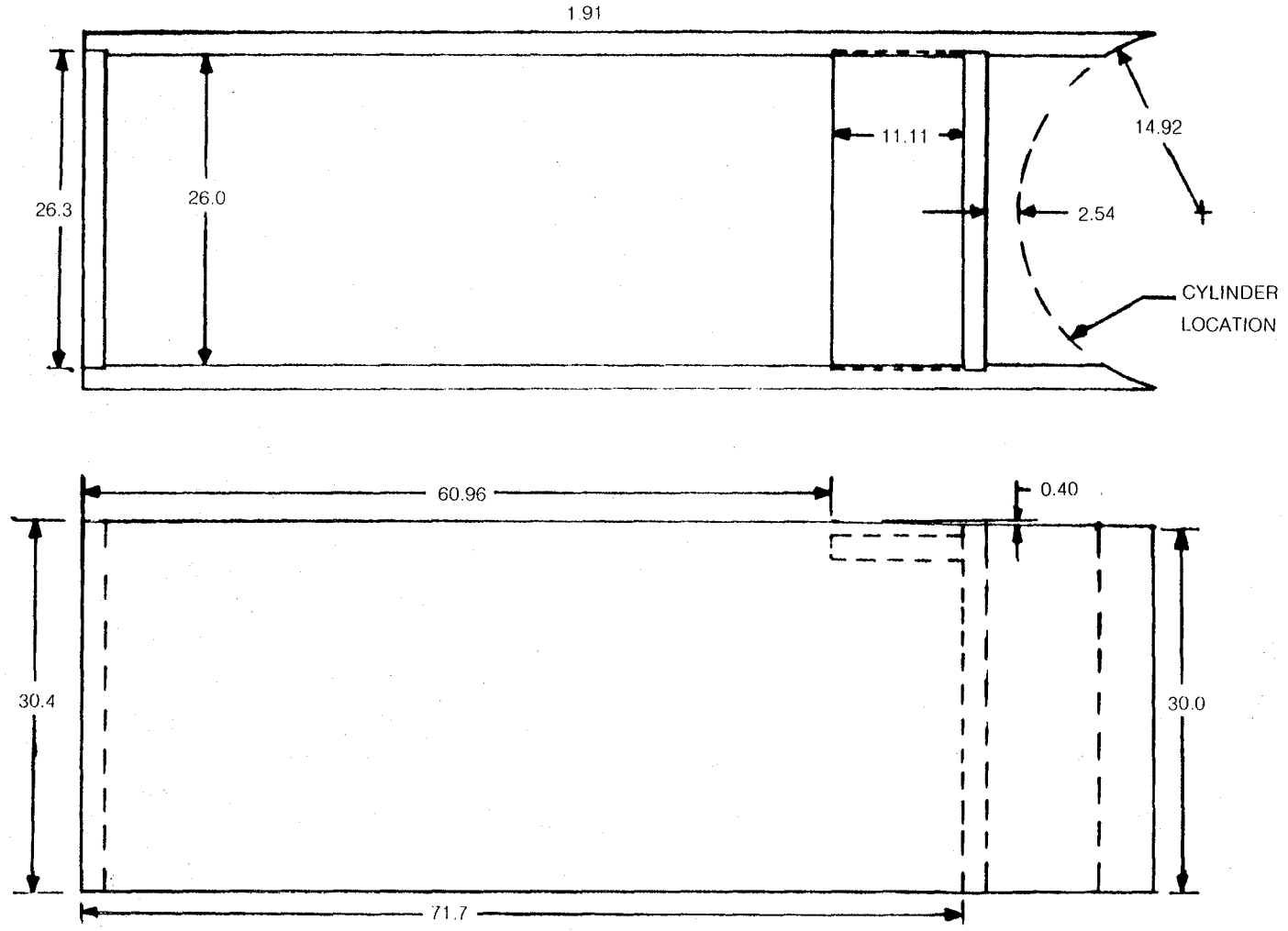


Figure 16 Test-Cylinder Afterbody

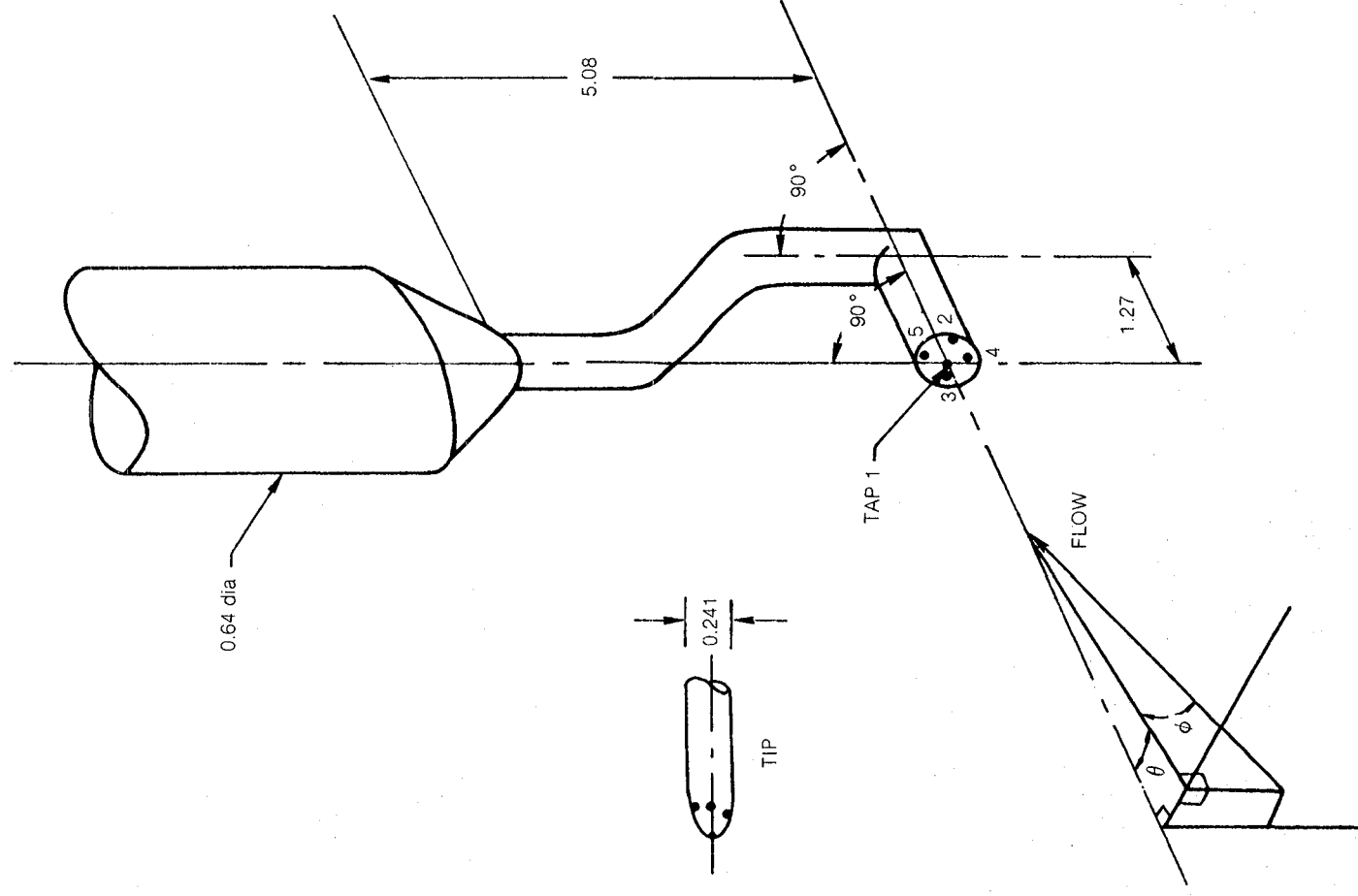


Figure 17 Five-Hole Probe Configuration

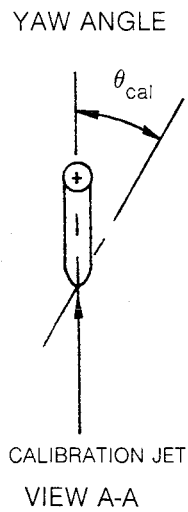
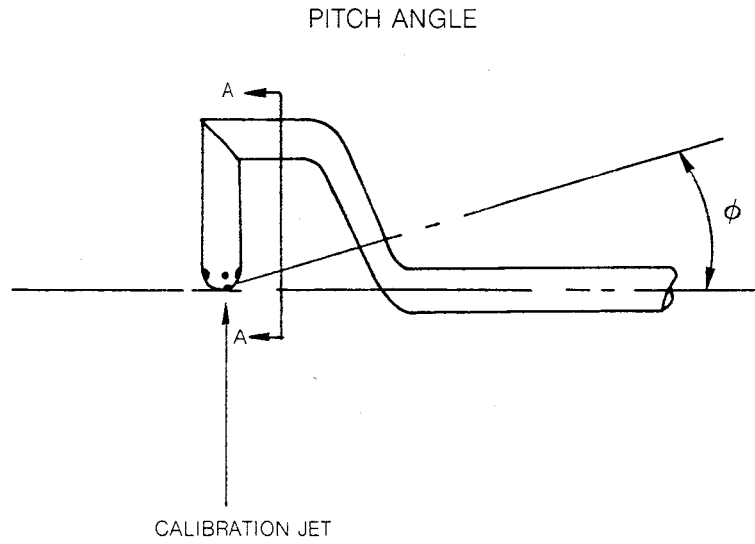


Figure 18 Sign conventions for Five-Hole Probe Calibration

$q = 6.5 \text{ cm H}_2\text{O}$ $P_{\text{BAR}} = 75.97 \text{ cmHg}$ $T_{\text{CAL}} = 74^\circ\text{F}$

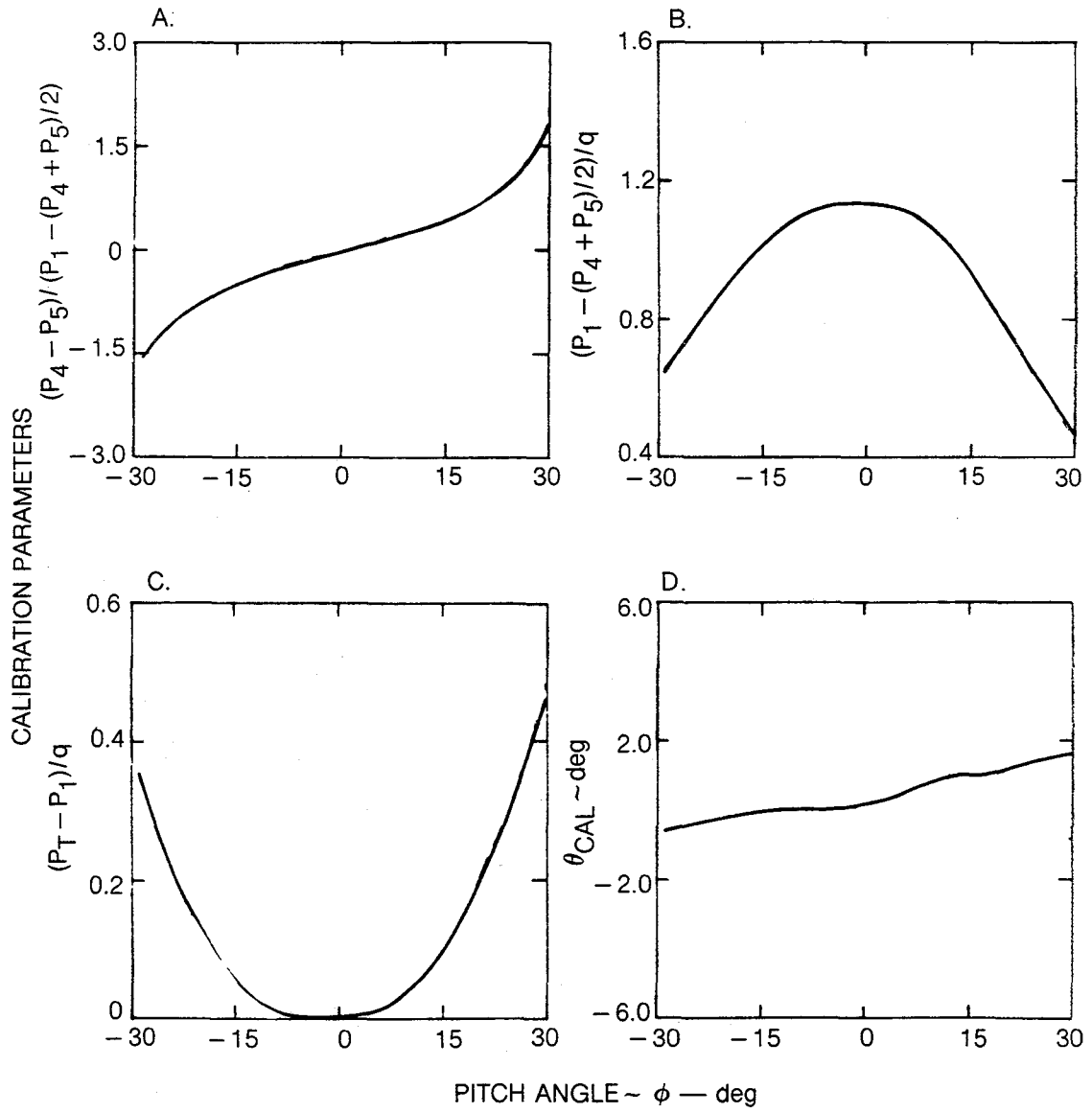


Figure 19 Five-Hole Probe Calibration Curves

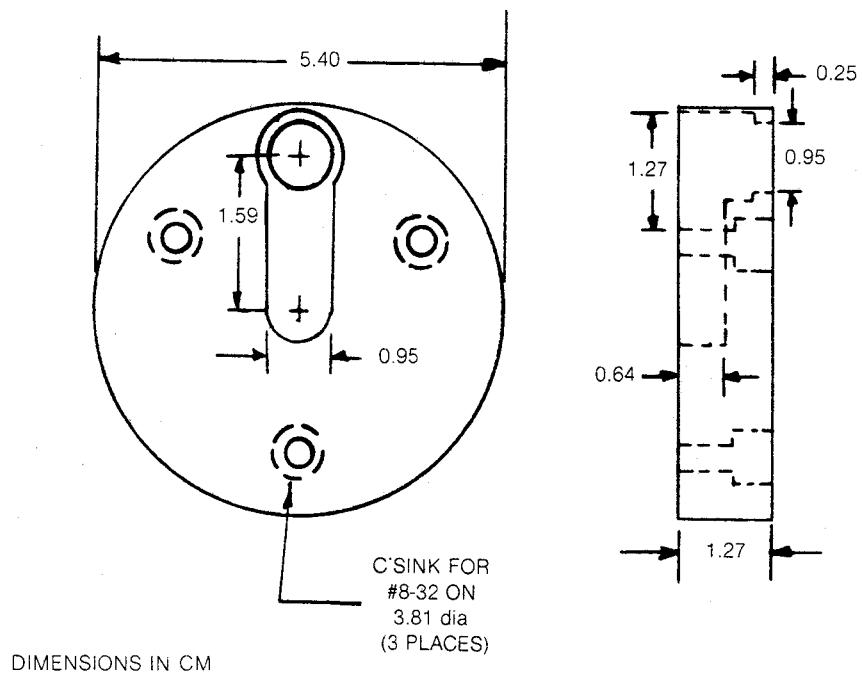
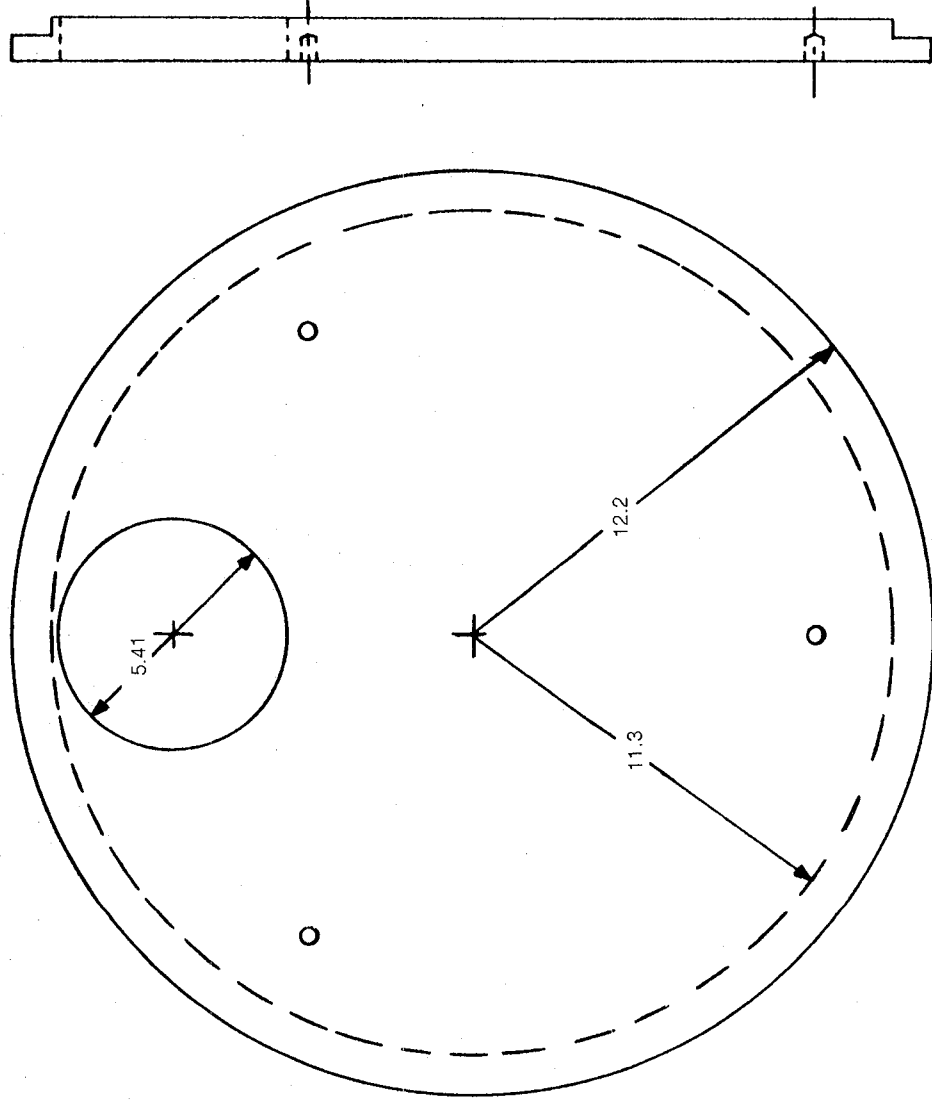


Figure 20 Removable Plug for Small Positioner Disk



DIMENSIONS IN CM

Figure 21 Small Positioner Plate

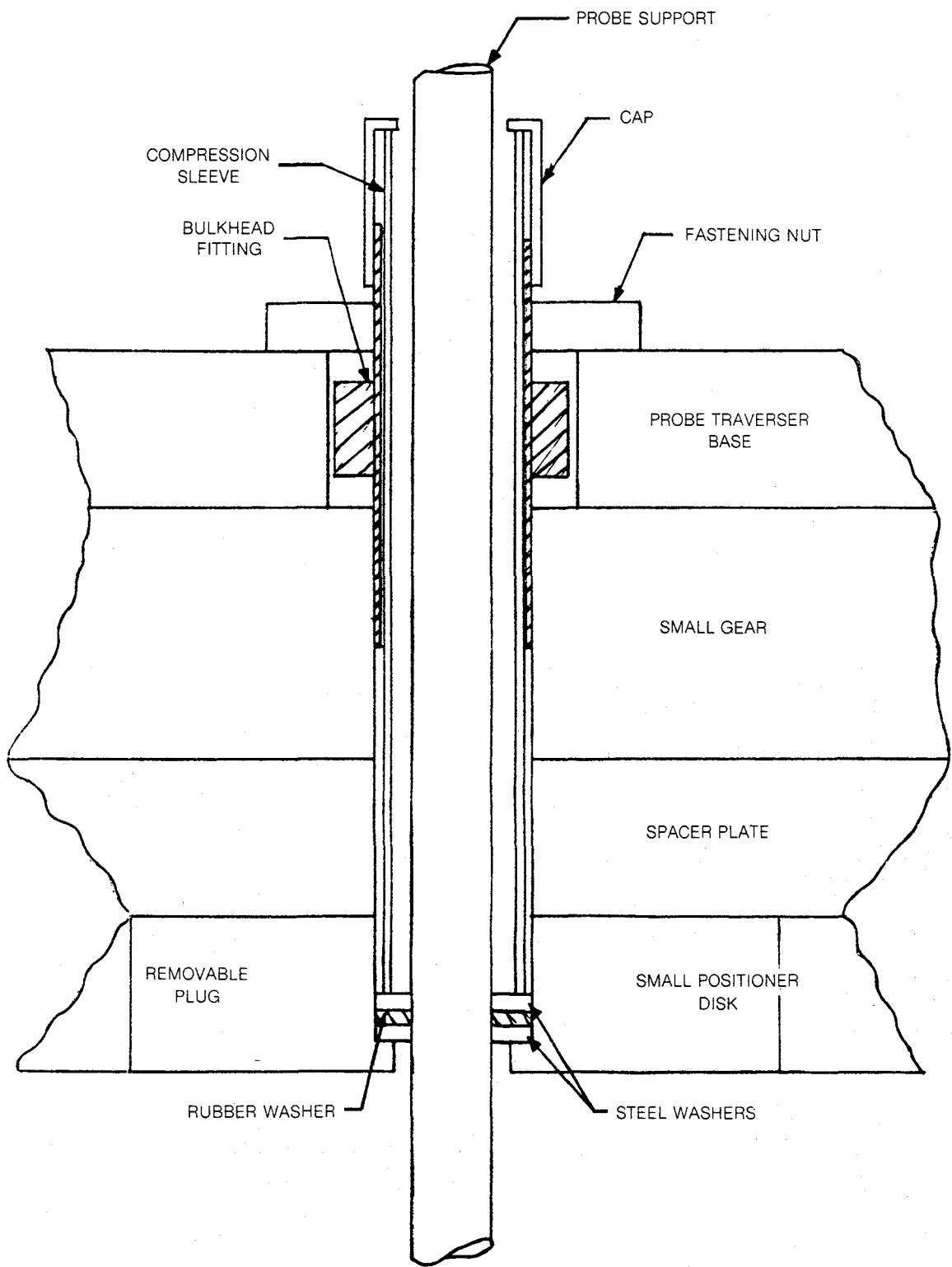


Figure 22 Seal Around Probe Support in Probe Positioner

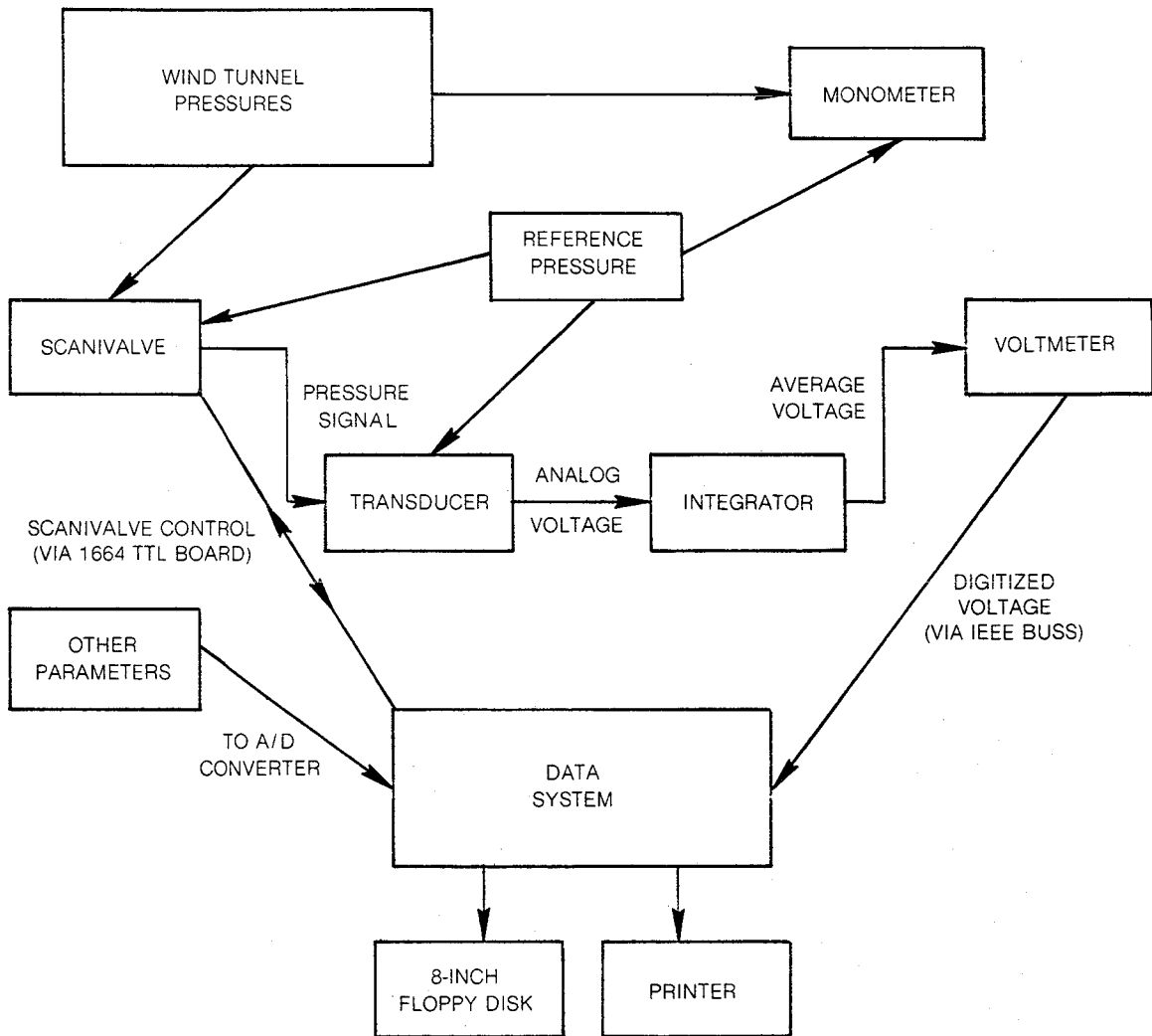


Figure 23 Data Acquisition Instrumentation

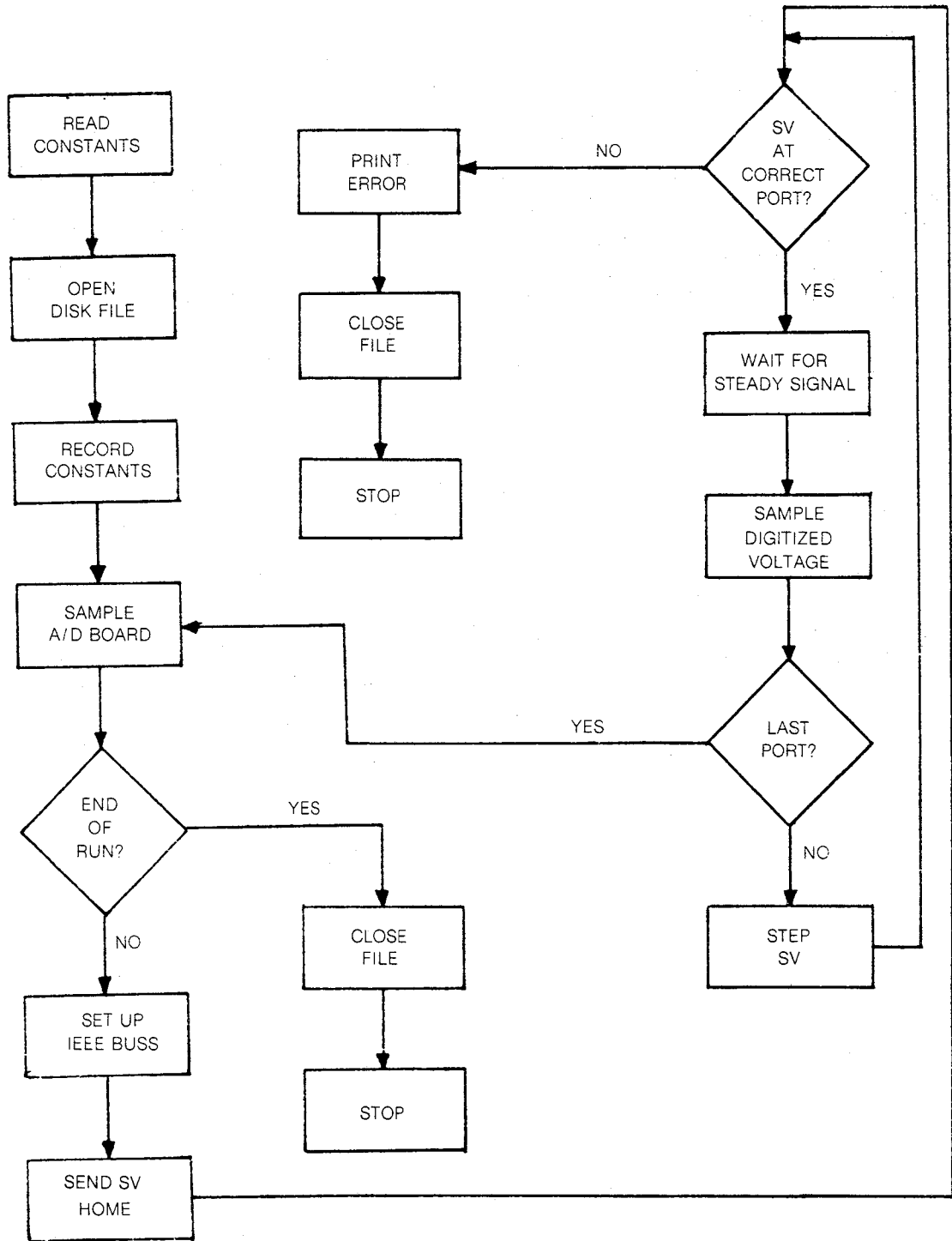


Figure 24 Data Acquisition Program Flow Chart

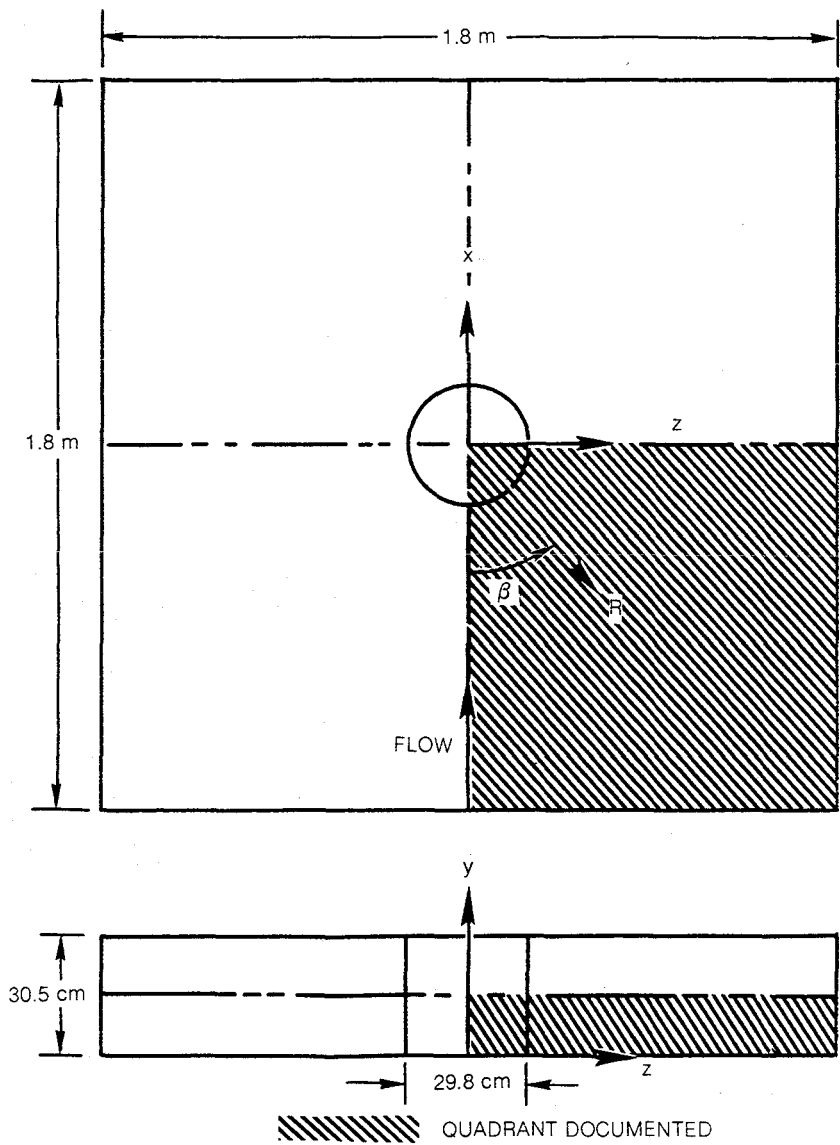


Figure 25 Schematic Showing Test Section with Cylinder and Coordinate Systems

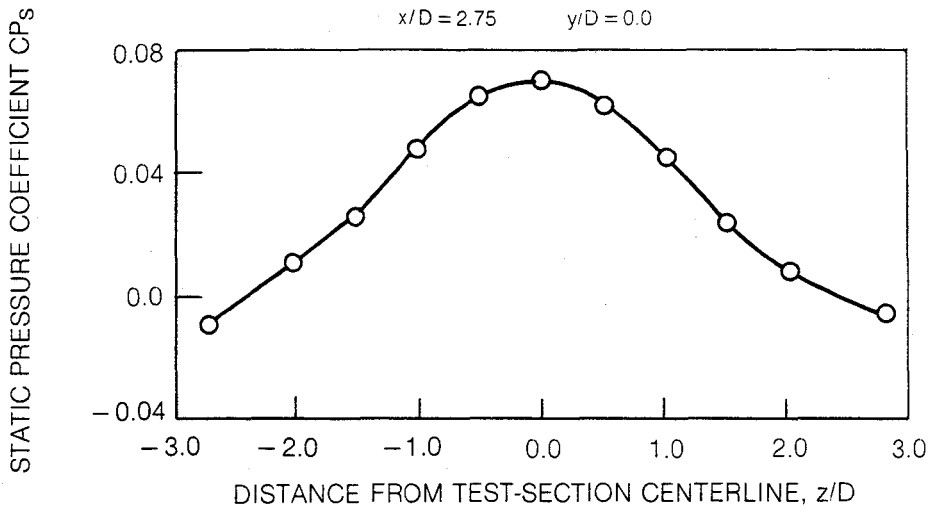


Figure 26 Test-Section Floor Entrance Static Pressure Distribution

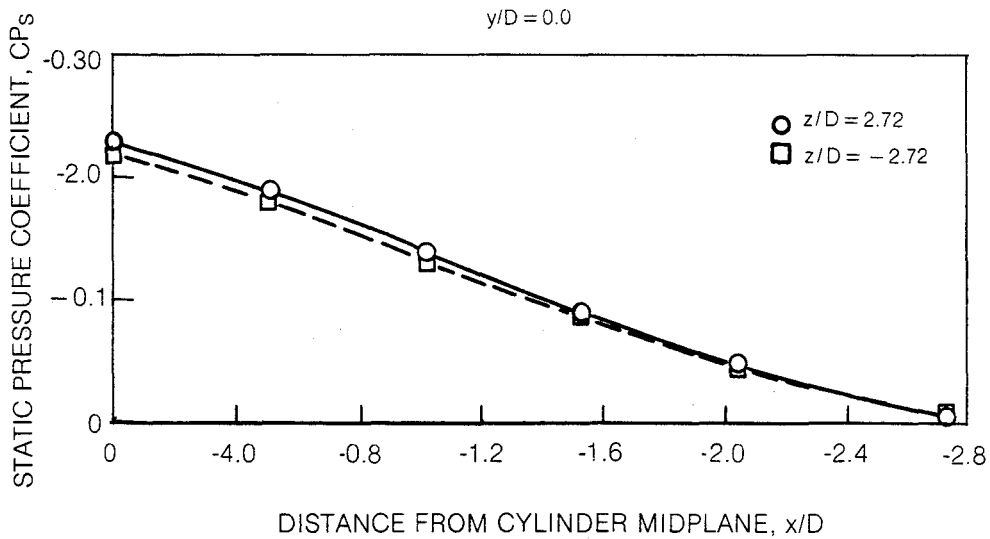


Figure 27 Static Pressure Distribution Near Test-Section Sidewalls

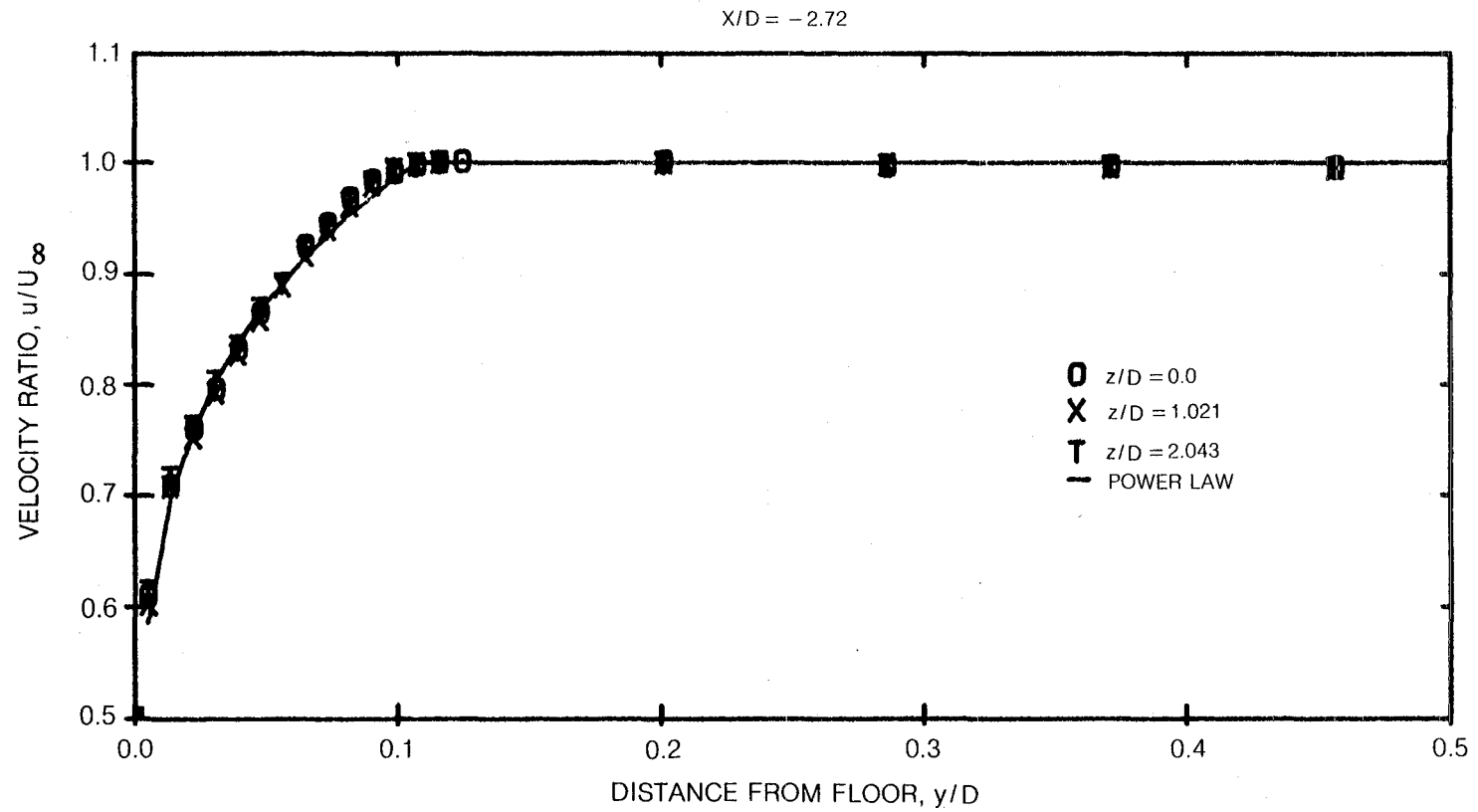


Figure 28 Test-Section Entrance Velocity Distribution

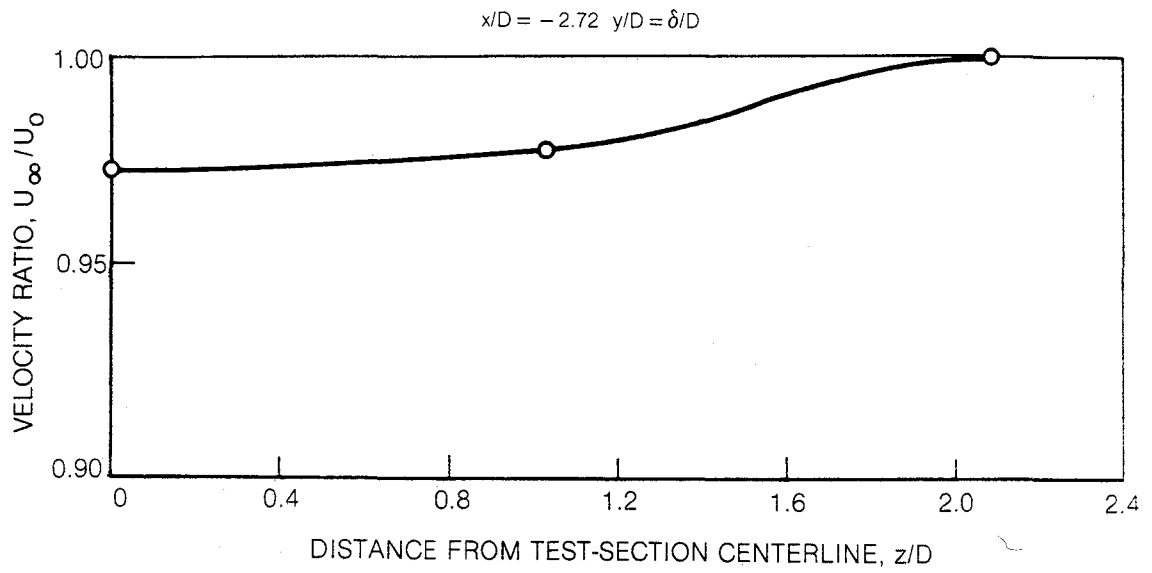


Figure 29 Freestream Entrance Velocity Variation

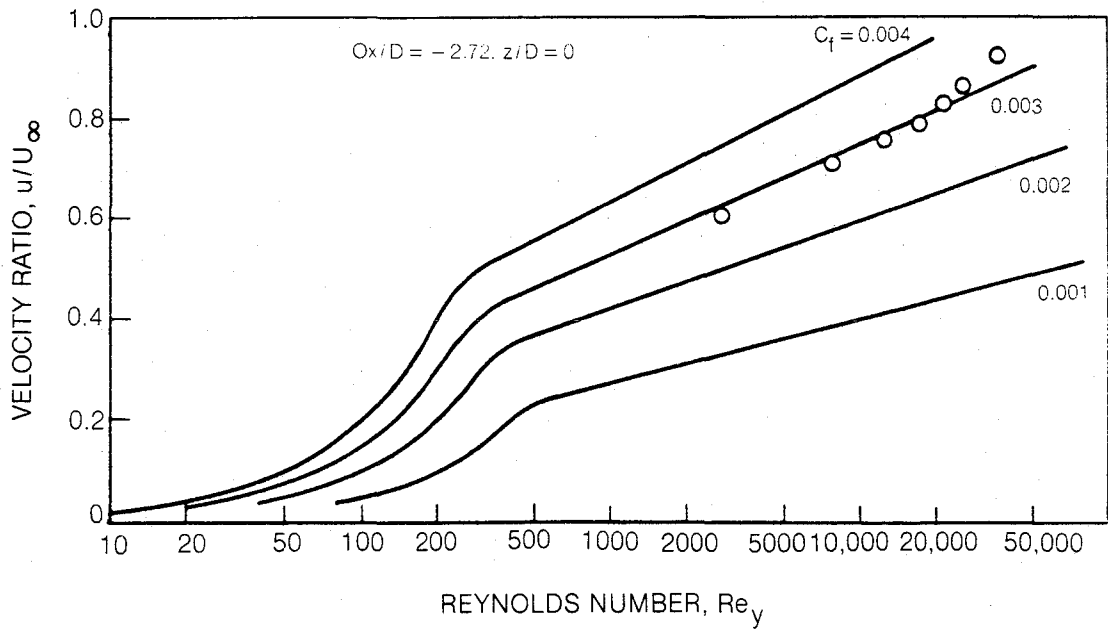


Figure 30 Typical Clauser Diagram

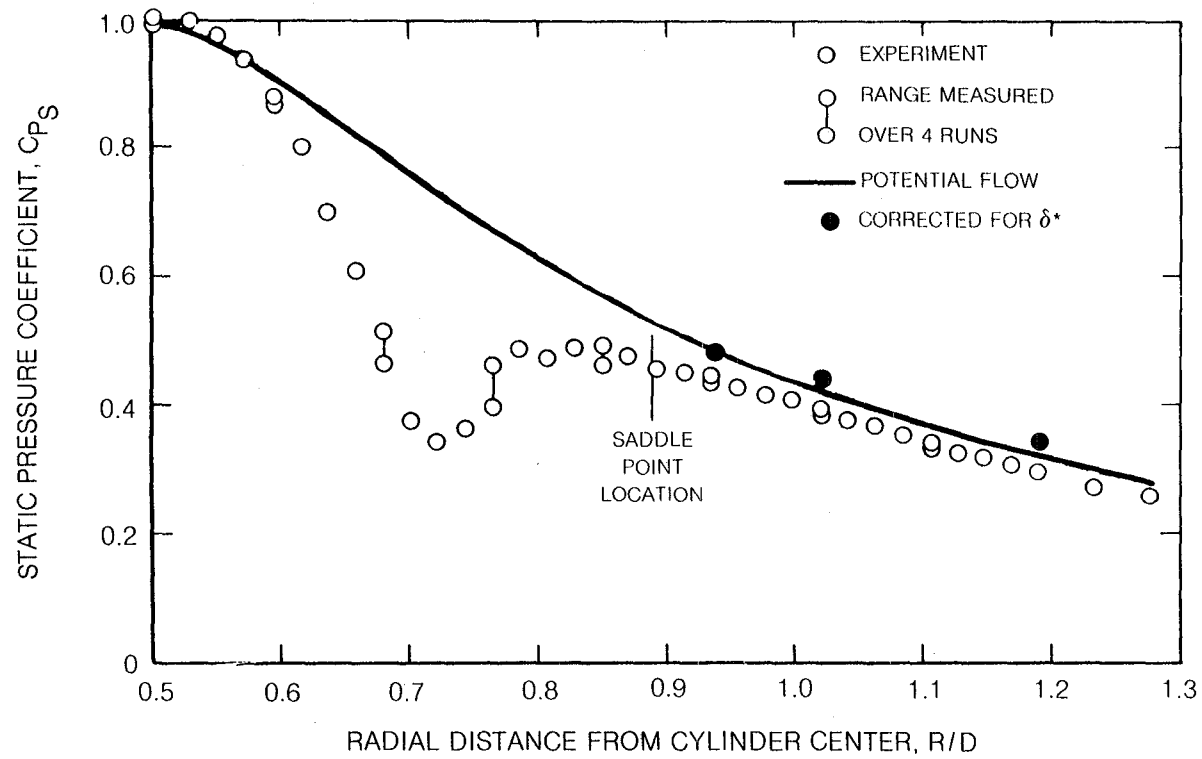


Figure 31 Endwall Static Pressure Distribution in Plane of Symmetry

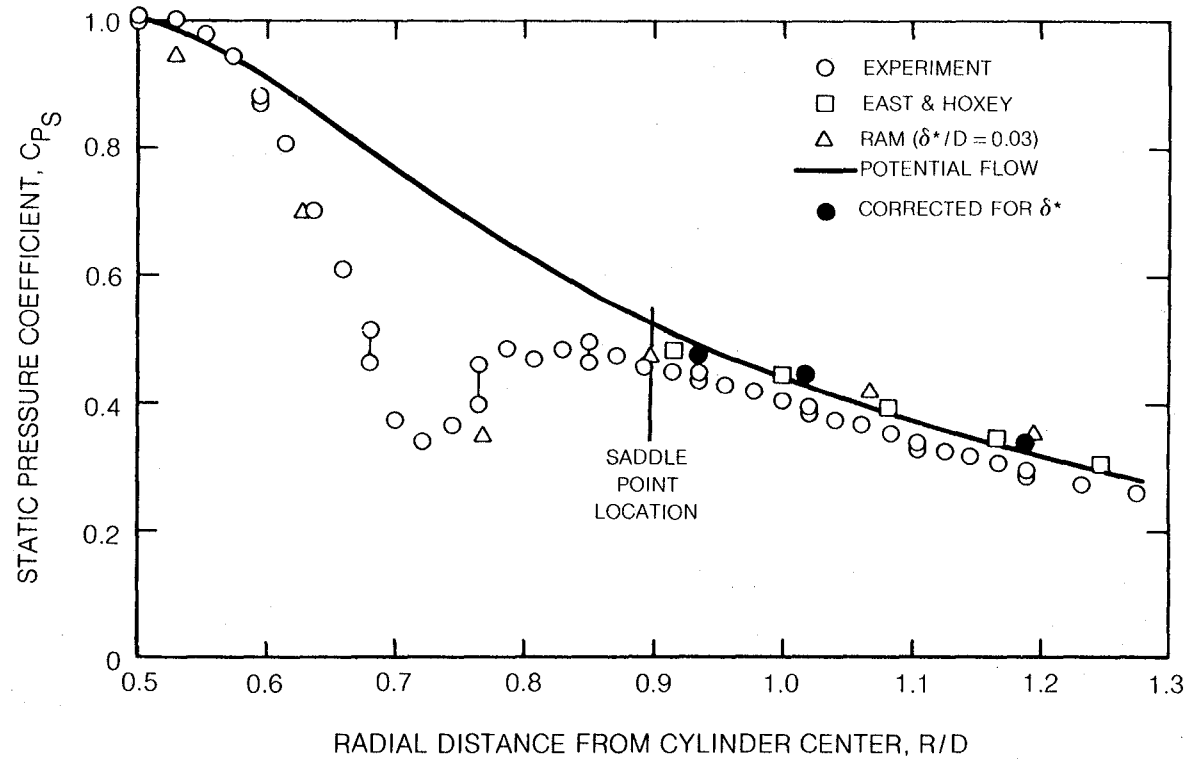


Figure 32 Comparison of Plane of Symmetry Static Pressure Distributions

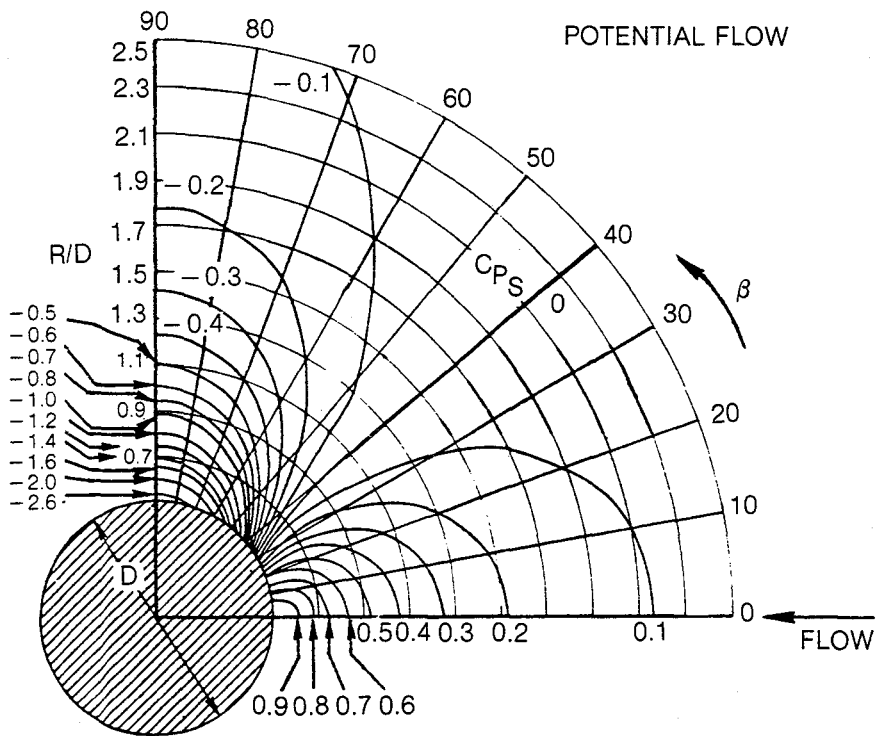
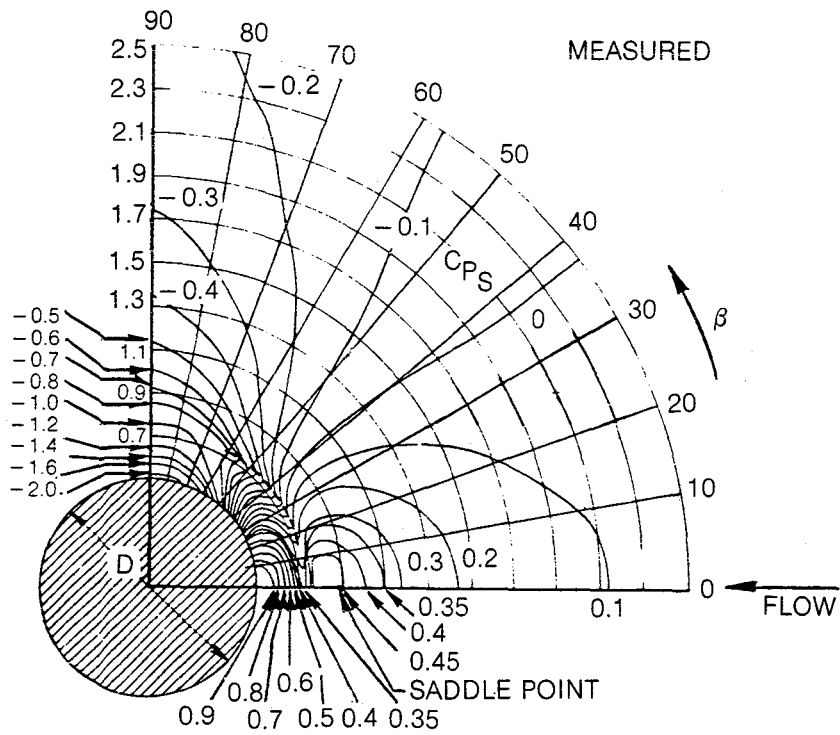


Figure 33 Comparison of Measured Endwall Pressure Distribution with Potential-Flow Pressure Distribution

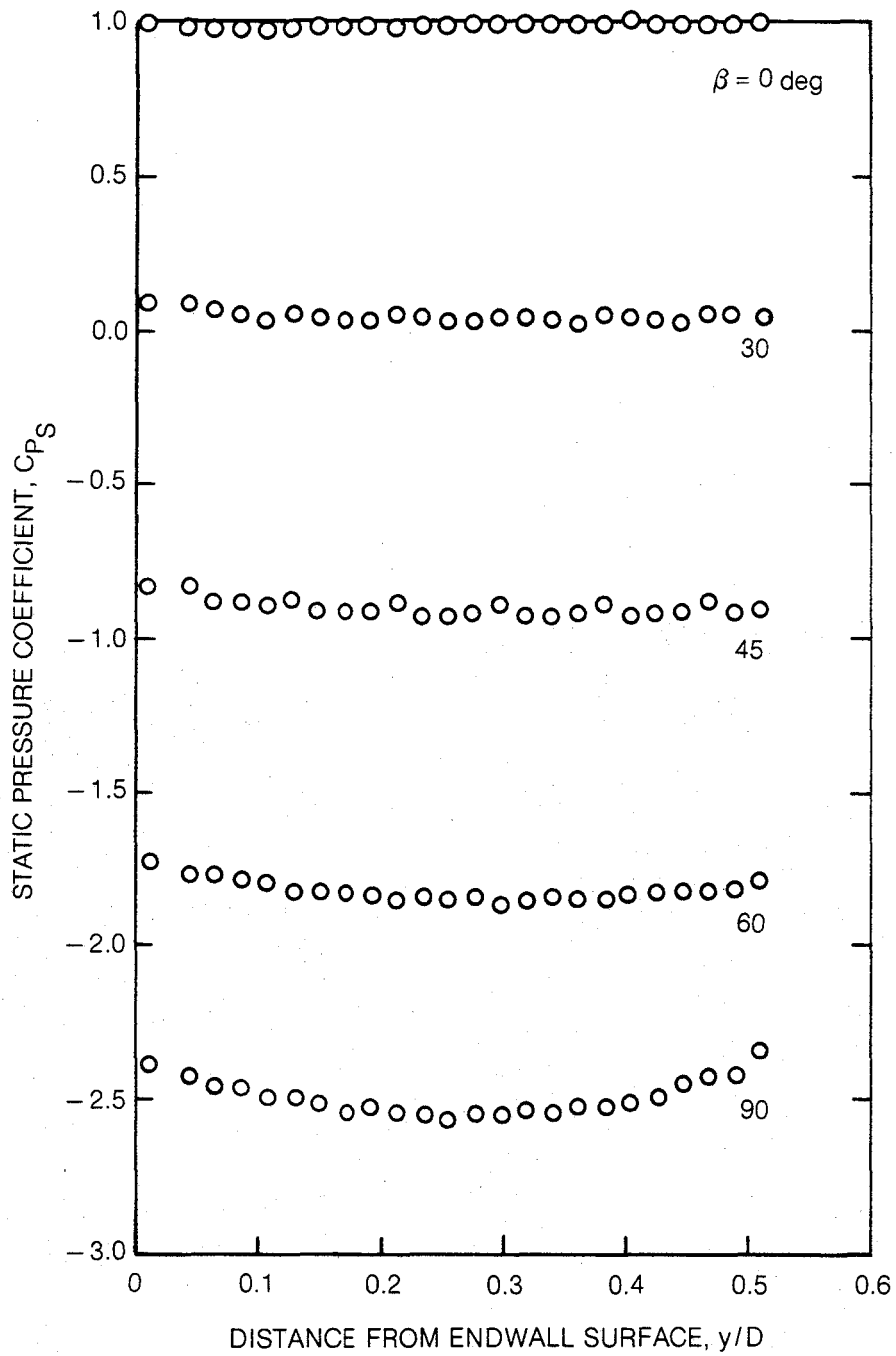


Figure 34 Cylinder Surface Lateral Pressure Distribution

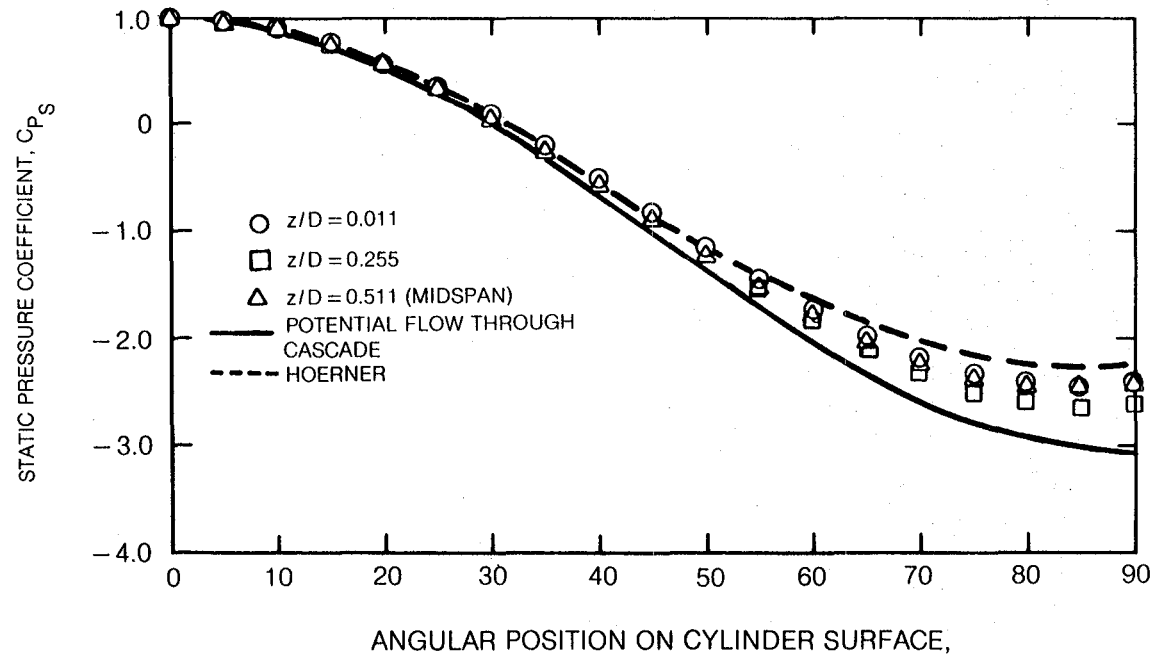


Figure 35 Cylinder Surface Angular Pressure Distribution

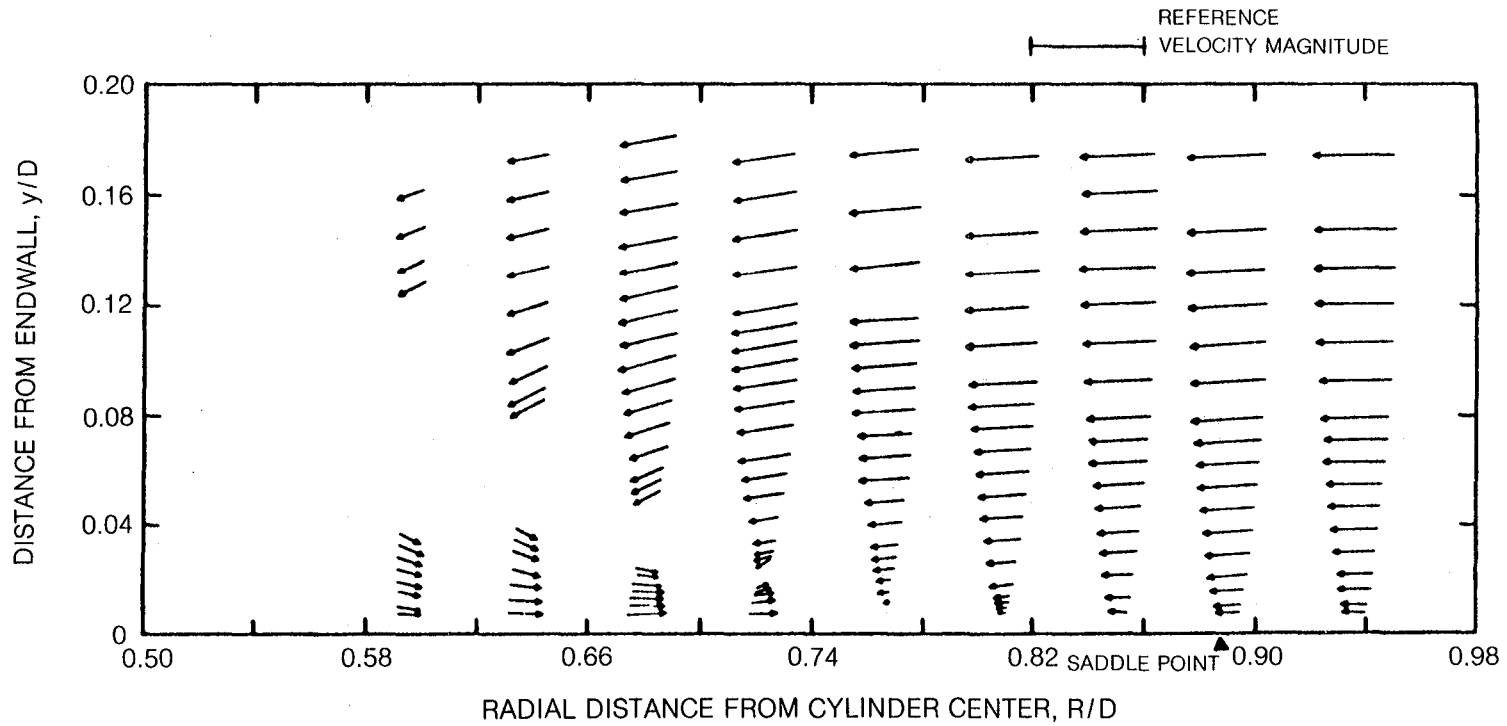


Figure 36 Velocity Vectors in the Plane of Symmetry

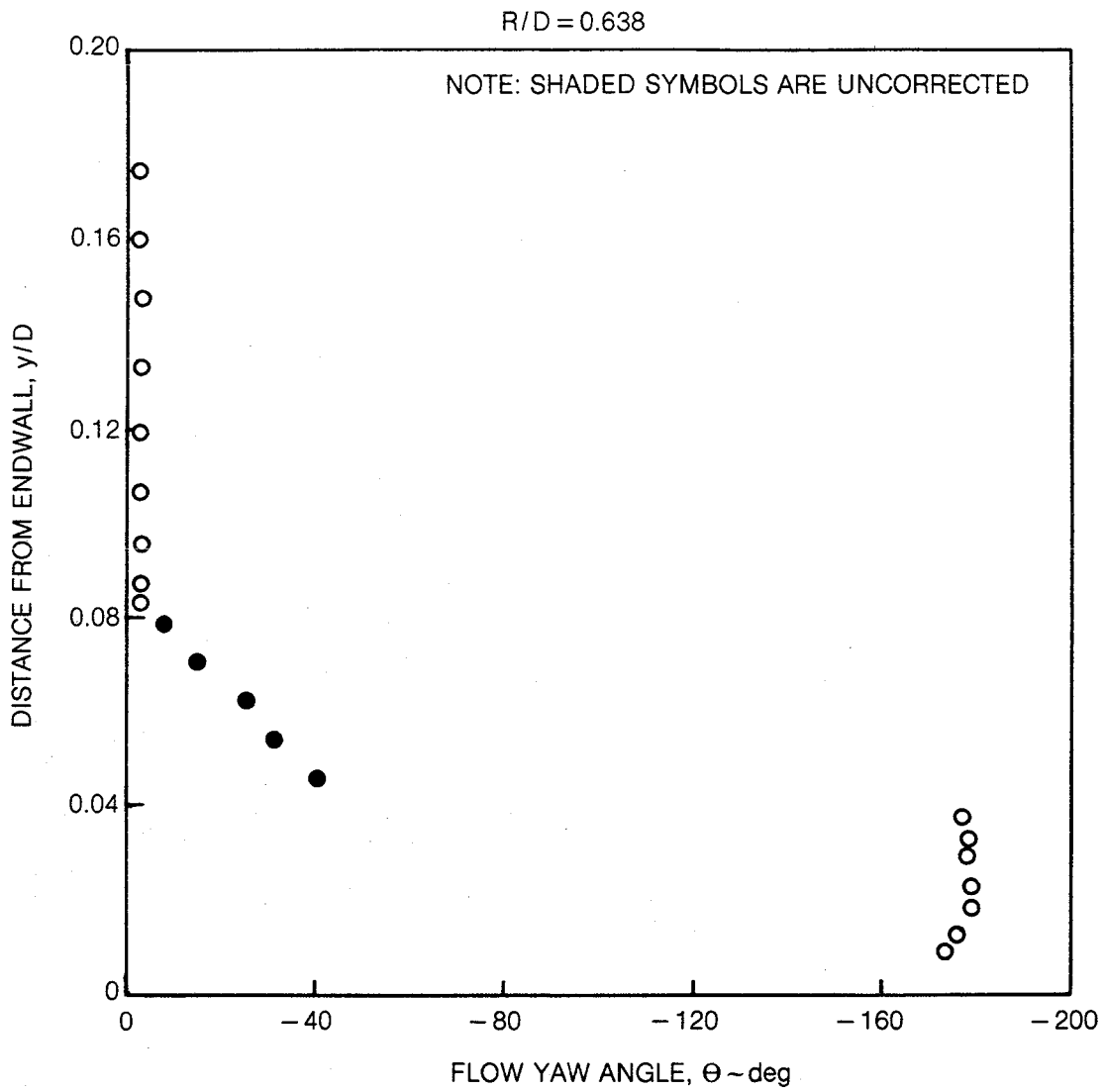


Figure 37 Plane of Symmetry Flow Yaw Angles

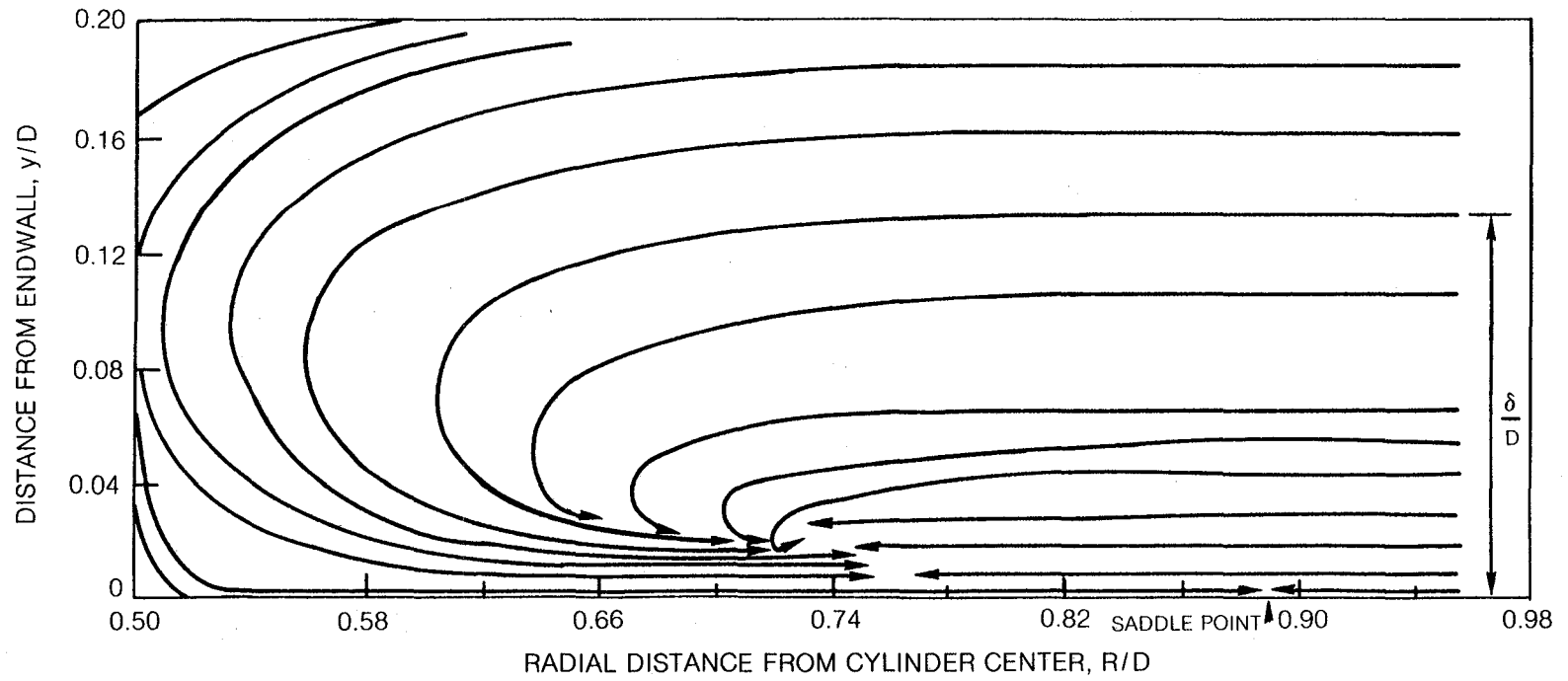


Figure 38 Flow Pattern in the Plane of Symmetry

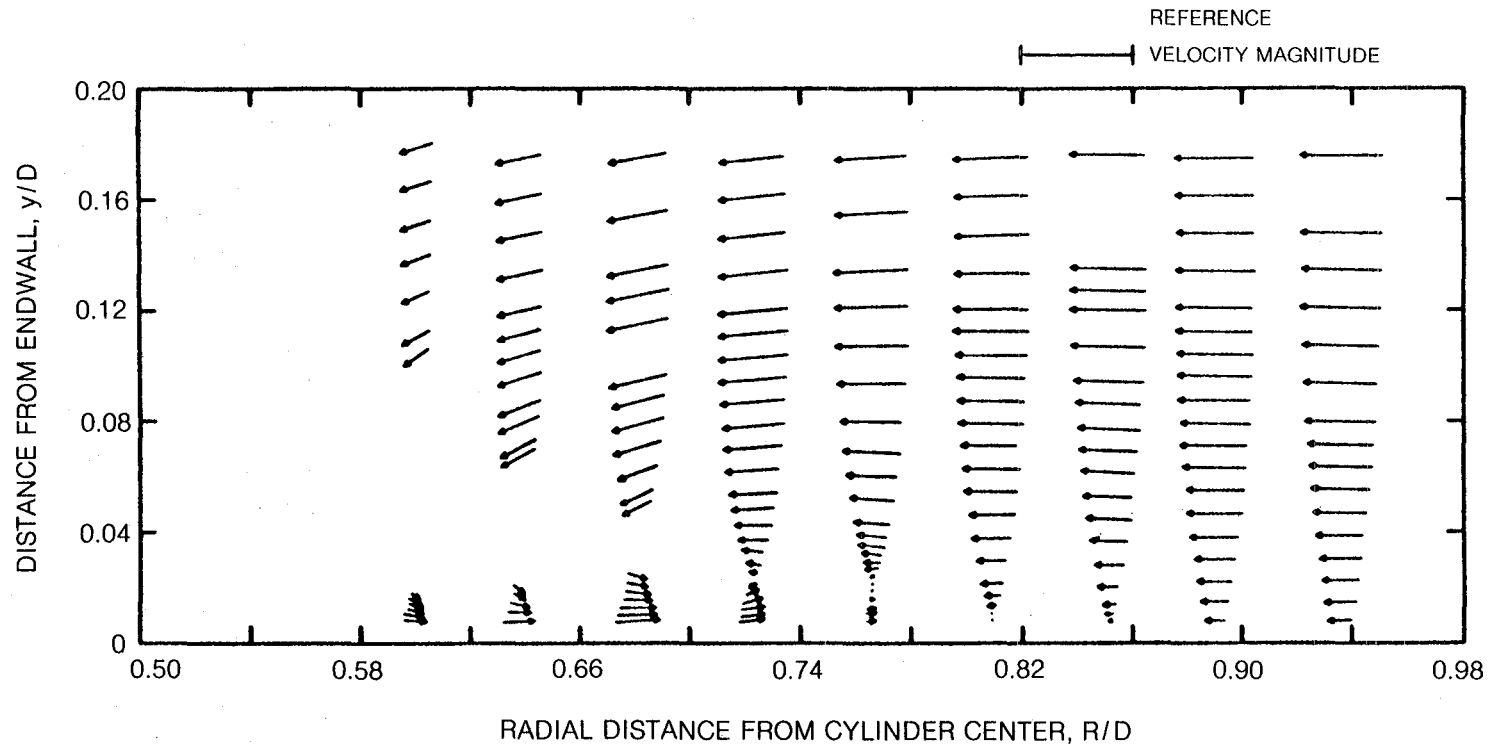


Figure 39 Velocity Vectors in the 5-deg Plane

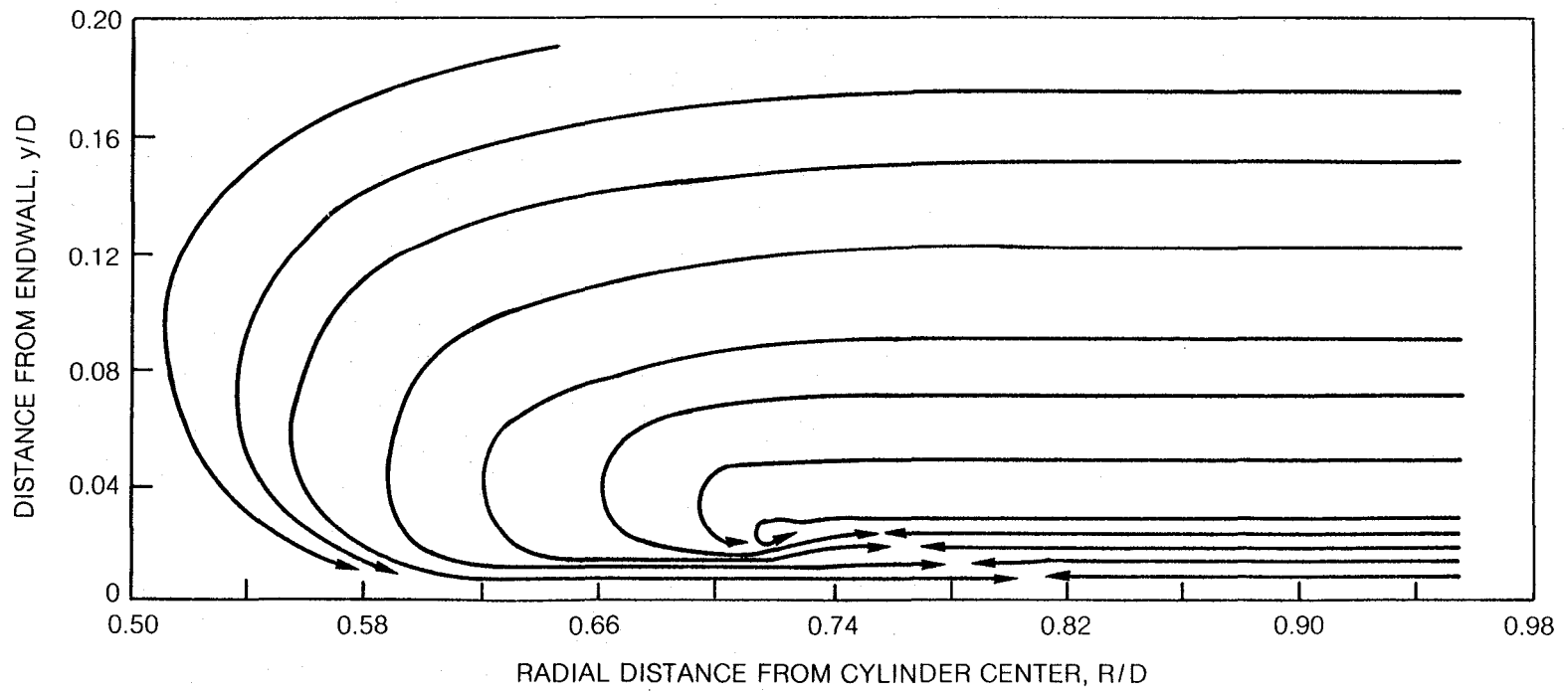


Figure 40 Flow Pattern in the 5-deg Plane

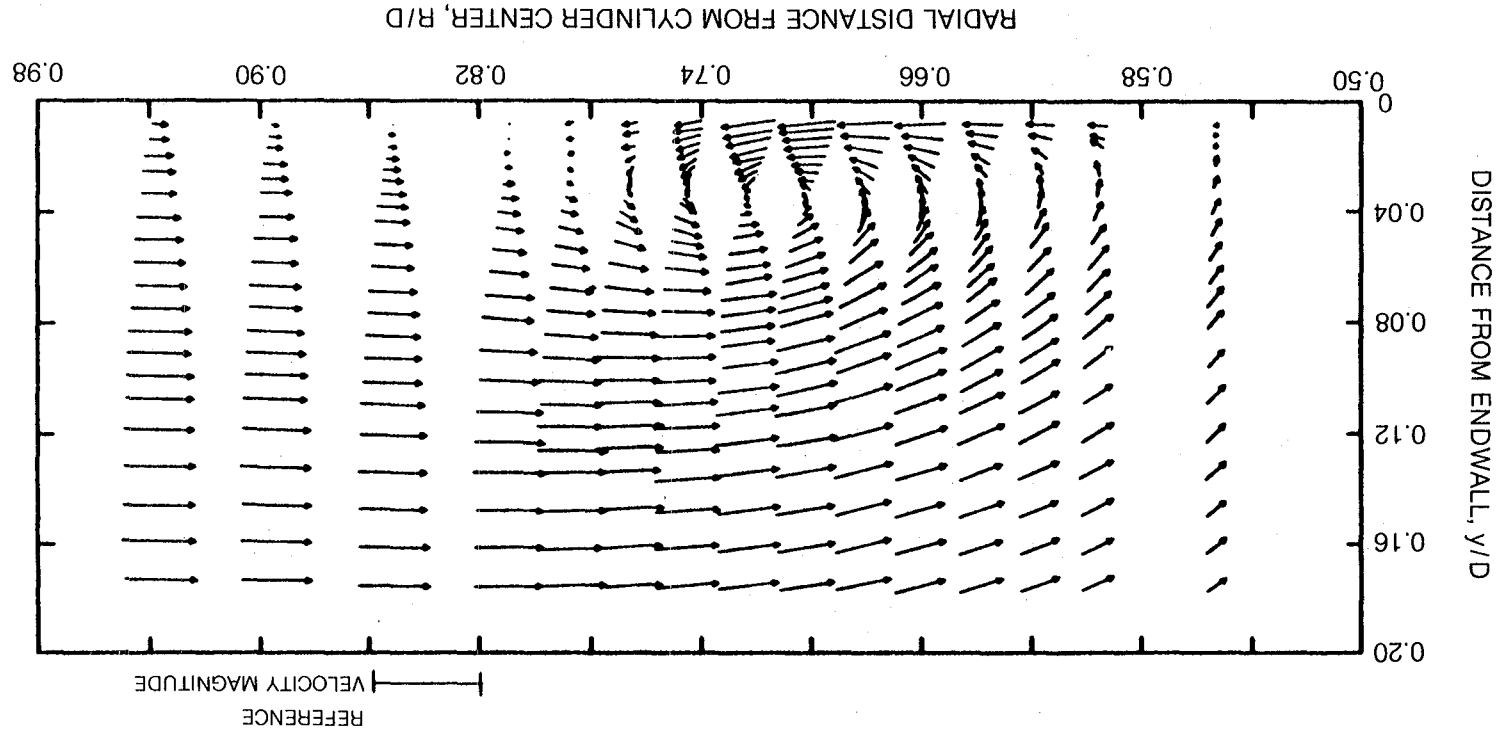


Figure 41 Velocity Vectors in the 25-deg Plane

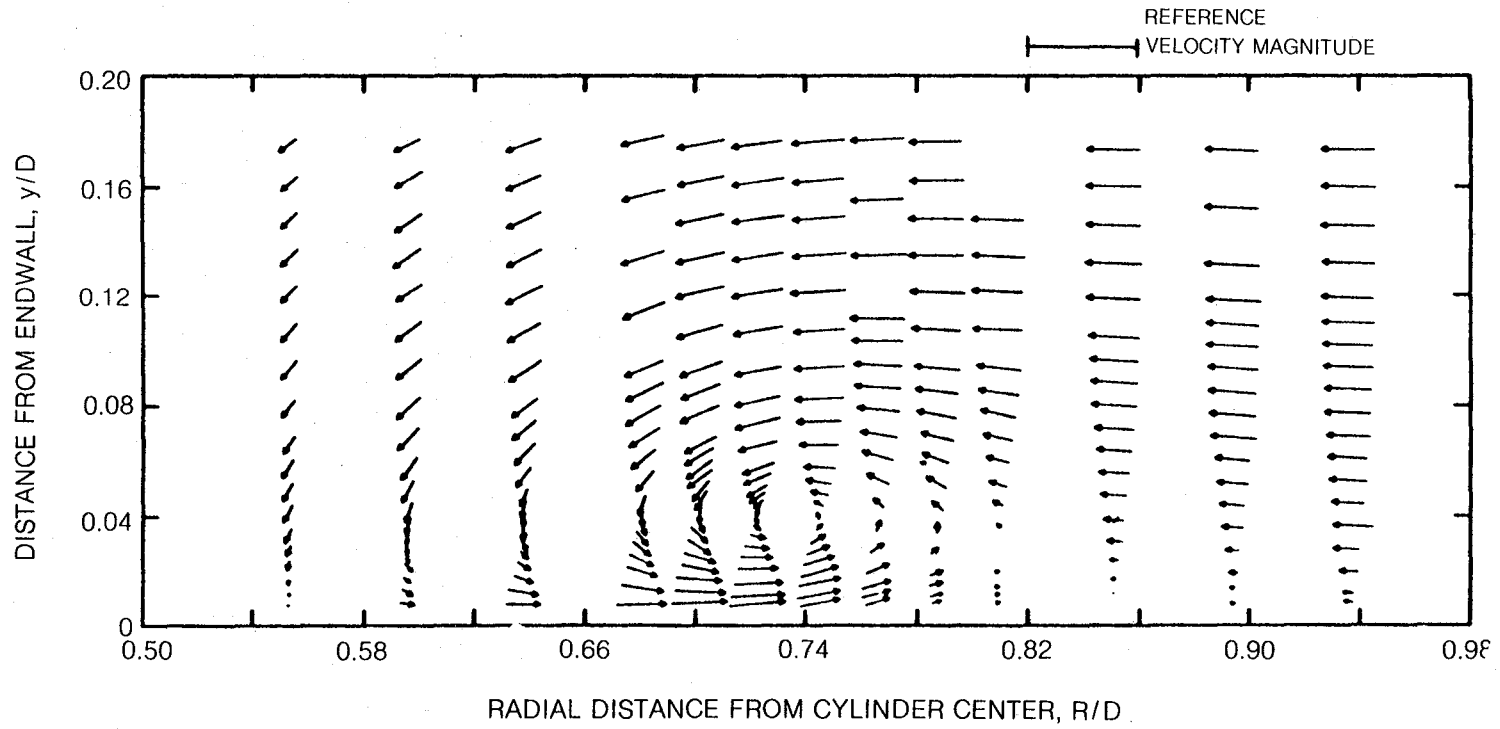


Figure 42 Velocity Vectors in the 45-deg Plane

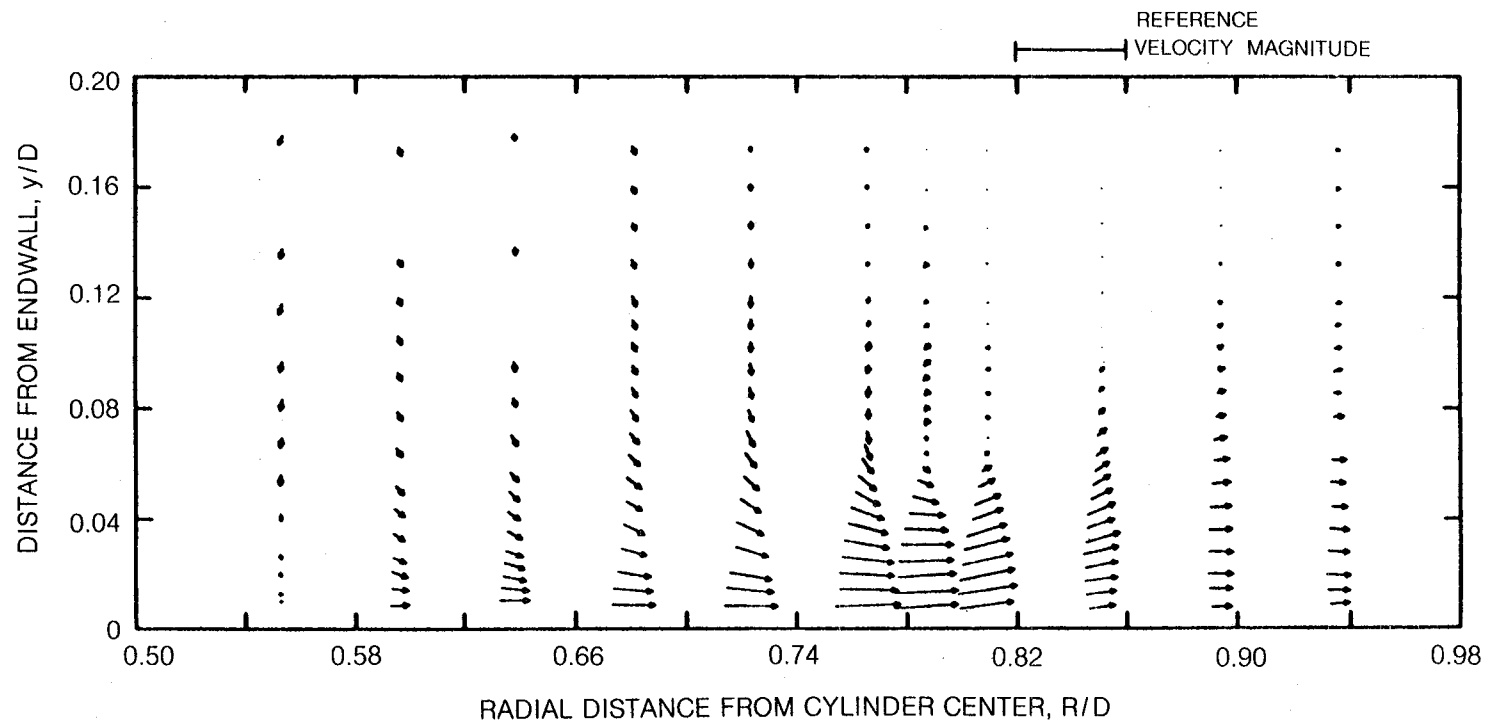


Figure 43 Velocity Vectors in the 90-deg Plane

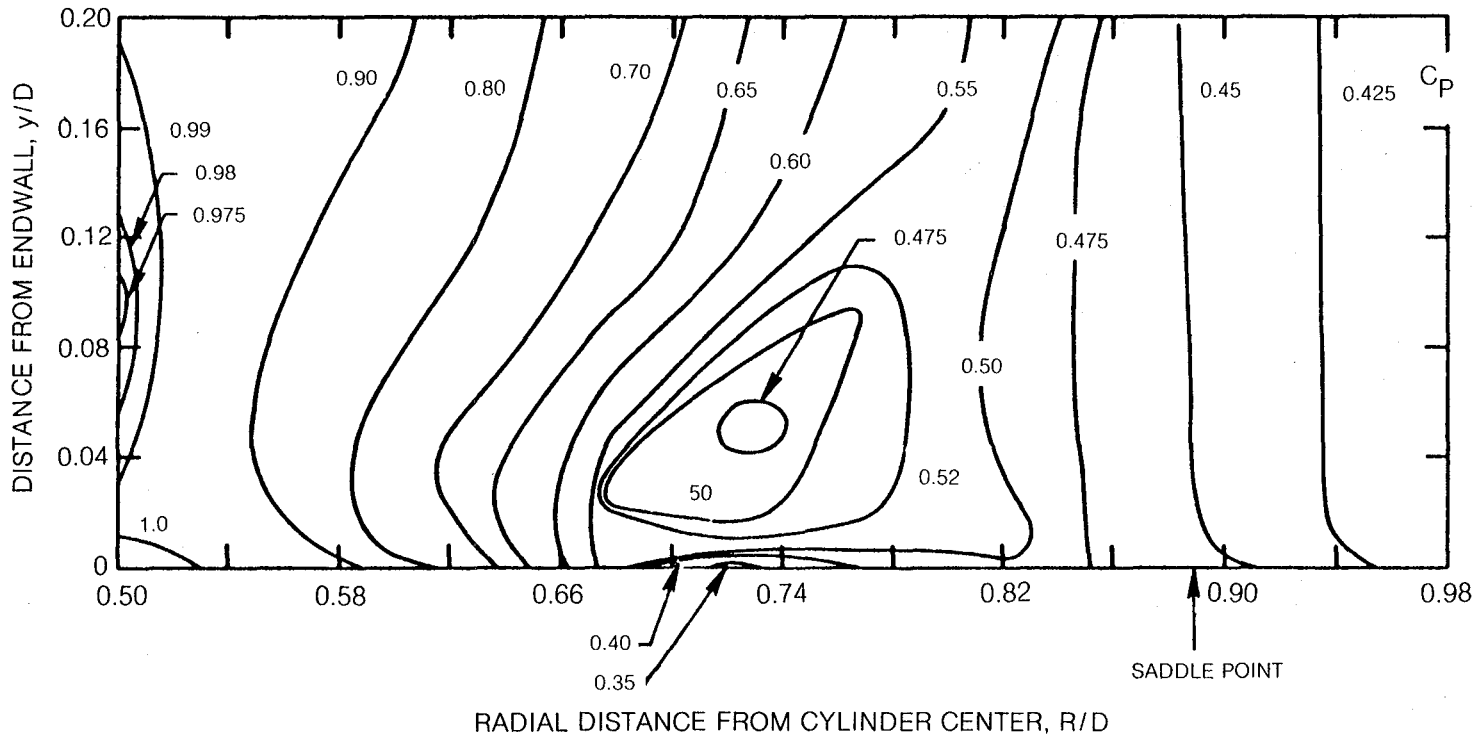


Figure 44 Static Pressure Contours in Plane of Symmetry

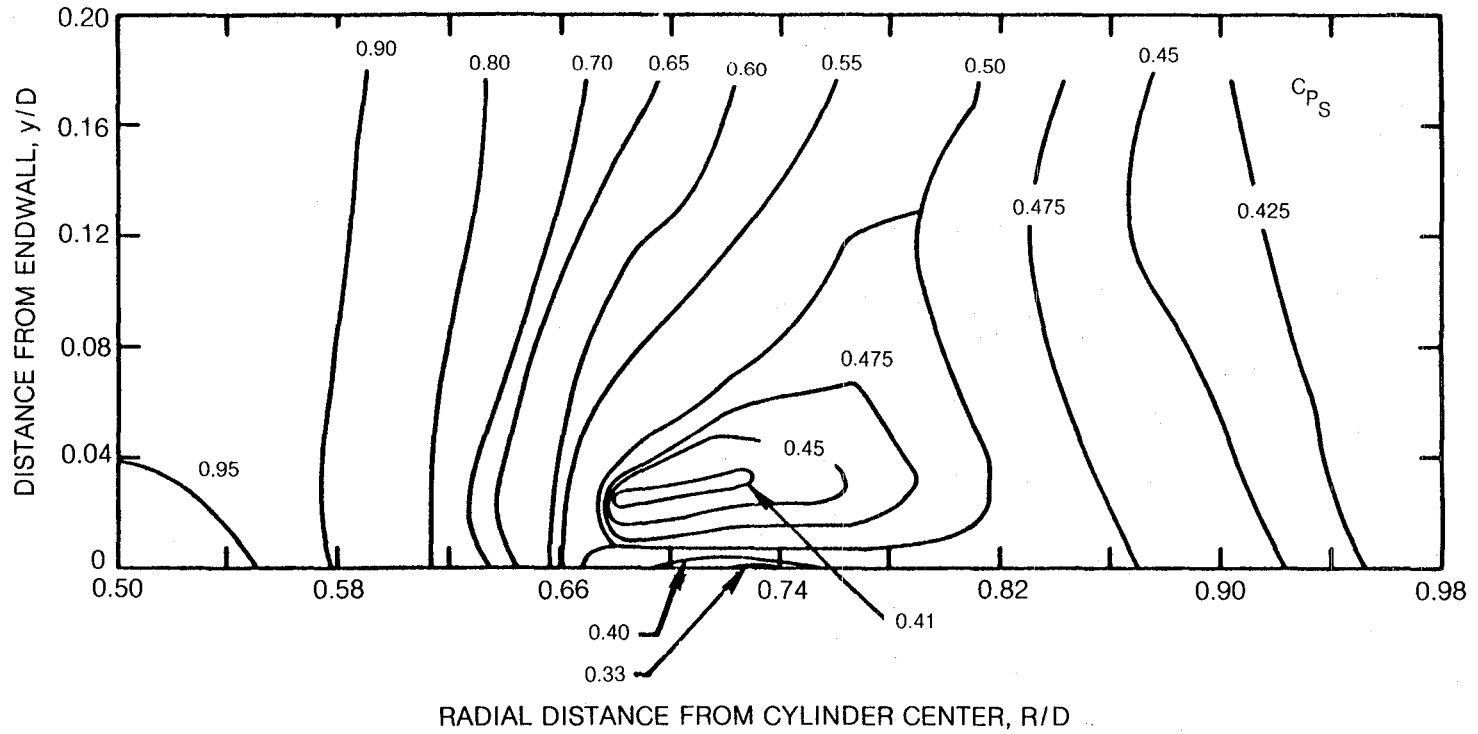


Figure 45 Static Pressure Contours in 5-deg Plane

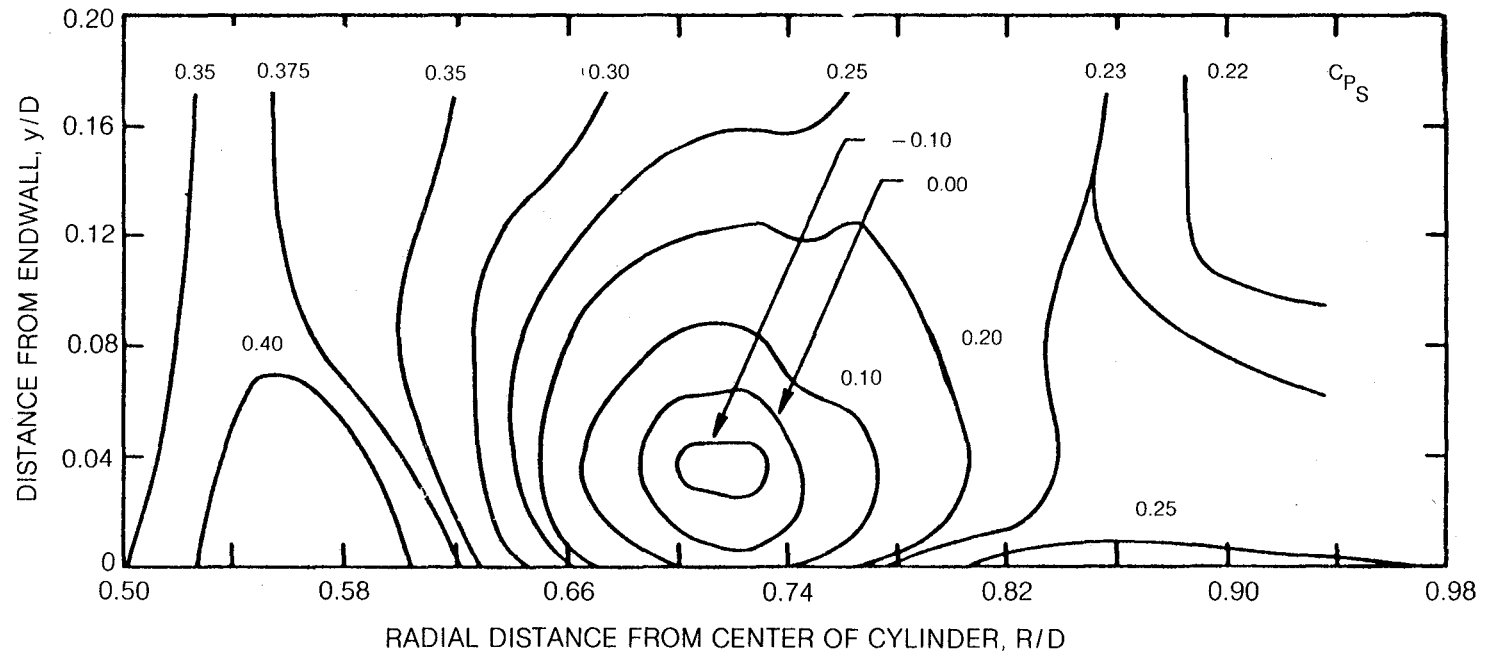


Figure 46 Static Pressure Contours in 25-deg Plane

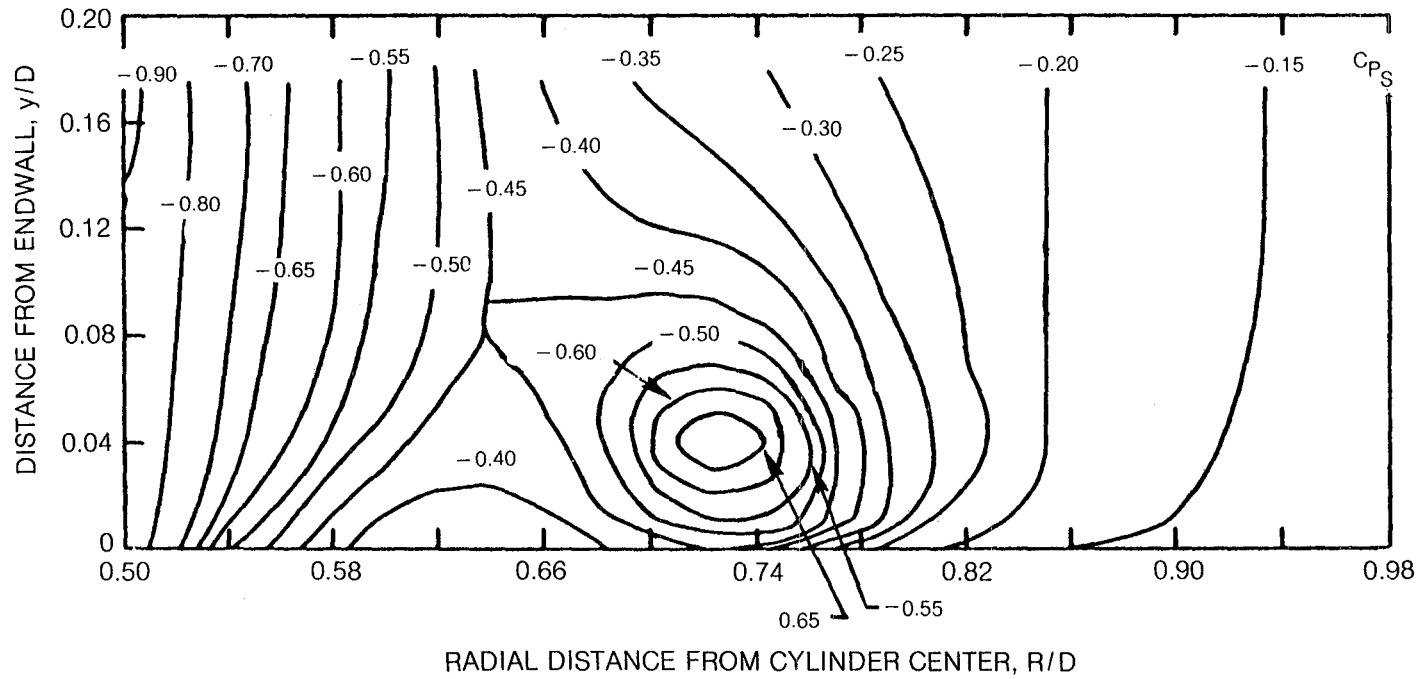


Figure 47 Static Pressure Contours in 45-deg Plane

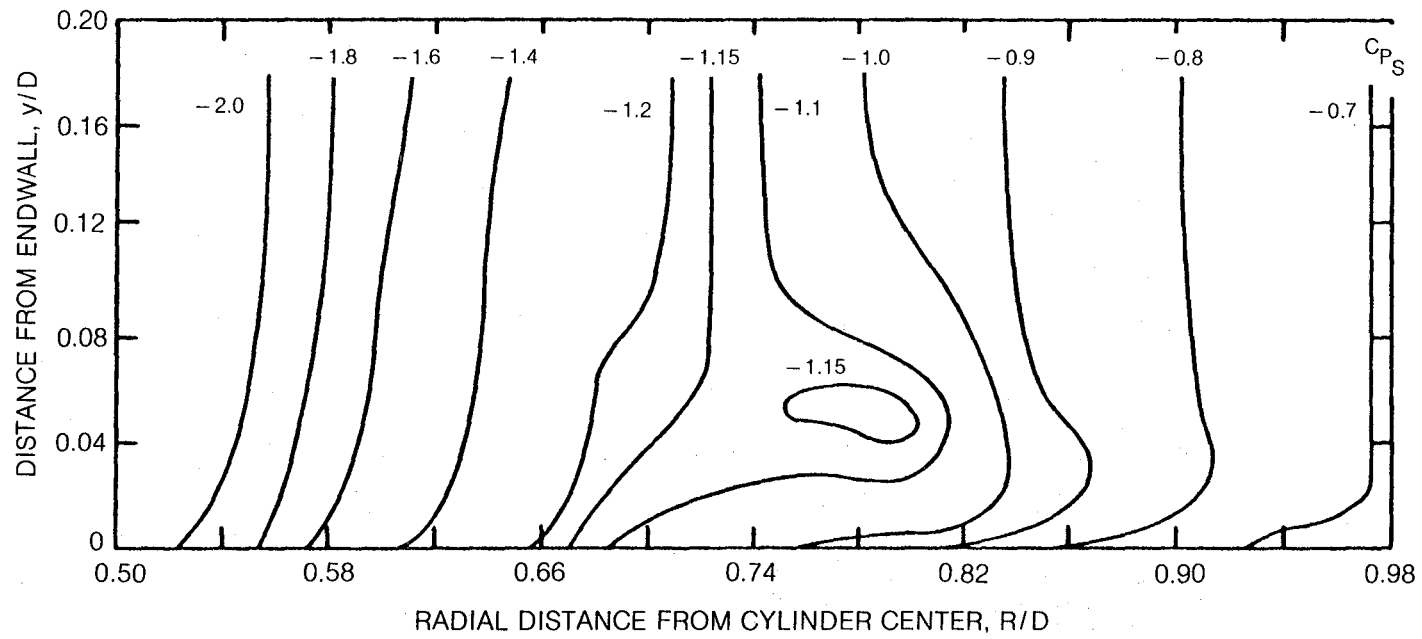


Figure 48 Static Pressure Contours in 90-deg Plane

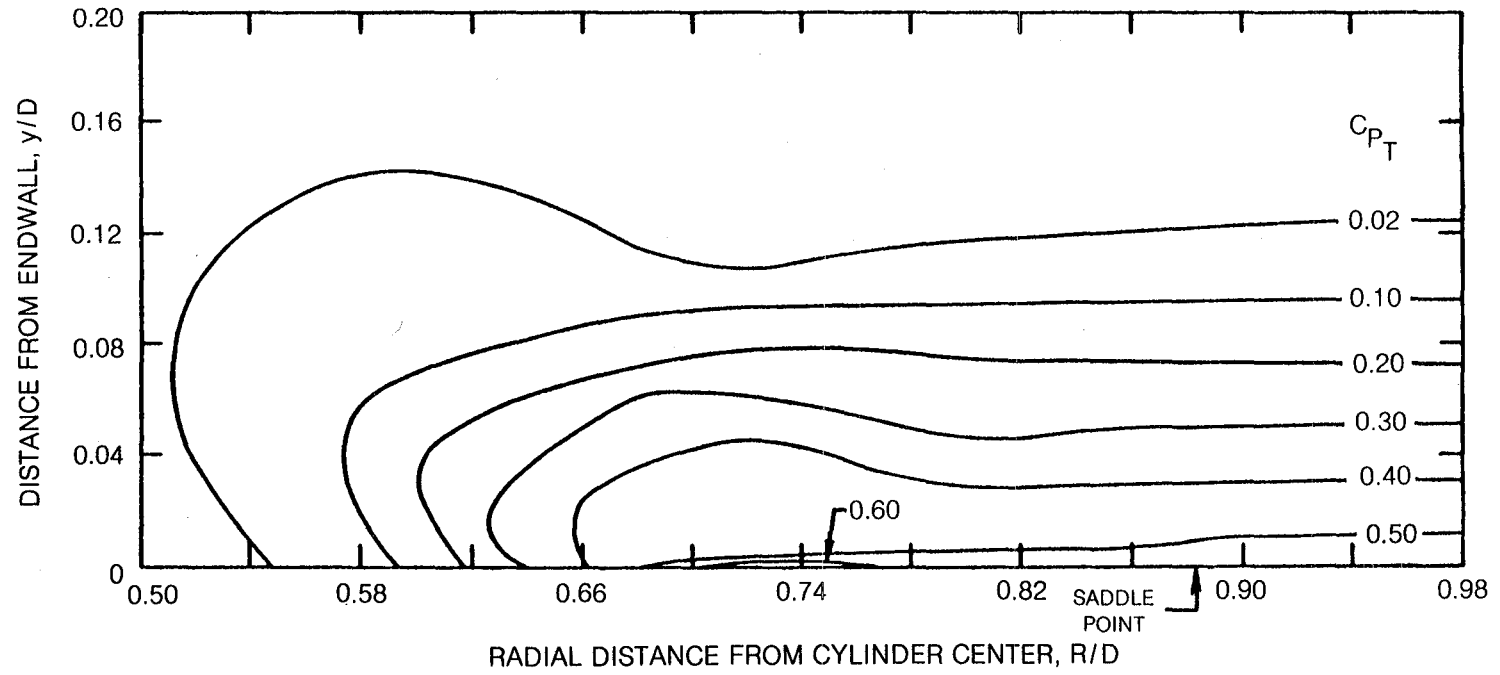


Figure 49 Total Pressure Loss in Plane of Symmetry

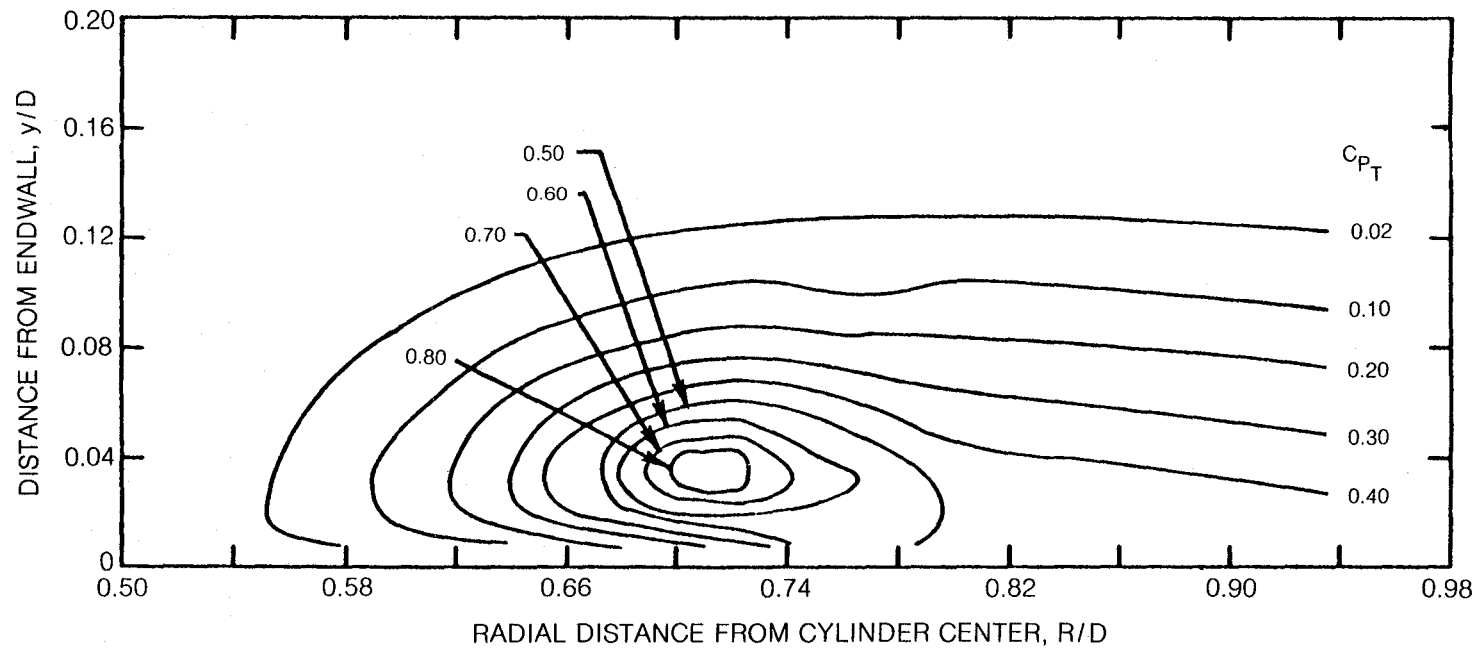


Figure 50 Total Pressure Loss in 25-deg Plane

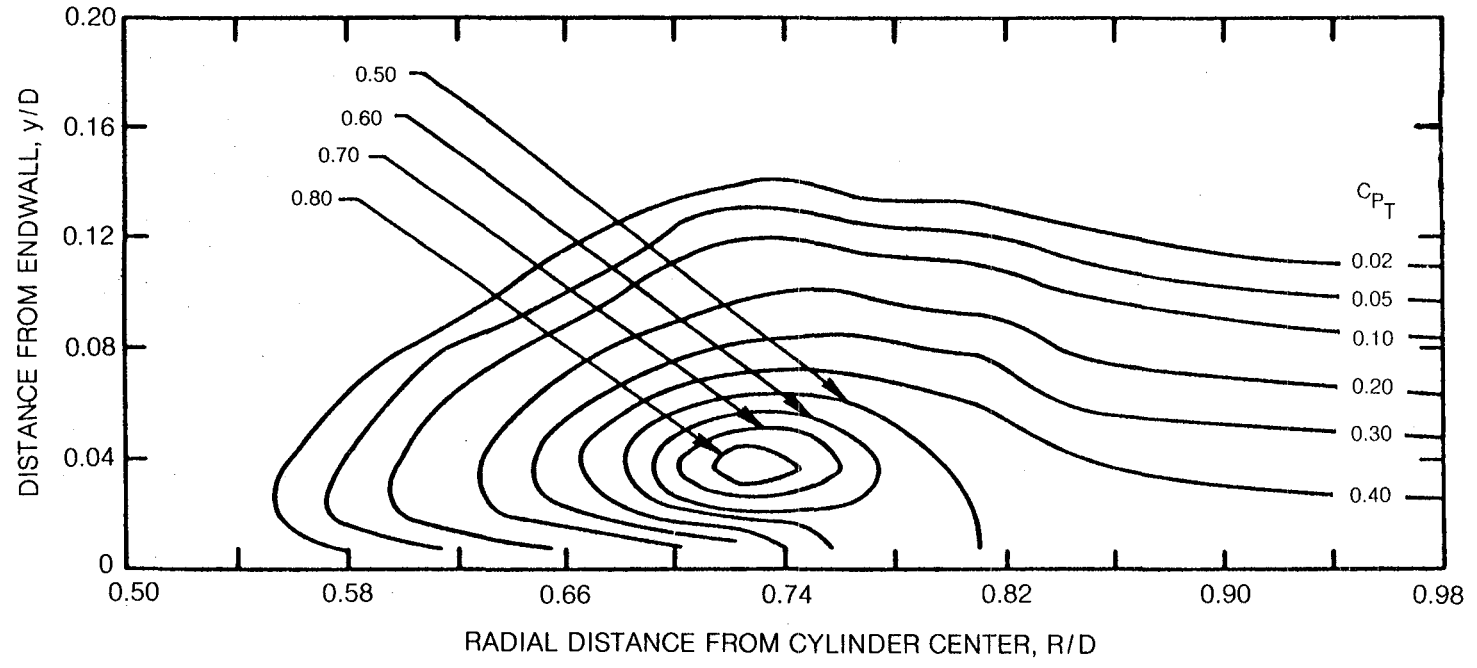


Figure 51 Total Pressure Loss in 45-deg Plane

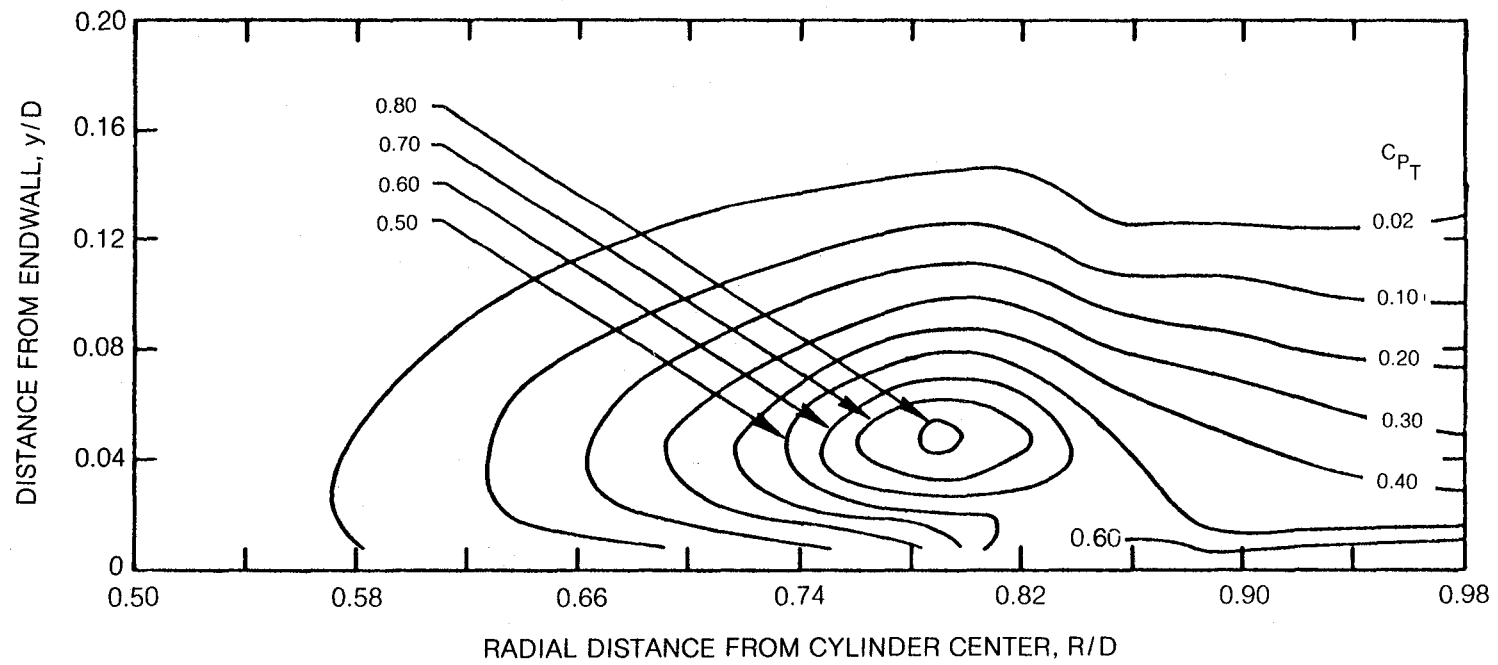


Figure 52 Total Pressure Loss in 90-deg Plane

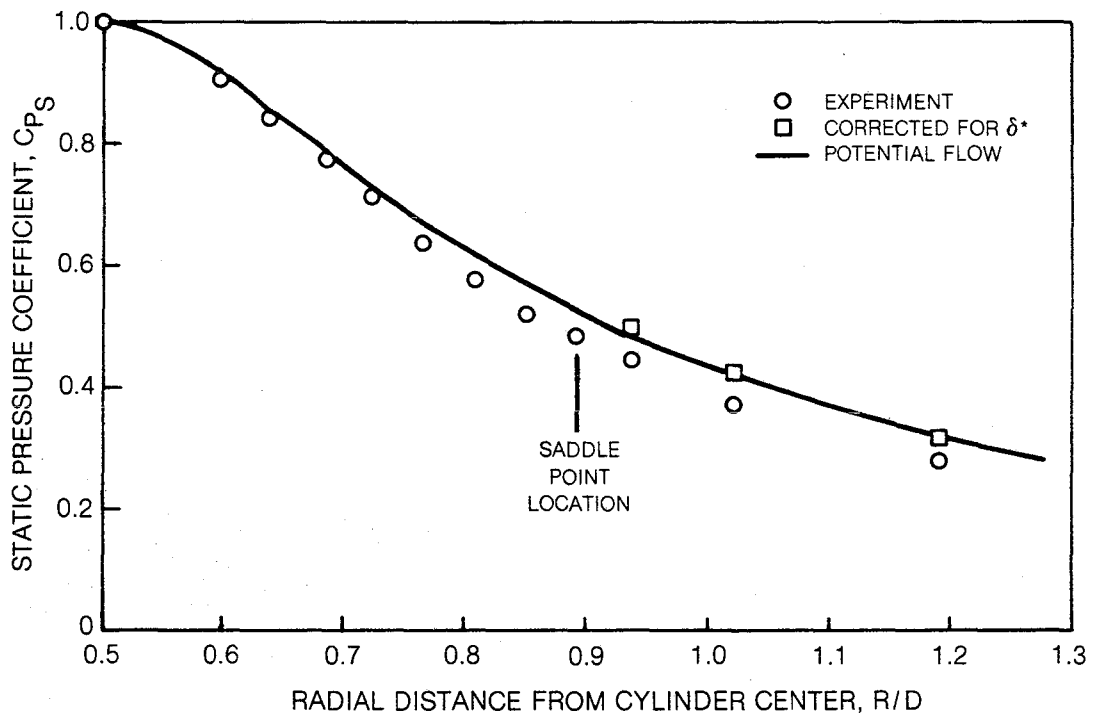


Figure 53 Midspan and Potential-Flow Static Pressure Distribution in Plane of Symmetry

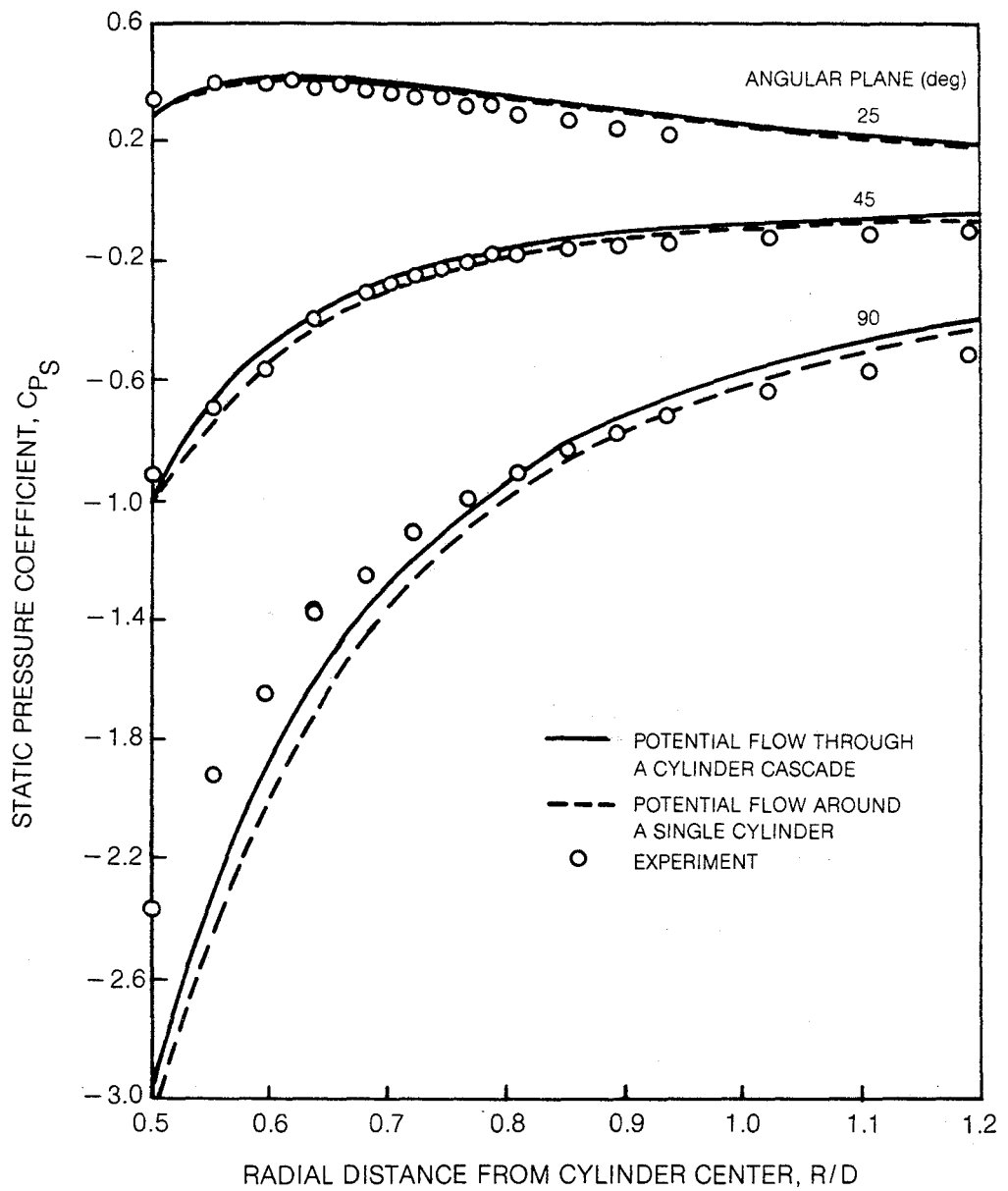


Figure 54 Midspan and Potential Flow Static Pressure Distribution in the 25-, 45-, and 90-deg Planes

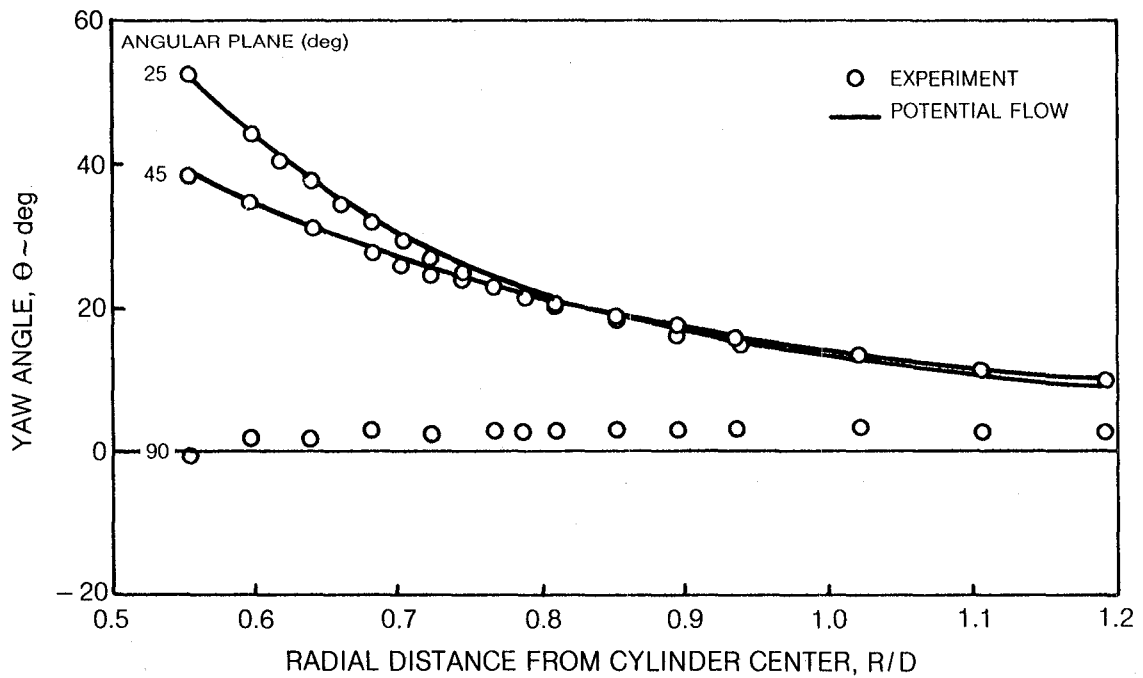


Figure 55 Midspan and Potential-Flow Yaw Angle Distribution

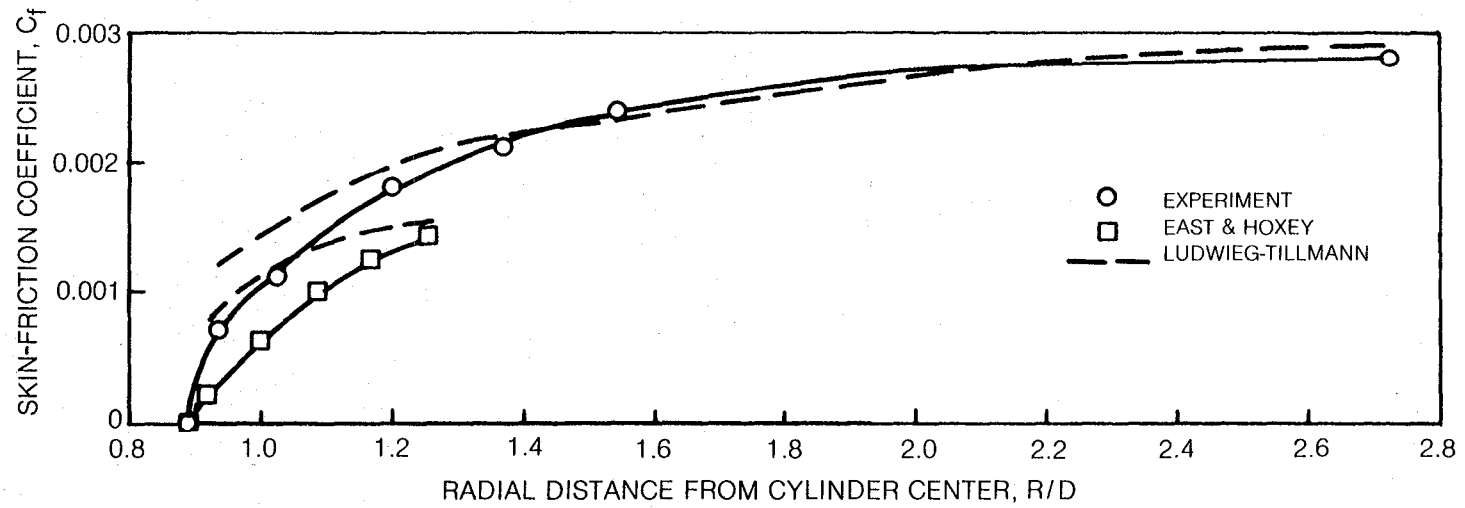


Figure 56 Variation of Skin-Friction Coefficient Along the Plane of Symmetry

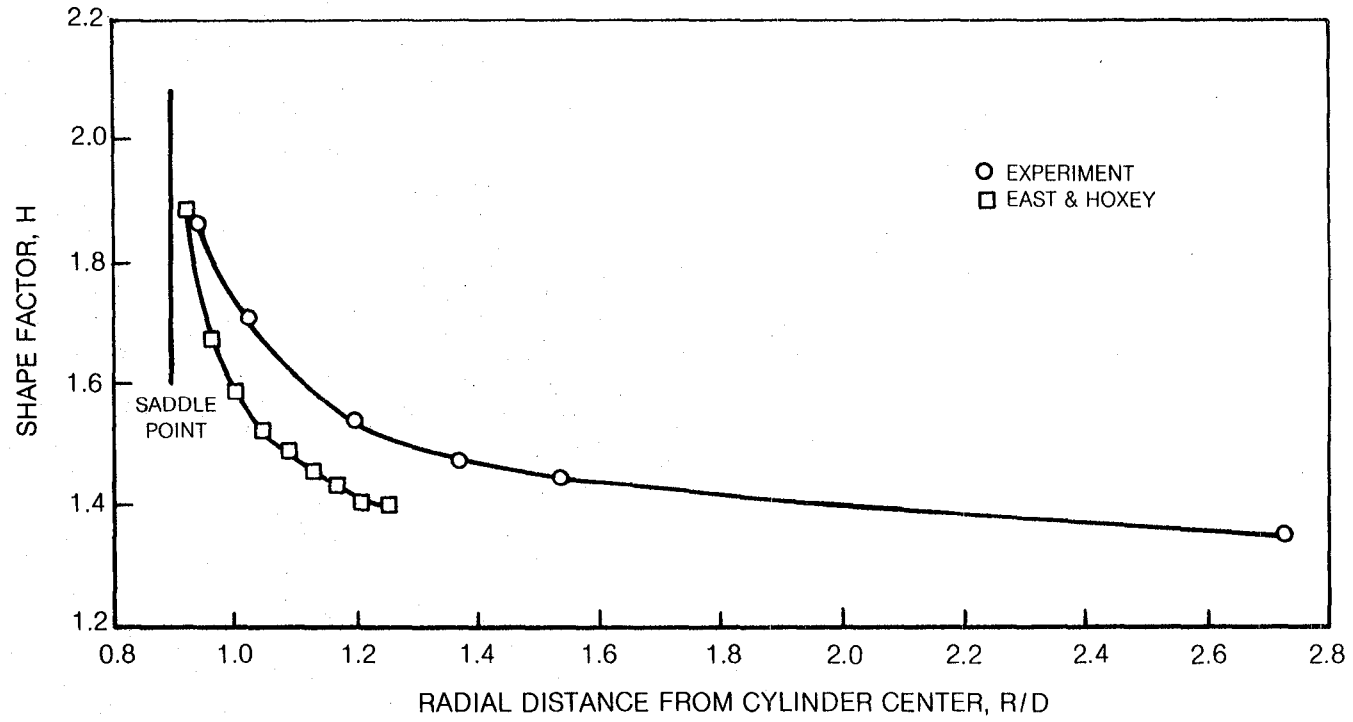


Figure 57 Variation of Boundary-Layer Shape Factor Along the Plane of Symmetry

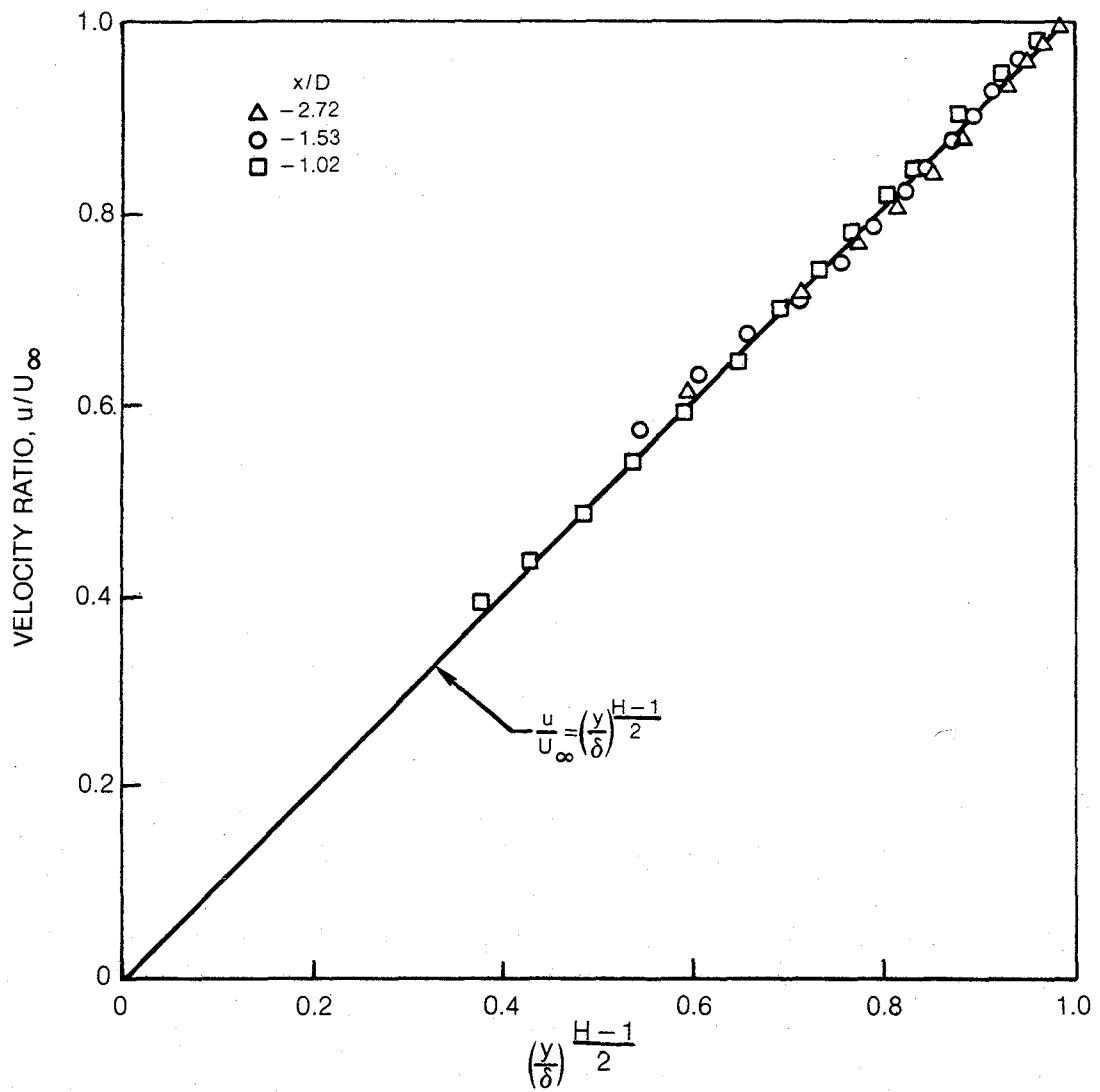


Figure 58 Velocity Profiles in the Plane of Symmetry

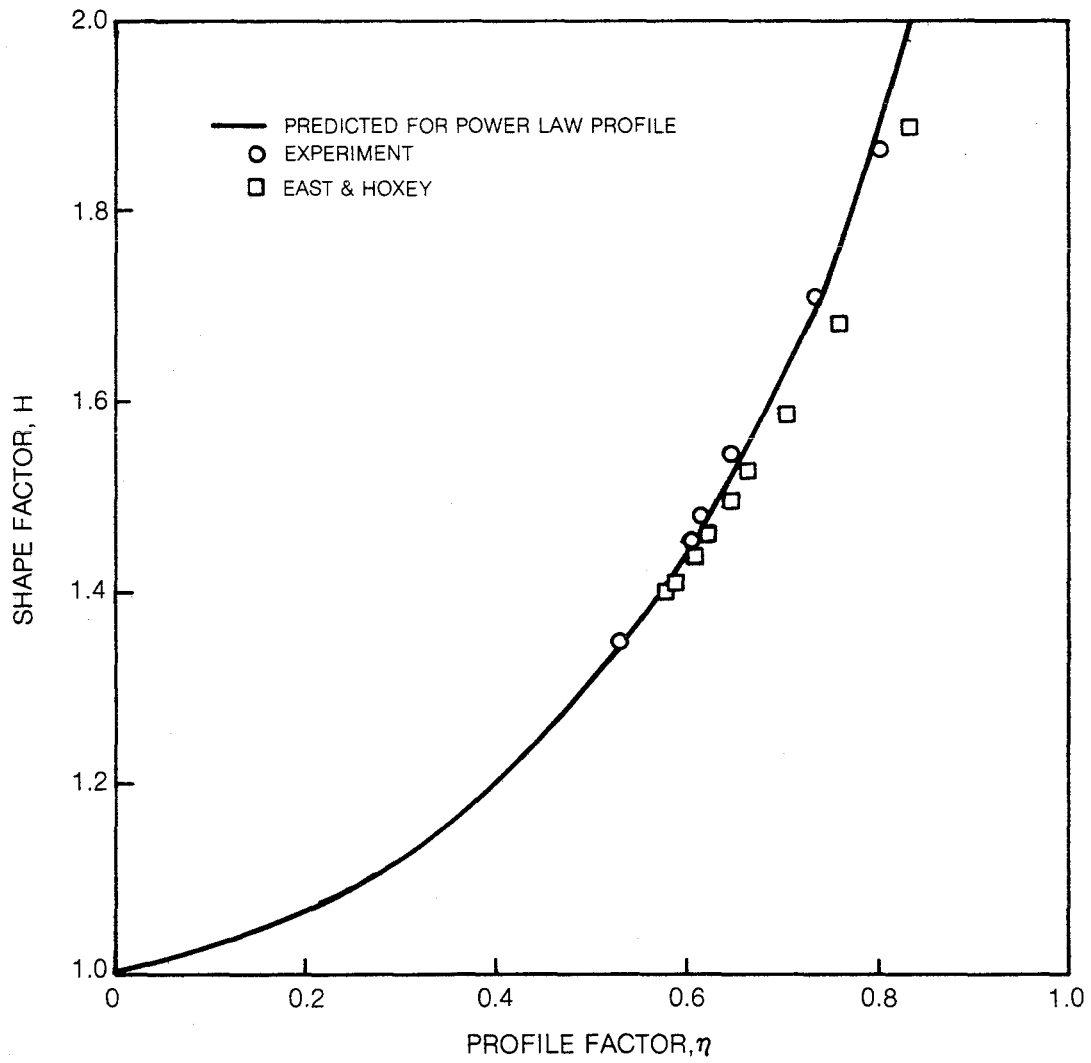


Figure 59 Shape and Profile Factors in the Plane of Symmetry

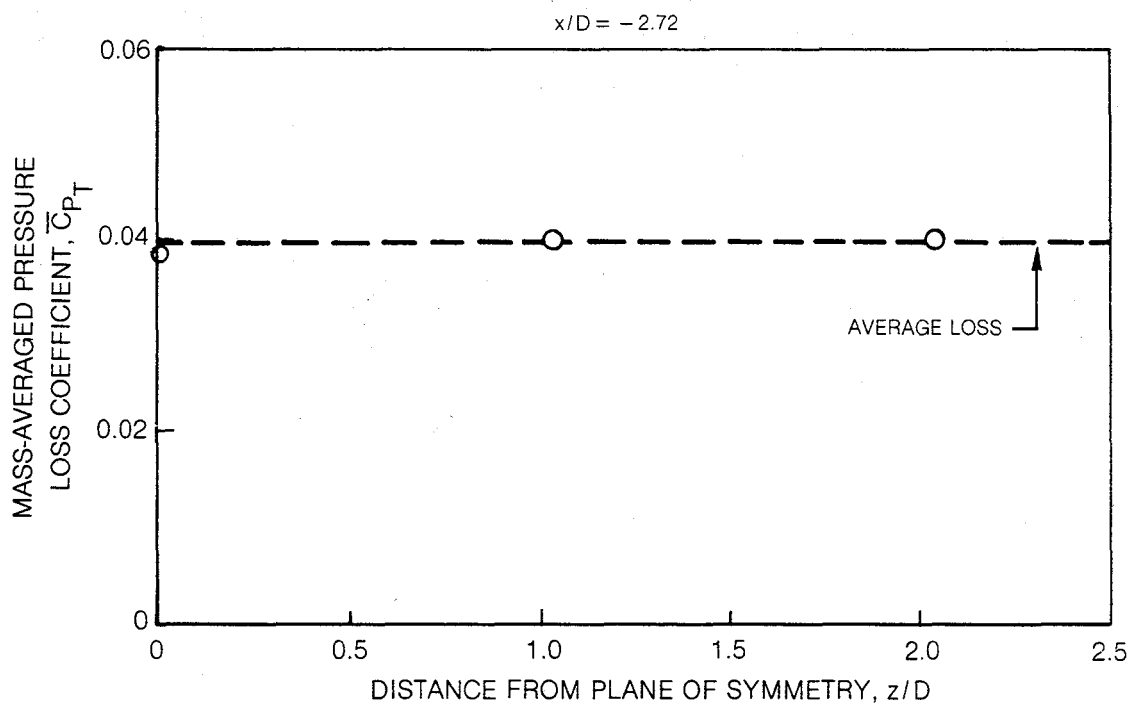


Figure 60 Pressure Loss Distribution in the Test-Section Entrance Plane

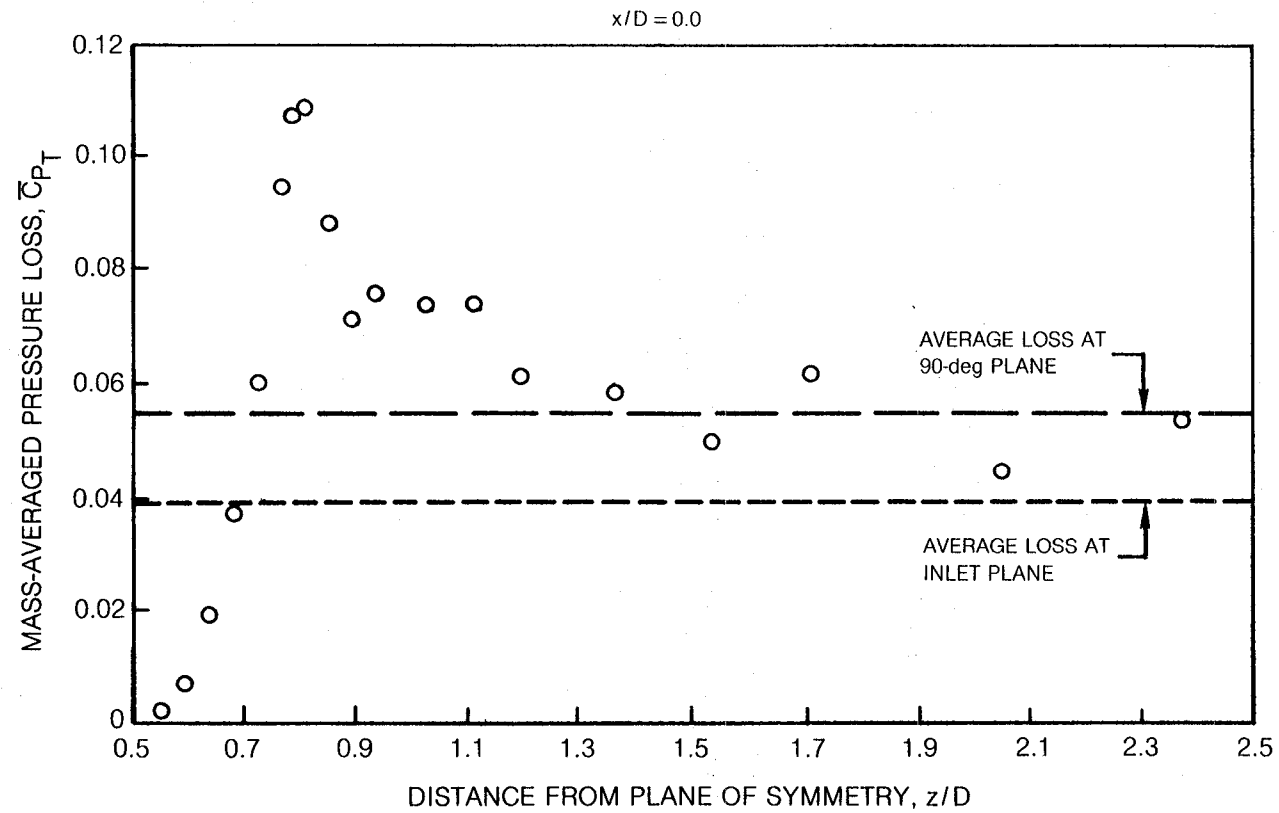


Figure 61 Pressure Loss Distribution in the 90-deg Plane

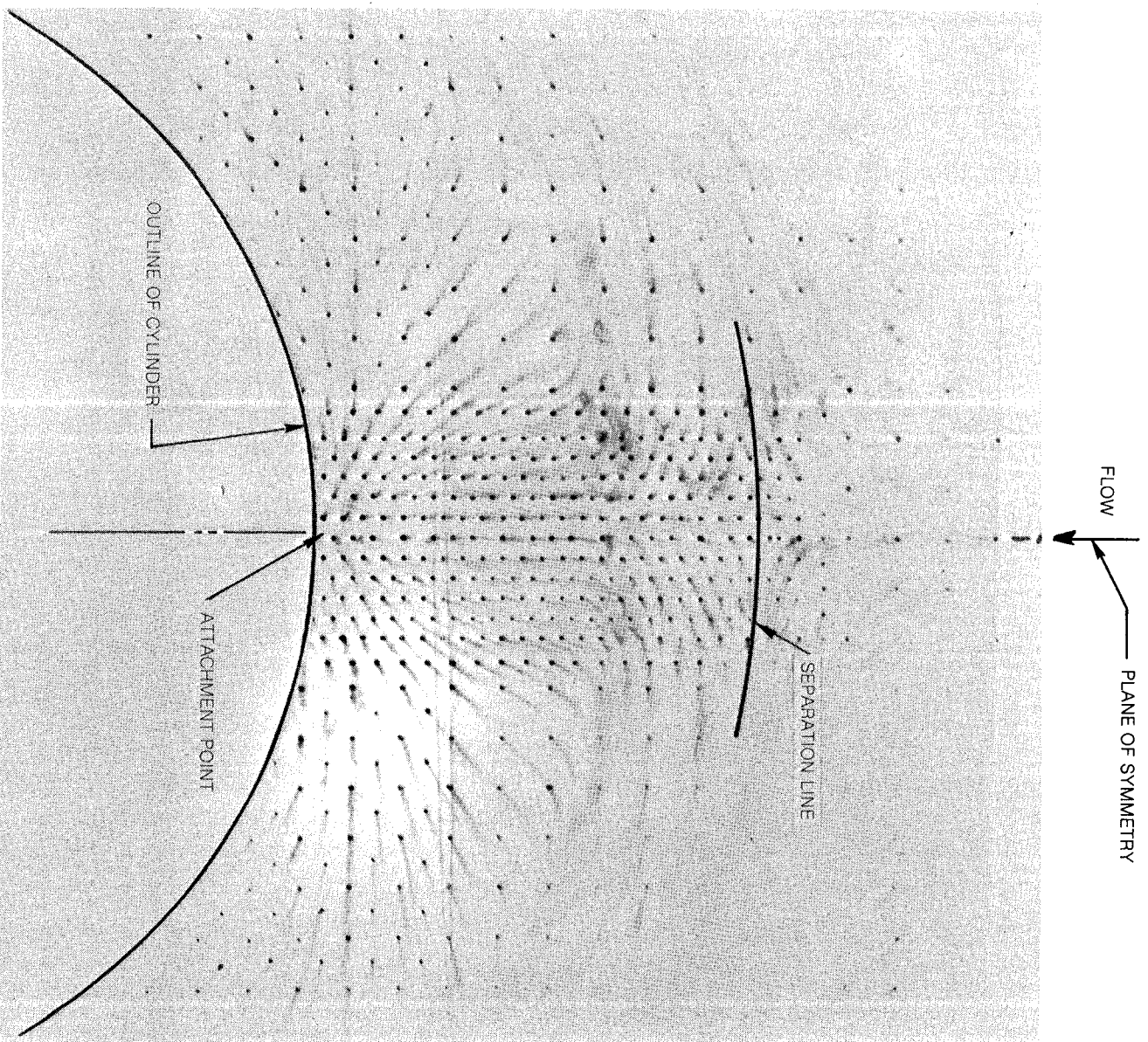


Figure 62 Partial Flow Visualization Pattern on the Endwall

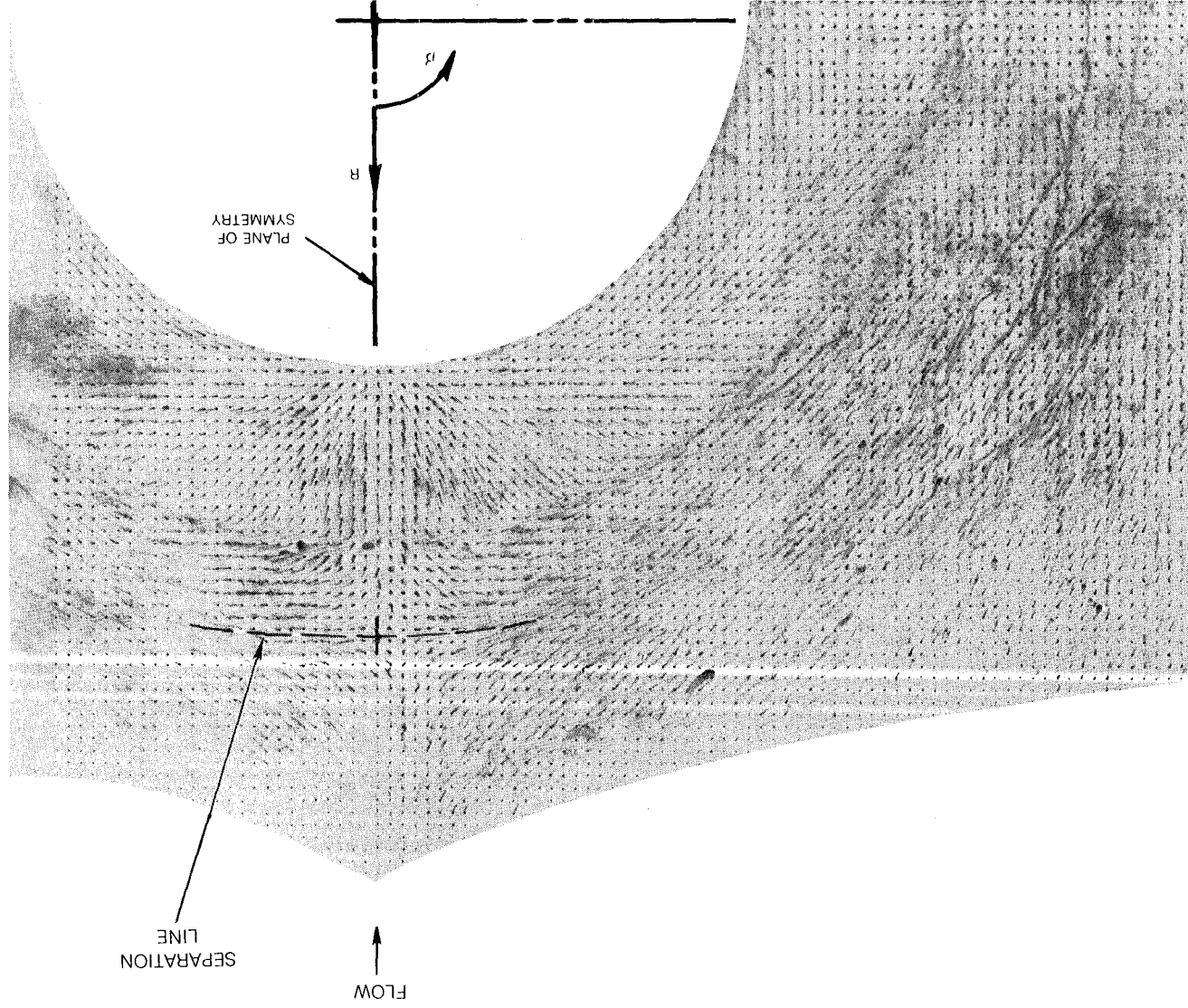


Figure 63 Endwall Flow Visualization Pattern

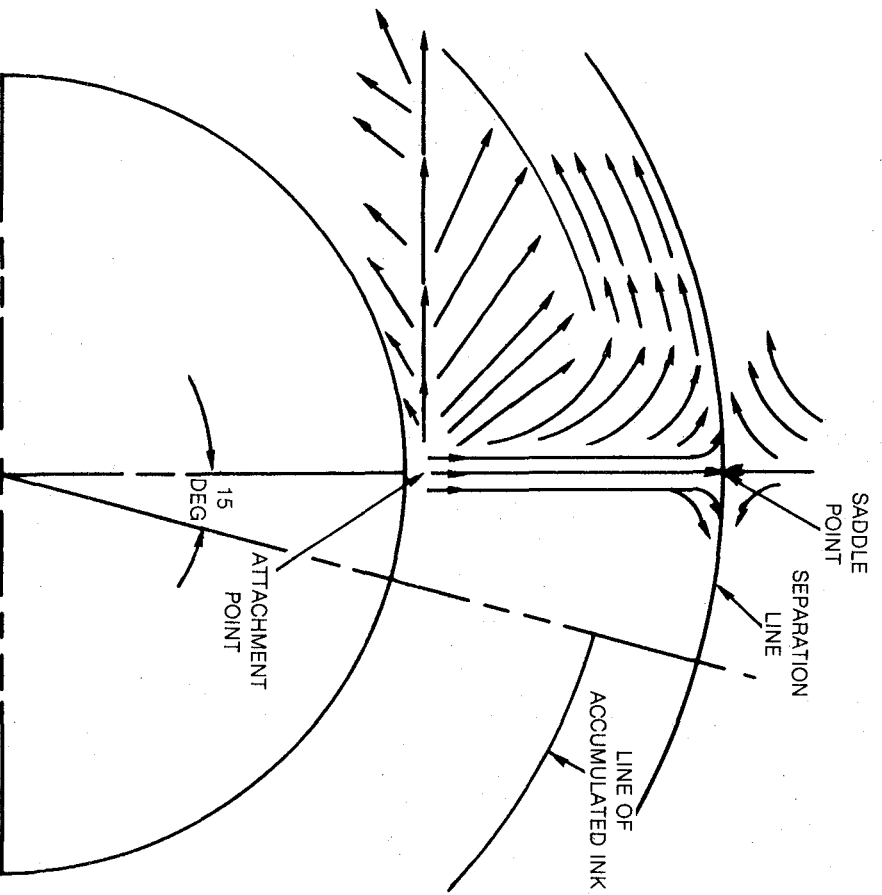


Figure 64 Endwall Flow Diagram

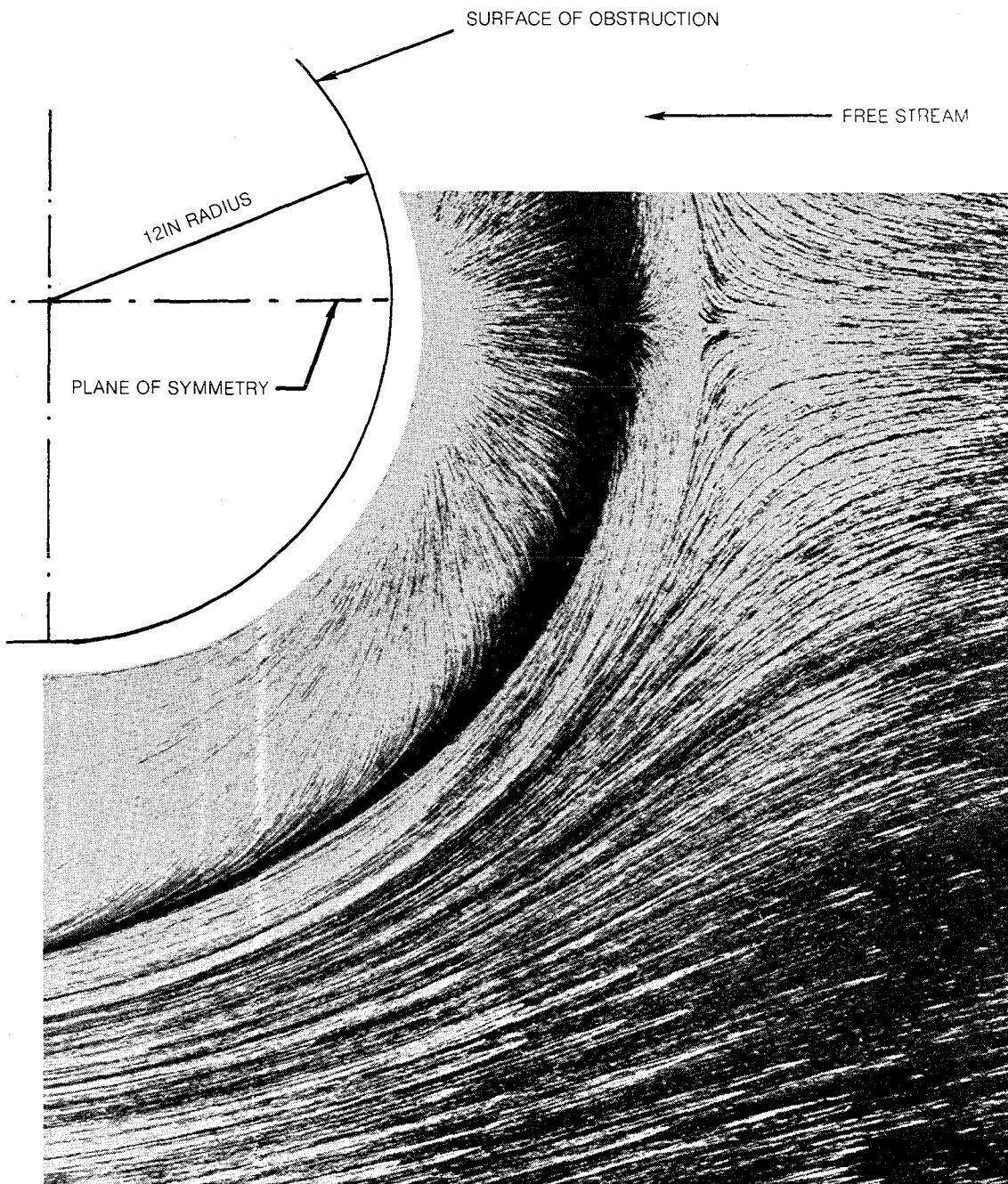


Figure 65 Endwall Flow Visualization Pattern Obtained by East and Hoxey

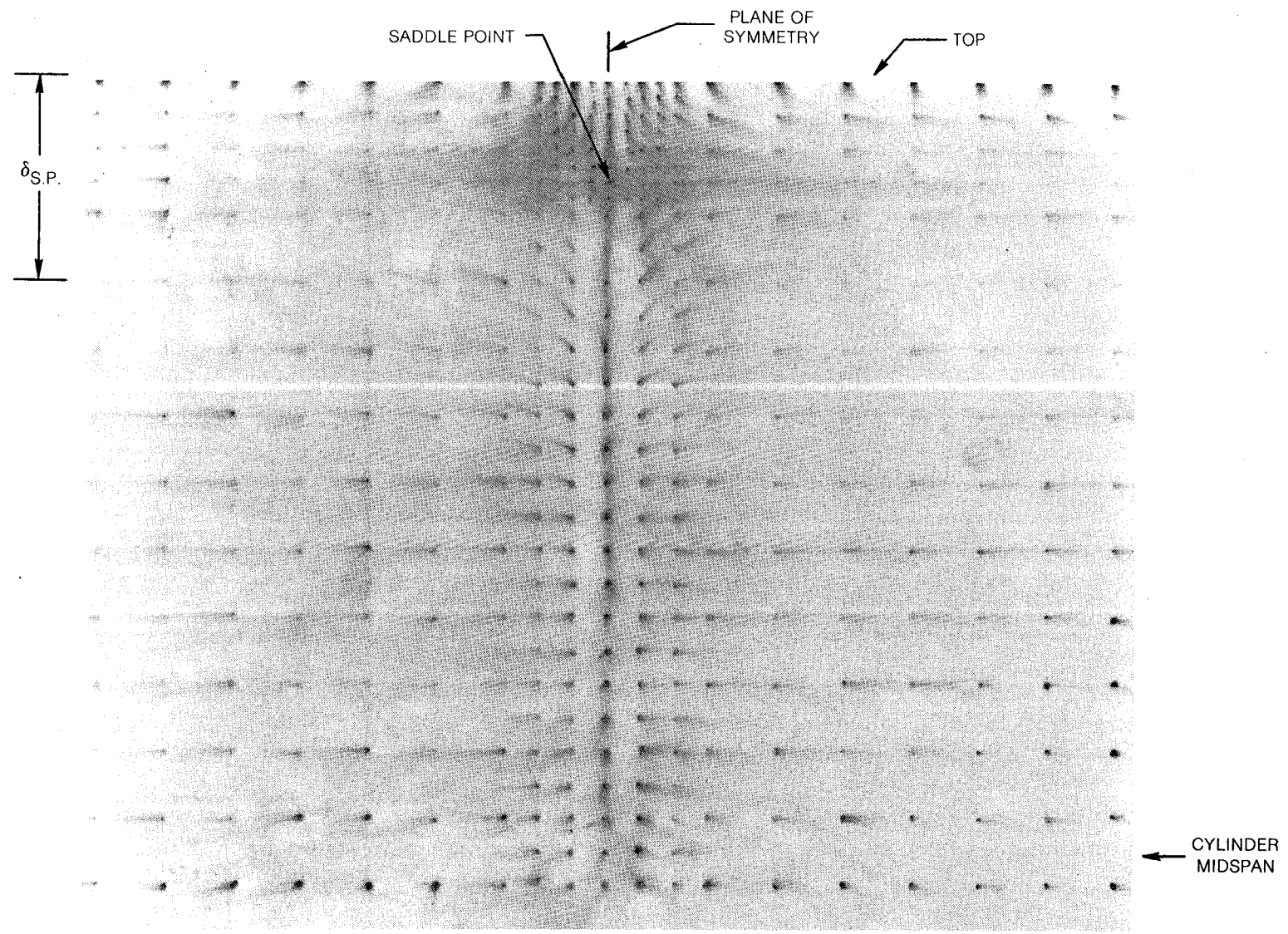


Figure 66 Flow Visualization on Top Part of Cylinder

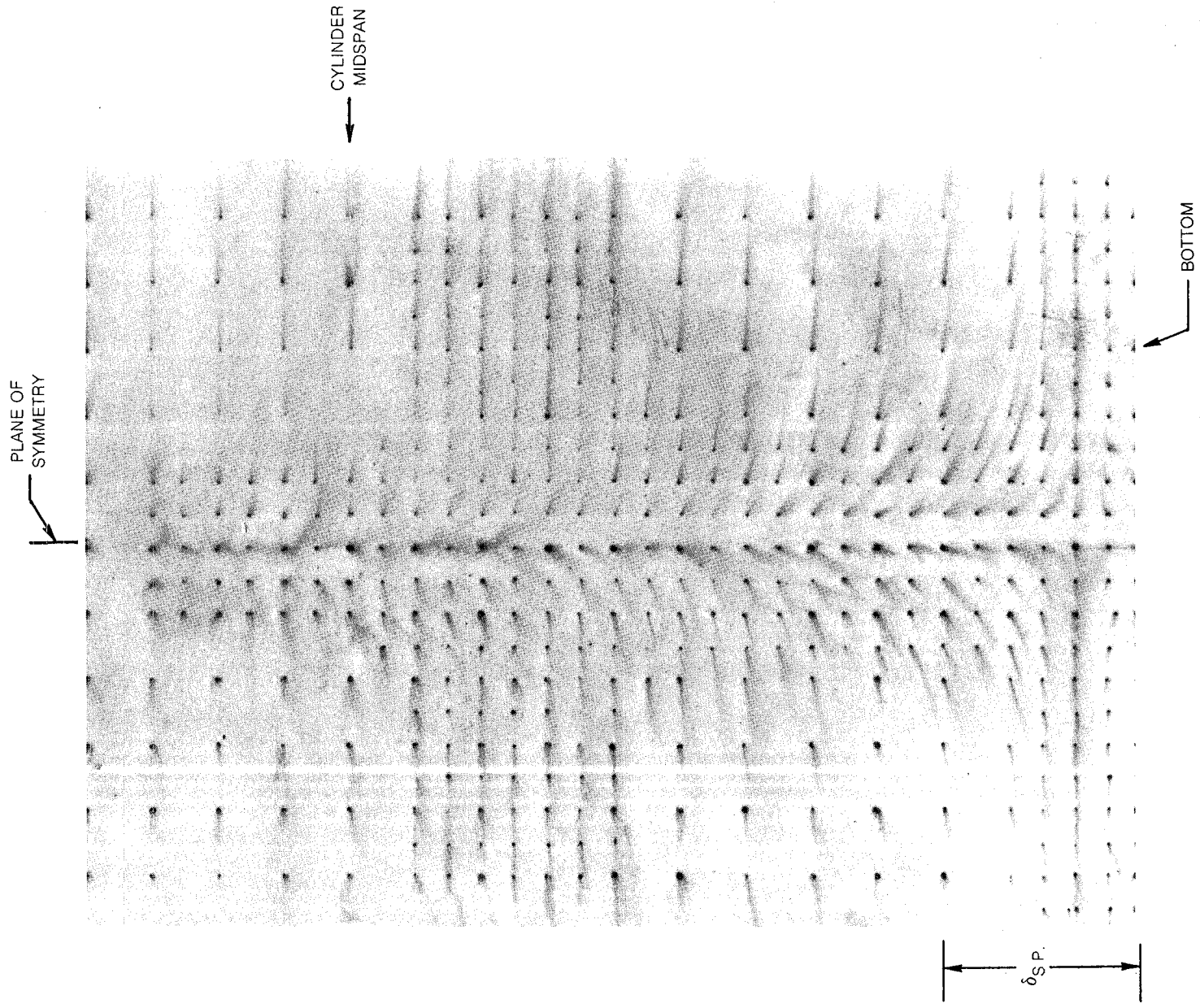


Figure 67 Flow Visualization on Lower Part of Cylinder

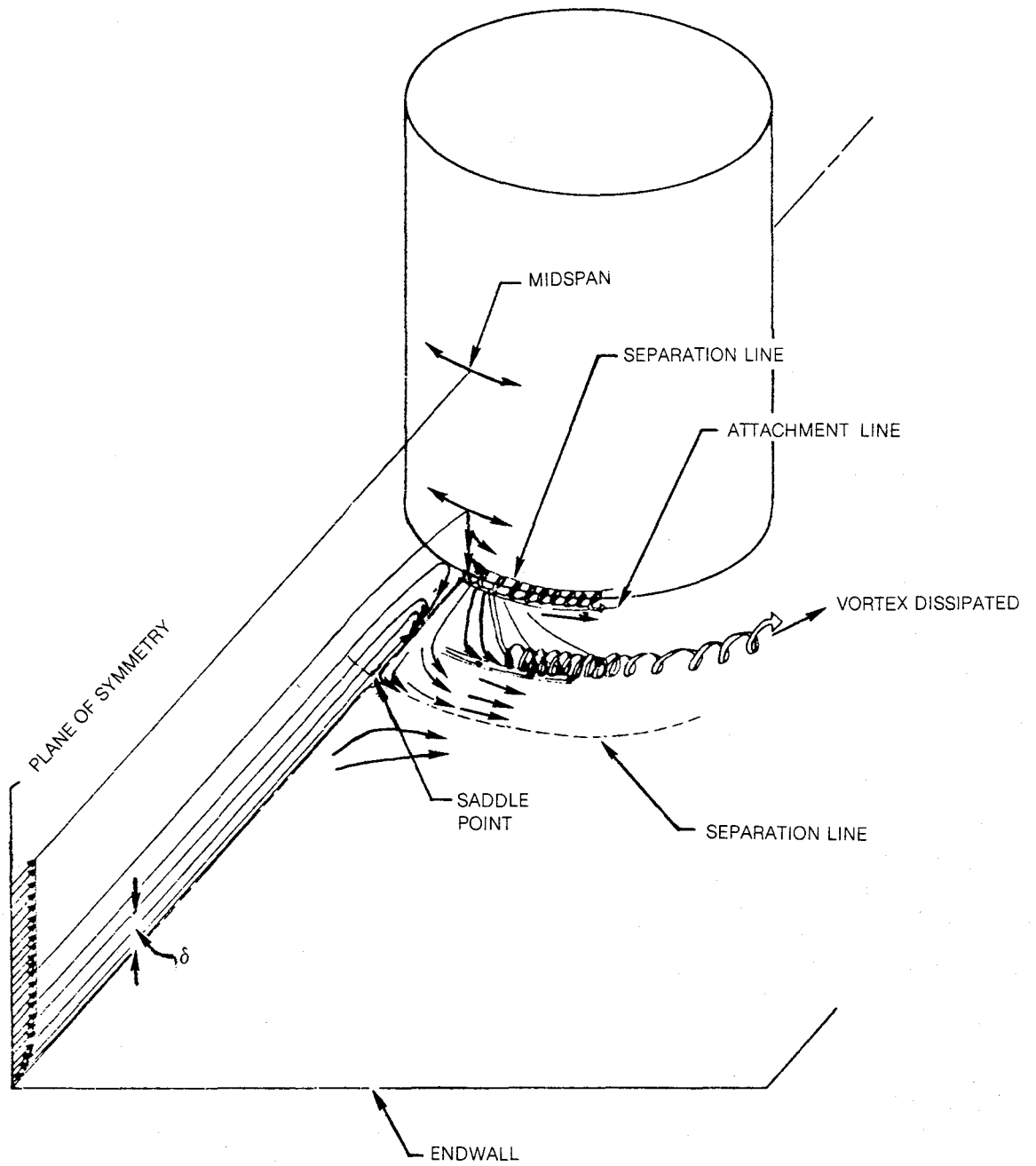
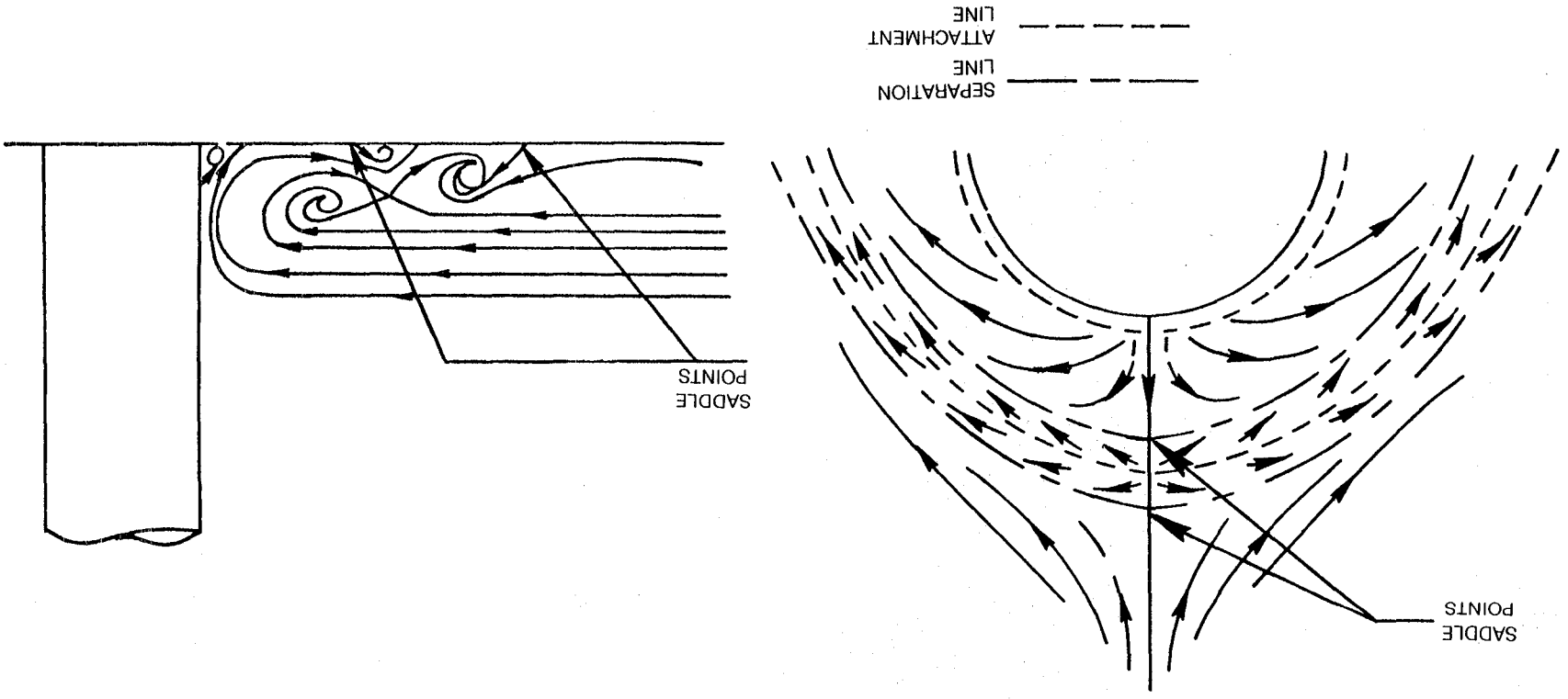


Figure 68 Horseshoe Vortex Formation

Figure 69 Four-Vortex Model



APPENDIX A - EXPERIMENTAL UNCERTAINTIES

This appendix outlines the procedure used to determine experimental uncertainties associated with the data in Appendix B.

Appendix Tables

1. Summary of Experimental Uncertainties

Appendix Symbols

C_{PS}	static pressure coefficient, equation (A4)
C_{PT}	loss coefficient, $(P_{T0} - P_T)/q_0$
P_S	local static pressure
P_{S0}	reference static pressure near test-section entrance
P_T	local total pressure
P_{T0}	reference total pressure near test-section entrance
q_0	reference dynamic pressure near test-section entrance
R	radial distance from instrumented-disk center, figure 25
Re_D	Reynolds number based on the cylinder diameter
T	any linear function for which an uncertainty level is needed, equation (A1)
U	local velocity magnitude
U_0	reference velocity magnitude near test section entrance
v_i	any independent variable
W_i	uncertainty interval for an independent variable, equation (A2)
y	vertical distance from endwall, figure 25
β	position angle relative to plane of symmetry, figure 25
ϕ	local flow pitch angle, figure 17
σ	standard deviation
θ	local flow yaw angle, figure 17

Uncertainty Analysis

The accuracy of data presented in Appendix B was assessed using the uncertainty analysis of Kline and McClintock (ref. A1). Theorem 3 of Kline and McClintock states that if T is a linear function of n independent normally distributed variables, v ,

$$T = T(v_1, v_2, v_3 \dots v_n) \quad (A1)$$

then the relationship between an uncertainty interval, W_i , for each of the independent variables and the corresponding uncertainty interval for T , W_T , is:

$$W_T = \left[\left(\left(\frac{\partial T}{\partial v_1} \right) W_1 \right)^2 + \left(\left(\frac{\partial T}{\partial v_2} \right) W_2 \right)^2 + \dots + \left(\left(\frac{\partial T}{\partial v_n} \right) W_n \right)^2 \right]^{1/2} \quad (A2)$$

Uncertainty intervals were calculated based on 20 to 1 odds that the measured value lies within the calculated uncertainty. The uncertainty intervals, then, correspond to four times the standard deviation of the measurement:

$$W_i = \pm 2 \sigma_i = 4 \sigma_i \quad (A3)$$

Surface Static Pressure Coefficients. - The surface static pressure coefficients are given by

$$C_{P_S} = \frac{P_S - P_{S_0}}{P_{T_0} - P_{S_0}} \quad (A4)$$

Since P_{S_0} was connected to the reference port of the Barocell differential pressure transducer, the numerator and the denominator represent separate transducer measurements. With the transducer calibration fitted with a straight line, using the method of least squares, the standard deviation between the calibration and fitted line is

$$\sigma_p = 0.00547 \text{ cm of water}$$

The uncertainty of any differential pressure measurement, then, is:

$$W_{\Delta P} = 4\sigma_p = 0.02186 \text{ cm H}_2\text{O}$$

Applying equation (A2) to equation (A4) gives the expression for the uncertainty in the pressure coefficient:

$$\begin{aligned}
 W_{C_{P_S}} &= \left[\left(\frac{\partial C_{P_S}}{\partial (P_S - P_{S_0})} W_{\Delta P} \right)^2 + \left(\frac{\partial C_{P_S}}{\partial (P_{T_0} - P_{S_0})} W_{\Delta P} \right)^2 \right]^{1/2} \\
 &= W_{\Delta P} \left[\frac{1}{q_0^2} + \left(\frac{C_{P_S}}{q_0} \right)^2 \right]^{1/2}
 \end{aligned}
 \tag{A5}$$

For these tests $q_0 \cong 5$ cm of water, and the largest measured absolute value of C_{P_S} was approximately 6.4 cm of water. Substituting these values into equation (A5) yields the desired uncertainty:

$$W_{C_{P_S}} = 0.0119$$

The odds are 20 to 1 that the surface pressure coefficients contained in Appendix B are within ± 0.0059 of the tabulated value.

Five-Hole Probe Measurements. - Uncertainty in the five-hole probe measurements were calculated in a manner similar to that shown for the surface static pressure coefficients. The calculations were more difficult, because of the added complexity of the calibration parameters. Each of the three pressure parameter curves shown in figure 19 was fitted with fifth order curves so that the appropriate derivatives required for equation (A2) could be evaluated. As with the surface coefficients, worst-case values of the derivatives were used to calculate the following uncertainties:

$$W_{C_{P_S}} = 0.0324 \quad W_{C_{P_T}} = 0.0124 \quad W_{\frac{U}{U_0}} = 0.0170 \quad W_{\phi} = 0.3 \text{ deg}$$

Position Parameters. - The five-hole probe radial position, R , and angular position, β , were determined from the static pressure taps in the instrumented floor disk. Since the taps were accurately machined into the disk, the uncertainties in these values are small:

$$W_R = 0.08 \text{ cm}$$

$$W_\beta = 0.4 \text{ deg}$$

At the beginning of each traverse, the probe was manually shimmed to 0.25 cm off the floor. The vertical position from that point was determined from the L. C. Smith probe traverser calibration. The uncertainty of the y-coordinate due to the uncertainty introduced by the calibration is:

$$W_y = 0.10 \text{ cm}$$

Uncertainty in the flow yaw angle, θ , was introduced by four calibrations: the L. C. Smith probe rotation, the two probe positioner potentiometers, and the pitch angle correction (fig. 19). The uncertainty associated with these calibrations is:

$$W_\theta = 1.0 \text{ deg}$$

Summary of Uncertainties. - A summary of the calculated uncertainty intervals is contained in Table A1.

TABLE A1. - SUMMARY OF EXPERIMENTAL UNCERTAINTIES

Quantity	C_{P_S} -Surf.	C_{P_T}	C_{P_S}	$\frac{U}{U_0}$	ϕ	θ	R	β	y
Uncertainty	± 0.0059	± 0.0062	± 0.0162	± 0.0085	± 0.15 deg	± 0.5 deg	± 0.04 cm	± 0.2 deg	± 0.05 cm

Error Due to Unsteadiness

Flow unsteadiness affects five-hole probe measurements. Bennett (ref. A2) has shown that turbulence intensities of 25 percent can lead to the following changes in the measurements:

yaw angle	2.0 deg
pitch angle	0.2 deg
q	1 percent
C_{P_T}	3.5 percent

These changes are larger than the typically quoted five-hole probe accuracies of 0.5 percent. Based on the measurements of McMahon, et. al. (ref. 12), unsteadiness near this level probably only occurred where the mean velocities were low. In this study, low mean velocities were only recorded near the endwall and in the shear layer between forward and reverse flow in the plane of symmetry region. The effect of unsteadiness on most of the measurements, then, was probably small. Only in a small region near the plane of symmetry are changes as large as those indicated above expected to be caused by unsteadiness.

Aerodynamic Effect of Five-Hole Probe

Some error was introduced into the five-hole probe measurements by the physical presence of the probe. Since the cylinder blockage was two orders of magnitude larger than that of the probe tip, probe interference effects were found to be small. Static pressures measured with the probe are in good agreement with endwall static pressures throughout most of the separation region. With the probe tip near the endwall in the plane of symmetry, though, core flow entering the endwall region near the cylinder passed around the large diameter probe support prior to reaching the measurement location. The reverse flow direction near the endwall was affected by the probe support. The yaw angle measurements for the traverse at $R/D = 0.638$ (fig. 37) show a variation near the endwall. The yaw angle decreased to approximately -173 deg whereas the flow visualization shows a limiting streamline angle of 180 deg. This effect was only encountered near the cylinder in the plane of symmetry.

REFERENCES

- A1. Kline, S. J., and McClintock, F. A., "Describing Uncertainties in Single-Sample Experiments," *Mechanical Engineering*, January 1953.
- A2. Bennett, J. C., "Use of Five-Hole Pneumatic Probe in Unsteady Flows," Experimental Diagnostics in Gas Phase Combustion Systems, *Progress in Aeronautics and Astronautics*, Vol. 53, Volume Editor: B. T. Zinn, 1977.

APPENDIX B - TABULATED DATA

This appendix contains a tabulation of the conditions specifying the inlet boundary conditions, endwall and cylinder surface static pressure coefficients, and data gathered via a five-hole probe. The coordinate system for presenting these data is contained in figure 25. Values of terms used to nondimensionalize quantities in the table are listed below. The reference conditions are nominal values for the test program.

Appendix Tables

1. Values of Terms for Nondimensionalizing Data
2. Inlet Profiles
3. Cylinder Surface Static Pressure Distributions
4. Endwall Static Pressure Distributions
5. Five Hole Probe Data

Appendix Symbols

C_{P_S}	static pressure coefficient, $(P_S - P_{S_0})/q_o$
C_{P_T}	loss coefficient, $(P_{T_0} - P_T)/q_o$
D	cylinder diameter
P_S	local static pressure
P_{S_0}	reference static pressure near test-section entrance
P_T	local total pressure
P_{T_0}	reference total pressure near test-section entrance
PHI	local flow pitch angle, figure 17
q_o	reference dynamic pressure near test-section entrance
R	radial distance from instrumented-disk center, figure 25
Re_D	Reynolds number based on the cylinder diameter
θ	local flow yaw angle, figure 17
U	local velocity magnitude
U_o	reference velocity magnitude near test section entrance
Y	vertical distance from endwall, figure 25
z	distance from vertical plane of symmetry, figure 25

Values of Terms for Nondimensionalizing Data

D	P_{S_0}	P_{T_0}	q_o	U_o
29.85 cm	0.1006 MPa	0.1011 MPa	486 Pa	29.0 m/sec

Inlet Profiles

z/D=0.0				z/D=1.021			
Y/D	CPT	CPS	U/U ₀	Y/D	CPT	CPS	U/U ₀
0.0051	0.591	0.059	0.592	0.0051	0.607	0.044	0.590
0.0140	0.467	0.060	0.688	0.0136	0.477	0.043	0.693
0.0226	0.396	0.059	0.738	0.0221	0.415	0.043	0.736
0.0311	0.343	0.060	0.773	0.0306	0.357	0.043	0.775
0.0396	0.287	0.059	0.808	0.0391	0.300	0.043	0.810
0.0481	0.235	0.059	0.840	0.0477	0.253	0.042	0.840
0.0651	0.134	0.060	0.898	0.0562	0.201	0.043	0.870
0.0736	0.099	0.059	0.918	0.0647	0.153	0.043	0.897
0.0821	0.057	0.060	0.940	0.0732	0.111	0.043	0.920
0.0906	0.029	0.060	0.955	0.0817	0.071	0.044	0.941
0.0991	0.015	0.060	0.962	0.0902	0.038	0.043	0.958
0.1077	0.002	0.061	0.968	0.0987	0.015	0.043	0.971
0.1162	-0.003	0.061	0.971	0.1072	0.003	0.044	0.977
0.1247	-0.006	0.060	0.972	0.1157	-0.004	0.045	0.979
0.2013	-0.006	0.062	0.972	0.2009	-0.003	0.045	0.979
0.2864	0.001	0.062	0.968	0.2860	-0.001	0.047	0.977
0.3715	0.000	0.064	0.968	0.3711	0.002	0.047	0.975
0.4566	0.001	0.064	0.967	0.4562	0.004	0.048	0.974
0.5417	0.004	0.065	0.965	0.5413	0.004	0.050	0.973

z/D=2.043			
Y/D	CPT	CPS	U/U ₀
0.0051	0.619	0.0048	0.614
0.0136	0.484	0.0031	0.716
0.0221	0.417	0.0028	0.762
0.0306	0.353	0.0030	0.803
0.0391	0.299	0.0037	0.835
0.0477	0.241	0.0027	0.869
0.0562	0.204	0.0020	0.891
0.0647	0.149	0.0030	0.921
0.0732	0.112	0.0031	0.941
0.0817	0.068	0.0030	0.964
0.0902	0.032	0.0033	0.982
0.0987	0.011	0.0032	0.993
0.1072	0.001	0.0029	0.998
0.1157	-0.003	0.0029	1.000
0.2009	-0.001	0.0035	0.999
0.2860	0.002	0.0050	0.997
0.3711	0.002	0.0049	0.996
0.4562	0.004	0.0058	0.995
0.5413	0.004	0.0072	0.994

Cylinder Surface Static Pressure Coefficients

Y/D	β									
	0	5	10	15	20	25	30	35	40	45
0.511	0.996	0.965	0.886	0.741	0.553	0.330	0.037	-0.267	-0.588	-0.908
0.489	0.999	0.972	0.882	0.732	0.557	0.314	0.044	-0.243	-0.586	-0.921
0.468	0.995	0.969	0.889	0.752	0.549	0.301	0.053	-0.259	-0.573	-0.883
0.447	0.996	0.968	0.883	0.750	0.543	0.303	0.023	-0.276	-0.588	-0.922
0.426	0.998	0.965	0.883	0.740	0.551	0.326	0.030	-0.272	-0.596	-0.926
0.404	0.999	0.972	0.883	0.733	0.553	0.309	0.040	-0.248	-0.593	-0.929
0.383	0.995	0.969	0.889	0.749	0.548	0.300	0.043	-0.266	-0.579	-0.896
0.362	0.997	0.969	0.886	0.751	0.542	0.303	0.024	-0.274	-0.590	-0.924
0.340	0.999	0.965	0.884	0.741	0.552	0.326	0.031	-0.276	-0.601	-0.927
0.319	0.999	0.972	0.884	0.733	0.550	0.310	0.039	-0.251	-0.597	-0.929
0.298	0.996	0.971	0.891	0.750	0.550	0.299	0.040	-0.268	-0.582	-0.899
0.277	0.996	0.969	0.882	0.750	0.543	0.303	0.026	-0.276	-0.589	-0.922
0.255	0.995	0.962	0.881	0.738	0.548	0.321	0.023	-0.279	-0.606	-0.930
0.234	0.996	0.971	0.881	0.730	0.550	0.310	0.041	-0.248	-0.594	-0.929
0.213	0.991	0.966	0.888	0.750	0.548	0.300	0.043	-0.267	-0.577	-0.890
0.191	0.991	0.963	0.882	0.749	0.543	0.304	0.027	-0.271	-0.587	-0.918
0.170	0.987	0.957	0.881	0.738	0.551	0.323	0.030	-0.273	-0.599	-0.916
0.149	0.985	0.963	0.875	0.730	0.552	0.313	0.041	-0.243	-0.584	-0.915
0.128	0.979	0.957	0.881	0.747	0.550	0.304	0.053	-0.250	-0.566	-0.877
0.106	0.975	0.954	0.872	0.744	0.544	0.310	0.038	-0.255	-0.567	-0.896
0.085	0.975	0.948	0.873	0.740	0.554	0.333	0.048	-0.251	-0.567	-0.867
0.064	0.978	0.958	0.876	0.734	0.561	0.330	0.068	-0.220	-0.552	-0.879
0.043	0.986	0.965	0.888	0.759	0.570	0.329	0.080	-0.221	-0.528	-0.836
0.011	1.000	0.981	0.902	0.776	0.582	0.358	0.093	-0.199	-0.504	-0.827

Cylinder Surface Static Pressure Coefficients
(continued)

Y/D	β								
	50	55	60	65	70	75	80	85	90
0.511	-1.227	-1.535	-1.800	-2.048	-2.233	-2.379	-2.447	-2.457	-2.366
0.489	-1.239	-1.550	-1.819	-2.062	-2.250	-2.388	-2.456	-2.479	-2.426
0.468	-1.235	-1.545	-1.832	-2.074	-2.256	-2.409	-2.471	-2.486	-2.432
0.447	-1.242	-1.545	-1.831	-2.084	-2.283	-2.432	-2.498	-2.523	-2.454
0.426	-1.242	-1.554	-1.832	-2.078	-2.279	-2.427	-2.521	-2.545	-2.494
0.404	-1.258	-1.565	-1.841	-2.093	-2.281	-2.438	-2.526	-2.560	-2.517
0.383	-1.251	-1.566	-1.854	-2.100	-2.296	-2.450	-2.533	-2.566	-2.523
0.362	-1.247	-1.559	-1.852	-2.102	-2.308	-2.458	-2.544	-2.578	-2.524
0.340	-1.246	-1.559	-1.843	-2.099	-2.306	-2.468	-2.547	-2.590	-2.551
0.319	-1.263	-1.570	-1.858	-2.107	-2.314	-2.461	-2.562	-2.598	-2.543
0.298	-1.258	-1.575	-1.863	-2.115	-2.318	-2.462	-2.554	-2.590	-2.551
0.277	-1.249	-1.560	-1.844	-2.115	-2.311	-2.475	-2.566	-2.600	-2.552
0.255	-1.255	-1.570	-1.857	-2.106	-2.313	-2.472	-2.570	-2.603	-2.569
0.234	-1.255	-1.564	-1.847	-2.101	-2.314	-2.465	-2.557	-2.603	-2.553
0.213	-1.248	-1.566	-1.857	-2.096	-2.310	-2.459	-2.548	-2.591	-2.545
0.191	-1.238	-1.547	-1.840	-2.101	-2.298	-2.458	-2.562	-2.590	-2.533
0.170	-1.234	-1.547	-1.834	-2.083	-2.296	-2.448	-2.542	-2.569	-2.544
0.149	-1.249	-1.550	-1.827	-2.075	-2.280	-2.435	-2.531	-2.563	-2.518
0.128	-1.227	-1.541	-1.825	-2.069	-2.275	-2.431	-2.514	-2.542	-2.496
0.106	-1.211	-1.520	-1.800	-2.058	-2.261	-2.421	-2.503	-2.532	-2.490
0.085	-1.205	-1.509	-1.791	-2.030	-2.243	-2.409	-2.486	-2.507	-2.465
0.064	-1.198	-1.501	-1.776	-2.021	-2.219	-2.368	-2.448	-2.507	-2.456
0.043	-1.174	-1.489	-1.771	-2.012	-2.211	-2.360	-2.448	-2.474	-2.423
0.011	-1.120	-1.443	-1.724	-1.980	-2.177	-2.327	-2.411	-2.452	-2.388

Endwall Static Pressure Coefficients

R/D	β									
	0	5	10	15	20	25	30	35	40	45
0.5021	1.005	0.982	0.902	0.762	0.596	0.370	0.116	-0.173	-0.470	-0.789
0.5319	1.001	0.978	0.095	0.786	0.640	0.435	0.209	-0.045	-0.311	-0.585
0.5532	0.976	0.959	0.897	0.787	0.638	0.453	0.238	0.004	-0.247	-0.505
0.5745	0.939	0.914	0.859	0.760	0.634	0.461	0.259	0.040	-0.192	-0.428
0.5957	0.867	0.864	0.810	0.714	0.593	0.439	0.260	0.056	-0.156	-0.374
0.6170	0.802	0.785	0.732	0.646	0.543	0.392	0.230	0.048	-0.144	-0.333
0.6383	0.701	0.681	0.645	0.567	0.469	0.331	0.181	0.013	-0.163	-0.350
0.6596	0.609	0.582	0.549	0.469	0.380	0.252	0.119	-0.037	-0.197	-0.359
0.6809	0.513	0.461	0.402	0.325	0.260	0.159	0.027	-0.103	-0.246	-0.391
0.7021	0.381	0.354	0.314	0.251	0.167	0.070	-0.050	-0.171	-0.305	-0.444
0.7234	0.341	0.327	0.275	0.231	0.154	0.056	-0.058	-0.181	-0.322	-0.449
0.7447	0.362	0.331	0.304	0.241	0.204	0.125	0.007	-0.123	-0.253	-0.391
0.7660	0.397	0.446	0.434	0.379	0.285	0.192	0.083	-0.040	-0.172	-0.302
0.7872	0.484	0.491	0.459	0.400	0.325	0.233	0.125	0.010	-0.116	-0.245
0.8085	0.471	0.471	0.456	0.402	0.339	0.251	0.146	0.037	-0.082	-0.199
0.8298	0.488	0.482	0.459	0.407	0.345	0.260	0.162	0.056	-0.060	-0.173
0.8511	0.476	0.481	0.452	0.403	0.343	0.263	0.172	0.074	-0.031	-0.144
0.8723	0.478	0.473	0.443	0.401	0.341	0.266	0.182	0.086	-0.014	-0.123
0.8936	0.459	0.457	0.435	0.389	0.337	0.264	0.181	0.093	-0.007	-0.111
0.9149	0.453	0.453	0.425	0.385	0.331	0.265	0.186	0.099	0.001	-0.098
0.9362	0.439	0.444	0.408	0.371	0.322	0.258	0.184	0.101	0.007	-0.088
0.9574	0.428	0.420	0.395	0.366	0.313	0.254	0.183	0.101	0.013	-0.076
0.9787	0.418	0.411	0.387	0.351	0.303	0.246	0.176	0.097	0.010	-0.074
1.0000	0.406	0.399	0.379	0.341	0.294	0.243	0.176	0.097	0.016	-0.066

Endwall Static Pressure Coefficients
(continued)

R/D	β									
	0	5	10	15	20	25	30	35	40	45
1.0213	0.392	0.382	0.358	0.329	0.283	0.233	0.166	0.094	0.017	-0.063
1.0426	0.376	0.364	0.347	0.321	0.273	0.224	0.160	0.091	0.017	-0.058
1.0638	0.369	0.358	0.336	0.307	0.263	0.217	0.152	0.084	0.013	-0.061
1.0851	0.353	0.346	0.327	0.294	0.259	0.212	0.152	0.086	0.015	-0.054
1.1064	0.341	0.330	0.312	0.286	0.247	0.201	0.142	0.080	0.015	-0.053
1.1277	0.326	0.316	0.305	0.277	0.240	0.193	0.139	0.078	0.017	-0.050
1.1489	0.319	0.312	0.292	0.266	0.231	0.185	0.129	0.072	0.011	-0.055
1.1702	0.308	0.301	0.283	0.256	0.225	0.182	0.129	0.072	0.013	-0.051
1.1915	0.296	0.288	0.271	0.246	0.216	0.172	0.122	0.070	0.011	-0.049
1.2340	0.273	0.267	0.255	0.229	0.200	0.160	0.115	0.066	0.011	-0.048
1.2766	0.259	0.254	0.239	0.215	0.187	0.148	0.106	0.059	0.005	-0.049
1.3191	0.244	0.238	0.224	0.204	0.174	0.140	0.100	0.053	0.003	-0.045
1.3617	0.226	0.221	0.210	0.186	0.163	0.130	0.092	0.048	0.002	-0.045
1.4043	0.212	0.207	0.196	0.175	0.153	0.122	0.086	0.045	0.003	-0.043
1.4468	0.201	0.197	0.187	0.166	0.139	0.112	0.075	0.037	-0.004	-0.051
1.4894	0.194	0.187	0.175	0.159	0.133	0.108	0.073	0.038	-0.001	-0.045
1.5319	0.181	0.177	0.167	0.147	0.128	0.104	0.070	0.035	-0.002	-0.043
1.5745	0.172	0.167	0.157	0.140	0.122	0.097	0.065	0.034	-0.003	-0.042
1.6170	0.163	0.159	0.151	0.135	0.114	0.090	0.060	0.029	-0.007	-0.046
1.6596	0.157	0.152	0.142	0.128	0.109	0.085	0.058	0.026	-0.008	-0.044
1.7021	0.148	0.145	0.136	0.127	0.103	0.082	0.056	0.024	-0.009	-0.043
1.7872	0.136	0.131	0.122	0.111	0.097	0.072	0.050	0.021	-0.010	-0.042
1.8723	0.126	0.122	0.115	0.104	0.087	0.068	0.044	0.018	-0.012	-0.043
1.9574	0.118	0.114	0.107	0.094	0.080	0.063	0.041	0.015	-0.012	-0.040
2.0426	0.107	0.105	0.099	0.088	0.074	0.060	0.037	0.012	-0.013	-0.038
2.1277	0.102	0.099	0.091	0.083	0.071	0.054	0.034	0.013	-0.011	-0.038
2.2128	0.095	0.094	0.086	0.079	0.065	0.051	0.030	0.011	-0.013	-0.040
2.2979	0.093	0.089	0.083	0.074	0.062	0.048	0.030	0.010	-0.012	-0.036
2.3830	0.087	0.085	0.079	0.071	0.062	0.048	0.031	0.010	-0.012	-0.034

Endwall Static Pressure Coefficients
(continued)

R/D	β								
	50	55	60	65	70	75	80	85	90
0.5021	-1.086	-1.368	-1.633	-1.868	-2.070	-2.212	-2.309	-2.283	-2.221
0.5319	-0.862	-1.126	-1.372	-1.598	-1.782	-1.896	-1.963	-1.993	-1.915
0.5532	-0.765	-1.006	-1.227	-1.409	-1.564	-1.695	-1.783	-1.812	-1.812
0.5745	-0.668	-0.891	-1.105	-1.280	-1.416	-1.511	-1.574	-1.609	-1.574
0.5957	-0.587	-0.783	-0.971	-1.146	-1.296	-1.406	-1.475	-1.478	-1.457
0.6170	-0.531	-0.725	-0.907	-1.066	-1.198	-1.282	-1.341	-1.368	-1.341
0.6383	-0.529	-0.701	-0.850	-0.979	-1.096	-1.191	-1.250	-1.289	-1.288
0.6596	-0.524	-0.691	-0.831	-0.955	-1.050	-1.109	-1.157	-1.178	-1.186
0.6809	-0.531	-0.664	-0.787	-0.906	-1.000	-1.077	-1.126	-1.123	-1.114
0.7021	-0.563	-0.694	-0.805	-0.914	-0.986	-1.036	-1.062	-1.073	-1.050
0.7234	-0.594	-0.712	-0.821	-0.910	-0.982	-1.033	-1.061	-1.066	-1.053
0.7447	-0.526	-0.653	-0.776	-0.875	-0.949	-0.911	-1.017	-1.030	-1.016
0.7660	-0.437	-0.563	-0.676	-0.787	-0.885	-0.946	-0.993	-1.000	-0.985
0.7872	-0.371	-0.490	-0.608	-0.712	-0.800	-0.864	-0.921	-0.945	-0.948
0.8085	-0.323	-0.440	-0.550	-0.648	-0.733	-0.804	-0.859	-0.896	-0.910
0.8298	-0.292	-0.404	-0.512	-0.611	-0.692	-0.755	-0.804	-0.838	-0.856
0.8511	-0.257	-0.363	-0.464	-0.559	-0.642	-0.712	-0.762	-0.790	-0.807
0.8723	-0.229	-0.336	-0.436	-0.528	-0.605	-0.666	-0.718	-0.755	-0.770
0.8936	-0.216	-0.316	-0.408	-0.494	-0.564	-0.634	-0.686	-0.726	-0.745
0.9149	-0.200	-0.296	-0.388	-0.466	-0.539	-0.601	-0.643	-0.685	-0.713
0.9362	-0.181	-0.271	-0.355	-0.439	-0.514	-0.575	-0.622	-0.654	-0.681
0.9574	-0.166	-0.255	-0.339	-0.418	-0.485	-0.541	-0.589	-0.624	-0.647
0.9787	-0.161	-0.245	-0.327	-0.400	-0.465	-0.522	-0.572	-0.610	-0.631
1.0000	-0.149	-0.236	-0.314	-0.394	-0.455	-0.511	-0.555	-0.589	-0.611

Endwall Static Pressure Coefficients
(continued)

R/D	β								
	50	55	60	65	70	75	80	85	90
1.0213	-0.142	-0.220	-0.295	-0.363	-0.428	-0.485	-0.527	-0.559	-0.581
1.0426	-0.133	-0.212	-0.286	-0.356	-0.412	-0.464	-0.507	-0.540	-0.561
1.0638	-0.136	-0.209	-0.278	-0.343	-0.400	-0.451	-0.498	-0.529	-0.550
1.0851	-0.127	-0.201	-0.270	-0.338	-0.394	-0.444	-0.484	-0.516	-0.538
1.1064	-0.122	-0.191	-0.257	-0.319	-0.378	-0.426	-0.463	-0.496	-0.518
1.1277	-0.117	-0.184	-0.251	-0.309	-0.362	-0.408	-0.446	-0.479	-0.503
1.1489	-0.122	-0.184	-0.245	-0.303	-0.354	-0.404	-0.444	-0.475	-0.497
1.1702	-0.112	-0.178	-0.239	-0.298	-0.348	-0.394	-0.431	-0.463	-0.483
1.1915	-0.111	-0.169	-0.226	-0.283	-0.335	-0.378	-0.415	-0.445	-0.463
1.2340	-0.104	-0.162	-0.220	-0.271	-0.317	-0.358	-0.391	-0.422	-0.444
1.2766	-0.103	-0.156	-0.209	-0.257	-0.302	-0.343	-0.379	-0.407	-0.428
1.3191	-0.095	-0.152	-0.202	-0.253	-0.292	-0.333	-0.365	-0.392	-0.412
1.3617	-0.094	-0.144	-0.192	-0.237	-0.281	-0.317	-0.349	-0.374	-0.396
1.4043	-0.091	-0.137	-0.184	-0.228	-0.263	-0.300	-0.333	-0.357	-0.378
1.4468	-0.099	-0.141	-0.187	-0.228	-0.267	-0.302	-0.335	-0.360	-0.379
1.4894	-0.088	-0.133	-0.175	-0.218	-0.253	-0.287	-0.315	-0.340	-0.360
1.5319	-0.085	-0.126	-0.166	-0.203	-0.241	-0.273	-0.298	-0.324	-0.345
1.5745	-0.082	-0.121	-0.161	-0.199	-0.230	-0.264	-0.291	-0.317	-0.335
1.6170	-0.084	-0.121	-0.159	-0.195	-0.228	-0.259	-0.288	-0.311	-0.329
1.6596	-0.081	-0.118	-0.153	-0.191	-0.221	-0.252	-0.276	-0.302	-0.321
1.7021	-0.078	-0.115	-0.149	-0.183	-0.215	-0.245	-0.267	-0.292	-0.309
1.7872	-0.075	-0.108	-0.144	-0.175	-0.201	-0.230	-0.256	-0.280	-0.296
1.8723	-0.073	-0.105	-0.137	-0.166	-0.195	-0.224	-0.250	-0.270	-0.289
1.9574	-0.068	-0.101	-0.130	-0.162	-0.187	-0.212	-0.236	-0.260	-0.275
2.0426	-0.068	-0.098	-0.126	-0.154	-0.183	-0.207	-0.227	-0.249	-0.264
2.1277	-0.066	-0.092	-0.122	-0.148	-0.171	-0.200	-0.219	-0.239	-0.255
2.2128	-0.066	-0.091	-0.117	-0.144	-0.169	-0.192	-0.218	-0.237	-0.251
2.2979	-0.061	-0.088	-0.113	-0.142	-0.163	-0.186	-0.209	-0.230	-0.247
2.3830	-0.060	-0.086	-0.110	-0.133	-0.161	-0.184	-0.202	-0.223	-0.240

Five-Hole Probe Data

ANGULAR PLANE: -5.000 DEG
 RADIUS/CYLINDER DIA: 0.809

Y/D	PHI DEG	THETA DEG	CPT	CPS	U/U ₀
0.0083	5.0	-104.6	0.519	0.443	0.195
0.0131	13.9	-101.1	0.547	0.431	0.145
0.0159	11.3	-97.9	0.548	0.430	0.148
0.0214	-1.1	-74.2	0.542	0.425	0.184
0.0294	1.5	-47.7	0.493	0.417	0.300
0.0377	4.2	-31.9	0.449	0.436	0.255
0.0460	7.4	-23.6	0.450	0.435	0.339
0.0543	4.0	-18.1	0.443	0.441	0.341
0.0625	4.8	-14.1	0.370	0.447	0.427
0.0706	7.5	-11.5	0.328	0.437	0.485
0.0787	2.2	-10.0	0.299	0.438	0.512
0.0871	4.6	-9.2	0.256	0.443	0.549
0.0954	1.0	-8.2	0.228	0.449	0.568
0.1036	1.3	-7.5	0.149	0.455	0.629
0.1117	-0.3	-7.3	0.124	0.462	0.643
0.1199	-0.3	-6.9	0.087	0.456	0.677
0.1334	0.3	-6.5	0.047	0.464	0.699
0.1472	-0.7	-6.1	0.016	0.465	0.720
0.1607	-0.5	-5.6	-0.004	0.468	0.732
0.1746	-1.6	-5.1	-0.006	0.476	0.729
0.2157	-2.1	-5.1	-0.003	0.496	0.712
0.2568	-2.5	-5.8	-0.003	0.517	0.697
0.3387	-2.4	-5.9	0.004	0.532	0.681
0.4210	-1.7	-6.1	0.005	0.536	0.677
0.5055	-0.8	-7.2	0.007	0.550	0.666

Five-Hole Probe Data
(continued)

ANGULAR PLANE: -5.000 DEG
RADIUS/CYLINDER DIA: 0.888

Y/D	PHI DEG	THETA DEG	CPT	CPS	U/U ₀
0.0085	-1.6	-45.9	0.533	0.440	0.164
0.0144	-2.6	-32.1	0.508	0.443	0.219
0.0213	-0.1	-23.3	0.493	0.439	0.261
0.0296	-1.6	-16.9	0.446	0.445	0.330
0.0376	0.1	-13.8	0.426	0.439	0.366
0.0459	1.5	-11.4	0.374	0.445	0.424
0.0541	1.4	-9.5	0.338	0.439	0.472
0.0624	1.3	-8.3	0.317	0.437	0.497
0.0704	1.3	-7.5	0.267	0.441	0.540
0.0787	1.5	-7.1	0.241	0.434	0.570
0.0870	1.2	-6.5	0.196	0.436	0.607
0.0952	1.1	-6.1	0.153	0.436	0.641
0.1033	1.1	-5.8	0.126	0.432	0.665
0.1118	1.0	-5.5	0.081	0.433	0.697
0.1199	0.8	-5.4	0.058	0.433	0.713
0.1336	0.8	-5.0	0.023	0.432	0.739
0.1472	0.6	-4.6	0.002	0.431	0.753
0.1607	0.5	-4.4	-0.008	0.430	0.760
0.1745	0.5	-4.1	-0.011	0.436	0.758
0.2156	-0.4	-4.1	-0.008	0.438	0.755
0.2566	-0.7	-4.7	-0.009	0.443	0.752
0.3387	-1.3	-4.5	-0.003	0.454	0.741
0.4208	-1.7	-4.6	-0.002	0.461	0.736
0.5054	-1.7	-5.0	-0.001	0.465	0.732

Five-Hole Probe Data
(continued)

ANGULAR PLANE: -5.000 DEG
RADIUS/CYLINDER DIA: 0.936

Y/D	PHI DEG	THETA DEG	CPT	CPS	U/U ₀
0.0083	-0.7	-29.1	0.546	0.414	0.200
0.0152	-3.5	-20.5	0.532	0.411	0.239
0.0228	0.0	-14.6	0.485	0.412	0.321
0.0311	-0.4	-11.7	0.456	0.412	0.362
0.0393	0.0	-9.4	0.419	0.415	0.407
0.0473	1.3	-7.9	0.391	0.409	0.447
0.0556	0.1	-7.1	0.355	0.404	0.491
0.0636	1.3	-6.1	0.325	0.405	0.521
0.0721	1.3	-5.4	0.278	0.407	0.561
0.0801	1.6	-4.8	0.251	0.403	0.588
0.0939	1.2	-4.1	0.200	0.400	0.632
0.1076	1.7	-3.6	0.140	0.395	0.682
0.1213	1.5	-3.2	0.085	0.398	0.720
0.1351	1.3	-2.9	0.062	0.395	0.737
0.1486	1.3	-2.6	0.025	0.397	0.760
0.1622	1.5	-2.5	0.007	0.395	0.773
0.1760	1.1	-2.4	0.000	0.396	0.777
0.2170	0.7	-2.0	-0.007	0.397	0.781
0.2580	0.0	-2.5	-0.006	0.398	0.779
0.3403	-0.6	-2.7	-0.004	0.409	0.771
0.4224	-1.0	-3.0	-0.001	0.416	0.765
0.5067	-1.0	-3.3	-0.001	0.419	0.763

Five-Hole Probe Data
(continued)

ANGULAR PLANE: -5.000 DEG
RADIUS/CYLINDER DIA: 1.021

Y/D	PHI DEG	THETA DEG	CPT	CPS	U/U ₀
0.0084	-1.4	-13.3	0.544	0.371	0.292
0.0157	-0.3	-10.4	0.508	0.367	0.354
0.0233	-0.1	-8.4	0.474	0.365	0.401
0.0316	-0.8	-7.1	0.441	0.365	0.440
0.0396	-0.4	-6.1	0.409	0.365	0.475
0.0479	0.2	-5.4	0.372	0.363	0.515
0.0561	0.4	-4.8	0.347	0.361	0.540
0.0644	0.0	-4.3	0.304	0.360	0.580
0.0724	0.5	-3.8	0.268	0.360	0.610
0.0807	0.1	-3.6	0.244	0.356	0.633
0.0943	0.7	-3.3	0.180	0.356	0.681
0.1081	0.7	-3.0	0.131	0.353	0.718
0.1219	0.9	-2.7	0.080	0.353	0.752
0.1354	0.9	-2.5	0.056	0.351	0.771
0.1492	1.0	-2.4	0.022	0.352	0.791
0.1628	1.2	-2.3	-0.001	0.348	0.808
0.1766	1.2	-2.1	-0.013	0.351	0.814
0.2174	0.7	-1.8	-0.014	0.347	0.817
0.2588	0.5	-2.2	-0.011	0.349	0.814
0.3405	-0.2	-2.4	-0.009	0.353	0.810
0.4230	-0.3	-2.6	-0.001	0.357	0.802
0.5073	-0.6	-2.8	-0.012	0.370	0.801

Five-Hole Probe Data
(continued)

ANGULAR PLANE: -5.000 DEG
RADIUS/CYLINDER DIA: 1.191

Y/D	PHI DEG	THETA DEG	CPT	CPS	U/U ₀
0.0083	1.2	-7.0	0.543	0.284	0.416
0.0160	0.7	-6.2	0.494	0.272	0.484
0.0244	-0.9	-5.4	0.441	0.276	0.533
0.0323	-0.3	-4.8	0.419	0.271	0.557
0.0406	-1.3	-4.3	0.383	0.272	0.587
0.0488	-0.6	-3.9	0.328	0.275	0.630
0.0572	-0.6	-3.7	0.313	0.267	0.648
0.0654	0.2	-3.4	0.278	0.273	0.669
0.0733	0.1	-3.2	0.247	0.270	0.695
0.0817	0.2	-3.1	0.211	0.268	0.722
0.0954	0.0	-2.9	0.154	0.269	0.760
0.1089	0.4	-2.7	0.108	0.270	0.789
0.1229	0.1	-2.5	0.076	0.267	0.811
0.1365	0.4	-2.3	0.040	0.265	0.834
0.1501	0.5	-2.2	0.008	0.270	0.850
0.1776	0.4	-1.8	-0.015	0.265	0.866
0.2185	0.5	-1.8	-0.010	0.264	0.863
0.2597	0.0	-1.9	-0.011	0.265	0.864
0.3418	-0.2	-2.1	-0.009	0.268	0.861
0.4238	-0.3	-2.4	-0.004	0.266	0.859
0.5083	-0.4	-2.4	-0.004	0.269	0.857

Five-Hole Probe Data
(continued)

ANGULAR PLANE: -5.000 DEG
RADIUS/CYLINDER DIA: 1.532

Y/D	PHI DEG	THETA DEG	CPT	CPS	U/U ₀
0.0085	0.1	-2.8	0.559	0.175	0.516
0.0140	-0.3	-2.7	0.520	0.171	0.556
0.0196	-0.6	-2.5	0.482	0.166	0.593
0.0278	0.3	-2.5	0.429	0.166	0.636
0.0361	-0.9	-2.2	0.401	0.166	0.658
0.0441	-0.3	-2.2	0.371	0.167	0.680
0.0524	-0.4	-2.0	0.323	0.163	0.717
0.0606	0.1	-2.0	0.296	0.161	0.736
0.0690	0.0	-1.8	0.261	0.160	0.761
0.0770	-0.1	-1.8	0.224	0.160	0.785
0.0852	0.0	-1.7	0.197	0.161	0.801
0.0991	0.2	-1.7	0.139	0.159	0.838
0.1125	0.0	-1.6	0.100	0.156	0.863
0.1264	0.1	-1.6	0.053	0.159	0.888
0.1399	0.6	-1.6	0.021	0.154	0.908
0.1537	0.4	-1.6	-0.005	0.157	0.921
0.1810	0.7	-1.3	-0.014	0.161	0.924
0.2221	0.5	-0.9	-0.017	0.157	0.927
0.2632	0.1	-1.1	-0.012	0.156	0.925
0.3453	-0.3	-1.4	-0.004	0.154	0.922
0.4273	0.1	-1.5	-0.004	0.161	0.918
0.5112	-0.3	-1.5	-0.004	0.160	0.919

Five-Hole Probe Data
(continued)

ANGULAR PLANE: 0.000 DEG
RADIUS/CYLINDER DIA: 0.596

Y/D	PHI DEG	THETA DEG	CPT	CPS	U/U ₀
0.0078	-2.2	-156.7	0.132	0.802	0.257
0.0101	-8.7	-158.4	0.144	0.795	0.247
0.0148	-12.2	-163.1	0.160	0.781	0.241
0.0186	-13.8	-173.6	0.166	0.770	0.255
0.0227	-15.0	179.0	0.171	0.764	0.255
0.0270	-17.9	177.5	0.173	0.759	0.261
0.0313	-22.8	177.4	0.179	0.751	0.263
0.0354	-27.1	178.3	0.193	0.745	0.249
0.1261	-27.1	-0.5	0.024	0.889	0.295
0.1344	-26.1	13.4	0.029	0.892	0.261
0.1468	-21.5	1.9	0.017	0.894	0.298
0.1605	-18.7	1.2	0.017	0.897	0.295
0.1946	-11.6	-0.5	0.007	0.907	0.293
0.2165	-8.5	-8.6	0.007	0.905	0.297
0.2575	-6.9	-4.6	0.001	0.912	0.295
0.2985	-3.8	-6.6	-0.002	0.915	0.295
0.3395	-1.3	-0.7	-0.004	0.921	0.288
0.3799	-3.4	-1.8	0.002	0.910	0.297
0.4628	-1.7	-1.6	-0.001	0.906	0.310

Five-Hole Probe Data
(continued)

ANGULAR PLANE: 0.000 DEG
RADIUS/CYLINDER DIA: 0.638

Y/D	PHI DEG	THETA DEG	CPT	CPS	U/U ₀
0.0083	-1.9	-172.6	0.211	0.669	0.345
0.0125	-3.1	-176.1	0.229	0.663	0.330
0.0181	-6.0	-179.1	0.255	0.646	0.315
0.0233	-14.8	-178.8	0.281	0.638	0.285
0.0288	-20.0	-177.9	0.302	0.626	0.268
0.0329	-23.7	-177.7	0.315	0.620	0.255
0.0371	-28.5	-177.2	0.331	0.613	0.237
0.0824	-27.6	-3.6	0.096	0.754	0.387
0.0865	-26.7	-2.9	0.083	0.758	0.399
0.0948	-24.6	-3.2	0.065	0.764	0.414
0.1056	-21.2	-3.4	0.038	0.772	0.436
0.1191	-18.3	-3.3	0.031	0.785	0.429
0.1328	-15.7	-3.3	0.020	0.799	0.425
0.1466	-13.0	-3.5	0.019	0.805	0.420
0.1602	-11.9	-3.2	0.012	0.810	0.422
0.1740	-10.2	-3.0	0.010	0.816	0.417
0.2151	-7.3	-2.4	0.002	0.830	0.410
0.2562	-5.3	-2.0	0.000	0.834	0.407
0.3384	-5.3	-2.0	0.002	0.842	0.395
0.4203	-3.0	-1.4	0.002	0.840	0.399
0.5053	-1.4	-1.3	0.002	0.842	0.395

Five-Hole Probe Data
(continued)

ANGULAR PLANE: 0.000 DEG
RADIUS/CYLINDER DIA: 0.681

Y/D	PHI DEG	THETA DEG	CPT	CPS	U/Uo
0.0082	2.1	-178.9	0.298	0.565	0.369
0.0113	-0.4	-178.3	0.326	0.555	0.345
0.0138	-2.2	-178.1	0.348	0.542	0.332
0.0162	-2.5	-178.1	0.372	0.534	0.307
0.0186	-5.3	-178.0	0.398	0.523	0.279
0.0216	-9.9	-178.0	0.432	0.505	0.251
0.0220	-7.6	-177.9	0.436	0.506	0.241
0.0228	-12.5	-177.5	0.444	0.500	0.235
0.0237	-13.6	-177.5	0.453	0.495	0.228
0.0504	-28.0	-7.8	0.369	0.548	0.288
0.0545	-25.6	-6.8	0.341	0.553	0.322
0.0585	-23.6	-3.2	0.316	0.558	0.354
0.0666	-18.7	-3.0	0.271	0.579	0.387
0.0750	-18.0	-1.8	0.195	0.605	0.447
0.0832	-17.0	-1.9	0.172	0.610	0.467
0.0911	-16.2	-1.3	0.099	0.638	0.513
0.0995	-15.8	-1.4	0.062	0.654	0.533
0.1078	-14.1	-1.2	0.041	0.659	0.548
0.1160	-13.3	-1.3	0.015	0.675	0.557
0.1244	-13.1	-1.2	0.010	0.684	0.553
0.1341	-11.7	-1.1	0.002	0.695	0.550
0.1434	-11.2	-1.0	-0.001	0.702	0.546
0.1558	-10.3	-0.7	-0.002	0.708	0.542
0.1677	-9.8	-0.5	-0.004	0.715	0.538
0.1803	-9.5	-0.2	-0.006	0.719	0.536
0.1943	-9.1	-0.2	-0.005	0.723	0.531
0.2093	-9.1	0.2	-0.009	0.729	0.529
0.2363	-8.7	0.3	-0.008	0.739	0.519
0.2637	-7.2	0.2	-0.002	0.746	0.502
0.3048	-7.1	0.0	-0.008	0.757	0.501
0.3460	-5.8	-0.6	0.002	0.761	0.491
0.3877	-5.3	-0.4	0.005	0.771	0.474
0.4282	-4.2	-0.2	-0.003	0.770	0.483
0.4689	-3.6	-0.2	-0.002	0.776	0.475

Five-Hole Probe Data
(continued)

ANGULAR PLANE: 0.000 DEG
RADIUS/CYLINDER DIA: 0.723

Y/D	PHI DEG	THETA DEG	CPT	CPS	U/U ₀
0.0083	2.0	-178.2	0.394	0.531	0.274
0.0104	4.7	-178.5	0.406	0.528	0.255
0.0124	5.7	-178.6	0.426	0.515	0.241
0.0152	5.8	-178.2	0.455	0.506	0.197
0.0166	15.2	-178.5	0.467	0.502	0.176
0.0179	21.4	-175.3	0.480	0.498	0.148
0.0263	-28.2	-15.0	0.478	0.495	0.164
0.0283	-14.1	-14.0	0.486	0.478	0.190
0.0304	-11.0	-11.3	0.469	0.490	0.205
0.0342	-9.4	-10.1	0.461	0.487	0.228
0.0426	-9.4	-6.1	0.419	0.476	0.324
0.0509	-7.9	-4.5	0.356	0.478	0.407
0.0577	-9.0	-3.0	0.333	0.470	0.444
0.0644	-8.3	-2.7	0.267	0.486	0.496
0.0755	-8.4	-2.0	0.198	0.501	0.549
0.0837	-8.4	-1.8	0.136	0.519	0.587
0.0850	-8.5	-1.7	0.137	0.524	0.581
0.0917	-8.1	-1.8	0.100	0.541	0.599
0.0989	-9.2	-1.4	0.056	0.561	0.618
0.1054	-9.2	-1.5	0.041	0.579	0.616
0.1123	-8.9	-1.3	0.015	0.599	0.621
0.1193	-9.2	-1.3	0.014	0.609	0.615
0.1329	-8.8	-1.0	-0.009	0.619	0.624
0.1466	-8.5	-1.0	-0.006	0.628	0.615
0.1601	-8.4	-0.8	-0.009	0.638	0.609
0.1741	-8.0	-0.5	-0.006	0.645	0.601
0.2150	-7.5	0.1	-0.010	0.657	0.594
0.2561	-5.7	-0.1	-0.011	0.668	0.586
0.3381	-3.7	-0.3	-0.004	0.696	0.555
0.4202	-2.9	-0.1	-0.001	0.709	0.540
0.5048	-1.5	-0.1	-0.003	0.712	0.538

Five-Hole Probe Data
(continued)

ANGULAR PLANE: 0.000 DEG
RADIUS/CYLINDER DIA: 0.766

Y/D	PHI DEG	THETA DEG	CPT	CPS	U/U ₀
0.0077	-27.9	-102.2	0.485	0.512	0.063
0.0090	4.4	-44.5	0.475	0.519	0.077
0.0104	-15.3	-41.1	0.467	0.519	0.122
0.0131	-25.8	-40.0	0.472	0.517	0.105
0.0157	-10.8	-21.9	0.456	0.523	0.145
0.0200	-8.3	-18.2	0.457	0.515	0.167
0.0241	-6.2	-12.9	0.434	0.511	0.235
0.0282	-6.8	-11.2	0.418	0.515	0.259
0.0323	-6.0	-9.0	0.426	0.506	0.261
0.0405	-5.0	-6.3	0.382	0.506	0.335
0.0487	-4.6	-5.0	0.337	0.513	0.387
0.0568	-3.1	-3.6	0.281	0.510	0.456
0.0651	-3.2	-2.7	0.259	0.512	0.479
0.0732	-2.9	-2.2	0.218	0.506	0.525
0.0776	-3.8	-2.2	0.190	0.508	0.550
0.0814	-3.4	-1.9	0.157	0.506	0.581
0.0858	-3.2	-1.8	0.145	0.512	0.585
0.0980	-4.5	-1.5	0.118	0.515	0.606
0.1062	-3.7	-1.4	0.071	0.516	0.643
0.1105	-3.6	-1.4	0.057	0.520	0.650
0.1146	-2.5	-1.1	0.055	0.527	0.647
0.1348	-5.3	-0.9	0.003	0.551	0.668
0.1555	-5.1	-0.6	-0.006	0.575	0.657
0.1760	-5.3	-0.4	-0.008	0.582	0.653
0.1965	-5.0	0.0	-0.009	0.584	0.652
0.2377	-4.1	0.0	-0.009	0.599	0.640
0.2786	-3.6	0.1	-0.004	0.609	0.629
0.3199	-3.5	-0.1	-0.003	0.617	0.621
0.3608	-3.3	-0.3	-0.003	0.626	0.613
0.4020	-2.7	0.0	-0.001	0.635	0.607
0.4430	-2.2	0.0	0.003	0.638	0.602
0.484	-1.7	0.0	-0.002	0.636	0.601

Five-Hole Probe Data
(continued)

ANGULAR PLANE: 0.000 DEG
RADIUS/CYLINDER DIA: 0.809

Y/D	PHI DEG	THETA DEG	CPT	CPS	U/U ₀
0.0079	-4.3	-13.5	0.474	0.516	0.105
0.0100	-5.1	-11.3	0.468	0.515	0.134
0.0120	-4.6	-8.3	0.460	0.514	0.164
0.0142	-8.7	-7.0	0.454	0.513	0.182
0.0183	-6.7	-4.5	0.432	0.510	0.239
0.0265	-4.7	-3.4	0.396	0.510	0.307
0.0345	-4.0	-2.7	0.358	0.509	0.365
0.0429	-3.5	-2.2	0.314	0.509	0.421
0.0512	-3.9	-1.9	0.276	0.509	0.464
0.0594	-3.0	-1.6	0.232	0.507	0.510
0.0674	-3.2	-1.5	0.196	0.505	0.547
0.0757	-2.9	-1.4	0.150	0.504	0.588
0.0839	-2.8	-1.3	0.112	0.503	0.621
0.0922	-2.7	-1.1	0.080	0.506	0.643
0.1058	-2.9	-0.9	0.032	0.506	0.680
0.1196	-3.1	-0.7	0.008	0.510	0.694
0.1331	-3.1	-0.6	-0.004	0.516	0.699
0.1466	-3.4	-0.5	-0.003	0.525	0.691
0.1743	-2.9	-0.3	-0.012	0.534	0.691
0.2154	-2.2	0.1	-0.007	0.538	0.685
0.2562	-2.4	0.3	-0.010	0.546	0.681
0.3383	-2.2	-0.1	-0.002	0.563	0.662
0.4206	-2.0	0.0	-0.005	0.572	0.658
0.5054	-1.3	-0.1	-0.002	0.576	0.653

Five-Hole Probe Data
(continued)

ANGULAR PLANE: 0.000 DEG
RADIUS/CYLINDER DIA: 0.851

Y/D	PHI DEG	THETA DEG	CPT	CPS	U/U ₀
0.0085	3.8	-10.4	0.489	0.477	0.184
0.0137	-0.4	-7.5	0.467	0.473	0.245
0.0220	-2.5	-4.7	0.436	0.474	0.298
0.0302	-2.4	-3.7	0.405	0.471	0.352
0.0375	-3.3	-3.2	0.367	0.469	0.405
0.0465	-3.3	-2.8	0.332	0.470	0.445
0.0548	-3.2	-2.4	0.293	0.469	0.488
0.0631	-2.6	-2.2	0.247	0.468	0.534
0.0711	-2.3	-2.0	0.218	0.471	0.558
0.0794	-2.2	-1.8	0.181	0.467	0.593
0.0929	-2.0	-1.7	0.126	0.469	0.636
0.1067	-1.7	-1.4	0.073	0.469	0.677
0.1205	-1.7	-1.1	0.034	0.469	0.705
0.1342	-1.4	-0.9	0.010	0.469	0.722
0.1477	-1.6	-0.8	-0.005	0.472	0.729
0.1614	-1.7	-0.7	-0.009	0.471	0.733
0.1752	-1.7	-0.4	-0.015	0.475	0.735
0.2162	-1.9	0.4	-0.010	0.483	0.727
0.2571	-1.5	0.6	-0.006	0.487	0.720
0.3393	-2.0	0.6	-0.004	0.497	0.711
0.4216	-2.0	0.4	-0.003	0.508	0.704
0.4496	-2.1	0.2	-0.002	0.515	0.699
0.5059	-2.5	0.1	-0.004	0.519	0.696

Five-Hole Probe Data
(continued)

ANGULAR PLANE: 0.000 DEG
RADIUS/CYLINDER DIA: 0.890

Y/D	FHI DEG	THETA DEG	CPT	CPS	U/U ₀
0.0085	-3.0	-5.1	0.515	0.449	0.257
0.0108	-5.6	-4.9	0.476	0.449	0.274
0.0163	-3.2	-4.5	0.451	0.448	0.318
0.0218	-4.1	-3.6	0.419	0.448	0.365
0.0301	-4.2	-2.8	0.381	0.446	0.416
0.0381	-4.0	-2.4	0.340	0.446	0.463
0.0464	-3.2	-2.1	0.300	0.441	0.509
0.0547	-3.0	-1.8	0.258	0.443	0.547
0.0629	-3.6	-1.6	0.219	0.440	0.584
0.0708	-3.2	-1.5	0.184	0.442	0.612
0.0792	-2.7	-1.5	0.144	0.443	0.643
0.0930	-2.5	-1.2	0.088	0.441	0.686
0.1065	-2.2	-1.2	0.047	0.443	0.714
0.1204	-2.2	-1.1	0.012	0.443	0.738
0.1338	-1.9	-0.9	0.000	0.441	0.748
0.1477	-2.1	-0.6	-0.006	0.442	0.751
0.1750	-2.1	0.0	-0.003	0.441	0.750
0.2570	-1.9	0.4	-0.009	0.443	0.752
0.3394	-2.4	0.2	0.004	0.454	0.736
0.4214	-2.7	0.0	-0.006	0.479	0.726
0.5052	-3.1	0.0	-0.005	0.483	0.722

Five-Hole Probe Data
(continued)

ANGULAR PLANE: 0.000 DEG
RADIUS/CYLINDER DIA: 0.936

Y/D	PHI DEG	THETA DEG	CPT	CPS	U/U ₀
0.0083	-0.4	-3.4	0.508	0.434	0.241
0.0110	0.6	-2.8	0.496	0.435	0.263
0.0166	-0.6	-2.3	0.467	0.434	0.315
0.0221	-1.9	-1.8	0.446	0.425	0.359
0.0301	-1.9	-1.4	0.410	0.430	0.401
0.0383	-1.5	-1.2	0.371	0.427	0.449
0.0467	-0.8	-1.3	0.325	0.425	0.500
0.0549	-0.5	-1.1	0.285	0.425	0.539
0.0632	-0.2	-1.1	0.236	0.428	0.579
0.0712	-0.8	-0.9	0.205	0.424	0.610
0.0794	-1.2	-0.9	0.163	0.423	0.643
0.0933	-0.6	-0.9	0.110	0.424	0.683
0.1069	-0.7	-0.8	0.061	0.420	0.720
0.1206	-0.3	-0.8	0.028	0.424	0.740
0.1343	-0.7	-0.6	-0.005	0.423	0.763
0.1479	-0.7	-0.2	-0.003	0.418	0.764
0.1752	-0.7	0.2	-0.013	0.423	0.769
0.2164	-0.9	0.6	-0.013	0.420	0.770
0.2575	-1.4	0.4	-0.013	0.423	0.768
0.3394	-2.3	0.4	-0.002	0.428	0.758
0.4216	-2.8	0.2	0.000	0.440	0.746
0.5060	-2.7	0.1	0.004	0.446	0.742

Five-Hole Probe Data
(continued)

ANGULAR PLANE: 0.000 DEG
RADIUS/CYLINDER DIA: 1.021

Y/D	PHI DEG	THETA DEG	CPT	CPS	U/U ₀
0.0085	1.0	-1.7	0.514	0.389	0.311
0.0118	0.3	-1.5	0.497	0.385	0.344
0.0174	-0.7	-1.2	0.468	0.383	0.386
0.0229	-0.3	-1.0	0.433	0.384	0.429
0.0312	-0.3	-1.0	0.399	0.379	0.470
0.0393	-0.2	-0.9	0.361	0.379	0.510
0.0475	-0.1	-0.8	0.313	0.379	0.555
0.0558	0.2	-0.8	0.279	0.375	0.588
0.0637	0.2	-0.8	0.242	0.375	0.619
0.0720	0.2	-0.9	0.202	0.375	0.650
0.0803	0.6	-0.9	0.178	0.372	0.671
0.0941	0.5	-0.8	0.113	0.371	0.718
0.1076	0.6	-0.9	0.065	0.370	0.752
0.1214	0.7	-0.7	0.028	0.366	0.778
0.1349	0.8	-0.6	0.002	0.367	0.794
0.1487	0.8	-0.3	-0.002	0.367	0.797
0.1762	0.7	0.1	-0.009	0.366	0.802
0.2172	0.8	0.5	-0.014	0.367	0.804
0.2580	0.4	0.2	-0.008	0.366	0.801
0.3403	-0.3	0.1	0.000	0.369	0.794
0.4224	-0.5	0.1	-0.003	0.371	0.795
0.5066	-1.0	-0.1	0.000	0.372	0.792

Five-Hole Probe Data
(continued)

ANGULAR PLANE: 0.000 DEG
RADIUS/CYLINDER DIA: 1.191

Y/D	PHI DEG	THETA DEG	CPT	CPS	U/U ₀
0.0083	1.1	-0.1	0.526	0.305	0.412
0.0132	0.2	-0.1	0.495	0.298	0.456
0.0187	-0.2	-0.1	0.457	0.295	0.498
0.0239	-0.4	-0.2	0.434	0.293	0.522
0.0322	-0.4	-0.2	0.396	0.294	0.558
0.0406	-0.4	-0.2	0.345	0.292	0.602
0.0488	-0.2	-0.4	0.301	0.292	0.638
0.0571	-0.1	-0.4	0.264	0.291	0.666
0.0654	0.1	-0.4	0.235	0.288	0.690
0.0734	0.3	-0.5	0.199	0.289	0.716
0.0816	0.3	-0.4	0.169	0.287	0.738
0.0954	0.4	-0.4	0.111	0.288	0.775
0.1090	0.2	-0.4	0.057	0.284	0.812
0.1228	0.7	-0.3	0.024	0.289	0.829
0.1363	0.4	-0.3	0.004	0.282	0.845
0.1502	0.3	-0.1	-0.016	0.284	0.856
0.1775	0.2	0.3	-0.006	0.283	0.850
0.2185	0.4	1.0	-0.011	0.287	0.851
0.2595	0.1	1.0	-0.014	0.279	0.857
0.3417	0.4	0.6	-0.008	0.281	0.853
0.4237	0.1	0.4	-0.007	0.282	0.851
0.5074	-0.4	0.2	-0.002	0.280	0.850

Five-Hole Probe Data
(continued)

ANGULAR PLANE: 0.000 DEG
RADIUS/CYLINDER DIA: 1.362

Y/D	PHI DEG	THETA DEG	CPT	CPS	U/U ₀
0.0085	1.6	0.0	0.534	0.236	0.481
0.0136	0.6	-0.1	0.499	0.231	0.520
0.0192	-0.1	-0.2	0.467	0.224	0.555
0.0261	-0.1	-0.2	0.423	0.225	0.593
0.0340	0.1	-0.3	0.375	0.225	0.632
0.0424	0.0	-0.3	0.344	0.220	0.660
0.0506	-0.1	-0.3	0.303	0.219	0.691
0.0586	0.1	-0.4	0.259	0.220	0.722
0.0668	-0.2	-0.4	0.220	0.221	0.748
0.0751	0.0	-0.5	0.171	0.220	0.780
0.0834	-0.1	-0.4	0.147	0.219	0.797
0.0972	0.2	-0.4	0.083	0.215	0.838
0.1108	0.3	-0.4	0.041	0.215	0.863
0.1246	0.4	-0.3	0.014	0.215	0.877
0.1383	0.4	-0.3	0.002	0.217	0.884
0.1520	0.3	-0.1	-0.010	0.217	0.891
0.1793	0.3	0.2	-0.013	0.215	0.894
0.2203	0.1	0.7	-0.006	0.216	0.889
0.2612	0.2	0.7	-0.007	0.216	0.890
0.3436	0.1	0.5	0.000	0.214	0.887
0.4257	-0.1	0.3	-0.001	0.212	0.888
0.5078	-0.3	0.2	-0.004	0.216	0.888

Five-Hole Probe Data
(continued)

ANGULAR PLANE: 0.000 DEG
RADIUS/CYLINDER DIA: 1.532

Y/D	PHI DEG	THETA DEG	CPT	CPS	U/U ₀
0.0085	1.8	0.0	0.539	0.189	0.722
0.0140	0.7	-0.1	0.490	0.180	0.758
0.0198	0.6	-0.1	0.449	0.178	0.781
0.0281	0.2	-0.2	0.407	0.176	0.803
0.0361	0.1	-0.2	0.361	0.175	0.825
0.0444	0.1	-0.3	0.316	0.174	0.845
0.0527	0.1	-0.3	0.269	0.173	0.864
0.0610	0.0	-0.4	0.237	0.174	0.876
0.0690	0.1	-0.4	0.196	0.172	0.891
0.0772	0.2	-0.3	0.156	0.173	0.905
0.0855	0.3	-0.3	0.118	0.170	0.918
0.0993	0.3	-0.3	0.069	0.169	0.934
0.1129	0.4	-0.3	0.024	0.170	0.947
0.1266	0.3	-0.2	0.003	0.169	0.954
0.1402	0.5	-0.2	-0.009	0.169	0.957
0.1540	0.4	-0.1	-0.012	0.170	0.958
0.1813	0.3	0.3	-0.014	0.170	0.958
0.2221	0.3	0.8	-0.016	0.169	0.959
0.2635	0.3	0.8	-0.009	0.168	0.957
0.3456	0.1	0.6	-0.004	0.169	0.956
0.4272	0.1	0.4	-0.003	0.168	0.956
0.5097	-0.2	0.2	-0.003	0.171	0.955

Five-Hole Probe Data
(continued)

ANGULAR PLANE: 5.000 DEG
RADIUS/CYLINDER DIA: 0.596

Y/D	PHI DEG	THETA DEG	CPT	CPS	U/U ₀
0.0082	-4.0	138.2	0.078	0.836	0.295
0.0101	-7.9	137.2	0.087	0.839	0.272
0.0119	-10.4	133.7	0.106	0.831	0.251
0.0137	-16.4	131.1	0.111	0.836	0.230
0.0155	-20.9	129.8	0.129	0.828	0.207
0.0175	-26.6	125.1	0.130	0.831	0.197
0.1032	-27.2	19.2	0.020	0.869	0.335
0.1100	-25.9	18.3	0.023	0.870	0.329
0.1248	-21.8	17.3	0.014	0.873	0.335
0.1382	-19.1	16.9	0.013	0.874	0.336
0.1509	-17.4	17.1	0.010	0.872	0.344
0.1645	-15.8	17.5	0.006	0.873	0.348
0.1787	-15.8	18.2	0.001	0.870	0.359
0.2199	-13.1	19.7	-0.005	0.871	0.367
0.2604	-10.8	21.4	-0.007	0.874	0.366
0.3012	-9.4	23.0	-0.004	0.878	0.355
0.3431	-7.8	23.6	-0.004	0.883	0.348
0.4244	-4.1	24.5	0.000	0.885	0.339
0.5067	-1.1	25.2	-0.006	0.890	0.341

Five-Hole Probe Data
(continued)

ANGULAR PLANE: 5.000 DEG
RADIUS/CYLINDER DIA: 0.638

Y/D	PHI DEG	THETA DEG	CPT	CPS	U/U ₀
0.0083	2.0	146.1	0.208	0.665	0.356
0.0115	-1.2	144.0	0.263	0.655	0.286
0.0142	-10.0	141.8	0.298	0.648	0.235
0.0170	-22.6	140.2	0.335	0.639	0.164
0.0198	-28.0	137.1	0.345	0.623	0.176
0.0668	-27.7	8.9	0.137	0.715	0.386
0.0703	-26.1	8.4	0.126	0.719	0.394
0.0785	-22.5	7.8	0.089	0.728	0.429
0.0868	-19.8	7.1	0.069	0.733	0.445
0.0951	-17.2	6.8	0.047	0.747	0.454
0.1031	-15.5	6.4	0.036	0.756	0.457
0.1115	-14.0	6.8	0.023	0.766	0.459
0.1197	-11.9	6.5	0.024	0.766	0.458
0.1332	-11.3	7.4	0.011	0.775	0.463
0.1470	-10.6	7.9	0.009	0.776	0.464
0.1605	-10.3	9.2	0.002	0.776	0.470
0.1744	-10.7	10.0	-0.003	0.777	0.475
0.2154	-9.6	11.8	-0.009	0.790	0.468
0.2563	-8.4	13.0	-0.007	0.798	0.457
0.3386	-5.6	14.1	0.000	0.811	0.435
0.4207	-3.1	15.3	0.003	0.817	0.424
0.5051	-0.7	15.4	0.000	0.819	0.425

Five-Hole Probe Data
(continued)

ANGULAR PLANE: 5.000 DEG
RADIUS/CYLINDER DIA: 0.681

Y/D	PHI DEG	THETA DEG	CPT	CPS	U/Uo
0.0082	3.1	159.7	0.311	0.497	0.438
0.0105	1.6	161.9	0.365	0.481	0.391
0.0131	0.1	162.3	0.421	0.463	0.341
0.0159	-1.4	167.6	0.466	0.447	0.295
0.0186	-4.5	168.9	0.504	0.426	0.265
0.0213	-9.8	170.0	0.549	4.020	0.221
0.0241	-17.1	170.1	0.575	0.383	0.205
0.0491	-26.2	6.5	0.376	0.512	0.335
0.0525	-24.3	6.3	0.363	0.513	0.352
0.0608	-19.7	5.5	0.300	0.533	0.407
0.0698	-16.4	4.3	0.231	0.549	0.470
0.0784	-15.1	4.5	0.184	0.563	0.502
0.0870	-14.0	4.9	0.131	0.578	0.539
0.0940	-12.9	4.3	0.090	0.587	0.568
0.1147	-11.5	4.4	0.021	0.616	0.602
0.1255	-10.9	4.7	0.005	0.625	0.608
0.1346	-10.5	4.9	0.000	0.635	0.604
0.1542	-9.7	5.5	-0.007	0.658	0.591
0.1751	-9.1	6.0	-0.005	0.671	0.578
0.2169	-7.5	8.0	-0.010	0.699	0.558
0.2581	-6.0	8.9	-0.005	0.720	0.534
0.3403	-4.4	9.7	-0.005	0.745	0.510
0.4218	-2.9	10.3	-0.002	0.754	0.499
0.5060	-1.2	10.4	-0.005	0.757	0.546

Five-Hole Probe Data
(continued)

ANGULAR PLANE: 5.000 DEG
RADIUS/CYLINDER DIA: 0.723

Y/D	PHI DEG	THETA DEG	CPT	CPS	U/U ₀
0.0084	5.4	156.5	0.426	0.494	0.281
0.0102	6.1	156.4	0.441	0.490	0.261
0.0130	6.5	156.3	0.460	0.478	0.247
0.0157	13.9	150.8	0.483	0.469	0.219
0.0185	16.4	141.9	0.506	0.463	0.173
0.0199	24.0	136.5	0.505	0.459	0.190
0.0213	22.6	126.4	0.528	0.450	0.148
0.0254	7.0	20.2	0.575	0.413	0.110
0.0293	8.2	14.4	0.566	0.407	0.164
0.0334	4.6	11.3	0.535	0.409	0.237
0.0375	0.6	8.1	0.488	0.419	0.305
0.0431	-0.8	6.0	0.417	0.442	0.375
0.0485	-3.7	5.1	0.362	0.453	0.429
0.0540	-2.8	4.2	0.305	0.471	0.473
0.0623	-4.1	3.9	0.233	0.492	0.524
0.0704	-4.6	3.6	0.178	0.502	0.567
0.0786	-4.5	3.5	0.138	0.510	0.594
0.0869	-4.7	3.3	0.095	0.515	0.624
0.0952	-4.7	3.2	0.059	0.526	0.644
0.1032	-4.7	3.2	0.035	0.532	0.658
0.1115	-4.9	3.4	0.017	0.545	0.662
0.1197	-4.9	3.3	0.009	0.553	0.662
0.1335	-5.6	3.4	-0.003	0.570	0.658
0.1472	-5.4	3.6	-0.001	0.581	0.648
0.1606	-5.7	4.0	-0.004	0.593	0.641
0.1745	-5.7	4.5	0.000	0.602	0.631
0.2155	-5.1	6.1	-0.004	0.627	0.614
0.2565	-4.6	6.9	-0.003	0.647	0.597
0.3386	-3.4	7.4	-0.003	0.669	0.578
0.4208	-2.7	8.0	0.003	0.681	0.562
0.5050	-1.3	8.2	0.001	0.684	0.561

Five-Hole Probe Data
(continued)

ANGULAR PLANE: 5.000 DEG
RADIUS/CYLINDER DIA: 0.766

Y/D	PHI DEG	THETA DEG	CPT	CPS	U/U ₀
0.0083	0.0	129.6	0.480	0.489	0.176
0.0107	0.4	126.5	0.486	0.482	0.179
0.0131	4.5	125.1	0.499	0.478	0.152
0.0146	18.3	117.8	0.511	0.470	0.134
0.0160	1.1	112.4	0.515	0.469	0.126
0.0174	-1.0	106.6	0.526	0.468	0.071
0.0187	-20.6	101.5	0.531	0.465	0.063
0.0215	-23.3	70.0	0.527	0.463	0.095
0.0228	-25.4	70.7	0.532	0.458	0.100
0.0242	-12.7	55.7	0.528	0.455	0.130
0.0267	-5.8	33.3	0.495	0.455	0.200
0.0296	-0.8	28.5	0.507	0.450	0.205
0.0323	5.0	21.5	0.498	0.453	0.221
0.0350	6.3	15.7	0.456	0.462	0.288
0.0391	4.5	14.3	0.457	0.454	0.298
0.0434	3.4	11.3	0.409	0.470	0.349
0.0520	4.3	7.8	0.348	0.467	0.429
0.0599	1.7	6.7	0.310	0.469	0.470
0.0686	2.5	5.7	0.227	0.478	0.543
0.0799	0.8	4.7	0.164	0.482	0.595
0.0935	0.0	4.5	0.096	0.487	0.646
0.1069	-0.5	4.3	0.036	0.491	0.688
0.1209	-1.2	4.1	0.010	0.502	0.699
0.1340	-2.1	4.2	-0.003	0.506	0.705
0.1551	-2.5	4.2	-0.008	0.525	0.695
0.1751	-3.1	4.5	-0.011	0.539	0.687
0.2158	-3.0	5.6	-0.006	0.559	0.669
0.2575	-2.6	6.3	-0.009	0.580	0.656
0.3394	-2.5	6.6	-0.003	0.605	0.631
0.4209	-2.1	7.4	-0.003	0.619	0.620
0.5040	-1.4	7.5	-0.004	0.623	0.617

Five-Hole Probe Data
(continued)

ANGULAR PLANE: 5.000 DEG
RADIUS/CYLINDER DIA: 0.809

Y/D	PHI DEG	THETA DEG	CPT	CPS	U/U ₀
0.0083	5.1	67.8	0.492	0.503	0.071
0.0107	18.9	58.9	0.494	0.496	0.105
0.0135	-6.8	44.1	0.478	0.500	0.148
0.0170	-2.8	25.3	0.460	0.499	0.202
0.0215	-2.5	17.9	0.436	0.496	0.261
0.0298	-0.8	11.8	0.403	0.498	0.315
0.0378	-1.0	8.8	0.338	0.504	0.397
0.0460	-0.5	6.8	0.298	0.503	0.445
0.0544	0.6	5.3	0.249	0.500	0.501
0.0626	0.7	4.2	0.193	0.503	0.551
0.0708	0.9	3.4	0.147	0.499	0.596
0.0789	0.7	3.2	0.108	0.498	0.628
0.0871	1.1	2.7	0.082	0.494	0.650
0.0954	0.3	2.5	0.047	0.497	0.675
0.1035	0.3	2.2	0.031	0.491	0.692
0.1119	0.2	2.1	0.008	0.491	0.708
0.1201	-0.2	2.1	0.003	0.495	0.709
0.1335	-0.5	2.0	-0.003	0.495	0.713
0.1472	-1.1	1.9	-0.004	0.495	0.713
0.1611	-1.4	2.2	-0.002	0.497	0.710
0.1747	-1.9	2.5	0.000	0.504	0.704
0.2157	-2.1	3.3	-0.006	0.512	0.703
0.2569	-2.4	3.8	-0.002	0.524	0.691
0.3389	-2.4	4.1	0.003	0.541	0.675
0.4211	-1.9	4.6	-0.002	0.556	0.668
0.5052	-1.7	4.6	0.001	0.554	0.667

Five-Hole Probe Data
(continued)

ANGULAR PLANE: 5.000 DEG
RADIUS/CYLINDER DIA: 0.851

Y/D	PHI DEG	THETA DEG	CPT	CPS	U/U ₀
0.0082	-1.0	54.7	0.513	0.469	0.134
0.0106	-4.0	41.0	0.508	0.472	0.141
0.0141	-2.9	30.3	0.493	0.474	0.179
0.0201	-1.0	19.7	0.472	0.473	0.235
0.0284	-0.1	13.2	0.429	0.473	0.313
0.0367	1.0	9.8	0.376	0.475	0.386
0.0449	1.6	7.7	0.326	0.476	0.445
0.0529	2.0	6.8	0.283	0.473	0.494
0.0614	3.0	5.8	0.242	0.471	0.536
0.0696	2.4	5.2	0.197	0.468	0.579
0.0773	2.8	4.9	0.165	0.464	0.609
0.0860	2.6	4.5	0.136	0.464	0.632
0.0939	1.9	4.3	0.085	0.461	0.674
0.1065	1.6	4.0	0.043	0.459	0.705
0.1199	1.4	3.7	0.014	0.456	0.729
0.1269	1.3	3.6	0.000	0.461	0.733
0.1349	1.1	3.5	-0.005	0.458	0.739
0.1763	0.3	3.5	-0.008	0.463	0.739
0.2582	-1.2	4.5	-0.009	0.479	0.729
0.3409	-1.9	4.4	-0.004	0.496	0.713
0.4277	-2.1	4.7	0.000	0.506	0.703
0.5069	-1.5	4.8	-0.006	0.510	0.704

Five-Hole Probe Data
(continued)

ANGULAR PLANE: 5.000 DEG
RADIUS/CYLINDER DIA: 0.890

Y/D	PHI DEG	THETA DEG	CPT	CPS	U/U ₀
0.0083	-0.2	20.3	0.484	0.470	0.214
0.0149	-1.0	13.2	0.449	0.467	0.290
0.0218	0.5	9.8	0.403	0.465	0.363
0.0298	-0.1	7.5	0.356	0.464	0.424
0.0381	0.0	6.0	0.307	0.461	0.482
0.0464	0.4	5.0	0.270	0.455	0.524
0.0547	0.7	4.3	0.226	0.455	0.565
0.0628	0.8	3.9	0.181	0.451	0.607
0.0709	0.7	3.5	0.132	0.450	0.647
0.0792	0.9	3.2	0.098	0.447	0.675
0.0874	0.7	2.9	0.068	0.445	0.698
0.0958	0.9	2.8	0.037	0.443	0.721
0.1038	0.7	2.6	0.021	0.444	0.732
0.1121	0.7	2.4	0.006	0.443	0.742
0.1204	0.6	2.3	0.004	0.440	0.746
0.1339	0.3	2.2	-0.001	0.439	0.749
0.1477	0.2	2.2	-0.002	0.439	0.750
0.1615	0.0	2.3	-0.008	0.437	0.756
0.1750	0.0	2.5	-0.003	0.432	0.756
0.2161	-0.6	3.3	-0.004	0.437	0.753
0.2571	-0.8	3.5	-0.007	0.444	0.750
0.3392	-1.6	3.4	0.000	0.456	0.738
0.4214	-2.0	3.5	0.002	0.459	0.734
0.5059	-1.6	3.4	0.002	0.461	0.733

Five-Hole Probe Data
(continued)

ANGULAR PLANE: 5.000 DEG
RADIUS/CYLINDER DIA: 0.936

Y/D	PHI DEG	THETA DEG	CPT	CPS	U/Uo
0.0083	-1.3	14.2	0.497	0.433	0.265
0.0153	-1.2	10.3	0.461	0.431	0.329
0.0225	-1.1	8.3	0.430	0.428	0.377
0.0305	-0.3	6.8	0.382	0.427	0.437
0.0389	0.3	5.9	0.348	0.425	0.477
0.0471	0.7	4.9	0.305	0.425	0.520
0.0554	0.9	4.2	0.255	0.423	0.567
0.0634	1.0	4.0	0.216	0.420	0.603
0.0716	1.1	3.5	0.183	0.417	0.632
0.0798	1.4	3.3	0.141	0.417	0.665
0.0937	1.4	2.9	0.084	0.413	0.709
0.1073	1.4	2.6	0.049	0.410	0.736
0.1210	1.2	2.3	0.014	0.407	0.761
0.1345	1.5	2.2	-0.001	0.404	0.773
0.1483	1.1	2.4	-0.011	0.408	0.777
0.1757	0.9	3.3	-0.009	0.403	0.778
0.2168	0.3	3.6	-0.016	0.408	0.780
0.2577	-0.3	3.8	-0.010	0.412	0.773
0.3400	-1.0	3.4	-0.001	0.416	0.765
0.4219	-1.3	3.6	-0.001	0.417	0.764
0.5066	-1.2	3.4	-0.010	0.431	0.762

Five-Hole Probe Data
(continued)

ANGULAR PLANE: 5.000 DEG
RADIUS/CYLINDER DIA: 1.021

Y/D	PHI DEG	THETA DEG	CPT	CPS	U/U ₀
0.0083	-0.3	8.1	0.485	0.382	0.365
0.0157	-0.8	6.3	0.435	0.377	0.434
0.0230	-0.6	5.3	0.386	0.374	0.490
0.0311	-0.8	4.6	0.347	0.370	0.532
0.0395	-0.6	4.0	0.296	0.371	0.576
0.0478	-0.5	3.5	0.249	0.369	0.618
0.0561	-0.1	3.1	0.208	0.366	0.653
0.0640	0.0	2.9	0.164	0.366	0.686
0.0722	0.0	2.7	0.126	0.365	0.713
0.0805	0.1	2.5	0.093	0.362	0.738
0.0944	0.3	2.2	0.049	0.358	0.770
0.1080	0.5	2.0	0.013	0.359	0.792
0.1218	0.6	1.9	-0.002	0.357	0.803
0.1353	0.6	1.8	-0.004	0.356	0.805
0.1491	0.4	1.9	-0.008	0.355	0.808
0.1765	0.4	2.4	-0.006	0.351	0.809
0.2175	0.3	3.2	-0.006	0.346	0.812
0.2584	0.1	3.0	-0.011	0.354	0.811
0.3407	-0.7	2.7	-0.006	0.357	0.806
0.4227	-0.7	2.8	-0.001	0.360	0.801
0.5069	-0.9	2.5	-0.004	0.363	0.801

Five-Hole Probe Data
(continued)

ANGULAR PLANE: 5.000 DEG
RADIUS/CYLINDER DIA: 1.191

Y/D	PHI DEG	THETA DEG	CPT	CPS	U/U ₀
0.0083	0.1	4.5	0.484	0.286	0.480
0.0164	-0.8	3.6	0.417	0.277	0.553
0.0247	-1.0	3.1	0.359	0.275	0.606
0.0330	-0.9	2.7	0.314	0.272	0.643
0.0410	-0.9	2.3	0.262	0.273	0.682
0.0493	-0.8	2.0	0.219	0.271	0.714
0.0576	-0.6	1.8	0.174	0.273	0.744
0.0656	-0.5	1.6	0.137	0.271	0.769
0.0740	-0.4	1.4	0.093	0.269	0.799
0.0821	-0.5	1.3	0.063	0.269	0.817
0.0959	-0.3	1.1	0.022	0.269	0.842
0.1095	-0.3	1.0	0.002	0.267	0.855
0.1232	-0.2	0.9	-0.004	0.266	0.859
0.1370	-0.2	0.9	0.002	0.262	0.858
0.1505	-0.2	1.0	-0.006	0.267	0.859
0.1778	-0.2	1.6	-0.004	0.266	0.859
0.2191	0.0	2.4	-0.009	0.264	0.863
0.2600	-0.1	2.4	-0.007	0.265	0.861
0.3420	-0.3	1.9	0.000	0.267	0.856
0.4242	-0.4	1.7	-0.001	0.265	0.858
0.5087	-0.8	1.6	0.001	0.263	0.858

Five-Hole Probe Data
(continued)

ANGULAR PLANE: 5.000 DEG
RADIUS/CYLINDER DIA: 1.532

Y/D	PHI DEG	THETA DEG	CPT	CPS	U/U ₀
0.0083	1.1	1.9	0.481	0.175	0.587
0.0142	.0	1.6	0.423	0.168	0.640
0.0200	-0.4	1.4	0.385	0.164	0.672
0.0280	-0.3	1.3	0.330	0.162	0.713
0.0363	-0.7	1.2	0.273	0.160	0.753
0.0446	-0.3	1.1	0.223	0.159	0.786
0.0530	-0.5	0.9	0.172	0.161	0.816
0.0612	-0.5	0.8	0.133	0.162	0.840
0.0694	-0.3	0.7	0.094	0.156	0.866
0.0774	-0.2	0.6	0.057	0.157	0.887
0.0857	-0.3	0.5	0.029	0.159	0.901
0.0995	-0.1	0.4	-0.001	0.158	0.918
0.1131	-0.1	0.4	0.004	0.154	0.918
0.1269	-0.2	0.4	-0.013	0.159	0.924
0.1407	-0.5	0.4	-0.011	0.157	0.924
0.1542	-0.5	0.5	-0.007	0.155	0.923
0.1816	-0.5	0.8	-0.004	0.153	0.922
0.2226	-0.3	1.2	-0.005	0.153	0.923
0.2635	-0.1	1.4	-0.006	0.154	0.923
0.3457	-0.2	1.2	-0.004	0.154	0.921
0.4279	-0.3	0.9	-0.001	0.155	0.920
0.5114	-0.4	0.9	0.001	0.155	0.919

Five-Hole Probe Data
(continued)

ANGULAR PLANE: 25.000 DEG
RADIUS/CYLINDER DIA: 0.553

Y/D	FHI DEG	THETA DEG	CPT	CPS	U/U ₀
0.0084	-0.2	69.0	0.008	0.476	0.718
0.0120	-3.6	67.6	0.013	0.459	0.727
0.0159	-5.7	65.6	0.021	0.450	0.727
0.0215	-8.7	63.6	0.020	0.440	0.735
0.0296	-10.3	61.0	0.016	0.429	0.745
0.0379	-12.2	58.7	0.012	0.420	0.753
0.0461	-12.8	57.2	0.007	0.414	0.761
0.0545	-13.4	55.9	0.002	0.408	0.769
0.0627	-13.7	54.6	0.001	0.399	0.775
0.0707	-13.8	53.6	-0.001	0.393	0.780
0.0789	-13.6	53.0	-0.002	0.394	0.780
0.0928	-13.1	52.2	-0.002	0.388	0.784
0.1063	-12.5	51.7	-0.002	0.383	0.787
0.1201	-12.0	51.4	-0.005	0.382	0.789
0.1338	-11.2	51.3	-0.008	0.381	0.792
0.1474	-10.5	51.2	-0.004	0.377	0.792
0.1609	-9.9	51.2	-0.004	0.377	0.792
0.1748	-9.4	51.2	-0.007	0.377	0.793
0.2159	-8.3	51.5	-0.015	0.377	0.799
0.2570	-5.9	51.6	-0.003	0.380	0.789
0.3388	-3.8	51.9	0.000	0.380	0.787
0.4211	-2.5	52.2	-0.001	0.382	0.787
0.5060	-0.8	52.1	-0.002	0.383	0.787

Five-Hole Probe Data
(continued)

ANGULAR PLANE: 25.000 DEG
RADIUS/CYLINDER DIA: 0.596

Y/D	FHI DEG	THETA DEG	CPT	CPS	U/U ₀
0.0088	-1.5	81.5	0.041	0.431	0.727
0.0136	-4.9	77.2	0.080	0.414	0.711
0.0157	-7.0	75.3	0.098	0.407	0.704
0.0239	-10.5	68.1	0.107	0.402	0.701
0.0319	-13.1	61.9	0.105	0.395	0.706
0.0402	-15.3	57.1	0.110	0.376	0.717
0.0485	-16.4	52.8	0.089	0.373	0.733
0.0568	-17.0	49.5	0.062	0.361	0.760
0.0649	-17.1	46.9	0.043	0.362	0.771
0.0731	-16.9	44.8	0.030	0.358	0.783
0.0813	-16.2	43.4	0.026	0.352	0.789
0.0924	-15.7	42.2	0.000	0.354	0.804
0.1060	-14.4	41.4	0.001	0.354	0.803
0.1197	-13.5	41.2	-0.004	0.355	0.806
0.1332	-12.1	41.1	-0.001	0.356	0.802
0.1468	-11.3	41.2	-0.011	0.362	0.806
0.1607	-10.5	41.2	-0.007	0.365	0.801
0.1744	-9.8	41.6	-0.007	0.365	0.801
0.2156	-8.3	42.4	-0.011	0.373	0.799
0.2567	-5.9	42.8	-0.002	0.380	0.789
0.3387	-3.7	43.5	0.000	0.386	0.784
0.4205	-2.4	43.9	-0.005	0.392	0.783
0.5053	-1.0	43.8	0.000	0.394	0.778

Five-Hole Probe Data
(continued)

ANGULAR PLANE: 25.000 DEG
RADIUS/CYLINDER DIA: 0.617

Y/D	PHI DEG	THETA DEG	CPT	CPS	U/U ₀
0.0085	-0.3	87.6	0.078	0.382	0.735
0.0133	-4.3	82.9	0.128	0.367	0.711
0.0189	-8.3	77.4	0.166	0.355	0.693
0.0244	-10.9	71.7	0.190	0.352	0.677
0.0296	-12.9	66.3	0.200	0.343	0.677
0.0351	-15.2	61.4	0.199	0.339	0.680
0.0421	-17.0	55.9	0.182	0.330	0.699
0.0490	-17.8	51.0	0.153	0.327	0.721
0.0571	-18.1	46.8	0.129	0.318	0.744
0.0652	-18.0	43.1	0.094	0.316	0.768
0.0735	-17.5	40.6	0.071	0.310	0.787
0.0817	-16.5	38.8	0.044	0.312	0.802
0.0900	-15.9	37.3	0.024	0.318	0.811
0.0980	-15.1	36.7	0.015	0.320	0.816
0.1091	-14.0	36.1	0.006	0.327	0.817
0.1198	-12.9	36.0	0.001	0.332	0.817
0.1337	-11.7	36.1	-0.003	0.340	0.814
0.1475	-10.7	36.4	0.001	0.346	0.808
0.1611	-9.9	36.6	-0.001	0.351	0.806
0.1749	-9.3	36.9	-0.004	0.355	0.806
0.2157	-8.0	38.1	-0.003	0.367	0.797
0.2569	-5.7	38.8	0.001	0.377	0.788
0.3389	-3.5	39.7	0.002	0.386	0.782
0.4211	-1.9	40.0	-0.002	0.395	0.779
0.5057	-0.8	40.1	0.000	0.396	0.777

Five-Hole Probe Data
(continued)

ANGULAR PLANE: 25.000 DEG
RADIUS/CYLINDER DIA: 0.638

Y/D	PHI DEG	THETA DEG	CPT	CPS	U/U ₀
0.0085	-0.7	93.8	0.108	0.289	0.777
0.0120	-3.5	90.3	0.159	0.292	0.741
0.0162	-5.8	85.9	0.211	0.290	0.706
0.0210	-9.2	80.5	0.252	0.282	0.683
0.0255	-11.4	75.3	0.272	0.277	0.672
0.0304	-13.7	70.1	0.295	0.270	0.660
0.0352	-15.9	65.0	0.287	0.265	0.669
0.0408	-17.1	59.4	0.282	0.264	0.675
0.0463	-17.5	54.2	0.275	0.253	0.687
0.0514	-18.6	50.5	0.246	0.257	0.706
0.0570	-18.5	46.7	0.219	0.251	0.728
0.0625	-17.7	43.3	0.195	0.251	0.744
0.0681	-17.8	40.8	0.176	0.248	0.759
0.0763	-17.0	38.1	0.122	0.257	0.788
0.0842	-16.3	35.7	0.095	0.261	0.802
0.0928	-15.1	34.1	0.055	0.266	0.824
0.1009	-14.4	33.2	0.033	0.277	0.831
0.1092	-13.4	32.6	0.017	0.280	0.838
0.1202	-12.5	32.4	0.001	0.295	0.839
0.1337	-11.4	32.7	-0.005	0.309	0.834
0.1475	-10.0	33.0	-0.001	0.314	0.829
0.1611	-9.2	33.5	-0.007	0.321	0.828
0.1749	-8.9	33.9	-0.005	0.333	0.820
0.2160	-7.4	35.0	-0.006	0.354	0.807
0.2571	-4.9	36.0	0.005	0.357	0.799
0.3392	-3.5	37.2	0.002	0.375	0.789
0.4210	-1.9	37.6	0.005	0.379	0.785
0.5067	-1.1	37.6	0.005	0.378	0.785

Five-Hole Probe Data
(continued)

ANGULAR PLANE: 25.000 DEG
RADIUS/CYLINDER DIA: 0.660

Y/D	PHI DEG	THETA DEG	CPT	CPS	U/Uo
0.0083	1.0	101.5	0.159	0.194	0.804
0.0131	-3.1	97.9	0.260	0.172	0.754
0.0176	-6.0	93.1	0.348	0.158	0.702
0.0218	-10.1	88.0	0.422	0.144	0.659
0.0257	-13.4	81.8	0.466	0.131	0.635
0.0300	-16.5	75.8	0.496	0.121	0.619
0.0340	-18.8	69.4	0.490	0.113	0.630
0.0380	-20.2	62.6	0.492	0.116	0.626
0.0423	-20.6	55.7	0.459	0.120	0.649
0.0465	-20.4	49.9	0.427	0.128	0.667
0.0519	-19.6	44.1	0.376	0.132	0.701
0.0574	-17.6	40.3	0.336	0.150	0.717
0.0629	-17.1	37.2	0.281	0.159	0.748
0.0696	-15.4	34.7	0.231	0.183	0.766
0.0765	-14.8	32.3	0.183	0.192	0.791
0.0847	-13.6	30.6	0.127	0.209	0.815
0.0930	-12.9	29.3	0.080	0.218	0.837
0.1011	-12.4	28.3	0.044	0.236	0.849
0.1094	-11.6	28.0	0.030	0.252	0.847
0.1204	-10.6	27.9	0.005	0.261	0.856
0.1339	-9.6	28.2	0.001	0.281	0.847
0.1476	-9.1	28.9	-0.004	0.295	0.842
0.1612	-8.5	29.4	-0.005	0.309	0.835
0.1751	-8.1	30.0	-0.010	0.319	0.831
0.2161	-6.0	31.2	-0.002	0.350	0.807
0.2571	-4.7	32.2	-0.001	0.362	0.799
0.3392	-3.1	33.6	-0.001	0.376	0.791
0.4214	-1.7	34.0	0.002	0.381	0.785
0.5056	-0.8	34.1	-0.001	0.386	0.784

Five-Hole Probe Data
(continued)

ANGULAR PLANE: 25.000 DEG
RADIUS/CYLINDER DIA: 0.681

Y/D	PHI DEG	THETA DEG	CPT	CPS	U/U ₀
0.0083	0.9	105.2	0.205	0.108	0.828
0.0129	-2.3	101.7	0.317	0.083	0.775
0.0178	-5.1	96.8	0.418	0.065	0.719
0.0226	-9.3	91.1	0.512	0.046	0.665
0.0264	-12.1	85.2	0.577	0.026	0.631
0.0305	-16.3	78.3	0.608	0.020	0.610
0.0347	-19.7	70.2	0.620	0.015	0.604
0.0389	-21.2	62.0	0.608	0.011	0.618
0.0430	-21.0	54.0	0.574	0.025	0.633
0.0482	-20.1	45.9	0.517	0.034	0.670
0.0540	-18.4	40.0	0.456	0.047	0.705
0.0623	-17.0	34.3	0.359	0.077	0.751
0.0703	-15.3	30.6	0.280	0.103	0.786
0.0785	-13.3	28.3	0.207	0.129	0.815
0.0866	-12.4	26.5	0.136	0.152	0.844
0.0952	-11.6	25.6	0.096	0.171	0.856
0.1059	-10.8	24.9	0.047	0.189	0.874
0.1197	-9.7	24.9	0.007	0.228	0.875
0.1334	-8.8	25.3	0.003	0.240	0.873
0.1470	-8.4	26.0	-0.007	0.260	0.864
0.1606	-8.1	26.7	-0.005	0.276	0.854
0.1744	-6.9	27.1	-0.007	0.285	0.850
0.2154	-5.3	28.5	0.000	0.322	0.823
0.2564	-4.3	29.7	-0.003	0.343	0.812
0.3386	-2.8	31.3	-0.004	0.360	0.802
0.4207	-1.8	31.7	-0.003	0.369	0.797
0.5053	-0.9	31.8	0.002	0.371	0.792

Five-Hole Probe Data
(continued)

ANGULAR PLANE: 25.000 DEG
RADIUS/CYLINDER DIA: 0.702

Y/D	PHI DEG	THETA DEG	CPT	CPS	U/U ₀
0.0083	3.5	105.7	0.274	0.025	0.838
0.0110	2.4	104.7	0.345	0.009	0.804
0.0138	2.0	102.7	0.421	-0.003	0.763
0.0170	2.3	100.4	0.498	-0.022	0.724
0.0201	1.0	96.7	0.577	-0.039	0.680
0.0232	0.3	92.6	0.653	-0.051	0.631
0.0260	-2.0	87.3	0.711	-0.058	0.589
0.0288	-1.6	81.2	0.778	-0.085	0.554
0.0315	-5.3	75.2	0.820	-0.106	0.535
0.0343	-6.1	68.4	0.829	-0.103	0.523
0.0371	-12.4	61.3	0.847	-0.105	0.508
0.0398	-12.4	54.7	0.821	-0.114	0.542
0.0426	-11.6	47.9	0.798	-0.106	0.555
0.0468	-12.4	40.4	0.689	-0.081	0.625
0.0522	-11.2	34.3	0.604	-0.050	0.668
0.0577	-10.2	30.9	0.515	-0.016	0.709
0.0632	-9.4	28.1	0.421	0.015	0.751
0.0684	-9.5	26.4	0.355	0.031	0.783
0.0740	-9.5	25.5	0.301	0.050	0.806
0.0795	-8.8	24.2	0.260	0.075	0.815
0.0878	-8.6	23.4	0.178	0.105	0.847
0.0961	-8.3	22.5	0.123	0.128	0.865
0.1041	-8.2	22.1	0.087	0.148	0.875
0.1123	-7.0	21.9	0.055	0.179	0.875
0.1232	-6.2	21.9	0.021	0.210	0.877
0.1342	-6.4	22.3	0.014	0.228	0.871
0.1477	-5.6	23.0	0.000	0.251	0.865
0.1616	-5.5	23.6	0.003	0.266	0.855
0.1754	-5.2	24.2	0.001	0.282	0.847
0.2165	-4.4	25.8	-0.004	0.313	0.831
0.2574	-3.9	26.9	-0.003	0.329	0.821
0.3397	-2.5	28.3	0.002	0.348	0.806
0.4218	-1.6	28.9	-0.005	0.357	0.804
0.5065	-0.6	29.0	-0.001	0.360	0.801

Five-Hole Probe Data
(continued)

ANGULAR PLANE: 25.000 DEG
RADIUS/CYLINDER DIA: 0.723

Y/D	PHI DEG	THETA DEG	CPT	CPS	U/Uo
0.0083	5.0	101.9	0.373	-0.031	0.811
0.0118	4.9	100.8	0.425	-0.036	0.782
0.0153	6.5	99.2	0.502	-0.049	0.740
0.0187	6.9	96.2	0.579	-0.059	0.693
0.0215	8.7	92.6	0.649	-0.088	0.663
0.0244	9.9	88.5	0.706	-0.094	0.623
0.0271	9.3	83.5	0.766	-0.108	0.584
0.0298	10.5	77.3	0.814	-0.127	0.559
0.0326	4.9	71.8	0.857	-0.142	0.533
0.0354	7.5	63.2	0.873	-0.129	0.506
0.0381	3.9	37.9	0.849	-0.142	0.541
0.0408	-3.1	51.1	0.886	-0.154	0.519
0.0450	-1.8	41.8	0.781	-0.103	0.567
0.0492	-4.2	35.9	0.679	-0.094	0.643
0.0547	-3.6	30.9	0.580	-0.043	0.680
0.0602	-3.7	28.0	0.507	-0.026	0.720
0.0653	-5.4	25.7	0.438	0.003	0.747
0.0709	-3.9	24.2	0.363	0.032	0.778
0.0765	-4.0	23.6	0.316	0.075	0.780
0.0820	-4.3	22.4	0.261	0.080	0.811
0.0876	-4.1	21.6	0.224	0.108	0.818
0.0954	-4.6	20.9	0.157	0.122	0.849
0.1040	-4.3	20.2	0.108	0.148	0.863
0.1121	-4.3	20.0	0.069	0.169	0.872
0.1232	-4.5	19.9	0.025	0.189	0.887
0.1341	-4.1	20.0	0.006	0.214	0.883
0.1477	-4.2	20.6	-0.002	0.233	0.877
0.1616	-4.1	21.4	-0.002	0.251	0.867
0.1751	-4.1	22.1	-0.002	0.262	0.860
0.2161	-3.9	23.6	-0.003	0.296	0.841
0.2570	-3.1	25.2	-0.004	0.312	0.832
0.3392	-2.1	26.1	-0.005	0.334	0.819
0.4214	-1.5	26.8	0.000	0.342	0.811
0.5061	-0.8	26.8	0.002	0.344	0.808

Five-Hole Probe Data
(continued)

ANGULAR PLANE: 25.000 DEG
RADIUS/CYLINDER DIA: 0.745

Y/D	PHI DEG	THETA DEG	CPT	CPS	U/U ₀
0.0083	4.5	89.3	0.518	0.072	0.640
0.0108	2.6	89.9	0.505	0.040	0.675
0.0136	5.6	89.4	0.523	0.057	0.648
0.0167	7.0	87.7	0.549	0.054	0.629
0.0198	8.4	84.5	0.581	0.032	0.622
0.0229	9.6	80.4	0.603	0.038	0.599
0.0259	11.0	76.1	0.635	0.021	0.587
0.0285	11.9	70.7	0.654	-0.001	0.589
0.0312	14.2	65.3	0.670	0.006	0.569
0.0339	9.4	60.6	0.680	0.014	0.552
0.0367	9.8	54.9	0.654	0.013	0.577
0.0395	10.6	49.3	0.654	0.005	0.584
0.0437	7.8	42.0	0.588	0.044	0.606
0.0478	8.4	37.2	0.549	0.049	0.634
0.0519	5.4	33.9	0.487	0.075	0.662
0.0560	4.5	31.0	0.456	0.081	0.680
0.0616	3.6	28.0	0.390	0.092	0.720
0.0684	1.6	25.8	0.318	0.115	0.753
0.0764	0.9	23.4	0.253	0.128	0.787
0.0847	-0.3	21.9	0.207	0.150	0.802
0.0930	-1.0	21.2	0.153	0.170	0.823
0.1010	-1.5	20.5	0.113	0.186	0.837
0.1094	-2.3	19.8	0.064	0.195	0.861
0.1177	-1.9	19.5	0.037	0.206	0.869
0.1259	-2.4	19.4	0.020	0.219	0.872
0.1367	-2.7	19.5	0.001	0.231	0.876
0.1478	-2.8	19.8	0.003	0.244	0.868
0.1613	-3.1	20.2	-0.008	0.256	0.867
0.1752	-3.3	20.5	-0.003	0.268	0.857
0.2162	-3.2	21.6	-0.003	0.292	0.844
0.2572	-2.8	22.5	0.000	0.308	0.832
0.3392	-1.8	24.0	-0.002	0.328	0.820
0.4213	-1.2	24.6	-0.001	0.335	0.816
0.5061	-0.8	24.7	0.000	0.342	0.811

Five-Hole Probe Data
(continued)

ANGULAR PLANE: 25.000 DEG
RADIUS/CYLINDER DIA: 0.766

Y/D	PHI DEG	THETA DEG	CPT	CPS	U/U ₀
0.0085	3.9	79.9	0.548	0.118	0.578
0.0120	3.6	80.8	0.537	0.104	0.600
0.0169	3.6	79.5	0.554	0.093	0.594
0.0217	6.8	74.8	0.573	0.089	0.581
0.0259	9.6	69.7	0.588	0.080	0.576
0.0297	11.2	64.6	0.585	0.084	0.575
0.0338	10.9	58.5	0.600	0.083	0.562
0.0380	10.4	52.1	0.567	0.082	0.592
0.0421	10.4	45.6	0.576	0.079	0.587
0.0463	10.3	40.1	0.522	0.086	0.626
0.0532	8.2	33.6	0.465	0.106	0.656
0.0601	6.3	29.1	0.412	0.120	0.685
0.0681	4.7	25.0	0.315	0.139	0.738
0.0764	2.9	23.1	0.253	0.152	0.771
0.0843	1.7	21.5	0.190	0.158	0.807
0.0928	1.0	19.8	0.140	0.164	0.834
0.1009	0.1	19.0	0.094	0.181	0.851
0.1092	-0.5	18.5	0.061	0.187	0.867
0.1175	-1.0	18.1	0.034	0.192	0.880
0.1253	-1.4	18.0	0.023	0.200	0.881
0.1340	-1.5	18.0	0.005	0.214	0.884
0.1475	-1.9	18.2	-0.005	0.225	0.883
0.1611	-2.3	18.6	-0.009	0.235	0.880
0.1749	-2.4	18.8	-0.006	0.245	0.872
0.2160	-2.6	19.8	-0.005	0.272	0.856
0.2571	-2.6	20.7	-0.001	0.286	0.846
0.3392	-2.0	22.2	-0.003	0.309	0.832
0.4212	-1.4	22.6	-0.001	0.318	0.826
0.5061	-0.9	22.8	-0.001	0.323	0.823

Five-Hole Probe Data
(continued)

ANGULAR PLANE: 25.000 DEG
RADIUS/CYLINDER DIA: 0.787

Y/D	PHI DEG	THETA DEG	CPT	CPS	U/U ₀
0.0085	2.7	71.1	0.501	0.207	0.540
0.0140	0.8	71.4	0.514	0.180	0.553
0.0196	1.5	68.3	0.521	0.171	0.556
0.0250	1.8	63.0	0.520	0.158	0.567
0.0302	3.6	58.1	0.515	0.168	0.563
0.0358	5.3	51.1	0.502	0.171	0.572
0.0413	4.8	45.4	0.475	0.182	0.586
0.0469	5.3	39.8	0.437	0.189	0.612
0.0538	5.0	34.4	0.390	0.197	0.643
0.0606	5.0	30.3	0.348	0.196	0.675
0.0686	4.0	26.5	0.299	0.204	0.705
0.0769	3.8	23.8	0.244	0.204	0.743
0.0852	2.9	21.8	0.197	0.207	0.772
0.0934	2.0	20.3	0.156	0.210	0.796
0.1015	1.5	19.3	0.114	0.211	0.822
0.1098	0.9	18.4	0.078	0.212	0.843
0.1178	0.5	17.8	0.045	0.214	0.861
0.1263	0.2	17.4	0.020	0.220	0.871
0.1343	-0.1	17.3	0.007	0.225	0.877
0.1482	-0.5	17.4	-0.004	0.232	0.879
0.1617	-0.8	17.8	-0.005	0.237	0.876
0.1750	-1.1	18.0	-0.003	0.245	0.871
0.2166	-1.7	18.6	-0.003	0.266	0.859
0.2577	-1.7	19.6	-0.001	0.278	0.850
0.3398	-1.5	20.7	-0.001	0.297	0.839
0.4219	-1.2	21.1	0.002	0.306	0.832
0.5065	-0.7	21.2	0.000	0.311	0.831

Five-Hole Probe Data
(continued)

ANGULAR PLANE: 25.000 DEG
RADIUS/CYLINDER DIA: 0.809

Y/D	PHI DEG	THETA DEG	CPT	CPS	U/U ₀
0.0084	1.1	67.0	0.482	0.240	0.527
0.0140	-0.2	64.0	0.487	0.221	0.540
0.0194	0.4	59.5	0.487	0.211	0.550
0.0246	-0.3	55.0	0.484	0.206	0.557
0.0302	0.1	50.1	0.472	0.214	0.560
0.0356	0.7	45.6	0.444	0.207	0.592
0.0412	2.6	41.5	0.415	0.211	0.612
0.0468	3.6	37.1	0.387	0.213	0.633
0.0547	3.6	32.6	0.360	0.222	0.647
0.0630	3.3	28.7	0.302	0.226	0.686
0.0713	2.9	25.4	0.261	0.224	0.718
0.0796	3.4	23.1	0.216	0.222	0.725
0.0907	2.3	20.8	0.156	0.228	0.785
0.1014	1.8	19.0	0.116	0.222	0.814
0.1125	1.2	17.9	0.059	0.223	0.847
0.1235	0.9	17.1	0.035	0.223	0.861
0.1344	0.7	16.7	0.016	0.221	0.873
0.1480	0.1	16.6	-0.004	0.231	0.879
0.1615	0.0	16.9	-0.004	0.235	0.877
0.1754	-0.5	17.1	-0.003	0.239	0.874
0.2165	-1.2	17.6	-0.003	0.255	0.865
0.2575	-1.5	18.2	-0.006	0.270	0.858
0.3397	-1.6	19.4	0.002	0.285	0.844
0.4218	-1.2	19.6	0.000	0.294	0.841
0.5063	-0.8	19.7	0.007	0.289	0.839

Five-Hole Probe Data
(continued)

ANGULAR PLANE: 25.000 DEG
RADIUS/CYLINDER DIA: 0.851

Y/D	FHI DEG	THETA DEG	CPT	CPS	U/Uo
0.0085	2.6	61.1	0.492	0.251	0.507
0.0125	1.0	57.5	0.492	0.238	0.520
0.0167	0.4	53.1	0.479	0.238	0.532
0.0208	0.5	48.8	0.470	0.236	0.542
0.0249	0.8	45.1	0.451	0.237	0.559
0.0289	0.5	42.1	0.432	0.237	0.574
0.0337	1.1	38.4	0.420	0.238	0.584
0.0384	1.1	35.8	0.400	0.238	0.601
0.0440	1.5	32.2	0.370	0.235	0.628
0.0523	1.6	28.7	0.332	0.238	0.657
0.0605	2.1	25.9	0.294	0.241	0.682
0.0687	2.1	23.6	0.261	0.241	0.706
0.0769	2.0	21.2	0.222	0.236	0.736
0.0851	2.2	20.0	0.185	0.233	0.763
0.0934	1.9	18.6	0.139	0.233	0.792
0.1017	1.7	17.6	0.114	0.232	0.809
0.1097	1.7	16.9	0.079	0.234	0.829
0.1208	1.4	15.9	0.045	0.232	0.851
0.1346	1.2	15.2	0.014	0.228	0.871
0.1481	0.9	15.0	-0.004	0.231	0.879
0.1615	0.7	15.1	-0.012	0.231	0.884
0.1755	0.6	15.2	-0.009	0.233	0.881
0.2165	-0.2	15.6	-0.008	0.241	0.876
0.2576	-0.8	16.0	-0.007	0.249	0.871
0.3399	-1.0	17.1	-0.004	0.264	0.860
0.4218	-0.6	17.3	-0.001	0.270	0.855
0.5065	-0.5	17.5	-0.005	0.274	0.855

Five-Hole Probe Data
(continued)

ANGULAR PLANE: 25.000 DEG
RADIUS/CYLINDER DIA: 0.894

Y/D	PHI DEG	THETA DEG	CPT	CPS	U/Uo
0.0086	1.6	52.9	0.506	0.242	0.502
0.0131	1.1	48.3	0.485	0.237	0.528
0.0172	0.8	44.8	0.473	0.234	0.541
0.0228	1.1	39.7	0.442	0.235	0.568
0.0280	0.9	36.1	0.423	0.234	0.586
0.0336	1.3	33.2	0.391	0.236	0.611
0.0419	1.7	29.1	0.349	0.234	0.646
0.0499	1.8	26.5	0.309	0.234	0.676
0.0584	1.9	24.2	0.273	0.234	0.702
0.0664	2.0	22.0	0.232	0.233	0.732
0.0747	2.0	20.7	0.200	0.229	0.755
0.0831	2.1	19.4	0.164	0.230	0.778
0.0913	1.9	18.0	0.129	0.224	0.804
0.0993	1.9	17.1	0.098	0.223	0.823
0.1076	1.8	16.3	0.070	0.220	0.843
0.1186	1.7	15.6	0.038	0.218	0.863
0.1321	1.6	15.1	0.011	0.216	0.879
0.1459	1.3	15.0	-0.002	0.214	0.888
0.1595	1.0	15.1	-0.004	0.213	0.889
0.1733	0.7	15.1	-0.003	0.214	0.888
0.2144	.0	15.1	-0.003	0.217	0.887
0.2554	-0.6	15.4	0.001	0.221	0.882
0.3376	-0.9	15.8	0.001	0.230	0.877
0.4197	-0.8	16.0	0.000	0.237	0.873
0.5043	-0.8	16.2	0.000	0.241	0.871

Five-Hole Probe Data
(continued)

ANGULAR PLANE: 25.000 DEG
RADIUS/CYLINDER DIA: 0.936

Y/D	PHI DEG	THETA DEG	CPT	CPS	U/U ₀
0.0086	1.7	44.4	0.501	0.243	0.506
0.0142	0.7	39.6	0.469	0.239	0.540
0.0200	0.6	35.2	0.441	0.238	0.567
0.0256	0.8	32.2	0.411	0.237	0.593
0.0336	1.0	28.5	0.381	0.236	0.619
0.0419	1.1	25.5	0.335	0.234	0.657
0.0502	1.3	22.9	0.301	0.231	0.683
0.0584	1.4	21.2	0.263	0.231	0.712
0.0664	1.3	19.5	0.229	0.228	0.737
0.0747	1.3	18.3	0.185	0.229	0.766
0.0831	1.4	17.1	0.152	0.224	0.790
0.0913	1.5	16.3	0.117	0.221	0.814
0.0993	1.3	15.6	0.081	0.223	0.834
0.1076	1.4	15.1	0.055	0.219	0.852
0.1186	1.4	14.4	0.028	0.215	0.870
0.1321	1.3	14.1	0.003	0.215	0.884
0.1459	1.2	14.0	-0.003	0.212	0.890
0.1595	0.9	14.0	-0.004	0.212	0.890
0.1732	0.7	14.0	-0.006	0.210	0.892
0.2144	0.1	13.9	-0.003	0.211	0.890
0.2554	-0.4	14.1	0.002	0.208	0.889
0.3376	-0.6	14.4	-0.001	0.218	0.885
0.4196	-0.9	14.5	0.001	0.222	0.881
0.5043	-0.9	14.7	0.001	0.225	0.880

Five-Hole Probe Data
(continued)

ANGULAR PLANE: 45.000 DEG
RADIUS/CYLINDER DIA: 0.553

Y/D	PHI DEG	THETA DEG	CPT	CPS	U/U ₀
0.0083	0.3	46.6	-0.001	-0.552	1.234
0.0122	-1.9	46.1	0.004	-0.558	1.246
0.0163	-3.2	44.9	0.013	-0.573	1.249
0.0219	-4.5	43.8	0.009	-0.592	1.258
0.0274	-5.3	42.9	0.011	-0.599	1.260
0.0330	-6.0	42.4	0.015	-0.606	1.261
0.0412	-7.5	41.5	-0.004	-0.620	1.274
0.0494	-8.1	40.7	-0.013	-0.630	1.282
0.0575	-8.3	40.0	-0.011	-0.635	1.283
0.0657	-8.3	39.2	-0.011	-0.641	1.286
0.0792	-8.3	38.9	-0.013	-0.653	1.291
0.0930	-8.2	38.2	-0.015	-0.658	1.293
0.1066	-8.2	37.8	-0.012	-0.661	1.293
0.1204	-8.0	37.6	-0.015	-0.670	1.298
0.1342	-7.4	37.5	-0.010	-0.671	1.297
0.1477	-7.0	37.5	-0.009	-0.674	1.297
0.1612	-6.3	37.4	-0.005	-0.673	1.295
0.1750	-5.8	37.3	-0.004	-0.675	1.296
0.2574	-4.1	37.5	0.002	-0.695	1.302
0.3402	-3.0	37.9	0.000	-0.073	1.305
0.4222	-1.9	38.1	0.001	-0.700	1.303
0.5058	-1.2	38.1	-0.001	-0.693	1.302

Five-Hole Probe Data
(continued)

ANGULAR PLANE: 45.000 DEG
RADIUS/CYLINDER DIA: 0.596

Y/D	PHI DEG	THETA DEG	CPT	CPS	U/Uo
0.0082	0.9	54.2	0.029	-0.378	1.161
0.0126	-2.1	52.6	0.057	-0.417	1.166
0.0167	-3.8	50.6	0.078	-0.435	1.165
0.0208	-4.7	48.4	0.090	-0.444	1.164
0.0250	-5.8	46.8	0.099	-0.446	1.161
0.0291	-7.0	45.4	0.094	-0.457	1.167
0.0331	-8.0	44.3	0.090	-0.471	1.175
0.0372	-8.5	42.7	0.086	-0.476	1.179
0.0413	-8.7	41.5	0.081	-0.494	1.189
0.0497	-9.3	39.5	0.073	-0.503	1.196
0.0579	-9.6	37.8	0.054	-0.512	1.207
0.0686	-9.8	35.8	0.035	-0.523	1.220
0.0796	-9.6	34.6	0.015	-0.529	1.230
0.0935	-9.4	33.9	0.002	-0.540	1.240
0.1070	-9.0	33.4	-0.007	-0.547	1.246
0.1208	-8.6	33.1	-0.006	-0.555	1.249
0.1343	-8.3	33.1	-0.012	-0.560	1.254
0.1471	-8.0	33.1	-0.012	-0.565	1.255
0.1624	-7.2	33.0	0.008	-0.566	1.254
0.1761	-6.2	32.9	0.000	-0.564	1.251
0.1887	-5.7	33.0	-0.001	-0.530	1.237
0.2588	-3.9	33.5	-0.001	-0.566	1.252
0.3401	-2.5	34.2	-0.001	-0.579	1.257
0.4218	-1.7	34.4	-0.003	-0.579	1.258
0.5054	-0.8	34.3	-0.002	-0.559	1.249

Five-Hole Probe Data
(continued)

ANGULAR PLANE: 45.000 DEG
RADIUS/CYLINDER DIA: 0.638

Y/D	PHI DEG	THETA DEG	CPT	CPS	U/Uo
0.0083	-0.3	62.6	0.075	-0.382	1.143
0.0125	-2.2	60.0	0.127	-0.391	1.124
0.0173	-3.8	56.2	0.183	-0.392	1.100
0.0219	-5.0	53.4	0.213	-0.396	1.088
0.0263	-6.3	50.6	0.234	-0.404	1.082
0.0302	-8.0	48.8	0.233	-0.413	1.086
0.0343	-8.5	46.4	0.237	-0.417	1.086
0.0385	-9.1	44.3	0.237	-0.423	1.089
0.0426	-9.4	42.5	0.232	-0.425	1.092
0.0466	-9.8	40.3	0.222	-0.427	1.098
0.0551	-10.3	37.3	0.192	-0.436	1.115
0.0631	-10.7	34.8	0.154	-0.443	1.135
0.0714	-10.7	32.5	0.121	-0.448	1.152
0.0796	-10.5	31.2	0.090	-0.451	1.167
0.0931	-9.9	29.5	0.038	-0.450	1.188
0.1069	-9.5	28.6	0.007	-0.451	1.202
0.1206	-9.0	28.2	-0.007	-0.448	1.206
0.1343	-8.4	28.3	-0.016	-0.446	1.209
0.1481	-7.8	28.5	-0.014	-0.441	1.206
0.1616	-6.9	28.6	-0.010	-0.433	1.201
0.1751	-6.1	28.7	-0.006	-0.431	1.199
0.2161	-4.8	29.1	-0.002	-0.417	1.191
0.2575	-3.9	29.8	-0.005	-0.409	1.189
0.3399	-2.6	30.6	-0.004	-0.401	1.185
0.4218	-1.7	30.8	0.000	-0.393	1.181
0.5062	-1.2	30.9	-0.005	-0.385	1.179

Five-Hole Probe Data
(continued)

ANGULAR PLANE: 45.000 DEG
RADIUS/CYLINDER DIA: 0.681

Y/D	PHI DEG	THETA DEG	CPT	CPS	U/U ₀
0.0086	0.7	69.9	0.133	-0.405	1.128
0.0141	-2.7	66.5	0.243	-0.449	1.098
0.0197	-4.7	62.0	0.350	-0.456	1.051
0.0238	-6.8	59.2	0.402	-0.476	1.036
0.0279	-8.6	55.9	0.435	-0.481	1.023
0.0321	-9.4	52.3	0.468	-0.485	1.008
0.0359	-10.2	49.4	0.492	-0.491	0.999
0.0402	-11.3	45.2	0.493	-0.496	1.001
0.0446	-11.6	41.5	0.484	-0.502	1.009
0.0525	-11.5	36.3	0.433	-0.507	1.036
0.0608	-10.7	31.9	0.357	-0.492	1.065
0.0688	-10.2	29.2	0.289	-0.487	1.094
0.0770	-9.9	27.3	0.242	-0.479	1.112
0.0854	-9.5	25.8	0.187	-0.465	1.130
0.0937	-9.0	24.8	0.132	-0.450	1.148
0.1144	-8.2	23.3	0.051	-0.428	1.173
0.1345	-6.7	22.9	0.004	-0.401	1.182
0.1570	-5.4	23.5	-0.006	-0.377	1.176
0.1771	-4.7	24.2	-0.002	-0.362	1.168
0.2586	-3.1	25.9	-0.003	-0.330	1.155
0.3412	-2.2	27.2	-0.005	-0.317	1.150
0.4231	-1.4	27.6	0.000	-0.309	1.144
0.5053	-1.0	27.7	-0.001	-0.303	1.142

Five-Hole Probe Data
(continued)

ANGULAR PLANE: 45.000 DEG
RADIUS/CYLINDER DIA: 0.702

Y/D	PHI DEG	THETA DEG	CPT	CPS	U/U ₀
0.0085	1.3	73.3	0.196	-0.480	1.134
0.0126	-0.7	71.9	0.288	-0.503	1.102
0.0168	-2.1	69.3	0.392	-0.528	1.066
0.0207	-3.7	66.3	0.481	-0.538	1.028
0.0247	-5.1	63.3	0.570	-0.566	0.998
0.0289	-8.2	59.2	0.628	-0.577	0.974
0.0330	-8.9	54.9	0.682	-0.600	0.958
0.0371	-10.1	49.9	0.710	-0.603	0.945
0.0413	-11.0	44.3	0.693	-0.613	0.959
0.0454	-11.7	39.5	0.670	-0.606	0.967
0.0493	-11.3	35.8	0.627	-0.603	0.988
0.0537	-10.5	31.9	0.549	-0.580	1.015
0.0575	-10.3	30.2	0.511	-0.571	1.030
0.0618	-9.8	28.1	0.448	-0.557	1.053
0.0659	-9.2	26.4	0.402	-0.545	1.069
0.0770	-8.5	24.1	0.293	-0.505	1.101
0.0852	-8.2	23.2	0.237	-0.480	1.115
0.0934	-8.0	22.2	0.188	-0.461	1.128
0.1069	-6.7	21.1	0.117	-0.428	1.145
0.1208	-5.8	20.5	0.066	-0.400	1.155
0.1342	-5.2	20.4	0.022	-0.389	1.169
0.1481	-4.7	21.0	0.002	-0.365	1.167
0.1617	-4.4	21.7	-0.008	-0.355	1.167
0.1755	-4.0	22.2	-0.009	-0.340	1.161
0.2162	-3.4	23.3	-0.009	-0.318	1.152
0.2577	-3.0	24.1	-0.003	-0.307	1.145
0.3394	-2.3	25.1	0.001	-0.288	1.134
0.4218	-1.6	25.5	-0.005	-0.280	1.133
0.5058	-1.2	25.7	0.000	-0.276	1.130

Five-Hole Probe Data
(continued)

ANGULAR PLANE: 45.000 DEG
RADIUS/CYLINDER DIA: 0.723

Y/D	PHI DEG	THETA DEG	CPT	CPS	U/U ₀
0.0085	2.6	74.1	0.269	-0.531	1.123
0.0114	1.6	73.2	0.329	-0.550	1.105
0.0155	1.2	71.4	0.421	-0.564	1.070
0.0211	0.6	68.3	0.568	-0.594	1.013
0.0252	-0.4	64.7	0.657	-0.626	0.984
0.0293	-1.4	60.5	0.748	-0.645	0.947
0.0331	-2.5	56.0	0.820	-0.667	0.921
0.0361	-4.3	50.9	0.849	-0.677	0.910
0.0387	-4.8	46.7	0.859	-0.681	0.906
0.0415	-5.5	43.2	0.867	-0.698	0.912
0.0442	-5.9	38.6	0.826	-0.683	0.926
0.0470	-7.2	34.5	0.759	-0.663	0.951
0.0497	-7.4	32.1	0.723	-0.660	0.968
0.0539	-6.8	28.7	0.636	-0.621	0.992
0.0577	-6.4	26.7	0.596	-0.615	1.010
0.0662	-5.7	23.0	0.456	-0.559	1.051
0.0743	-5.4	21.5	0.366	-0.528	1.078
0.0826	-5.2	20.6	0.296	-0.492	1.094
0.0933	-4.7	19.9	0.221	-0.452	1.109
0.1074	-4.4	19.3	0.149	-0.417	1.126
0.1208	-4.2	18.9	0.093	-0.390	1.139
0.1344	-4.0	18.9	0.039	-0.369	1.153
0.1485	-3.6	19.3	0.009	-0.350	1.158
0.1620	-3.4	19.8	-0.004	-0.337	1.158
0.1756	-3.2	20.4	-0.010	-0.325	1.156
0.2166	-3.0	21.6	-0.006	-0.299	1.142
0.2580	-2.9	22.4	-0.003	-0.288	1.137
0.3401	-2.0	23.7	-0.003	-0.267	1.127
0.4223	-1.4	24.2	-0.005	-0.258	1.124
0.5064	-1.1	24.4	-0.001	-0.251	1.119

Five-Hole Probe Data
(continued)

ANGULAR PLANE: 45.000 DEG
RADIUS/CYLINDER DIA: 0.745

Y/D	PHI DEG	THETA DEG	CPT	CPS	U/U _c
0.0090	4.4	68.9	0.435	-0.531	1.047
0.0118	4.2	69.3	0.438	-0.544	1.052
0.0159	4.6	68.8	0.488	-0.557	1.034
0.0200	5.8	66.7	0.558	-0.574	1.007
0.0239	5.8	64.4	0.636	-0.591	0.978
0.0281	6.4	60.4	0.695	-0.608	0.956
0.0322	6.3	55.2	0.765	-0.622	0.926
0.0364	6.1	49.9	0.802	-0.632	0.911
0.0405	5.3	43.9	0.824	-0.635	0.901
0.0447	3.7	37.6	0.791	-0.631	0.917
0.0486	2.0	33.1	0.727	-0.613	0.941
0.0527	2.1	29.5	0.679	-0.602	0.961
0.0562	0.7	26.0	0.574	-0.567	0.996
0.0664	-0.2	22.9	0.464	-0.522	1.029
0.0747	-0.9	21.1	0.387	-0.484	1.047
0.0830	-1.2	19.8	0.312	-0.451	1.067
0.0939	-1.9	18.8	0.242	-0.421	1.085
0.1076	-2.1	18.0	0.156	-0.386	1.109
0.1214	-2.1	17.6	0.090	-0.361	1.128
0.1350	-2.2	17.7	0.032	-0.337	1.142
0.1485	-2.2	18.0	0.006	-0.327	1.149
0.1622	-2.2	18.6	-0.008	-0.311	1.148
0.1759	-2.3	19.2	-0.007	-0.302	1.144
0.2170	-2.6	20.7	-0.003	-0.277	1.131
0.2582	-2.4	21.5	-0.004	-0.265	1.126
0.3394	-2.0	22.7	-0.007	-0.244	1.118
0.4225	-1.5	22.8	-0.003	-0.237	1.114
0.5064	-1.2	23.4	-0.006	-0.225	1.110

Five-Hole Probe Data
(continued)

ANGULAR PLANE: 45.000 DEG
RADIUS/CYLINDER DIA: 0.766

Y/D	PHI DEG	THETA DEG	CPT	CPS	U/U ₀
0.0093	4.8	61.2	0.547	-0.434	0.941
0.0120	4.2	62.4	0.517	-0.452	0.967
0.0155	5.2	62.5	0.521	-0.462	0.970
0.0213	6.6	61.2	0.559	-0.463	0.951
0.0291	8.3	55.5	0.619	-0.478	0.927
0.0373	9.2	47.3	0.644	-0.485	0.917
0.0457	7.8	37.4	0.621	-0.471	0.921
0.0540	6.3	31.0	0.558	-0.456	0.948
0.0623	4.9	26.3	0.478	-0.424	0.973
0.0703	3.4	23.6	0.404	-0.398	0.996
0.0787	2.1	21.4	0.345	-0.376	1.015
0.0869	1.4	20.7	0.290	-0.384	1.046
0.0951	1.1	19.3	0.243	-0.385	1.069
0.1037	0.3	18.4	0.171	-0.334	1.078
0.1119	0.1	18.0	0.112	-0.331	1.104
0.1349	-0.5	17.7	0.020	-0.312	1.136
0.1556	-1.0	18.2	-0.001	-0.278	1.131
0.1768	-1.4	19.1	-0.014	-0.276	1.136
0.2585	-1.8	21.0	-0.011	-0.240	1.118
0.3402	-1.5	21.9	-0.003	-0.217	1.105
0.4229	-1.2	22.4	-0.003	-0.210	1.101
0.5047	-0.9	22.7	-0.004	-0.205	1.100

Five-Hole Probe Data
(continued)

ANGULAR PLANE: 45.000 DEG
RADIUS/CYLINDER DIA: 0.787

```
=====
```

Y/D	PHI DEG	THETA DEG	CPT	CPS	U/U ₀
0.0088	2.9	52.6	0.545	-0.330	0.886
0.0116	2.3	53.6	0.538	-0.359	0.906
0.0156	2.2	54.4	0.531	-0.365	0.913
0.0197	3.3	53.9	0.533	-0.371	0.915
0.0278	5.0	50.5	0.537	-0.369	0.912
0.0361	6.3	44.9	0.542	-0.368	0.909
0.0443	6.6	38.2	0.521	-0.355	0.913
0.0526	6.3	32.6	0.476	-0.348	0.934
0.0607	5.4	28.4	0.427	-0.333	0.952
0.0689	4.5	25.0	0.383	-0.323	0.970
0.0772	3.6	22.7	0.319	-0.316	0.999
0.0854	2.7	20.8	0.271	-0.306	1.017
0.0938	2.1	19.8	0.211	-0.303	1.045
0.1074	1.4	18.1	0.128	-0.292	1.079
0.1210	0.7	17.2	0.060	-0.282	1.105
0.1347	0.1	16.9	0.018	-0.273	1.120
0.1485	-0.3	17.2	0.001	-0.267	1.125
0.1621	-0.5	17.5	-0.006	-0.256	1.123
0.1759	-0.9	18.0	-0.007	-0.250	1.122
0.2170	-1.4	19.1	-0.004	-0.232	1.112
0.2572	-1.5	19.7	-0.003	-0.222	1.107
0.3391	-1.6	20.7	-0.001	-0.205	1.098
0.4218	-1.4	21.1	0.000	-0.192	1.092
0.5051	-1.1	21.3	-0.003	-0.186	1.090

Five-Hole Probe Data
(continued)

ANGULAR PLANE: 45.000 DEG
RADIUS/CYLINDER DIA: 0.809

Y/D	PHI DEG	THETA DEG	CPT	CPS	U/U ₀
0.0090	2.3	48.4	0.506	-0.240	0.857
0.0119	0.6	49.2	0.497	-0.262	0.875
0.0147	0.2	49.4	0.499	-0.272	0.880
0.0203	0.6	49.2	0.501	-0.294	0.891
0.0286	1.0	46.1	0.496	-0.295	0.894
0.0368	2.0	42.2	0.482	-0.291	0.899
0.0452	3.3	37.4	0.462	-0.281	0.906
0.0518	3.7	33.6	0.442	-0.275	0.913
0.0607	3.9	29.5	0.398	-0.262	0.929
0.0690	4.1	26.3	0.347	-0.260	0.955
0.0774	3.7	23.6	0.308	-0.256	0.974
0.0853	3.3	21.5	0.256	-0.255	0.999
0.0940	2.8	20.2	0.196	-0.255	1.029
0.1077	2.0	18.5	0.117	-0.252	1.065
0.1213	1.5	17.4	0.055	-0.249	1.093
0.1351	1.0	16.8	0.014	-0.242	1.108
0.1483	0.5	16.9	-0.001	-0.239	1.114
0.2580	-1.0	18.8	-0.011	-0.207	1.104
0.3399	-1.4	19.7	-0.002	-0.193	1.093
0.4225	-1.2	20.0	-0.003	-0.183	1.089
0.5069	-1.0	20.2	-0.005	-0.176	1.087

Five-Hole Probe Data
(continued)

ANGULAR PLANE: 45.000 DEG
RADIUS/CYLINDER DIA: 0.851

Y/D	PHI DEG	THETA DEG	CPT	CPS	U/U ₀
0.0118	0.8	44.4	0.476	-0.189	0.844
0.0174	-0.2	41.8	0.464	-0.195	0.855
0.0243	0.1	37.9	0.449	-0.198	0.865
0.0309	0.6	34.7	0.414	-0.199	0.886
0.0392	0.8	31.3	0.375	-0.197	0.907
0.0475	0.9	28.0	0.337	-0.194	0.926
0.0558	0.9	25.8	0.287	-0.191	0.951
0.0638	1.3	23.9	0.244	-0.191	0.973
0.0719	1.2	22.1	0.207	-0.194	0.993
0.0803	1.4	20.8	0.164	-0.192	1.014
0.0885	1.3	19.7	0.130	-0.194	1.032
0.0965	1.2	19.0	0.091	-0.195	1.051
0.1048	1.1	18.2	0.072	-0.197	1.061
0.1187	0.9	17.4	0.028	-0.196	1.081
0.1321	0.7	17.0	0.003	-0.196	1.093
0.1460	0.6	17.0	-0.003	-0.197	1.095
0.1595	0.3	17.0	-0.006	-0.198	1.097
0.1734	0.1	17.0	-0.006	-0.194	1.095
0.2145	-0.5	17.3	-0.003	-0.187	1.091
0.2556	-0.9	17.5	-0.001	-0.185	1.089
0.3373	-1.2	18.0	0.000	-0.175	1.084
0.4197	-1.1	18.1	0.002	-0.169	1.080
0.5039	-1.0	18.4	0.001	-0.161	1.077

Five-Hole Probe Data
(continued)

ANGULAR PLANE: 45.000 DEG
RADIUS/CYLINDER DIA: 0.894

Y/D	PHI DEG	THETA DEG	CPT	CPS	U/U ₀
0.0085	1.5	42.8	0.508	-0.147	0.799
0.0140	0.6	40.5	0.482	-0.161	0.825
0.0196	0.4	37.4	0.461	-0.163	0.838
0.0275	0.5	33.6	0.436	-0.166	0.854
0.0358	0.9	30.5	0.403	-0.163	0.872
0.0441	1.0	27.3	0.359	-0.162	0.896
0.0523	1.2	25.2	0.318	-0.166	0.921
0.0606	1.5	23.2	0.276	-0.165	0.942
0.0687	1.5	21.6	0.234	-0.163	0.964
0.0770	1.7	20.2	0.186	-0.165	0.989
0.0852	1.6	19.1	0.154	-0.167	1.066
0.0935	1.7	18.4	0.105	-0.170	1.032
0.1015	1.7	17.7	0.073	-0.171	1.048
0.1097	1.7	17.1	0.038	-0.173	1.006
0.1181	1.6	16.6	0.015	-0.173	1.076
0.1316	1.3	16.2	-0.002	-0.176	1.085
0.1522	1.1	16.0	-0.004	-0.178	1.087
0.1728	0.8	16.2	-0.007	-0.182	1.090
0.2139	0.1	16.2	-0.004	-0.178	1.087
0.2140	-0.3	16.6	-0.004	-0.174	1.085
0.2549	-0.7	16.7	0.002	-0.166	1.079
0.3371	-0.6	16.8	0.001	-0.161	1.077
0.4192	-0.8	17.1	0.001	-0.154	1.074
0.5037	-0.9	17.1	-0.001	-0.150	1.073

Five-Hole Probe Data
(continued)

ANGULAR PLANE: 45.000 DEG
RADIUS/CYLINDER DIA: 0.936

Y/D	PHI DEG	THETA DEG	CPT	CPS	U/U ₀
0.0092	1.0	36.9	0.506	-0.120	0.784
0.0120	0.6	35.7	0.489	-0.126	0.798
0.0202	0.3	31.7	0.440	-0.130	0.831
0.0283	0.5	28.8	0.403	-0.134	0.855
0.0366	0.7	26.2	0.355	-0.132	0.881
0.0449	0.5	24.0	0.315	-0.133	0.904
0.0532	0.9	22.5	0.274	-0.138	0.930
0.0614	0.7	20.9	0.223	-0.134	0.954
0.0694	0.9	19.6	0.193	-0.140	0.973
0.0777	0.7	18.7	0.146	-0.141	0.998
0.0861	0.8	17.9	0.106	-0.144	1.019
0.0943	1.0	17.3	0.073	-0.143	1.034
0.1023	0.9	16.7	0.042	-0.148	1.052
0.1106	0.7	16.4	0.021	-0.141	1.058
0.1189	0.6	16.0	0.004	-0.145	1.068
0.1325	0.6	15.8	-0.002	-0.148	1.072
0.1461	0.4	15.7	-0.002	-0.149	1.073
0.1598	0.3	15.6	-0.003	-0.147	1.073
0.1736	0.1	15.6	-0.005	-0.149	1.074
0.2147	-0.2	15.7	-0.005	-0.150	1.075
0.4199	-0.9	15.9	-0.001	-0.140	1.068
0.5042	-0.9	15.9	-0.001	-0.137	1.067

Five-Hole Probe Data
(continued)

ANGULAR PLANE: 45.000 DEG
RADIUS/CYLINDER DIA: 1.021

Y/D	PHI DEG	THETA DEG	CPT	CPS	U/U ₀
0.0078	1.8	29.6	0.514	-0.075	0.748
0.0098	1.0	28.9	0.487	-0.088	0.775
0.0154	0.0	27.1	0.435	-0.100	0.815
0.0210	-0.4	25.0	0.398	-0.104	0.840
0.0289	-0.4	22.8	0.345	-0.111	0.875
0.0371	-0.1	21.3	0.305	-0.109	0.896
0.0455	-0.1	19.6	0.254	-0.108	0.924
0.0537	-0.2	18.4	0.201	-0.111	0.954
0.0621	0.0	17.3	0.167	-0.112	0.972
0.0701	0.0	16.4	0.119	-0.111	0.996
0.0783	0.0	15.8	0.083	-0.109	1.013
0.0865	-0.1	15.3	0.061	-0.112	1.025
0.0948	-0.2	14.8	0.031	-0.118	1.043
0.1029	-0.1	14.6	0.018	-0.124	1.052
0.1108	-0.1	14.2	0.010	-0.117	1.052
0.1195	-0.2	13.9	-0.003	-0.116	1.058
0.1332	-0.1	13.6	-0.002	-0.119	1.059
0.1741	-0.1	13.2	-0.003	-0.122	1.061
0.2152	-0.2	13.2	-0.004	-0.123	1.062
0.2564	-0.4	13.1	-0.002	-0.123	1.061
0.3385	-0.9	13.1	0.002	-0.121	1.058
0.4205	-1.0	13.1	0.005	-0.117	1.055
0.5043	-0.9	13.3	0.000	-0.121	1.059

Five-Hole Probe Data
(continued)

ANGULAR PLANE: 45.000 DEG
RADIUS/CYLINDER DIA: 1.106

Y/D	PHI DEG	THETA DEG	CPT	CPS	U/U ₀
0.0077	1.7	25.1	0.502	-0.072	0.755
0.0096	0.9	24.5	0.478	-0.082	0.777
0.0153	0.0	23.0	0.435	-0.093	0.812
0.0207	-0.2	21.5	0.386	-0.097	0.843
0.0287	-0.3	19.8	0.355	-0.100	0.863
0.0370	-0.3	18.3	0.314	-0.097	0.885
0.0453	-0.2	17.0	0.275	-0.101	0.908
0.0536	-0.4	16.1	0.234	-0.100	0.930
0.0618	-0.3	15.2	0.193	-0.100	0.952
0.0699	-0.4	14.5	0.163	-0.098	0.967
0.0781	-0.3	13.9	0.132	-0.102	0.985
0.0864	-0.2	13.3	0.099	-0.105	1.003
0.0944	0.0	12.9	0.065	-0.102	1.018
0.1028	-0.2	12.5	0.045	-0.105	1.030
0.1110	-0.1	12.3	0.020	-0.105	1.042
0.1193	0.3	12.1	0.013	-0.108	1.046
0.1328	-0.1	11.8	-0.002	-0.105	1.052
0.1737	-0.1	11.7	-0.002	-0.102	1.051
0.2151	-0.5	11.7	0.000	-0.110	1.054
0.2562	-0.5	11.5	0.002	-0.112	1.053
0.3383	-0.5	11.6	-0.003	-0.108	1.054
0.4199	-0.8	11.4	-0.001	-0.106	1.053
0.5048	-0.7	11.4	-0.004	-0.102	1.052

Five-Hole Probe Data
(continued)

ANGULAR PLANE: 45.000 DEG
RADIUS/CYLINDER DIA: 1.191

Y/D	PHI DEG	THETA DEG	CPT	CPS	U/U ₆
0.0079	1.3	21.1	0.523	-0.063	0.735
0.0099	0.8	20.7	0.503	-0.067	0.751
0.0152	-0.3	19.3	0.449	-0.079	0.794
0.0210	0.0	17.8	0.404	-0.078	0.821
0.0290	-0.6	16.8	0.357	-0.082	0.851
0.0374	-0.7	15.7	0.306	-0.078	0.879
0.0456	-0.5	14.7	0.250	-0.083	0.913
0.0538	-0.6	13.9	0.228	-0.088	0.927
0.0621	-0.4	13.1	0.194	-0.086	0.944
0.0701	-0.5	12.5	0.163	-0.086	0.961
0.0785	-0.5	11.8	0.119	-0.081	0.981
0.0867	-0.8	11.5	0.102	-0.088	0.993
0.0947	-0.7	11.1	0.095	-0.090	0.997
0.1030	-0.4	10.8	0.054	-0.088	1.017
0.1113	-0.6	10.4	0.034	-0.085	1.026
0.1193	-0.3	10.2	0.025	-0.097	1.035
0.1331	-0.6	10.0	0.005	-0.093	1.043
0.1743	-0.2	10.0	-0.002	-0.092	1.045
0.2153	-0.4	9.7	0.003	-0.097	1.045
0.2562	-0.2	9.8	-0.001	-0.095	1.047
0.3386	-0.6	9.8	-0.001	-0.094	1.046
0.4206	-0.6	9.6	-0.004	-0.092	1.047
0.5048	-0.9	9.7	0.004	-0.092	1.043

Five-Hole Probe Data
(continued)

ANGULAR PLANE: 90.000 DEG
RADIUS/CYLINDER DIA: 0.553

Y/D	PHI DEG	THETA DEG	CPT	CPS	U/U ₀
0.0099	0.7	1.3	0.002	-1.832	1.682
0.0131	-0.4	1.3	0.003	-1.871	1.694
0.0203	-1.4	0.9	-0.002	-1.895	1.702
0.0266	-1.9	0.6	0.002	-1.910	1.705
0.0404	-2.8	0.1	-0.002	-1.937	1.714
0.0540	-3.2	-0.2	-0.004	-1.953	1.720
0.0677	-3.5	-0.5	0.000	-1.968	1.723
0.0815	-3.7	-0.7	-0.003	-2.001	1.733
0.0950	-3.8	-0.9	0.001	-2.006	1.734
0.1158	-4.0	-1.1	0.002	-2.029	1.740
0.1362	-4.1	-1.2	0.004	-2.047	1.744
0.1773	-4.0	-1.3	0.002	-2.073	1.752
0.2181	-3.9	-1.2	0.003	-2.079	1.754
0.2595	-3.9	-1.2	0.001	-2.075	1.753
0.3005	-4.1	-1.1	-0.002	-2.070	1.752
0.3416	-4.1	-1.1	0.007	-2.055	1.746
0.3824	-4.1	-1.0	0.003	-2.031	1.740
0.4233	-4.2	-1.0	0.005	-2.000	1.730
0.4625	-4.5	-0.9	0.004	-1.974	1.723
0.5080	-4.4	-0.7	0.001	-1.921	1.709

Five-Hole Probe Data
(continued)

ANGULAR PLANE: 90.000 DEG
RADIUS/CYLINDER DIA: 0.596

Y/D	PHI DEG	THETA DEG	CPT	CPS	U/U ₀
0.0089	0.4	7.7	0.029	-1.469	1.562
0.0144	-0.9	6.9	0.037	-1.512	1.573
0.0200	-2.0	6.1	0.041	-1.526	1.576
0.0252	-2.3	5.5	0.043	-1.537	1.579
0.0335	-2.9	4.5	0.043	-1.549	1.583
0.0417	-3.3	3.7	0.040	-1.561	1.588
0.0500	-3.4	3.0	0.037	-1.563	1.589
0.0638	-3.6	2.1	0.027	-1.567	1.594
0.0773	-3.7	1.7	0.013	-1.602	1.609
0.0911	-3.7	1.5	0.004	-1.611	1.614
0.1046	-3.5	1.3	0.001	-1.629	1.621
0.1184	-3.4	1.3	-0.001	-1.634	1.623
0.1322	-3.3	1.2	-0.002	-1.655	1.630
0.1731	-3.3	0.8	0.003	-1.685	1.638
0.2142	-3.0	0.9	-0.001	-1.703	1.645
0.2554	-2.9	1.0	0.005	-1.708	1.644
0.3373	-2.9	1.0	0.002	-1.717	1.648
0.4196	-3.0	1.2	0.004	-1.697	1.641
0.5037	-3.2	1.5	0.003	-1.645	1.625

Five-Hole Probe Data
(continued)

ANGULAR PLANE: 90.000 DEG
RADIUS/CYLINDER DIA: 0.638

Y/D	PHI DEG	THETA DEG	CPT	CPS	U/U ₀
0.0106	-0.1	11.3	0.050	-1.304	1.502
0.0150	-1.1	10.5	0.083	-1.328	1.498
0.0192	-1.8	9.4	0.105	-1.328	1.491
0.0233	-2.5	8.3	0.117	-1.336	1.490
0.0274	-2.7	7.4	0.125	-1.343	1.489
0.0341	-3.4	6.3	0.134	-1.350	1.489
0.0410	-3.7	5.2	0.132	-1.351	1.490
0.0478	-4.2	4.5	0.129	-1.358	1.493
0.0548	-4.3	3.5	0.116	-1.363	1.499
0.0682	-4.6	2.3	0.095	-1.378	1.511
0.0821	-4.6	1.3	0.068	-1.386	1.522
0.0955	-4.5	0.7	0.040	-1.401	1.537
0.1367	-3.9	0.2	-0.007	-1.431	1.561
0.1778	-3.6	0.2	-0.005	-1.444	1.565
0.2187	-3.5	0.3	-0.005	-1.450	1.567
0.2599	-3.5	0.5	0.002	-1.467	1.570
0.3417	-3.3	0.7	-0.001	-1.455	1.567
0.4242	-3.3	1.1	-0.003	-1.432	1.560
0.5084	-3.4	1.5	0.001	-1.381	1.543

Five-Hole Probe Data
(continued)

ANGULAR PLANE: 90.000 DEG
RADIUS/CYLINDER DIA: 0.681

Y/D	PHI DEG	THETA DEG	CPT	CPS	U/U ₀
0.0090	0.3	17.0	0.094	-1.121	1.424
0.0144	-1.0	15.6	0.151	-1.148	1.413
0.0200	-2.0	13.8	0.197	-1.161	1.402
0.0280	-2.9	11.5	0.243	-1.174	1.390
0.0363	-3.9	9.5	0.278	-1.177	1.379
0.0446	-4.2	7.7	0.267	-1.179	1.383
0.0528	-4.8	6.3	0.251	-1.185	1.391
0.0610	-4.9	5.0	0.234	-1.192	1.399
0.0690	-5.1	4.0	0.199	-1.210	1.418
0.0773	-5.1	3.1	0.159	-1.211	1.432
0.0856	-5.0	2.4	0.135	-1.222	1.445
0.0937	-4.5	2.0	0.090	-1.219	1.459
0.1019	-4.5	1.7	0.063	-1.231	1.472
0.1102	-4.4	1.5	0.049	-1.239	1.480
0.1184	-4.3	1.4	0.023	-1.252	1.493
0.1321	-4.1	1.4	0.009	-1.245	1.495
0.1454	-3.7	1.5	0.001	-1.255	1.501
0.1593	-3.3	1.4	-0.001	-1.262	1.505
0.1732	-3.4	1.3	-0.002	-1.267	1.507
0.2142	-2.8	1.6	-0.007	-1.271	1.509
0.2552	-2.6	1.7	-0.002	-1.282	1.511
0.3375	-2.5	2.1	-0.004	-1.285	1.513
0.4195	-2.5	2.3	0.002	-1.261	1.503
0.5039	-2.6	2.6	0.006	-1.247	1.497

Five-Hole Probe Data
(continued)

ANGULAR PLANE: 90.000 DEG
RADIUS/CYLINDER DIA: 0.723

Y/D	FHI DEG	THETA DEG	CPT	CPS	U/U ₀
0.0085	0.2	21.2	0.138	-1.066	1.389
0.0144	-1.4	19.7	0.219	-1.096	1.370
0.0198	-2.7	17.6	0.303	-1.099	1.340
0.0282	-4.0	14.6	0.377	-1.109	1.316
0.0363	-5.3	12.4	0.417	-1.112	1.302
0.0445	-6.1	9.3	0.425	-1.124	1.303
0.0528	-6.8	7.2	0.408	-1.131	1.313
0.0610	-6.9	5.0	0.371	-1.146	1.332
0.0692	-6.7	3.2	0.323	-1.149	1.351
0.0773	-6.0	2.1	0.280	-1.152	1.368
0.0855	-5.6	1.2	0.233	-1.150	1.385
0.0939	-5.3	0.6	0.185	-1.150	1.402
0.1021	-5.0	0.3	0.129	-1.150	1.422
0.1102	-4.7	0.0	0.089	-1.150	1.436
0.1184	-4.5	-0.2	0.061	-1.158	1.448
0.1322	-4.0	-0.1	0.023	-1.156	1.460
0.1457	-3.5	0.1	0.003	-1.160	1.468
0.1595	-3.2	0.3	-0.001	-1.151	1.467
0.1730	-3.0	0.3	-0.001	-1.155	1.468
0.2142	-2.8	0.8	-0.001	-1.158	1.469
0.2554	-2.6	1.2	0.001	-1.154	1.468
0.3373	-2.4	1.7	0.002	-1.151	1.466
0.4194	-2.6	2.0	0.004	-1.132	1.459
0.5042	-2.6	2.3	0.003	-1.101	1.448

Five-Hole Probe Data
(continued)

ANGULAR PLANE: 90.000 DEG
RADIUS/CYLINDER DIA: 0.766

Y/D	PHI DEG	THETA DEG	CPT	CPS	U/Uo
0.0091	0.8	27.2	0.241	-1.044	1.343
0.0146	-0.2	26.2	0.328	-1.060	1.316
0.0202	-1.4	24.9	0.444	-1.080	1.279
0.0254	-2.4	23.5	0.532	-1.085	1.246
0.0309	-3.4	21.3	0.615	-1.108	1.222
0.0365	-4.4	18.9	0.667	-1.122	1.206
0.0420	-5.7	15.2	0.724	-1.143	1.191
0.0475	-6.5	11.6	0.744	-1.153	1.187
0.0527	-7.1	8.4	0.721	-1.164	1.201
0.0585	-7.4	5.2	0.661	-1.158	1.224
0.0637	-7.5	2.8	0.594	-1.143	1.245
0.0692	-6.1	1.0	0.548	-1.124	1.255
0.0776	-5.4	-0.2	0.453	-1.122	1.292
0.0857	-4.7	-1.0	0.373	-1.098	1.313
0.0938	-4.2	-1.1	0.294	-1.087	1.339
0.1022	-3.8	-1.1	0.238	-1.069	1.353
0.1104	-3.2	-1.1	0.175	-1.064	1.374
0.1187	-3.3	-1.0	0.118	-1.061	1.394
0.1321	-2.6	-0.7	0.047	-1.046	1.414
0.1459	-2.3	0.3	0.014	-1.042	1.424
0.1595	-2.1	0.1	0.002	-1.037	1.427
0.1733	-2.1	0.4	-0.004	-1.033	1.427
0.2144	-2.0	1.1	-0.002	-1.031	1.425
0.2556	-2.0	1.5	-0.006	-1.028	1.426
0.3376	-1.7	2.0	0.000	-1.021	1.422
0.4196	-2.0	2.4	0.003	-1.009	1.461
0.5041	-2.1	2.7	0.000	-0.989	1.411

Five-Hole Probe Data
(continued)

ANGULAR PLANE: 90.000 DEG
RADIUS/CYLINDER DIA: 0.787

```
=====
```

Y/D	PHI DEG	THETA DEG	CPT	CPS	U/U ₀
0.0085	1.8	27.9	0.321	-1.041	1.311
0.0140	1.1	27.4	0.366	-1.064	1.303
0.0198	1.0	26.5	0.476	-1.087	1.269
0.0250	0.6	25.2	0.570	-1.100	1.237
0.0307	0.2	23.3	0.658	-1.118	1.208
0.0361	-0.7	20.5	0.740	-1.136	1.182
0.0416	-1.3	16.8	0.795	-1.158	1.167
0.0471	-2.8	12.3	0.825	-1.173	1.161
0.0527	-2.9	8.1	0.823	-1.169	1.160
0.0582	-3.6	4.2	0.766	-1.160	1.181
0.0634	-3.5	1.5	0.687	-1.137	1.204
0.0690	-3.3	-0.3	0.613	-1.122	1.228
0.0744	-3.0	-1.7	0.542	-1.105	1.251
0.0799	-3.2	-2.3	0.486	-1.092	1.267
0.0855	-2.8	-2.7	0.418	-1.077	1.288
0.0907	-2.7	-2.7	0.369	-1.062	1.302
0.0962	-2.6	-2.6	0.316	-1.053	1.318
0.1018	-2.4	-2.4	0.275	-1.043	1.330
0.1101	-2.0	-2.2	0.209	-1.027	1.348
0.1184	-2.0	-1.9	0.143	-1.021	1.370
0.1318	-1.8	-1.4	0.068	-1.005	1.392
0.1456	-1.9	-1.0	0.019	-0.998	1.407
0.1593	-1.8	-0.4	0.001	-0.985	1.409
0.1730	-1.8	0.0	-0.006	0.985	1.411
0.2141	-1.8	0.9	-0.006	0.981	1.409
0.2552	-2.4	1.3	-0.001	-0.994	1.412
0.3372	-1.9	1.7	0.000	-0.971	1.404
0.4194	-2.0	2.2	0.003	-0.961	1.399
0.5041	-2.2	2.4	0.005	-0.946	1.393

Five-Hole Probe Data
(continued)

ANGULAR PLANE: 90.000 DEG
RADIUS/CYLINDER DIA: 0.809

Y/D	PHI DEG	THETA DEG	CPT	CPS	U/Uc
0.0085	3.2	24.9	0.518	-1.034	1.232
0.0144	3.6	25.6	0.456	-1.061	1.267
0.0200	4.5	25.0	0.504	-1.062	1.248
0.0254	5.0	23.8	0.571	-1.082	1.229
0.0309	5.3	21.9	0.635	-1.094	1.208
0.0362	5.6	19.4	0.684	-1.104	1.192
0.0417	5.3	15.8	0.749	-1.122	1.172
0.0472	4.6	11.8	0.756	-1.136	1.174
0.0528	4.0	8.3	0.745	-1.125	1.175
0.0582	2.9	4.6	0.711	-1.117	1.186
0.0638	2.4	2.0	0.636	-1.091	1.206
0.0692	1.6	0.0	0.591	-1.088	1.224
0.0772	1.2	-1.6	0.504	-1.057	1.246
0.0855	0.5	-2.2	0.417	-1.036	1.272
0.0939	-0.1	-2.2	0.350	-1.028	1.295
0.1019	-0.1	-2.2	0.270	-1.006	1.318
0.1102	-0.2	-1.9	0.200	-0.986	1.336
0.1184	-0.6	-1.8	0.141	-0.985	1.358
0.1322	-0.9	-1.4	0.065	-0.969	1.380
0.1451	-1.1	-1.1	0.024	-0.967	1.394
0.1596	-1.2	-0.6	0.001	-0.957	1.399
0.1731	-1.2	-0.1	0.000	-0.955	1.398
0.2140	-1.6	0.9	0.003	-0.950	1.395
0.2554	-1.8	1.2	-0.003	-0.948	1.397
0.3373	-2.1	1.9	0.001	-0.935	1.391
0.4195	-2.2	2.3	-0.001	-0.927	1.389
0.5041	-2.4	2.8	0.004	-0.905	1.379

Five-Hole Probe Data
(continued)

ANGULAR PLANE: 90.000 DEG
RADIUS/CYLINDER DIA: 0.851

Y/D	PHI DEG	THETA DEG	CPT	CPS	U/U ₀
0.0092	2.1	13.6	0.652	-0.887	1.111
0.0146	1.9	15.1	0.568	-0.917	1.161
0.0201	2.1	16.6	0.546	-0.927	1.175
0.0256	3.1	16.8	0.548	-0.931	1.176
0.0311	3.5	16.6	0.529	-0.922	1.180
0.0364	4.8	16.0	0.543	-0.925	1.176
0.0420	4.7	14.5	0.536	-0.919	1.176
0.0474	5.4	12.7	0.524	-0.921	1.182
0.0530	5.0	11.0	0.514	-0.919	1.185
0.0585	5.1	9.2	0.485	-0.909	1.193
0.0637	4.7	7.4	0.459	-0.896	1.199
0.0695	4.2	6.0	0.421	-0.892	1.213
0.0774	3.9	4.6	0.366	-0.891	1.235
0.0858	3.3	3.4	0.311	-0.886	1.255
0.0940	2.3	2.6	0.246	-0.877	1.277
0.1021	1.9	2.0	0.198	-0.874	1.295
0.1104	1.4	1.3	0.124	-0.874	1.323
0.1186	1.1	0.9	0.087	-0.871	1.336
0.1321	0.6	0.7	0.031	-0.870	1.356
0.1460	0.4	0.6	0.008	-0.869	1.364
0.1597	-0.1	0.7	-0.007	-0.867	1.369
0.1733	-0.3	0.8	-0.007	-0.865	1.369
0.2142	-0.8	1.4	-0.007	-0.859	1.366
0.2556	-1.2	1.7	-0.008	-0.855	1.365
0.3375	-1.8	2.3	0.002	-0.852	1.361
0.4195	-1.9	2.7	0.000	-0.844	1.358
0.5040	-2.1	2.9	-0.001	-0.827	1.352

Five-Hole Probe Data
(continued)

ANGULAR PLANE: 90.000 DEG
RADIUS/CYLINDER DIA: 0.894

```
=====
```

Y/D	FHI DEG	THETA DEG	CPT	CPS	U/Uo
0.0086	0.6	10.7	0.583	-0.796	1.101
0.0145	0.0	11.6	0.490	-0.817	1.152
0.0200	-0.2	12.1	0.479	-0.832	1.164
0.0283	-0.3	12.0	0.476	-0.844	1.170
0.0363	0.1	11.5	0.440	-0.846	1.186
0.0446	0.6	10.4	0.420	-0.834	1.189
0.0530	0.8	9.0	0.391	-0.828	1.199
0.0612	0.9	7.6	0.359	-0.824	1.211
0.0692	1.3	6.5	0.306	-0.830	1.235
0.0774	1.3	5.5	0.272	-0.818	1.243
0.0857	1.3	4.6	0.206	-0.815	1.268
0.0940	1.2	3.9	0.175	-0.812	1.279
0.1022	1.1	3.2	0.118	-0.797	1.296
0.1103	1.4	2.7	0.092	-0.811	1.311
0.1185	1.0	2.1	0.049	-0.806	1.326
0.1321	1.0	1.5	0.017	-0.806	1.338
0.1459	0.5	1.3	0.002	-0.798	1.340
0.1597	0.4	1.2	-0.005	-0.803	1.345
0.1732	-0.1	1.2	0.003	-0.811	1.345
0.2144	-0.7	1.3	-0.001	-0.800	1.342
0.2553	-1.0	1.5	0.004	-0.796	1.339
0.3375	-1.6	1.9	-0.002	-0.796	1.341
0.4196	-2.0	2.3	0.004	-0.783	1.334
0.5040	-2.1	2.7	-0.007	-0.768	1.332

Five-Hole Probe Data
(continued)

ANGULAR PLANE: 90.000 DEG
RADIUS/CYLINDER DIA: 0.936

Y/D	PHI DEG	THETA DEG	CFT	CPS	U/U ₀
0.0088	0.9	11.0	0.619	-0.711	1.045
0.0142	0.1	12.1	0.517	-0.731	1.102
0.0198	-0.3	12.4	0.459	-0.740	1.132
0.0278	-0.4	11.6	0.425	-0.743	1.148
0.0360	-0.5	10.4	0.398	-0.750	1.163
0.0443	-0.2	9.0	0.365	-0.751	1.177
0.0527	-0.3	7.7	0.324	-0.740	1.190
0.0609	0.1	6.9	0.287	-0.743	1.207
0.0771	0.3	5.6	0.199	-0.743	1.243
0.0855	0.4	4.9	0.155	-0.739	1.258
0.0937	0.6	4.4	0.124	-0.737	1.270
0.1017	0.5	4.0	0.087	-0.738	1.285
0.1100	0.5	3.5	0.052	-0.737	1.298
0.1183	0.6	3.2	0.028	-0.735	1.307
0.1321	0.5	2.8	0.006	-0.740	1.316
0.1456	0.4	2.6	-0.002	-0.737	1.319
0.1594	0.2	2.3	-0.006	-0.737	1.320
0.1730	0.1	2.2	-0.007	-0.739	1.321
0.2140	-0.4	2.2	-0.002	-0.736	1.318
0.2549	-0.7	2.1	-0.001	-0.735	1.318
0.3373	-1.1	2.3	-0.002	-0.729	1.316
0.4193	-1.5	2.5	0.000	-0.724	1.313
0.5037	-1.7	2.9	0.003	-0.715	1.308

Five-Hole Probe Data
(continued)

ANGULAR PLANE: 90.000 DEG
RADIUS/CYLINDER DIA: 1.021

Y/D	PHI DEG	THETA DEG	CPT	CPS	U/Uc
0.0083	1.5	8.5	0.683	-0.596	0.956
0.0111	0.5	9.2	0.610	-0.615	1.003
0.0166	0.1	10.0	0.500	-0.627	1.062
0.0221	-0.2	10.2	0.439	-0.642	1.097
0.0304	-0.3	9.5	0.386	-0.642	1.121
0.0384	-0.2	8.7	0.347	-0.639	1.137
0.0467	-0.1	7.8	0.308	-0.644	1.156
0.0549	-0.1	6.9	0.271	-0.640	1.170
0.0632	-0.1	6.3	0.231	-0.646	1.190
0.0714	-0.2	5.6	0.200	-0.640	1.200
0.0794	0.1	5.1	0.157	-0.639	1.218
0.0878	0.0	4.5	0.131	-0.639	1.228
0.0960	0.0	4.2	0.101	-0.643	1.242
0.1043	-0.2	3.8	0.090	-0.643	1.246
0.1123	-0.1	3.6	0.063	-0.641	1.256
0.1206	-0.1	3.3	0.041	-0.645	1.266
0.1341	-0.2	3.0	0.035	-0.638	1.266
0.1479	-0.2	2.9	0.010	-0.638	1.276
0.1617	-0.3	2.8	0.000	-0.639	1.280
0.1753	-0.2	2.7	0.002	-0.643	1.281
0.2164	-0.4	2.6	-0.007	-0.648	1.286
0.2575	-0.6	2.6	-0.001	-0.652	1.286
0.3395	-1.0	2.7	0.001	-0.650	1.284
0.4216	-1.4	2.8	0.002	-0.641	1.281
0.5057	-1.7	3.0	-0.001	-0.629	1.277

Five-Hole Probe Data
(continued)

ANGULAR PLANE: 90.000 DEG
RADIUS/CYLINDER DIA: 1.106

Y/D	PHI DEG	THETA DEG	CPT	CPS	U/U ₀
0.0083	1.4	6.8	0.664	-0.525	0.928
0.0103	0.5	7.2	0.600	-0.542	0.971
0.0159	-0.1	8.0	0.496	-0.559	1.031
0.0214	-0.1	8.0	0.440	-0.566	1.061
0.0293	0.0	7.6	0.392	-0.567	1.084
0.0376	-0.2	7.7	0.366	-0.568	1.096
0.0461	0.0	6.2	0.328	-0.567	1.113
0.0542	0.2	5.7	0.324	-0.564	1.114
0.0625	0.0	5.0	0.297	-0.569	1.128
0.0707	0.1	4.5	0.278	-0.569	1.136
0.0787	0.2	4.2	0.241	-0.567	1.152
0.0870	0.1	3.8	0.223	-0.571	1.161
0.0954	0.1	3.5	0.209	-0.573	1.168
0.1033	0.0	3.3	0.181	-0.572	1.179
0.1117	0.0	3.0	0.145	-0.569	1.193
0.1199	-0.1	2.9	0.132	-0.570	1.199
0.1337	-0.3	2.7	0.090	-0.572	1.218
0.1472	-0.3	2.5	0.045	-0.547	1.237
0.1611	-0.5	2.5	0.023	-0.573	1.245
0.1746	-0.6	2.5	0.005	-0.573	1.252
0.2157	-0.7	2.3	-0.001	-0.575	1.255
0.2569	-0.9	2.3	0.000	-0.576	1.255
0.3388	-1.1	2.2	0.000	-0.572	1.254
0.4209	-1.2	2.3	0.002	-0.569	1.252
0.5054	-1.4	2.5	0.002	-0.562	1.249

Five-Hole Probe Data
(continued)

ANGULAR PLANE: 90.000 DEG
RADIUS/CYLINDER DIA: 1.191

Y/D	FHI DEG	THETA DEG	CPT	CPS	U/U ₀
0.0084	1.0	5.2	0.695	-0.477	0.884
0.0105	0.4	5.6	0.641	-0.488	0.920
0.0161	-0.4	6.3	0.547	-0.507	0.979
0.0216	-0.4	6.5	0.475	-0.508	1.016
0.0296	-0.3	6.2	0.422	-0.512	1.044
0.0379	-0.3	5.8	0.381	-0.514	1.064
0.0462	-0.4	5.3	0.331	-0.514	1.088
0.0541	-0.3	5.0	0.286	-0.509	1.106
0.0627	-0.3	4.7	0.263	-0.511	1.117
0.0706	-0.4	4.5	0.200	-0.510	1.145
0.0789	-0.3	4.2	0.172	-0.507	1.155
0.0873	-0.1	4.1	0.124	-0.508	1.176
0.0955	-0.2	4.0	0.113	-0.516	1.184
0.1035	-0.4	3.8	0.092	-0.520	1.195
0.1118	-0.4	3.8	0.090	-0.519	1.195
0.1201	-0.5	3.6	0.050	-0.521	1.212
0.1336	-0.4	3.7	0.027	-0.522	1.223
0.1474	-0.4	3.2	0.004	-0.513	1.228
0.1609	-0.3	3.0	-0.006	-0.518	1.235
0.1784	-0.4	2.8	-0.007	-0.517	1.235
0.2159	-0.5	2.6	-0.005	-0.518	1.234
0.2568	-0.6	2.5	-0.001	-0.519	1.233
0.3391	-1.0	2.4	-0.002	-0.516	1.232
0.4211	-1.2	2.5	0.003	-0.509	1.227
0.5052	-1.4	2.6	0.001	-0.506	1.227

Five-Hole Probe Data
(continued)

ANGULAR PLANE: 90.000 DEG
RADIUS/CYLINDER DIA: 1.362

Y/D	FHI DEG	THETA DEG	CPT	CPS	U/U ₀
0.0085	0.5	5.2	0.635	-0.404	0.877
0.0147	-0.6	5.7	0.519	-0.422	0.951
0.0216	-0.9	5.9	0.429	-0.431	1.001
0.0296	-1.0	5.9	0.375	-0.432	1.028
0.0378	-1.0	5.6	0.331	-0.433	1.050
0.0462	-1.0	5.3	0.291	-0.435	1.070
0.0544	-0.9	5.0	0.250	-0.434	1.089
0.0625	-0.8	4.7	0.233	-0.432	1.099
0.0707	-0.9	4.6	0.199	-0.435	1.112
0.0790	-0.8	4.3	0.177	-0.438	1.123
0.0873	-0.8	4.1	0.156	-0.433	1.130
0.0952	-0.6	3.9	0.125	-0.431	1.143
0.1035	-0.7	3.8	0.103	-0.435	1.154
0.1117	-0.6	3.7	0.081	-0.436	1.164
0.1201	-0.6	3.6	0.068	-0.434	1.169
0.1337	-0.5	3.5	0.040	-0.436	1.182
0.1475	-0.6	3.4	0.008	-0.436	1.195
0.1611	-0.6	3.4	-0.004	-0.435	1.200
0.1748	-0.6	3.4	-0.006	-0.438	1.202
0.2159	-0.6	3.4	-0.003	-0.435	1.199
0.2569	-0.6	3.5	-0.003	-0.434	1.199
0.3391	-0.7	3.4	0.001	-0.434	1.197
0.4212	-0.7	3.5	-0.001	-0.430	1.196
0.5061	-0.9	3.3	0.002	-0.425	1.193

Five-Hole Probe Data
(continued)

ANGULAR PLANE: 90.000 DEG
RADIUS/CYLINDER DIA: 1.532

=====

Y/D	PHI DEG	THETA DEG	CPT	CPS	U/U ₀
0.0084	1.7	3.9	0.617	-0.337	0.848
0.0149	0.3	4.5	0.498	-0.356	0.926
0.0218	-0.2	4.7	0.430	-0.362	0.966
0.0300	-0.3	4.6	0.365	-0.367	1.001
0.0381	-0.4	4.5	0.322	-0.367	1.023
0.0465	-0.5	4.3	0.271	-0.365	1.046
0.0547	-0.4	4.1	0.229	-0.367	1.066
0.0629	-0.4	3.9	0.199	-0.370	1.082
0.0711	-0.6	3.7	0.158	-0.370	1.101
0.0792	-0.2	3.6	0.136	-0.366	1.109
0.0875	-0.2	3.5	0.103	-0.368	1.125
0.0955	-0.3	3.4	0.077	-0.362	1.134
0.1039	-0.3	3.3	0.054	-0.361	1.143
0.1121	-0.3	3.1	0.029	-0.364	1.155
0.1204	-0.2	3.0	0.019	-0.371	1.163
0.1339	-0.1	3.0	0.003	-0.368	1.168
0.1478	-0.2	3.1	-0.004	-0.372	1.173
0.1613	-0.2	3.2	-0.005	-0.368	1.172
0.1751	-0.1	3.2	-0.007	-0.369	1.173
0.2161	0.0	3.3	-0.005	-0.364	1.170
0.2571	-0.2	3.2	-0.002	-0.364	1.169
0.3393	-0.4	3.1	-0.005	-0.368	1.172
0.4215	-0.3	3.2	-0.002	-0.359	1.167
0.5060	-0.5	3.4	-0.008	-0.359	1.169

Five-Hole Probe Data
(continued)

ANGULAR PLANE: 90.000 DEG
RADIUS/CYLINDER DIA: 1.702

Y/D	PHI DEG	THETA DEG	CPT	CPS	U/U ₀
0.0085	1.7	3.1	0.661	-0.302	0.800
0.0150	0.5	3.6	0.550	-0.317	0.876
0.0220	0.3	3.6	0.483	-0.331	0.921
0.0300	0.1	3.5	0.427	-0.324	0.947
0.0382	0.3	3.3	0.364	-0.318	0.977
0.0465	0.2	3.2	0.347	-0.325	0.989
0.0549	0.2	3.0	0.306	-0.324	1.009
0.0631	0.4	2.8	0.258	-0.322	1.031
0.0712	0.3	2.7	0.216	-0.319	1.050
0.0794	0.3	2.6	0.188	-0.321	1.064
0.0876	0.3	2.5	0.165	-0.326	1.077
0.0959	0.3	2.4	0.133	-0.326	1.092
0.1039	0.1	2.4	0.105	-0.325	1.105
0.1122	0.1	2.4	0.076	-0.326	1.118
0.1206	0.2	2.3	0.052	-0.319	1.126
0.1340	0.2	2.3	0.019	-0.326	1.143
0.1479	0.2	2.3	-0.005	-0.325	1.153
0.1613	0.2	2.3	0.000	-0.323	1.150
0.1752	0.2	2.3	0.001	-0.325	1.151
0.2163	0.1	2.4	-0.007	-0.326	1.154
0.2573	0.1	2.6	-0.005	-0.324	1.153
0.3394	0.2	2.3	-0.002	-0.320	1.149
0.4216	0.1	2.4	0.003	-0.325	1.149
0.5061	-0.3	2.7	-0.006	-0.322	1.152

Five-Hole Probe Data
(continued)

ANGULAR PLANE: 90.000 DEG
RADIUS/CYLINDER DIA: 2.043

Y/D	PHI DEG	THETA DEG	CPT	CPS	U/U ₀
0.0083	2.0	1.1	0.611	-0.253	0.801
0.0142	1.0	1.4	0.522	-0.268	0.864
0.0211	0.3	1.6	0.444	-0.274	0.911
0.0294	0.2	1.6	0.369	-0.278	0.953
0.0374	0.3	1.6	0.309	-0.274	0.982
0.0458	-0.1	1.5	0.249	-0.276	1.013
0.0540	0.0	1.4	0.208	-0.281	1.036
0.0623	-0.1	1.4	0.168	-0.278	1.054
0.0702	-0.1	1.3	0.129	-0.279	1.072
0.0785	0.0	1.3	0.091	-0.281	1.091
0.0868	-0.1	1.2	0.062	-0.282	1.105
0.0951	0.0	1.1	0.034	-0.281	1.117
0.1031	-0.2	1.2	0.023	-0.282	1.122
0.1115	-0.1	1.1	0.006	-0.283	1.130
0.1225	0.0	1.1	-0.001	-0.282	1.133
0.1360	-0.1	1.0	-0.001	-0.282	1.133
0.1497	-0.1	1.0	-0.002	-0.282	1.134
0.1633	-0.1	1.0	-0.003	-0.278	1.132
0.1772	-0.2	1.0	-0.002	-0.276	1.131
0.2183	-0.2	1.0	-0.005	-0.281	1.134
0.2593	-0.4	1.0	-0.001	-0.276	1.130
0.3413	-0.2	0.8	0.002	-0.277	1.130
0.4235	0.1	0.8	0.004	-0.284	1.131
0.5069	-0.2	1.0	-0.006	-0.272	1.130

Five-Hole Probe Data
(continued)

ANGULAR PLANE: 90.000 DEG
RADIUS/CYLINDER DIA: 2.375

Y/D	PHI DEG	THETA DEG	CPT	CPS	U/U ₀
0.0085	2.1	2.0	0.666	-0.230	0.751
0.0142	1.0	2.0	0.560	-0.244	0.826
0.0209	0.4	2.1	0.483	-0.249	0.875
0.0293	0.2	2.1	0.414	-0.257	0.918
0.0372	0.1	2.0	0.354	-0.256	0.950
0.0456	0.1	2.0	0.314	-0.253	0.969
0.0538	0.0	1.9	0.261	-0.253	0.996
0.0621	0.0	1.9	0.227	-0.255	1.014
0.0703	-0.1	1.8	0.191	-0.256	1.032
0.0783	-0.1	1.7	0.161	-0.257	1.047
0.0867	-0.2	1.7	0.120	-0.256	1.066
0.0949	-0.1	1.7	0.086	-0.257	1.082
0.1092	0.0	1.5	0.060	-0.255	1.093
0.1113	-0.1	1.5	0.034	-0.254	1.105
0.1251	0.0	1.4	0.008	-0.255	1.117
0.1386	-0.1	1.3	-0.004	-0.254	1.122
0.1524	0.0	1.3	-0.007	-0.254	1.123
0.1659	0.0	1.2	-0.003	-0.255	1.122
0.1798	0.0	1.1	-0.005	-0.255	1.122
0.2208	0.0	1.1	-0.002	-0.255	1.121
0.2619	0.0	1.1	0.000	-0.252	1.119
0.3440	-0.1	1.1	-0.001	-0.252	1.119
0.4261	-0.1	0.9	0.000	-0.251	1.118
0.5082	-0.1	0.7	-0.002	-0.252	1.120

1. Report No. NASA CR-3986	2. Government Accession No.	3. Recipient's Catalog No.	
4. Title and Subtitle Measurements of a Turbulent Horseshoe Vortex Formed Around a Cylinder		5. Report Date June 1986	
		6. Performing Organization Code	
7. Author(s) W.A. Eckerle and L.S. Langston		8. Performing Organization Report No. None	
		10. Work Unit No.	
9. Performing Organization Name and Address University of Connecticut Department of Mechanical Engineering Storrs, Connecticut 06268		11. Contract or Grant No. NSG-3238	
		13. Type of Report and Period Covered Contractor Report	
12. Sponsoring Agency Name and Address National Aeronautics and Space Administration Washington, D.C. 20546		14. Sponsoring Agency Code 505-62-21 (E-3027)	
		15. Supplementary Notes Final report. Project Manager, Louis J. Goldman, Internal Fluid Mechanics Division, NASA Lewis Research Center, Cleveland, Ohio 44135. W.A. Eckerle, United Technologies Research Center, East Hartford, Connecticut 06108; L.S. Langston, University of Connecticut, Department of Mechanical Engineering, Storrs, Connecticut 06268.	
16. Abstract An experimental investigation was conducted to characterize a symmetrical horseshoe vortex system in front of and around a single large-diameter right cylinder centered between the sidewalls of a wind tunnel. Surface flow visualization and surface static pressure measurements as well as extensive mean velocity and pressure measurements in and around the vortex system were acquired. The results lend new insight into the formation and development of the vortex system. Contrary to what has been assumed previously, a strong vortex was not identified in the streamwise plane of symmetry, but started a significant angular distance away from it. Rather than the multiple vortex systems reported by others, only a single primary vortex and saddle point were found. The scale of the separation process at the saddle point was much smaller than the scale of the approaching boundary layer thickness. Results of the present study not only shed light on such phenomena as the nonsymmetrical endwall flow in axial turbomachinery but can also be used as a test case for three-dimensional computational fluid mechanics computer codes.			
17. Key Words (Suggested by Author(s)) Horseshoe vortex formation; Cylinder on endwall junction flows; Three-dimensional aerodynamic measurements		18. Distribution Statement Unclassified - unlimited STAR Category 02	
19. Security Classif. (of this report) Unclassified	20. Security Classif. (of this page) Unclassified	21. No. of pages 206	22. Price* A10

*For sale by the National Technical Information Service, Springfield, Virginia 22161

NASA-Langley, 1986

End of Document